# Imaging Glycogenesis as a Novel Biomarker of Drug-induced Senescence/Quiescence

A dissertation submitted for the Degree of Doctor of Philosophy

by

Cen Chen

December 2020

Department of Surgery and Cancer

Faculty of Medicine

Imperial College London

## Declaration

I declare that the data presented in this thesis is my own and original work, except where acknowledged otherwise. The work has not been submitted for any other degrees from Imperial College London or any other university.

## Abstract

Cellular senescence, which is a state of irreversible growth arrest in response to diverse stimuli, has been implicated in many age-related diseases and shown to play complex roles in tumorigenesis. Since the first description of senescence by Hayflick and colleagues in 1961, significant progress has been made in understanding the characteristics and functions of cellular senescence. However, efforts to identify senescence remain limited due to a lack of robust and universal biomarkers for this cell fate. As enhanced glycogenesis has been associated with cell growth arrest, it has been hypothesized in this thesis that PET imaging agents that measure glycogenesis could be a potential tool for assessment of senescence-directed anticancer therapies.

The profile of glycogenesis of a panel of cancer cell lines characterised by various genetic backgrounds was first assessed. Cancer cell lines showed distinct patterns of glycogenesis, among which an AKT-GSK3β-dependent regulation of glycogen synthase (GYS1) through PI3K pathway was observed in PTEN-null tumour cells. A cell growth-related regulation of glycogenesis was found in the tested cells, in which cells when cultured under the G0/G1 phase arrest increased glycogen synthesis via a GYS1-dependent manner and thereby led to an increase in glycogen accumulation. Moreover, tumour cells under hypoxic condition were more susceptible to GYS1 knockdown as glycogenesis was more significantly attenuated under hypoxia than normoxic condition.

Additionally, one of the four tested anticancer drugs, namely palbociclib, was shown to dose- and time-dependently induce senescence in ER-positive breast cancer cell lines *in vitro,* as shown by the presence of senescence-like morphology, increased SA-β-gal activity and upregulation of p21 expression. An increase in glycogenesis was found in response to palbociclib treatment via a G6P-dependent elevation in GYS1 activity.

Correspondingly, $^{18}$F-NFTG, a glycogenesis-based PET radiotracer previously developed by our group, was largely accumulated in palbociclib-induced quiescent/senescent cells. To extend the exploration, the attempts were made to develop and evaluate a novel senescence-specific probe based on detection of lipofuscin formation. Not only did the non-radioactive reference compound [$^{19}$F]FET-SBB show specific staining of lipofuscin aggregates in

palbociclib-treated cell, but also the radiolabelled [$^{18}$F]FET-SBB was significantly retained, suggesting potential application of [$^{18}$F]FET-SBB in targeting senescence.

In summary, while senescence mechanisms can be varied, drug-induced senescence is detectable *in vitro* as increased glycogenesis and lipofuscin formation in some contexts. These methods described here have potential for translation *in vivo*.

## Acknowledgement

I would like to take this opportunity to thank my supervisor, Professor Eric Aboagye, for his invaluable guidance and support throughout my PhD project. I would also like to thank my co-supervisor Dr. Kathrin Heinzmann for her helpful advice on my routine and especially my laboratory work. It is truly a great honour for me to have had the opportunity to learn a great amount from Eric and Kathrin.

I am grateful to Dr. Louis Allott and Dr. Diana Brickute for their inputs in developing and synthesizing all the radiotracers used in this thesis. Without their support on all the chemistry related work, the project would not have been possible. I would also like to thank Chris Barnes for his inputs in radiolabelling, to Dr. Laurence Carroll, for synthesising [$^{18}$F]NFTG at the start of my project. Many thanks go to Dr. Marta Braga and Dr. Gilberto Serrano de Almeida for allowing me to shadow them during their *in vivo* work. I would also like to thank Dr. Verena Wagner and Professor Jesus Gil for the exciting collaboration on the lipofuscin study.

I would like to express my appreciation to members of the CCIC group with whom I performed this project. I would particularly like to thank Dr. Vessela Vassileva, Ning Wang, Caroline Haegeman and Millie Li for their fruitful discussions, Ala Amgheib for her help with FACS data analysis, Dr. Haonan Lu for his support with fluorescence microscopy. My sincere thanks to the rest of the group for their friendship and keeping me company. Thank you to Mr John Latigo and Ms Maureen Francis for their administrative support.

Funding provided by King's College London and Imperial College London EPSRC Centre for Doctoral Training in Smart Medical Imaging forms the essential foundation for which this PhD project takes place. My gratitude to everyone involved in CDT, particularly the help and friendship from cohort-II students.

Most importantly, I would like to express my deep gratitude to my parents, my husband and all my friends for their support and encouragement throughout the time of this thesis.

# Publications

**Part of Chapter 5 of this thesis has been published:**

Allott L., Brickute D., **Chen C.**, Braga M., Barnes C., Wang N. & Aboagye E (2020). Development of a fluorine-18 radiolabelled fluorescent chalcone: evaluated for detecting glycogen. *EJNMMI Radiopharmacy and Chemistry,* 5: 17.

# Table of Contents

# List of Figures

## List of Tables

## Abbreviations

| | |
|---|---|
| 2-NBDG | 2-[N-(7-nitrobenz-2-oxa-1,3-diazol 4-yl) amino]-2-deoxyglucose |
| 53BP1 | p53-binding protein 1 |
| γ-H2AX | Histone H2AX phosphorylated at Ser139 |
| AML | Acute myeloid leukemia |
| AMPK | 5' AMP-activated protein kinase |
| ARF | ADP-ribosylation factor |
| BRAF | B-Raf proto-oncogene |
| C/EBPβ | CCAAT/enhancer-binding protein-β |
| CAFs | Cancer-associated fibroblasts |
| CCCP | Carbonyl cyanide m-chlorophenyl hydrazone |
| CCFs | Cytoplasmic chromatin fragments |
| cGAS/STING | Cyclic GMP–AMP synthase/stimulator of interferon genes |
| CHK1/2 | Checkpoint kinase 1/2 |
| COPD | chronic obstructive pulmonary disease |
| CREB | cAMP response element-binding protein |
| CT | Computed tomography |
| DDR | DNA damage response |
| DPP4 | Dipeptidyl peptidase 4 |
| dUMP | Deoxyuridine monophosphate |
| ECM | Extracellular matrix |
| EGFR | Epidermal growth factor receptor |
| EMT | Epithelial-mesenchymal transition |
| eNOs | Endothelial nitric oxide synthase |
| ER | Estrogen receptor |
| [$^{18}$F]FDG | 2-[$^{18}$F]fluoro-2-deoxy-D-glucose |
| [$^{18}$F]FES | 16α-[$^{18}$F]fluoro-17β-oestradiol |
| [$^{18}$F]FLT | 3-deoxy-3-[$^{18}$F]fluoro-L-thymidine |

| | |
|---|---|
| [$^{18}$F]FMAU | 1-(2'-deoxy-2'- [$^{18}$F]fluoro-β-D-arabinofuranosyl)-thymine |
| [$^{18}$F]ICMT-11 | $^{18}$F-(S)-1-((1-(2-fluoroethyl)-1H-[1,2,3]-triazol-4-yl)methyl)-5-(2(2,4-difluorophenoxymethyl)-pyrrolidine-1-sulfonyl)isatin |
| [$^{18}$F]ML-10 | 2-(5-[$^{18}$F]fluoro-pentyl)-2-methyl-malonic acid |
| [$^{18}$F]NFTG | $^{18}$F-N-(methyl(2-fluoroethyl)- 1H-[1,2,3]triazole-4-yl)glucosamine |
| FOXO4 | Forkhead box protein O4 |
| G1P | Glucose 1-phosphate |
| G6P | Glucose 6-phosphate |
| GAA | α-1,4-Glucosidase |
| GATA4 | GATA binding protein 4 |
| GBE | Glycogen branching enzyme |
| GDE | Glycogen debranching enzyme |
| GLB1 | Galactosidase beta 1 |
| GLUTs | Glucose transporters |
| GN | Glycogenin |
| GSK3β | Glycogen synthase kinase 3β |
| GYS | Glycogen synthase |
| HCC | Hepatocellular carcinoma |
| HDFs | Human diploid fibroblasts |
| hENT1 | Human equilibrative nucleoside transporter 1 |
| HER2 | Human epidermal growth factor receptor 2 |
| HGF | Hepatocyte growth factor |
| HIF | Hypoxia inducible factor |
| HMGA | High Mobility Group A |
| HMGB1 | High mobility group box 1 |
| HP1 | Heterochromatin protein 1 |
| HSP90 | Heat shock protein 90 |
| IL-8 | Interleukin-8 |
| JNK | c-Jun N-terminal kinase |
| LMNB1 | Lamin B1 |
| mAbs | Monoclonal antibodies |

| | |
|---|---|
| MDM2 | Mouse double minute 2 homolog |
| MEK | Mitogen-activated protein kinase kinase |
| MiDAS | Mitochondrial dysfunction-associated senescence |
| MMPs | Matrix metalloproteinases |
| MRI | Magnetic resonance imaging |
| microRNA | miRNA |
| mTOR | Mammalian target of rapamycin |
| MSNs | Mesoporous silica nanoparticles |
| $NAD^+$ | Nicotinamide adenine dinucleotide |
| NADH | Nicotinamide adenine dinucleotide hydrogen |
| NF-κB | Nuclear factor kappa B |
| NK | Natural killer |
| NSCLC | Non-small-cell lung cancer |
| OIS | Oncogene-induced senescence |
| OXPHOS | Oxidative phosphorylation |
| p38 MAPKs | p38 Mitogen-activated protein kinases |
| PAS | Periodic acid-Schiff |
| PDH | Pyruvate dehydrogenase |
| PDK1 | Pyruvate dehydrogenase kinase 1 |
| PDP2 | Pyruvate dehyrogenase phosphatase catalytic subunit 2 |
| PET | Positron emission tomography |
| PGM | Phosphoglucomutase |
| PhK | Phosphorylase kinase |
| PI3K | Phosphoinositide 3-kinase |
| PKA | Protein kinase A |
| PP1 | Protein phosphatase 1 |
| PPP | Pentose phosphate pathway |
| PTEN | Phosphatase and tensin homolog |
| PTG | Protein target to glycogen |
| PYGL | Glycogen phosphorylase |

| | |
|---|---|
| RB | Retinoblastoma protein |
| ROS | Reactive oxygen species |
| RTK | Receptor tyrosine kinase |
| SA-β-GAL | Senescence-associated β-galactosidase |
| SAHF | Senescence-associated heterochromatin foci |
| SAPD | Senescence-associated protein degradation |
| SASP | Senescence-associated secretory phenotype |
| SBB | Sudan black B |
| SCAPs | Senescent cell anti-apoptotic pathways |
| SHMT2 | Serine hydroxymethyltransferase 2 |
| SIRT1 | Sirtuin 1 |
| SMCs | Smooth muscle cells |
| Stbd1 | Starch-binding domain protein 1 |
| TCA | Tricarboxylic acid |
| TERT | Telomerase reverse transcriptase |
| TK1 | Thymidine kinase 1 |
| TS | Thymidylate synthase |
| UGP | UDP-glucose pyrophosphorylase |
| UGP2 | UTP-glucose-1-phosphate uridylyltransferase |
| UPP | Ubiquitin proteasome pathway |
| UTP | Uridine 5’-triphosphate |

# Chapter 1 Introduction

## 1.1 Cellular senescence

The term cellular senescence was formally described by Hayflick and his colleagues for the first time in 1961, when they observed the finite proliferative capacity of normal human fibroblasts upon extended culture *in vitro* [1; 2]. Since then, senescence has been in general used to describe the irreversible cell cycle arrest caused by various stresses among a wide range of cell types, such as fibroblasts, epithelial cells, endothelial cells, lymphocytes and chondrocytes, and possibly even post-mitotic cells such as neurons and glial cells [3]. Cellular senescence has attracted widespread attention over recent years, with the focus not only on the causes and characteristics of senescence, but also on its physiological relevance to cancer and aging.

### 1.1.1 Causes of cellular senescence

Cells can senesce when they encounter endogenous and exogenous stimuli, including telomere shortening, DNA damage, oncogenic activation and extrinsic stress. One of the key molecular mechanisms underlying senescence was firstly proposed by Harley in 1990 [4], when decreased amount and length of telomeric DNA was observed in fibroblasts after serial passage. This type of senescence induced by telomere shortening is termed replicative senescence. Telomeres locate at the terminal of chromosomes with the unique nucleotide sequences of TTAGGG, which protect the DNA ends from degradation and recombination [5]. Telomere shortening progressively occurs with ages due to the intrinsic end-replication problem where cells lose 50 - 200 base pairs of telomeric DNA during each round of cell division [4]. When reaching a critical short length, telomere loss generates a persistent DNA damage response (DDR) that initiates and maintains senescence growth arrest [6]. Although this telomere lose can be restored by telomerase which adds telomeric DNA repeats directly to chromosome ends, the functional component of telomerase, which contains a catalytic protein (telomerase reverse transcriptase; TERT), does not normally present in normal cells [7]. Telomerase cannot prevent senescence caused by non-telomeric DNA damage or other senescence inducers [8].

Accumulation of different types of non-telomeric DNA damage also leads to senescence in human and mouse cells. It has been well known that DDR system is capable of sensing and repairing most of the DNA errors, which ensures the integrity of cell genome and the normal functionality of that organism [6]. However, when the damages are beyond the capability of the cell to repair, DDR directs alternative ways to either cease cell proliferation via senescence or eliminate cells by mediating apoptosis. Once activated, the DDR upregulates many downstream effectors to initiate and maintain senescence, including the histone H2AX phosphorylated at Ser139 (γ-H2AX) and p53-binding protein 1 (53BP1), as well as four serine/threonine kinases ATM, ATR and check point kinase 1/2 (Chk1/2) [9; 10].

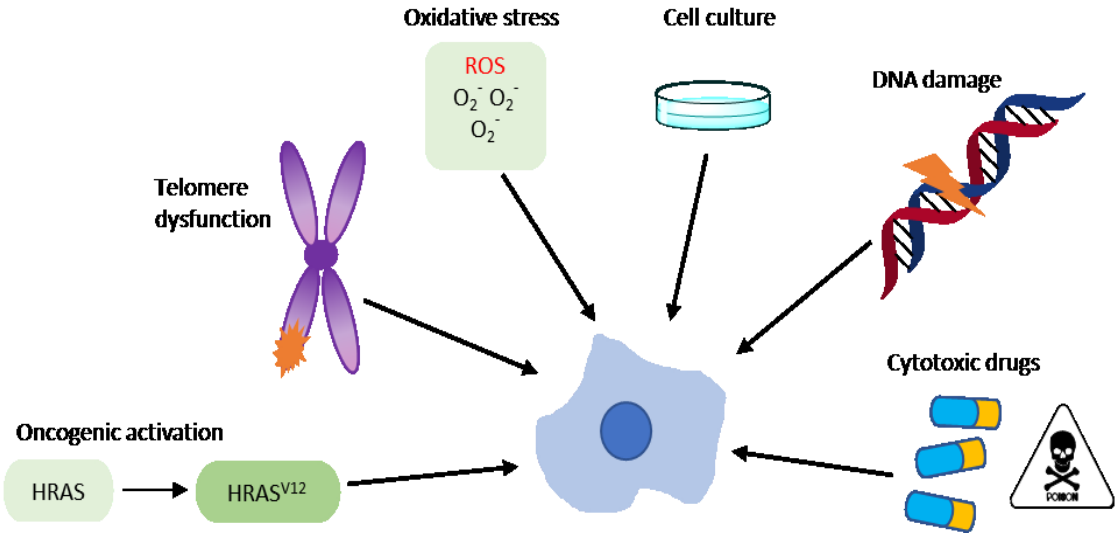


**Figure 1.1 Stimuli that induce cellular senescence.**

Senescence can be triggered by replicative factors such as telomere dysfunction and non-telomeric DNA damage, or by premature signals such as oncogenic activation (or tumour suppressor dysfunction), oxidative stress, culture stress and cytotoxic drugs. [Adapted from Collado et al., 2006].

Senescence can also arise when cells harbour certain types of activated oncogenes [11]. Oncogenes are a group of genes that have been altered by mutations, which could potentially transform normal cells to a tumorigenic state when in conjunction with other mutations. Oncogene-induced senescence (OIS) was first observed in 1997 by Serrano et al. [12], where oncogenic RAS triggered an irreversible proliferation arrest in primary rodent and human cells with concomitant activation of p53 and p16 proteins. Similarly, overexpression of other

oncogenes involved in the RAS signalling such as B-Raf proto-oncogene (BRAF) and mitogen-activated protein kinase kinase (MEK) has shown to cause irreversible growth arrest *in vitro* [11; 13]. Loss of tumour suppressor proteins such as phosphatase and tensin homolog (PTEN) also triggers cellular senescence [14]. As most of these studies are dependent on experimental methods to either upregulate oncogenes or silence suppressor genes, it has been debated that if normal endogenous levels of activated oncogenes or dysfunctional suppressor genes are sufficient to induce senescence. It was then shown that oncogene-induced senescence does occur *in vivo* in human and mouse tumour models [14]. Another question arising from this context is what factors determine cells to enter senescence rather than progressing to malignant tumour cells in the presence of activated oncogenes or disordered tumour suppressor genes [15]. Although the reasons remain unexplained, one possibility is that activated oncogenes such as RAS only engages specific biological pathways which are essential for the occurrence of senescence. From this perspective, OIS could serve as a tumour-suppressive mechanism by which normal or benign tumour cells cease proliferation.

Cultured cells may enter senescence in response to several cell-culture stresses, such as hyperphysiological or inadequate growth conditions. Oxidative stress is another senescence inducer defined as excessive accumulation of reactive oxygen species (ROS) in mitochondria that leads to severe damage to many cellular components, such as DNA, proteins and lipids, eventually initiating the aging process [16-18]. The excessive ROS is involved in regulation of many cell fates including apoptosis, necrosis, autophagy and senescence. At least four molecular mechanisms have been described as responsible for oxidative-induced senescence, including 1) oxidative stress causes DDR via damage to telomeric as well as non-telomeric DNA [17], which subsequently upregulates the expression of p53 and p21; 2) excessive ROS activating nuclear factor kappa B (NF-κB), which results in the elevated expression of interleukin-8 (IL-8) and increased p53 stability; 3) ROS upregulates p38 mitogen-activated protein kinases (p38 MAPKs) pathway which further enhances p19 expression and inhibits cell self-renew; 4) ROS has effects on the amount of microRNA (miRNA), which promotes senescence [19; 20]. One study showed that inhibition of mitochondria function using a chemical inhibitor of oxidative phosphorylation, carbonyl cyanide m-chlorophenyl hydrazone

(CCCP), impaired ROS-induced senescence as characterised by massively decreased SA-β-gal activity and absence of the senescence-associated secretory phenotype (SASP) factors, suggesting that mitochondria plays an essential role in ROS-induced senescence [21]. Most recently, it has been proposed that the function of mitochondrial in senescence relies not only on ROS levels, but also altered redox state and altered metabolism. Mitochondrial dysfunction, which caused by decreased nicotinamide adenine dinucleotide ($NAD^+$)/nicotinamide adenine dinucleotide hydrogen (NADH) ratio, has been found to induce senescence via 5' AMP-activated protein kinase (AMPK)-mediated p53 induction [22].

Collectively, cellular senescence can be triggered by many intrinsic and extrinsic stimuli in a variety of human and mouse cells, as well as *in vivo* in mouse models. The last major type of senescence – senescence induced by chemotherapy in tumour cells - will be discussed in **Section 1.1.5**.

### 1.1.2 Control of cellular senescence

Regardless of the initial trigger, both replicative and non-replicative senescent cells share two major tumour suppressor networks to implement irreversible growth arrest, which are the p53/p21 and INK4/ARF pathways [23; 24]. The two transduction cascades interact but can independently regulate cellular senescence. The dominant role of each pathway largely depends on species, cell types and initial induction signals. For example, experimental disruption of telomeres induces senescence via both the p53/p21 and INK4/ARF pathway in human cells, whereas the p53/p21 pathway is mainly responsible for senescence in mouse cells [23].

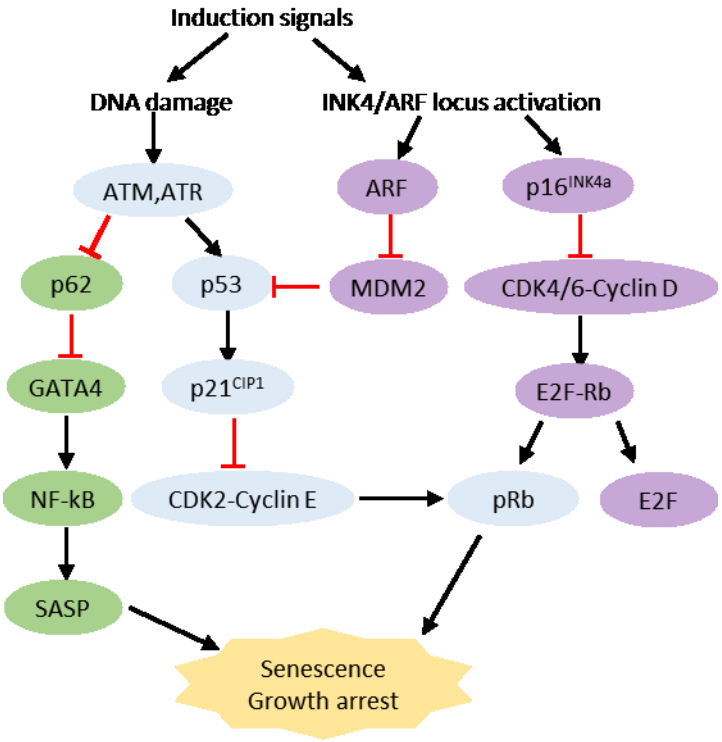


**Figure 1.2 Molecular pathways controlling cellular senescence.**

Cellular senescence is regulated by the p53/p21 and INK4/ARF pathways. A new pathway through p62-GATA4 has been recently reported. [Adapted from Herranz et al., 2018 and Kang et al., 2015.]

### The p53/p21 pathway

Stimuli such as telomere shortening, ionizing radiation or genotoxic drugs that generate persistent DDR primarily engage the p53/p21 pathway to induce and maintain senescence. The activated DDR regulators including ATM and ATR enhance the activity of p53 [25]. Alternatively, ADP ribosylation factor (ARF), apart from ATM and ATR, is responsible for neutralizing the ability of MDM2 to promote p53 degradation, thus leading to the stabilization and accumulation of p53 in oncogene-induced senescence. P53 then mediates the transcription of the cyclin-dependent inhibitor p21 (CIP1/WAF1), which further inhibits the activity of CDK2-Cyclin E as well as CDK4/6-Cylin D, leading to hyperphosphorylated retinoblastoma protein (Rb) and irreversible cell cycle arrest. In addition to a crucial role in regulating senescence, p21 is also associated with DNA-damage-induced transient growth inhibition (quiescence or dormancy). Possibly, stimuli that generate rapid DNA damage reversibly stop cell growth and cells can re-enter proliferation when exposed to stimuli.

Whereas slow and incomplete repair triggered by persistent stresses contributes to constant signalling and senescence [23].

**The INK4/ARF pathway**

It has been suggested that the INK4/ARF pathway functions as a complementary signalling of the p53/p21 pathway in DNA-damage-initiated senescence. Upon the stimuli, p53/p21 pathway dominantly controls the onset of senescence, while the INK4/ARF maintains a durable growth arrest [23]. The INK4/ARF locus, including three tumour suppressors $p16^{INK4a}$, $p15^{INK4b}$ and ARF ($p14^{ARF}$ in human and $p19^{Arf}$ in mouse), tightly controls the anti-proliferative effects through modulation of Rb and p53 [26; 27]. Upon stimulation, $p16^{INK4a}$ selectively inhibits the activity of CDK4/6-Cyclin D complex, which increases the inhibitory effect of hyperphosphorylated pRb on the transcription factor E2F, eventually blocking cell progression from G0/G1 to S phase. The $p16^{INK4a}$/pRb pathway also contributes to producing senescence-associated heterochromatin foci (SAHF), which silences genes that are needed for cell proliferation [28]. This activity is possibly associated with the formation of a complex of repressive chromatin with Rb and histone-modifying enzymes [29].

**An emerging pathway**

Beyond the two established controlling pathways, a novel signalling cascade was described in 2015 by Kang et al [30; 31]. It was shown that the transcription factor GATA binding protein 4 (GATA4) is activated via DDR regulators ATM and ATR, but not on p53 or $p16^{INF4a}$ in senescent cells. The degradation of GATA4 triggered by p62-mediated selective autophagy is suppressed during senescence, thereby stabilizing GATA4. GATA4 also triggers the SASP via activation of NF-κB, thus facilitating senescence. *In vivo* data confirmed the accumulation of GATA4 in multiple tissues in mice treated with senescence-inducing stimuli. These findings pave the way for further investigating GATA4 pathway as a driver of age-dependent inflammation.

### 1.1.3 Characteristics of senescent cells

Senescent cells display a wide range of characteristics, however, they are not exclusively nor consistently induced in senescence.

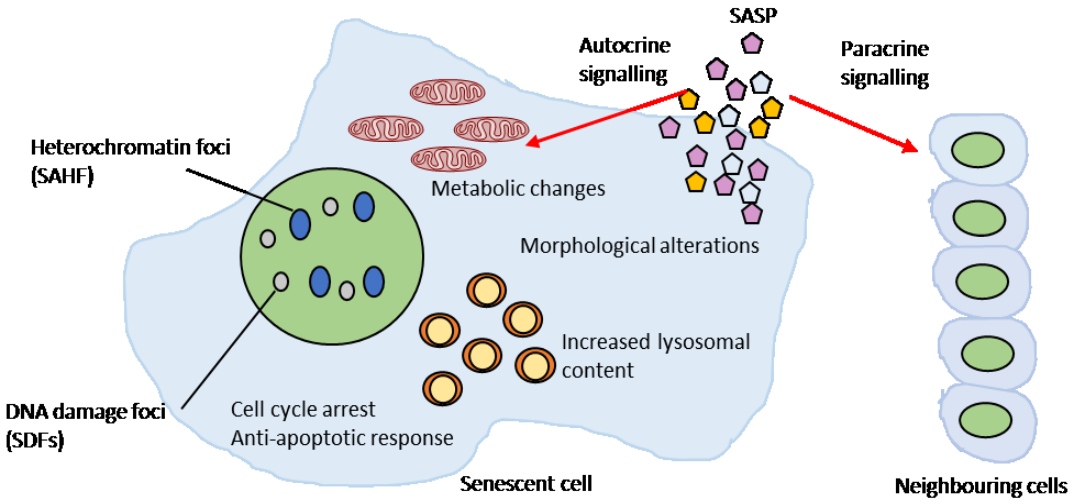


**Figure 1.3 Hallmarks of cellular senescence.**

Senescent cells differ from other non-dividing cells (quiescence or dormancy) in several ways, although none has been identified as being unique to this state. Hallmarks of senescent cells include morphological alterations, an irreversible growth arrest, anti-apoptotic response, increased lysosomal contents, changes in nucleus, metabolic changes and secretion of numerous growth factors, cytokines, proteases and other proteins (SASP). SASP can act in both autocrine and paracrine manner affecting other biologic processes. [Adapted from Gonzalez-Meljem et al., 2018 and Hernandez-Segura et al., 2018]

### Morphological alterations

One of the key features of *in vitro* senescent cells is the enlarged, flattened and irregular shape that can be easily detected by normal or fluorescent microscopy. However, its application is limited in tissue samples or *in vivo* [32].

### Irreversible growth arrest

A primary hallmark of senescence is that senescent cells are irreversibly arrested in G0/G1 and are not able to re-start proliferation upon any stimulations. One study revealed that some senescent cells induced by telomere erosion could re-start growth after genetic interventions that inactivate the p53 tumour suppressor. These senescent cells have been shown to be associated with low levels of p16 [33]. Senescent cells remain metabolically active but lose the ability to initiate DNA replication even under adequate growth conditions. In contrast to senescence, quiescent growth arrest (or termed dormancy) is a reversible state, where cells can re-enter cell cycle upon certain physiological stimuli.

**Apoptosis resistance**

It has been found that when cells undergo senescence, most of them become resistant to certain apoptotic signals. This could partially explain why senescent cells are so stable in culture, and profoundly accumulate with age. The ability of senescent cells to exempt from apoptosis might be due to the upregulation of several pro-survival factors which have recently been termed senescent cell anti-apoptotic pathways (SCAPs) [34]. The anti-apoptotic protein Bcl-2 is shown to be enriched in senescent cells due to the chronic activation of the transcription factor cAMP response element-binding protein (CREB) that prevents Bcl-2 inhibition [35]. More recently, other members of Bcl-2 family such as Bcl-XL and Bcl-W are recognized as crucial factors responsible for the survival of senescent cells [36]. In addition to these anti-apoptotic proteins, FOXO4 (forkhead box protein O4) is also overexpressed in senescent cells and inhibits cell death by blockage of p53 in the nucleus [37]. P21 was recently found to be involved in maintaining the viability of senescent cells by suppressing c-Jun N-terminal kinase (JNK) pathway under persistent DNA damage [38].

The sensitivity to apoptosis between senescent endothelial cells and fibroblasts may differ due to distinct modulation of pro-survival factors, for example, senescent fibroblasts displayed reduced sensitivity to apoptosis due to up-regulation of endothelial nitric oxide synthase (eNOS) via PI3K/AKT signalling, whereas senescent endothelial cells were more susceptible to apoptosis in the presence of increased expression of eNOS [39; 40].

**Increased lysosomal content**

One of the defining features of senescent cells is the alterations in cellular lysosome as characterised by the upregulation of many proteins and increased lysosomal contents [41]. Among them, increased SA-β-gal activity has been used as one of the most common markers to identify senescence *in vitro* and *ex vivo*. This enzyme activity is measured by increased rate of the conversion of its substrate x-Gal to a blue-coloured product at a pH of 6.0 in senescent cells, while the optimal pH of this enzyme in normal cells is 4.0. The mechanism underlying increased activity of β-galactosidase in senescent cells is still unclear, although the physiological regulation of this enzyme has been widely reported as encoded by the galactosidase beta 1 (GLB1) gene and can be regulated by a known transcriptional and translational pathway [42]. Despite being the most commonly used method, SA-β-gal assay

may produce false-positive results in cells when cultured under confluent conditions or in quiescent cells. Another disadvantage of this method is that it cannot be used for paraffin-embedded tissue sections and live cells. Similar to β-galactosidase, increased activity of the enzyme α-fucosidase produced in lysosome has also been used as a biomarker of senescence [43].

Another senescent feature, which is related to lysosome, is the enhanced accumulation of lipofuscin. Lipofuscin, aggregates of massive oxidized proteins and lipids, sugars and transition metals, was initially found to largely accumulate in various tissues such as liver, kidney and skeletal muscle in aged organisms [44]. Von Zglinicki et al. in 1995 observed an accumulation of lipofuscin in replicative senescence in human fibroblasts [45]. The mechanism might be that increased ROS production during senescence results in the carbonylation of several protein residues such as proline, threonine, lysine and arginine, in the presence of metal. These carbonyl residues further convert to Schiff bases via reacting with amino groups and promote protein aggregation. The insoluble lipofuscin is eventually formed by cross linking the protein aggregates with sugars and lipids [46]. Lipofuscin was recently found to upregulate the anti-apoptotic protein Bcl-2 in senescent cells, which appears to be an additional cause of apoptosis resistance. Cellular lipofuscin can be detected by fluorescent microscopy based on its autofluorescence feature, or by histochemical methods such as Sudan Black B (SBB) stain. Most recently, a new compound (GL13) synthesized by attaching a biotin group to SBB has been successfully used to detect lipofuscin with advanced specificity in several senescent settings [47]. Another advantage of using SBB to detect lipofuscin is that this method can detect senescent cells in paraffin-embedded archival materials.

**Changes in nucleus, chromatin and gene regulation**

A common feature of senescent cells is altered nuclear phenotype and patterns of gene expression such as downregulation of cell cycle genes and upregulation of senescence-associated genes [48]. Lamin B1 (LMNB1), a protein located in the inner nuclear membrane, is shown to be decreased in senescent cells at different levels [49]. Experimental silencing of LMNB1 by RNAi seems to inhibit cell proliferation and sufficiently induce senescence through modulating the production of ROS [50]. The downregulation of LMNB1 in senescent cells

might be associated with increased activity of miRNA-23a which inhibits the translation of LMNB1 [51]. The LMNB1 dysfunction impairs the nuclear integrity, which as a result leads to other changes within the nucleus such as the bedding of cytoplasmic chromatin fragments (CCFs). These CCFs can further trigger the inflammatory response in senescent cells via activation of the cyclic GMP–AMP synthase–stimulator of interferon genes (cGAS/STING) pathway [52].

The most striking change in chromatin is the formation of senescence-associated heterochromatic foci (SAHFs). These foci are characterised by accumulation of trimethylated H3K9, heterochromatic protein 1 (HP1), high mobility group A (HMGA) proteins and loss of linker histone H1 [53]. However, SAHFs are mainly found in OIS, which limits its application as a universal biomarker of senescence. Genes that are involved in senescence regulatory pathway are upregulated such as p21 and p16. Several other genes that result in alterations of tissue environment are also activated in senescent cells, which are discussed below as SASP.

**Presence of the SASP**

One of the most distinct features of senescence is the SASP which describes the secretion of a wide range of factors including cytokines, chemokines, growth factors, extracellular MMPs and other signalling molecules by senescent cells [54]. Until the discovery of SASP in 2008 [55], senescence had long been regarded as a cell-intrinsic program which only led to 'individual' intracellular changes. SASP highlights the ability of senescent cells to influence their surrounding environment and interact with neighbouring cells. SASP is a complicated programme, and the types of secretion components and the individual regulation mechanisms are highly dependent on cell type, source of senescence stimuli and duration of senescence [56].

The SASP is regulated in senescent cells at various levels including transcriptional activation, translational activation and post-transcriptional modifications. The two transcriptional factors, which are NF-κB and CCAAT/enhancer-binding protein-β (C/EBPβ), are substantially involved in mediating SASP. The activated NF-κB and C/EBPβ upon persistent DDR bind to chromatin and induce the expression of inflammatory cytokines such as IL-6 and IL-8. The increased IL-6 and IL-8 can in turn reinforce the activity of NF-κB and C/EBPβ through a positive feedback loop and amplify SASP signalling [57].

The transcriptional regulation of SASP genes can also occur at an epigenetic level. Takahashi et al. observed induction of IL-6 and IL-8 resulting from a reduction of H3K9 dimethylation on gene promoters. The decreased H3K9 dimethylation is related to the degradation of methyltransferase G9a through Cdc14B- and $p21^{Waf1/Cip1}$-dependent activation of $APC/C^{Cdh1}$ ubiquitin ligase complex upon DDR signal [58]. Downregulation of sirtuin 1 (SIRT1) during senescence results in an activation of IL-6 and IL-8 though histone acetylation of the promoter regions [59]. MacroH2A1, a tumour suppressive histone variant, plays a complex role in regulating SASP. MacroH2A1 initially induces the expression of some SASP genes and maintains the paracrine senescence through a positive feedback loop. Subsequently, macroH2A1 is quickly removed from SASP gene chromatin via a negative feedback loop activated by SASP expression [60]. Accumulation of another histone variant H2A.J in senescent cells promotes the expression of SASP genes [61].

At the post-transcriptional level, the mTOR pathway plays a central role in regulation of SASP. mTOR can directly activate the translation of IL-1α through suppression of the translation suppressor protein 4EBP, which thus promotes the expression of NF-kB and C/EBPβ. In parallel, mTOR indirectly inhibits ZFP36L1, which is an RNA binding protein, thereby preventing SASP components from mRNA degradation [62; 63]. SASP regulation is also associated with autophagy pathway in senescent cells via a complex mechanism (will be discussed below in 'metabolic reprogramming').

SASP factors have been reported to exert complex and controversial effects on modulating several biological processes of senescent cells through both autocrine and paracrine signalling. The function of SASP can be beneficial or deleterious, dependent on the types of secretory components, the nature of surrounding cells and the signalling network triggered. For example, secreted factors, such as IL-1 and IL-6, could in turn reinforce the senescence state through an autocrine positive-feedback loop [64], providing a tumour-suppressive mechanism as it prolongs the duration of cell arrested in non-proliferative state.

A cell-extrinsic effect through paracrine signalling is more widely observed in response to SASP, in which senescent cells can interact with neighbouring cells and alter surrounding microenvironment. This cell-to-cell communication has shown some beneficial properties such as wound healing, tissue repair and immune surveillance [65], however, the deleterious

effects mediated by SASP through paracrine network possibly overwhelms its benefits. For example, several SASP factors produced from senescent cells can promote tumour initiation and metastasis in premalignant or advanced tumour cells, which is discussed in **Section 1.1.5**.

The SASP components such as many pro-inflammatory cytokines in senescent cells have also been linked to aging and age-associated pathologies. For example, increased secretion of IL-6 and IL-8, as well as extracellular matrix (ECM) macromolecules by senescent smooth muscle cells (SMCs) result in formation of several characteristic symptoms of atherosclerosis. SASP has also been found to play a role in diseases related to cognitive impairment such as Alzheimer's and Parkinson's disease, or chronic obstructive pulmonary disease (COPD) [66].

**Metabolic reprogramming**

Despite a permanent cessation of proliferation, senescent cells remain metabolically active to meet energy requirements for supporting several senescence-associated programmes such as SASP. Reprogrammed metabolism in senescent cells is associated with many signalling cascades including protein synthesis, lipid synthesis, glycolysis, autophagy and mitochondrial regulation.

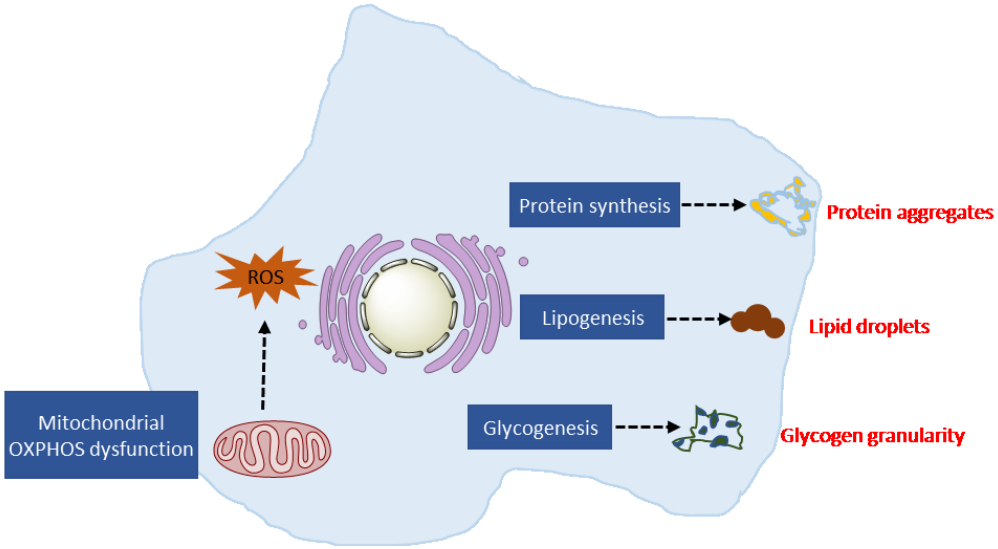


**Figure 1.4 Summary of metabolic features in cellular senescence.**

Reprogrammed metabolic pathways in senescent cells include dysfunctional oxidative phosphorylation in mitochondrial, and dysregulated protein synthesis, lipogenesis and glycogenesis. [Adapted from Kwon et al., 2019]

It has been recently reported that senescent human diploid fibroblasts (HDFs) induced by oncogenic $BRAF^{V600E}$ upregulates mitochondrial oxidative phosphorylation (OXPHOS) as characterised by the increased tricarboxylic acid (TCA) cycle activity and ROS production. Further studies revealed that increased activity of pyruvate dehydrogenase (PDH) is responsible for the mitochondrial activation in OIS. PDH is an enzyme that links glycolysis to TCA cycle through catalysing the conversion of pyruvate to acetyl-CoA. During $BRAF^{V600E}$-induced senescence, the increased PDH activity results from the simultaneous induction of the PDH-activating enzyme pyruvate dehydrogenase kinase 1 (PDK1) and inhibition of the PDH-inhibitory enzyme pyruvate dehydrogenase phosphatase 2 (PDP2) [67]. Consistent with these observations, Takebayashi et al. reported an upregulation of glycolysis and OXPHOS in senescent HDFs caused by oncogene $H\text{-}RAS^{V12}$ in a retinoblastoma protein (Rb)-dependent manner [68]. Rb protein also promotes metabolic remodelling through activation of gene expression involved in glycolysis and accelerating production of metabolites from glycolytic pathway in OIS cells. Changes in mitochondrial are not only the consequence of senescence, but also may contribute to maintaining this state. For example, increased ROS production caused by mitochondrial remodelling is associated with initiation and maintenance of senescence when occurring in conjunction with DDR signalling cascade [69]. High ratios of AMP to ADP in senescent fibroblasts trigger the activation of AMP-activated protein kinase (AMPK) through suppression of its phosphorylation. AMPK subsequently implements senescence phenotype through inducing a HuR cytoplasmic presence [70]. The production of SASP might be promoted in senescent cells through a multiplex regulation pathway linking DDR, mTOR complex 1 (mTORC1) and mitochondrial activity. The enhanced ATM induces expression of active Akt and mTORC1, resulting in the activation of PGC-1β-dependent mitochondrial biogenesis, thus maintaining persistent DDR and stabilization of SASP in senescent cells [21]. Most recently, dysfunctional mitochondrial induced a distinct type of senescence which is termed mitochondrial dysfunction-associated senescence (MiDAS) controlled by an NAD-AMPK-P53 pathway [22].

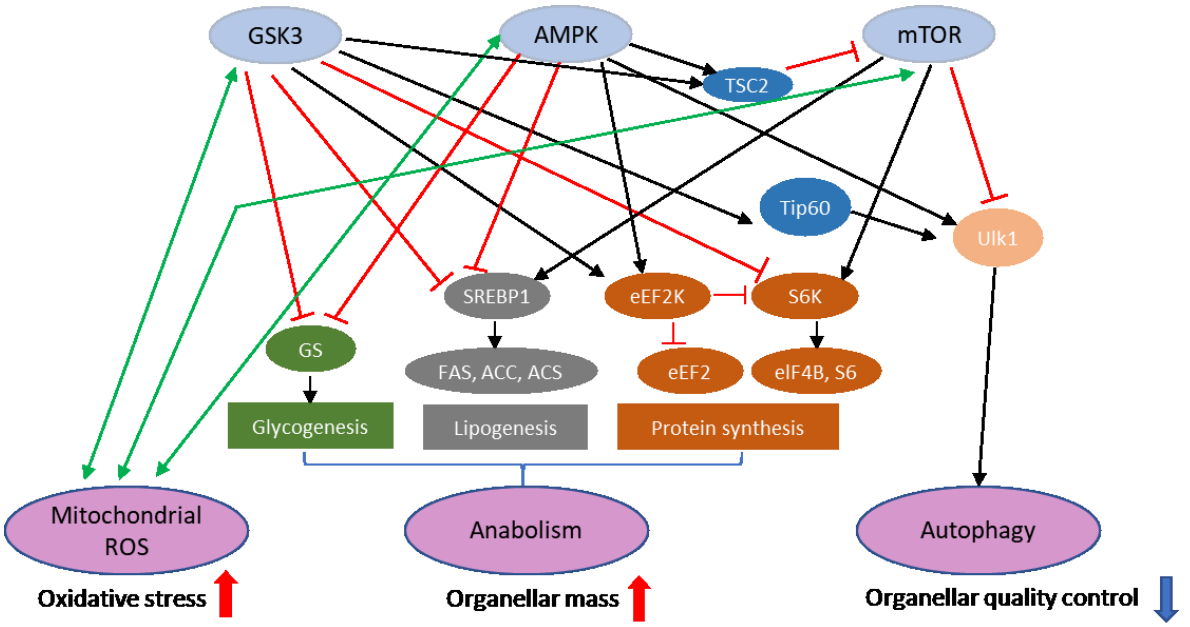


**Figure 1.5 The key signalling pathways that regulate senescence-associated metabolic changes.**

Metabolic reprogramming in senescent cells are regulated by several signalling cascades and initiated by effectors such as GSK3, AMPK and mTOR. [Adapted from Kwon et al., 2019]

The protein degradation system is another metabolic pathway that is reprogrammed in some senescent cells. It has been well documented that there are two major protein degradation systems in eukaryotic cells, which are autophagy and the ubiquitin-proteasome pathway (UPP), both of which have been recently found to be closely associated with senescence. One of the studies showed that activation of autophagy occurs alongside the dynamic process of oncogene-induced senescence in HDFs cells, which together results in increased expression of genes involved in both lysosome biogenesis and autophagy [71]. Changes in the expression of autophagy-related genes appear to be at similar kinetics as that of SASP production, suggesting a functional correlation between autophagy and SASP [53]. Induction of autophagy could attenuate proteotoxic stress which results from increased SASP components. Several studies also indicate that autophagy functions as a cell defence mechanism, which to some extent protects senescent cells from death upon the onset of cellular stress [72]. Enhanced autophagy in conjunction with increased protein synthesis effectively supports a rapid protein turnover which supplies amino acid that is required for SASP production [73]. An upregulation of protein synthesis has also been identified as a

positive regulator of senescence, which is mediated by mTOR. Although protein degradation via UPP system has functional relevance to senescence, senescent HDFs gradually shift their protein degradation from the UPP pathway to autophagy. Recently, it is shown that aberrant RAS/ERK pathway is engaged in breaking down several 'selective' proteins that are required for cell cycle progression, cell migration, mitochondrial functions and cell signalling, leading to senescence-associated protein degradation (SASD) [74].

Changes in lipid metabolism have also been reported in senescence, however, it remains unclear how it functionally contributes to senescence phenotype. Enhanced ROS production in dysfunctional mitochondrial can cause lipid accumulation as well as lipid damage [75; 76]. Ogrodnik et al observed that accumulation of senescent cells promotes hepatic fat accumulation and steatosis [75].

Recently, emerging studies reported increased accumulation of glycogen granules in several senescence systems, including replicative senescence of primary human fibroblasts [77]. The involvement of glycogen metabolism in senescence might be through the PI3K/Akt/GSK3 signalling cascade. GSK3 is not only a key upstream regulator of glycogenesis though inhibition of the activity of glycogen synthase, but also plays a role in modulation of cell cycle arrest [78]. The role of glycogen as the stored form of efficient energy in senescence needs to be further exploited.

### 1.1.4 Emerging strategies to target/eliminate senescent cells

**Targeting senescent cells**

Targeting senescent cells for detection would open up the possibilities of studying age-related diseases and monitoring senescence-directed anticancer therapies. Current strategy for developing senescence-targeting detection agents mainly relies on tracking increased β-galactosidase activity. For example, Lee et al. reported a ratiometric two-photon fluorescent probe to detect the level of β-galactosidase in replicative senescence in primary HDFs, in which a shift from blue to yellow emission colour is observed in control and senescent cells, respectively [79]. Gal-Pro, which is another fluorescent probe with the structure of a hemicyanine skeleton and a D-galactose residue, has been used to track senescent cells induced by oxidative stress. Its action relies on a sensitive turn-on fluorescent response to β-

galactosidase in senescent cells [80]. Increased β-gal activity in chemotherapy-induced senescence *in vivo* has been measured by a fluorescent probe AHGa. The probe is based on a naphthalimide fluorophore as signalling unit containing an L-histidine methyl ester linker and an acetylated galactose attached to one of the aromatic nitrogen atoms of the L-histidine through a hydrolysable N-glycosidic bond. In senescent cells, AHGa is hydrolysed by β-galactosidase into AH, which leads to an enhanced fluorescent emission intensity ($\lambda_{ex}$ = 405 nm, $\lambda_{em}$ = 540 nm) [81]. Another fluorescent probe NIR-BG is also validated to track DNA-damage induced senescence *in vitro* and in mice bearing HeLa xenografted tumours [82].

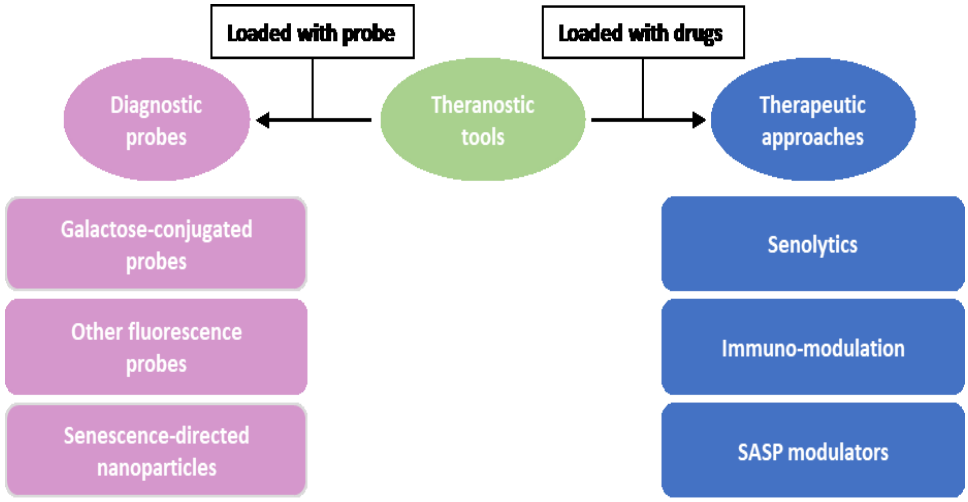


**Figure 1.6 Diagnostic and therapeutic approaches targeting cellular senescence.**

Fluorescent probes and nanoparticles loaded with galactose have been extensively explored as diagnostic probes towards senescent cells, while senolytics or currently used drugs that activate immune system or target SASP are being studied as therapeutic strategies against detrimental senescent cells. [Adapted from Paez-Ribes et al., 2019]

Another approach to target senescent cells or selectively deliver drugs to senescent cells is via nanoparticles. The first study toward this perspective was used mesoporous silica nanoparticles (MSNs) to specifically deliver cargos to different types of senescent cells. Rhodamine-B as a model drug was loaded to MSNs and then capped with galacto-oligosaccgarides (GOs), resulting in spherical particles with a diameter of 100 nm. The functional nanoparticles are taken via endocytosis, after fusion with lysosomes, the loaded cargos are released via exocytosis [83]. A similar drug delivery system was developed by the same group in 2018, where a homogenous coating consisting of a 6-mer galacto-oligosaccharide (Gal) was used [84]. Three compounds were loaded including rhodamine B

for senescence labelling, and doxorubicin and navitoclax for killing senescent cells. The gal-encapsulated cargos were preferentially released in several senescent cancer cells triggered by a CDK4/6 inhibitor palbociclib. The three loaded-compounds were activated in senescent lesions in mice with palbociclib-treated tumour xenografts and fibrotic lungs damaged by bleomycin [84]. Furthermore, porous calcium carbonate nanoparticles ($CaCO_3$), loaded with rapamycin and wrapped with a conjugate of lactose and polyethylene glycol, were assessed for targeting and treating senescent cells. The binding efficacy was improved by functionalization of the nanoparticles with a monoclonal antibody against CD9 which is a cell surface glycoprotein receptor overexpressed in senescent HDFs [85].

**Senolytic elimination of senescent cells**

Elimination of senescent cells might contribute to prevention, alleviation and treatment of multiple age-related disorders or as the second-line adjuvant therapeutics for current cancer treatment. Many efforts have been made to develop approaches that therapeutically target and remove senescent cells in preclinical models.

The pharmacological agents that are capable of inducing cell death in senescent cells are termed ‘senolytic drugs’ or ‘senolytics’. As described, one of the features of senescence is resistance to apoptotic signals, which is mainly caused by upregulation of several anti-apoptotic proteins. Hence, compounds correspondingly targeting these signalling cascades have shown effectiveness in eliminating senescent cells. Among them, drugs capable of inhibiting the Bcl-2 family proteins such as Bcl-2, Bcl-W and Bcl-XL are regarded as the most promising candidates. For example, the small-molecule ABT-737 inhibits protein expression of Bcl-W and Bcl-XL and results in cell apoptosis in senescent cells in two independent *in vivo* models which are DNA-damage induced senescence in lungs and $p14^{ARF}$-p53 mediated senescence in the epidermis [36]. ABA-263 (also known as navitoclax), which is the next-generation of ABT-737, also selectively kills senescent cells that are induced by various senescence stimuli *in vitro* [86]. Oral administration of ABT263 induces clearance of senescent cells in both irradiated p16-3MR transgenic mice and normally aged mice. In another study, ABT263, in combination with a naturally occurring piperlongumine, could synergistically induce cell death in irradiation-induced senescent WI-38 cells [87]. Although the broad-spectrum inhibitors targeting Bcl-2 protein family increasingly contribute to eliminating

senescent cells, these agents have shown toxicities on the haematological system such as severe damage to neutrophils and platelets. The safety issues might limit the translation of these Bcl-2 inhibitors into clinical practice, which emphasize the urgent need for developing alternative treatment strategies. UBX0101, which is a MDM2/p53 inhibitor, is currently in a phase II trial for treatment of osteoarthritis (OA) of the knee. Pre-clinical evaluation has shown its effects on down-regulation of SASP and induction of apoptosis in senescent cells *in vitro*, as well as improvement of joint function as measured in a mouse model of osteoarthritis [88]. A phase I study was completed in June 2019, in which UBX0101 is well tolerated and significantly improved several clinical measurements in pain and related functions.

Another attempt to overcoming the limitations of drug toxicity is the combined use of drugs at low doses. For example, a combination of the tyrosine kinase inhibitor dasatinib and the naturally occurring flavonoid quercetin can trigger the elimination of senescent cell. The use of dasatinib plus quercetin was the first introduced strategy to selectively kill senescent cells. In 2015, Zhu et al. by using transcript assay revealed an enhanced expression of genes involved in several pro-survival networks in senescent preadipocytes. By employing RNA interference, six genes were found to induce cell death in senescent cells, with no effect on cell viability of non-senescent cells in two human cell types [89]. The combination of dasatinib and quercetin, which target some of the six genes effectively killed senescent cells *in vitro*, and relieved senescent cell burden in mice transplanted with senescent preadipocytes or naturally aged mice. Since then, this drug combination has been successfully used for eliminating senescent cells in several mouse models with various age-related disorders such as athrogenesis, idiopathic pulmonary fibrosis and bone loss. Most recently [90], preliminary data obtained from an ongoing clinical trial of dasatinib plus quercetin showed a decrease in senescent cell abundance in individuals with diabetic kidney disease, in parallel with a reduction in β-galactosidase activity, the expression of p16 and p21, and SASP factors. Similar to quercetin, another flavonoid polyphenol-fisetin has shown to diminish senescence-associated phenotypes in multiple tissues and naturally aged mice [91].

In addition to targeting Bcl-2 network, senescent cells can also be eliminated through interfering with p53-FOXO4 interaction [37], suppression of PI3K/AKT-mediated anti-apoptotic pathway by HSP90 inhibitors [92] and inhibition of ATM [93].

**Immune-mediated clearance of senescent cell**

Accumulation of senescent cells in old organisms is associated with impaired immune system over time. Activation of immune system has been regarded as a potent strategy for eliminating senescent cells. Restoration of p53 in senescent hepatocellular carcinoma (HCC) cells can trigger an innate immune response including infiltrating leukocytes, neutrophils, macrophages and natural killer (NK) cells, thus inhibiting tumour growth in a model of hepatocellular carcinoma HCC. NK-mediated clearance of senescent hepatic stellate cells results in the resolution of fibrosis [94]. MICA and ULBP2, which are two ligands of an activating NK cell receptor (NKG2D), are upregulated in senescent cells upon various stimuli. The increased expression ensures a NK-mediated clearance of senescent fibroblasts [95]. A cell surface protein dipeptidyl peptidase 4 (DPP4) has been identified as a potential biomarker of senescent human diploid fibroblasts, in which anti-DPP4 antibodies that specifically target this membrane protein trigger the elimination of senescent cells through an NK-mediated cell death pathway [96]. Immune activation might be a powerful means of removing senescent cells from organisms to treat age-related diseases, however, a better understanding of precise immune modulators involved in senescent elimination is needed.

**Modulation of SASP**

Targeting upstream regulators of the SASP could potentially suppress the secretion of certain factors that are disadvantageous, thus relieving SASP-mediated damage to cells. Generally, three major strategies have been adopted to block SASP and attenuate senescent cell burden, which are inhibiting the up-stream factors of SASP-promoting signalling networks, blocking the secretion of the SASP and down-regulating the activity of certain products of the SASP [97].

### 1.1.5 The dual roles of senescence in cancer

Senescence was initially thought to be an alternative strategy to protect against malignancies due to its permanent inhibition of cell proliferation. However, emerging evidence also reveals the role of senescence as a cause of tumorigenesis, which drives either the transformation of premalignant cells to carcinomas or the formation of secondary tumour and cancer relapse.

Several studies also indicate that senescence is associated with side effects of several anticancer drugs.

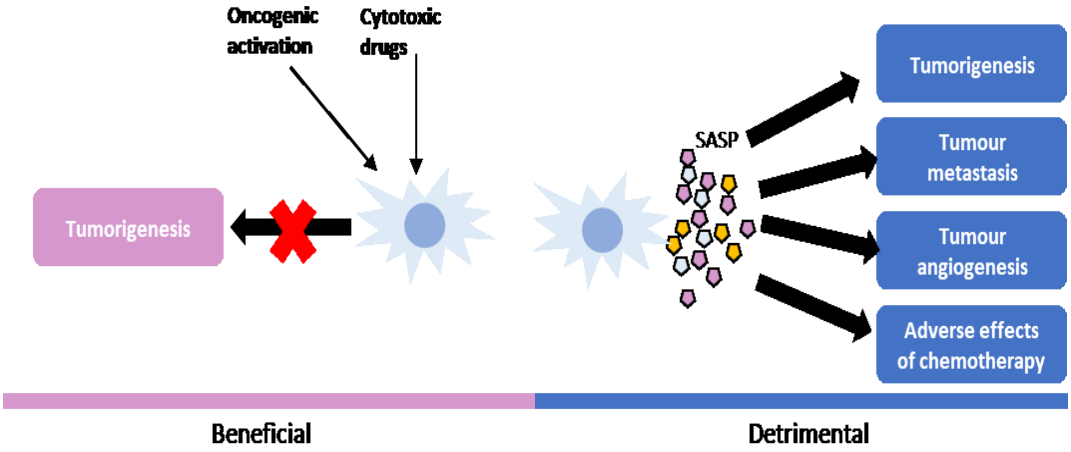


**Figure 1.7 Senescence plays a dual role in developing tumours.**

Senescence induced by oncogene activation serves as a tumour-suppressive mechanism, and the induction of senescence by chemotherapy is a useful strategy to stop cancer cell proliferation. However, senescent fibroblasts could promote the growth of neighbouring pre-neoplastic or neoplastic cells through SASP secretion.

### Oncogene-/therapy-induced senescent cells

Cells with oncogene activation or loss of the tumour suppressing gene PTEN undergo senescence, suggesting that cellular senescence is a barrier for tumorigenesis in this context. The ability of oncogenes to cause senescence or promote proliferation depends on the relative expression of oncogenes or cellular context. For instance, RAS at higher levels triggers senescence in an INK4a-ARF-dependent manner in mammary glands *in vivo*, whereas lower RAS levels lead to mammary tumour formation [98].

Drugs that are capable of inducing cellular senescence have been regarded as an alternative therapy for cancer treatment. The targets and mechanisms of these drugs differ substantially from one to the other, and can be divided into several groups, such as genotoxic drugs targeting many aspects of DNA, CDK inhibitors, activators of protein kinase C and inducers of ROS. Another class of drugs relies on manipulating components of the senescence secretome for pro-senescence therapies [99]. Most recently, by high-throughput functional genetic and compound screens, multiple aurora kinase inhibitors have been identified as

potent inducers of senescence in RAS mutant lung cancer [100]. Despite a promising role in cancer treatment, growing evidence indicates that therapy-induced senescence might produce a pro-carcinogenic microenvironment, thus promoting tumour recurrence or invasion. In this context, the second-step therapy which selectively eliminates senescent cells is highly needed to avoid deleterious side effects [101]. Therefore, senescence-directed anticancer therapies must be applied specifically and require stratification of patients by tumour type and genotype.

Senescence induced by telomere shortening occurs less in cancer cells. That is because all human cancer cells maintain an effective length of telomere through the expression of high levels of telomerase. One exception to this general trend occurs in telomerase-deficient mice expressing the oncogene Myc in B cells. Telomere-dependent senescence induction reduces the incidence of cancer in these animals, which acts as an efficient mechanism to tumour suppression *in vivo* [24].

**The SASP and cancer**

Although SASP factors can reinforce senescence through autocrine and paracrine regulation, many studies have shown that they can be more detrimental than beneficial, because in many settings they can promote tumorigenesis and tumour progression [48].

Senescent cells such as fibroblasts can promote the growth and proliferation of pre-neoplastic or neoplastic cells via SASP both *in vitro* and *in vivo* [102-105]. For example, osteopontin (OPN) produced from senescent fibroblasts activates MAPK signalling in pre-neoplastic keratinocytes to drive its proliferation both *in vitro* and *in vivo* [106; 107]. Furthermore, senescent fibroblasts when induced by prolonged CDK4/6 inhibition efficiently promote melanoma cell growth *in vitro* and *in vivo* [108]. In xenograft models, co-injection of senescent fibroblasts has shown to increase tumorigenicity of primary breast cancer tissues [104]. MMP produced by senescent human fibroblasts indirectly promotes early tumour growth in a mouse model by increasing the accessibility of mitogens and cytokines, and the mitogen hepatocyte growth factor (HGF) directly triggers the growth of MDA-MB-231 breast cancer cells [109]. The contributions of specific SASP components have been demonstrated using genetic knockdown, siRNAs, and other molecular inhibitors. For example, the use of

siRNA and blocking antibodies against amphiregulin (AREG) reduced the growth of benign prostate epithelial cells induced by conditioned media from senescent fibroblasts [110].

In addition to triggering proliferation, some of the SASP such as MMPs might lead to tumour invasion and metastasis via induction of epithelial-mesenchymal transition (EMT) [111; 112]. Breast cancer cells, when incubated with the conditioned media from senescent fibroblasts, show metastatic features *in vitro*, which is associated with the SASP factors IL-6 and IL-8 [113]. Induction of senescence in tumour cells can also affect the metastatic potential of neighbouring non-senescent tumour cells. For example, constitutive HER2 expression triggers senescence in breast cancer cells, eventually promoting the ability of proliferating breast cancer cells to metastasize in a non-cell-autonomous manner [114].

Senescent cells also produce some pro-angiogenic factors that result in tumour angiogenesis. For example, senescent fibroblasts can drive angiogenesis by producing vascular endothelial growth factor (VEGF), which can drive endothelial cell invasion and increase vascularization. Furthermore, the senescence-associated VEGF increases tumour vasculature when senescent fibroblasts are co-injected into mice with poorly malignant epithelial EpH4 cells [115]. In a mouse prostate model, connective tissue growth factor (CTGF) promotes angiogenesis and tumorigenesis [116].

Most recently, Demaria [117] et al. found that senescent cells induced by chemotherapies such as DNA-damaging reagents excrete some SASP components that are associated with the adverse effects of the treatment. In this context, selective elimination of senescent cells might be an additional approach for anticancer therapies.

The SASP also plays a complex role in cell immune response, although the mechanism is less understood. The SASP may suppress immune response of tumour cells. For example, when premalignant senescent hepatocytes coexist with liver cancer cells, the SASP-dependent recruitment of immature myeloid cells may promote HCC progression by impairing the function of NK cells [118]. In contrast, SASP factors can activate immune response in tumour cells, thus contributing to tumour inhibition. One of the studies showed that restoration of p53 induced senescence in an H-Ras-driven mouse liver cancer model *in vivo*, followed by recruitment of NK cells by SASP that effectively eliminate tumour cells [93; 119]. During cancer initiation, SASP-dependent recruitment of TH1, NK cells and macrophages

is essential to clear pre-neoplastic cells and prevent the progression of HCC [93; 120]. Collectively, there is a multi-faced interaction between the SASP, immune cells and cancer.

## 1.2 Role of glycogenesis in cancer

Glycogen is a highly branched polymer of glucose that functions as the major storage form of intracellular energy under physiological conditions. Reprogrammed glycogen metabolism has been increasingly observed in various types of tumour cells such as breast, kidney, ovarian and bladder tumours. Particularly, a subset of tumours, namely clear cell carcinoma, is characterized by high levels of intracellular glycogen [121]. Although many efforts have been made to understand the characteristics and function of glycogen in tumours, there are so far still several questions to be addressed.

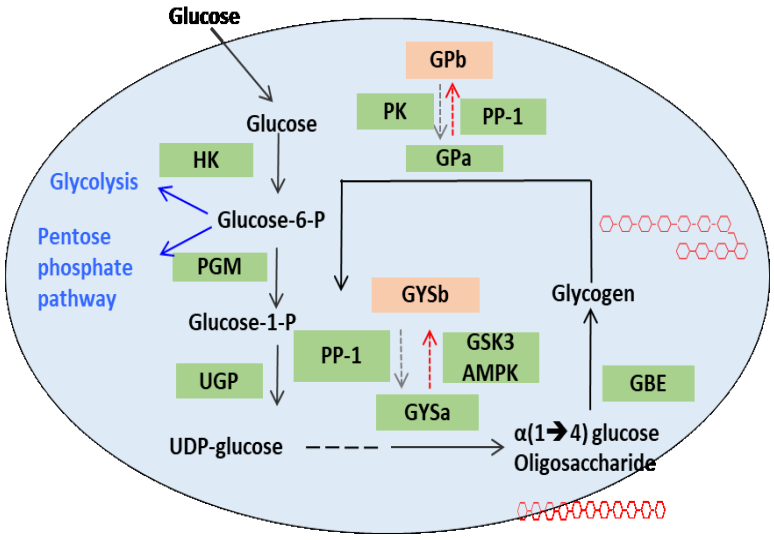


**Figure 1.8 Key pathways of glycogen synthesis and degradation in the cytosol.**

After transported into cells, glucose is converted into glucose 6-phosphate (G6P) and further glucose 1-phosphate (G1P) by hexokinase and phosphoglucomutase (PGM), respectively. G1P and uridine 5'-triphosphate (UTP) form UDP-glucose by the enzyme UDP-glucose pyrophosphorylase (UGP). Glycogenin (GN) initiates the first step of glycogen synthesis by self-glycosylation of a short glucose oligosaccharide primer. Glycogen synthase (GYS) elongates the glucose oligossacharide primer. Glycogen branching enzyme (GBE) catalyses the transfer of the newly-formed chain including 6 – 8 units at the distal end to the glucose residue from the existing chain through an α-1,6 linkage, which eventually leads to the spherical and branched structure of the glycogen granule. Glycogen phosphorylase (PYG) cleaves α-1,4-glycosidic bond between adjacent glucose molecules. When a branch of glycogen has been digested to 4 glucose residues, glycogen debranching enzyme (GDE) catalyses the transfer of three residues to the end of a nearby chain as well as cleavage of the remaining α-1,6-glycosidic branching point, producing a molecule of glucose and a linear chain of glycogen. [Adapted from Zois et al., 2014]

### 1.2.1 Physiological regulation of glycogen metabolism

**Glycogen structure**

Glycogen is the major intracellular storage form of glucose which mainly deposit in the liver to regulate blood glucose homeostasis, and in muscle tissues to fuel muscle contraction. The other tissues that also deposit glycogen include kidney, heart, fat and brain [122]. Three different types of glycogen structures have been identified by electron microscopy (EM), which are defined as γ-particles, β-granules and α-granules [123]. The γ-particle is the smallest subtype with a diameter of 1 nm and has a high electron density. γ-particles, together with protein-rich subunits, form the β-granules which are individual glycogen granules and mainly present in muscle. The β-granules are 10 - 40 nm in diameter and $10^6$ - $10^7$ in molecular weight. α-Granules that are formed by several β-granules and found in liver have a larger size, with a diameter of 50 – 300 nm and a molecular weight of >$10^8$ [123]. The basic structure of β-granule includes a priming protein, glycogenin, covalently bound to the glucose polymer which is formed by chains of approximately 13 glucose residues bound through α-1,4-glycosidic linkages and interconnected by α-1,6-glycosidic linkages at branch points [124]. In addition to glycogenin, many different proteins that are engaged glycogen metabolism pathway have been identified as part of the glycogen granule. Proteins including laforin [125; 126] and starch-binding domain protein 1 (Stbd1)/genethonin 1 [127] have recently been found bound to glycogen via a CBM20 domain.

The ratio of proteins to carbohydrate within a glycogen granule is responsible for the solubility of glycogen in acid. The acid-insoluble glycogen is termed pro-glycogen which is thought to be in a smaller size and has a sufficient proportion of protein, whereas macro-glycogen is more soluble in acid due to a larger ratio of carbohydrate and normally present in the late phase of glycogenesis [126; 128]. Although majorly composed of glucose residues and proteins, glycogen contains other trace constituents, such as glucosamine and covalent phosphate [122].

**Glycogen synthesis**

Total levels of intracellular glycogen are determined by the coordinated actions of glycogen synthesis and glycogen degradation. Glycogen synthesis can occur directly via transportation

of extracellular glucose into cells by one or more of several glucose transporters (GLUTs), or indirectly via the conversion from gluconeogenic precursors such as lactate and amino acids [122].

Glucose is converted into glucose 6-phosphate (G6P) by the action of hexokinase or glucokinase, and further into glucose 1-phosphate (G1P) by phosphoglucomutase (PGM). G1P and uridine 5'-triphosphate (UTP) form UDP-glucose by the enzyme UDP-glucose pyrophosphorylase (UGP) in the presence of $Mg^{2+}$. Next, glycogenin which is a self-glycosyltransferase acts as the primer of glycogenesis by catalysing the transfer of glucose residues from UDP-glucose to itself, forming α-1,4-glycosydic linkages. Once sufficient glucose residues have been built up, glycogen synthase (GYS) drives the extending of the chain. When the length of main chain reaches 10 – 20, glycogen branching enzyme (GBE) catalyses the transfer of the newly-formed chain including 6 – 8 units at the distal end to the glucose residue from the existing chain through an α-1,6 linkage, which eventually leads to the spherical and branched structure of the glycogen granule [121-123; 129].

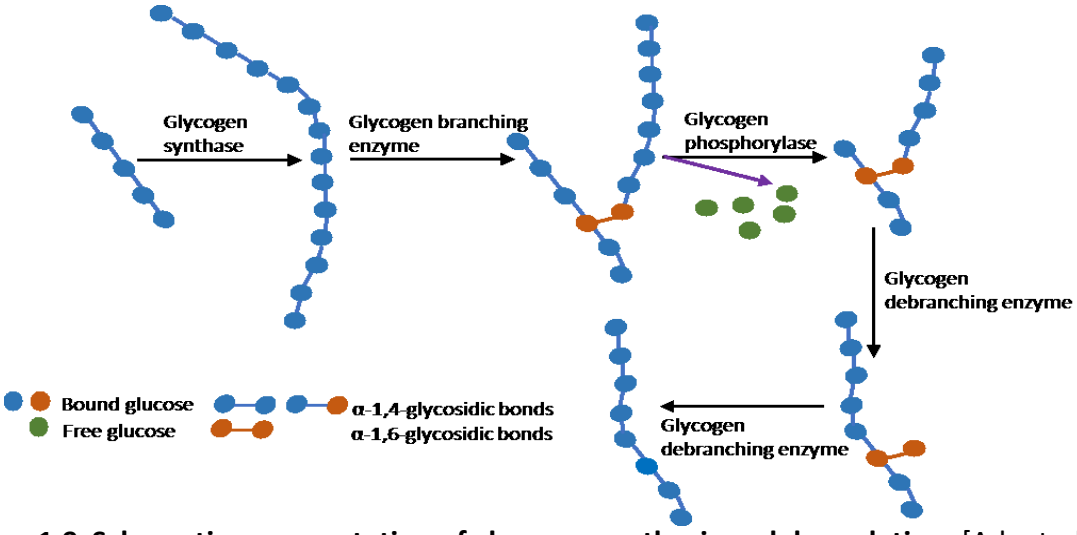


**Figure 1.9 Schematic representation of glycogen synthesis and degradation.** [Adapted from Lew et al., 2015]

Among these steps, GYS regulation is thought to be one of the rate-limiting factors. There are two isoforms of GYS, glycogen synthase 1 (GYS1), which is expressed in muscle and most other tissues, and glycogen synthase 2 (GYS2), which is stored mainly in the liver [130]. The mechanisms that regulate the activity of glycogen synthases are complicated and differ in muscle and liver. One of the major regulators is the reversible phosphorylation and

dephosphorylation of the enzyme. GYS is inactivated through phosphorylation at various sites such as serine 7 (S7) and serine 641 (S641), by a variety of enzymes including glycogen synthase kinase 3β (GSK3β), protein kinase A (PKA) and AMP-activated protein kinase (AMPK) [131]. In contrast, protein phosphatase-1 (PP1) could restore the activity of GYS by catalysing the dephosphorylation of this enzyme [132]. In addition to phosphorylation and dephosphorylation, GYS is modulated by an allosteric activator – G6P. G6P not only plays a role in allosteric regulation, but also makes glycogen synthase a more suitable substrate for PP1 which initiates the covalent activation of glycogen synthase [133].

Insulin is another determinant of glycogen synthesis and accumulation. On one hand, insulin activates insulin receptor tyrosine kinase (RTK), which leads to activation of the phosphoinositide 3-kinase (PI3K) pathway and further stimulates glycogen synthesis via inhibition of GSK3β and activation of PP1. On the other hand, insulin stimulates glucose uptake by promoting the translocation of glucose transporters to cell membrane, which subsequently increases glycogen synthesis. When insulin cannot be produced sufficiently by pancreas or does not work effectively, the synthesis of glycogen from blood glucose is impaired, thus causing high levels of glucose in bloodstream which is the cause of diabetes [134].

Apart from enzyme regulation, the initiation of a new glycogen granule is also closely associated with the actin cytoskeleton, to which glycogenin is bound at the beginning of glycogen synthesis. Disruption of the actin cytoskeleton by cytochalasin D results in granule dispersion, suggesting that the alignments of glycogen granules are strongly associated with cytosolic filaments [135]. Upon glucose administration, GYS has also been found to translocate to cytoplasmic spherical structures, supporting the crucial role of actin cytoskeleton in the early phase of glycogen synthesis [136; 137].

**Glycogen degradation**

Glycogen utilization may occur in cytoplasm through the coordinated action of glycogen debranching enzyme (GDE) and glycogen phosphorylase (PYG) or via lysosome by the action of α-glucosidase (GGA).

During cytosolic degradation, PYG is a rate-limiting enzyme that cleaves α-1,4-glycosidic bond between adjacent glucose molecules. When a branch of glycogen has been digested to 4 glucose residues, glycogen debranching enzyme catalyses the transfer of three residues to the end of a nearby chain as well as cleavage of the remaining α-1,6-glycosidic branching point, producing a molecule of glucose and a linear chain of glycogen. G1P is the major product of glycogen breakdown and is further converted to G6P by phosphoglucomutase. The resulting G6P is either internally used as a source of glycolysis flux or transported into the ER lumen in gluconeogenic tissues (such as liver, kidney and intestine) where it is dephosphorylated to glucose [121; 122; 129; 138]. There are three isoforms of PYG which are encoded by different genes, named PYGM (muscle), PYGL (liver) and PYGB (brain). Similar to GYS, PYG is modulated through both allosteric control and reversible phosphorylation/dephosphorylation. PYG has two forms - phosphorylase a and phosphorylase b, and each of the form exists in a T (tense) state and R (relaxed) state. Normally, phosphorylase a exists in R state and is activated, while phosphorylase b exists in T state which is less active. Phosphorylation at serine-14 of PYGb (less active) to PYGa (active) is catalysed by phosphorylase kinase (PhK), which is activated by cAMP-dependent protein kinase A and increased levels of calcium. PP1 in conjugation with the glycogen target subunit family proteins dephosphorylates the PYGa to the inactive form, PYGb [121; 139; 140].

Lysosome is another organelle where glycogen is deposited and degraded by GAA. It has been reported that around 10% of total liver glycogen and 5% of muscle glycogen is presented in lysosome. Although the exact mechanism how glycogen is transferred to lysosome remains unclear, it is likely related to autophagic or autophagy-like vesicular trafficking. Glycogen metabolism in lysosome has been found in newborns in liver, and serves as an additional glucose source [141]. Furthermore, laforin, which is a phosphatase, is involved in the regulation of glycogen and degradation of glycogen-associated proteins via autophagy-lysosomal pathway, while malin plays a similar role in modulating glycogen via ubiquitin-proteasome pathway [142].

### 1.2.2 Methods for detecting glycogen accumulation

Several methods have been used to detect glycogen accumulation in cells involving EM, biochemistry, immunohistochemistry, fluorescence imaging and radioisotope methods [121; 129].

In brief, periodic acid-Schiff (PAS) is one of the most commonly used methods to stain structures containing glycogen both in cells and tissues [143]. The distribution of glycogen can be studied by using a fluorescent antibody against glycogen, which was developed by Dr. Baba [144]. At least, three biochemical methods have been used for analysis of glycogen in tissue homogenates, including enzymatic analysis of glucose produced by acid hydrolysis of the tissue, measurement of glucose produced by enzymatic hydrolysis of the tissue with amylo-α-1,4-α-1,6-glucosidase and analysis of G1P produced by degradation of glycogen with phosphorylase and debranching complex.

To evaluate dynamic glycogen turnover, the fluorescent 2-NBDG (2-(N-(7-nitrobenz-2-oxa-1,3-diazol 4-yl) amino)-2-deoxyglucose), which is a glucosamine derivative, has been used and proved to be a good probe *in vitro*. However, this probe is not useful for *in vivo* detection because of weak tissue penetration of the emitted green fluorescence [145]. More recently, a PET imaging agent [$^{18}$F]NFTG has been developed to measure glycogenesis in cultured tumour cells and tumour xenografts *in vivo*, showing potential role as a non-invasive method to evaluate tumour treatment response according to changes of glycogen level [146].

### 1.2.3 Glycogen metabolism in cancer

Metabolism has been an extensively studied topic in cancer research over the last decade. Although the role of glucose metabolism in cancer has been widely investigated, aberrations in other metabolic pathways are only just beginning to be understood. One such pathway is glycogen metabolism which is being explored as reprogrammed in several types of tumours [147].

An inverse correlation between glycogen content and cell proliferative state has been found in a wide range of cancer cell lines such as breast, bladder, ovarian and colorectal cells [148; 149], and suggesting that stored glycogen is profoundly consumed for providing energy for cell growth during S phase. Similarly, Favaro et al. observed that increased glycogen

accumulation caused by PYGL deletion is related to a p53-dependent senescence in U87 cells. This result is further confirmed *in vivo*, where the growth of PYGL-deficient tumour xenografts is markedly impaired [150]. Taken together, the changes in glycogen level might be a crucial indicator of cell proliferative state in some tumours.

Genetic regulation of glycogen metabolism has been reported in several studies. For example, the small GTPase Rab25 has been found as a positive regulator of glycogen synthesis in cancer cells. A possible mechanism is that Rab25 inhibits GSK3β through activation of Akt, which in turn activates GYS and facilitates glycogenesis. The increased glycogen accumulation then provides the energy to proliferative cells cultured under nutrient stress condition [151]. Another study reports that KIAA1199 (also known as cell migration-inducing and hyaluronan-binding protein), which is often overexpressed in multiple cancers, increases the phosphorylation of PYGL by depolymerizing hyaluronan and thereby promotes glycogen degradation and cell survival [152]. It remains unknown whether other oncogenic pathways, such as oncogene MYC which is a master regulator of tumour cell metabolism, are associated with glycogen metabolic reprogramming in cancer cells.

Glycogen storage and utilization could be a crucial means for supplying energy under environmental conditions of nutrient deprivation, thus protecting cancer cells from cell death. For example, protein target to glycogen (PTG) subunit PPP1R3C, which is an enzyme involved in glycogen synthesis, has been found to protect liver cancer cells from cell death in the absence of glucose via modulation of oxidative stress and autophagy, whereas silencing of PTG induced cell apoptosis [153]. Additionally, PYGB activity and glycogen breakdown have shown to be increased upon serum starvation in gastric cancer cells, which in turn lead to cancer cell survival and reduced apoptosis.

Hypoxia, one of the remarkable hallmarks of tumours, refers to the reduction or lack of oxygen within tumour microenvironment resulting from abnormal blood vessels, defective blood perfusion and limited nutrients [121]. It has been observed that hypoxia induces increased glycogen turnover in tumour cells *in vitro* and *in vivo*, and similarly in non-cancer cells. The increased glycogen accumulation has been shown to be associated with increased activity of glycogen synthetic enzymes in a hypoxia inducible factor (HIF)-dependent manner. GYS1, UTP:glucose-1-phosphate uridylyltransferase (UGP2) and 1,4-alpha glucan branching

enzyme (GBE1) were significantly increased under hypoxia condition, resulting in elevated levels of glycogen in hepatoma cells. Further, knockdown of either HIF-1α or GYS1 attenuated hypoxia-induced glycogen accumulation, whereas GYS1 overexpression was sufficient to mimic this effect, suggesting that regulation of GYS1 by HIF-1α plays a central role in the hypoxic accumulation of glycogen [154]. Another study showed that PPP1R3C (PP1 Regulatory Subunit 3C) induction correlates with a significant glycogen storage in MCF-7 cells under hypoxia whilst knockdown of either HIF-1α or PPP1R3C suppresses glycogen accumulation [155]. What is less understood is how glycogen degradation is regulated under cancer-associated hypoxic conditions [150].

Some studies have shown that dysregulation of glycogen metabolism is associated with aggressive cancer cell phenotypes *in vitro* and poor survival outcomes in patients. For example, an 18% of increase in the expression of GYS1, GYS2 and GBE1 has been reported in acute myeloid leukemia (AML) patients where a significantly poor survival outcome is seen. Leukemic cells might sustain aberrant proliferation by suppressing excess AMPK activity through elevated glycogenic flux. Knockdown of GYS1 in leukaemia cells *in vitro* and *in vivo* not only significantly lowered flux toward glycogen, but also reduced cell growth and metabolic reprogramming [156]. The PhKG1 (the γ-subunit) of the holoenzyme phosphorylase kinase, which is involved in activation of glycogen phosphorylase, is upregulated in several human tumour samples. The increased activity is associated with tumour progression, angiogenesis and tumour metabolism, suggesting that PhKG1 could be a potential target for cancer therapy. Another study demonstrates that inhibition of PYGL by a small molecule inhibitor (CP-320626) leads to growth arrest and cell death in a human pancreatic cancer MIA PaCa-2 cell line *in vitro* via limiting glucose oxidation, and synthesis of ribose and fatty acid [157].

It has been recently shown that the human glycogen debranching enzyme (AGL) is a tumour growth suppressor in human bladder cancer. Loss of AGL results in a decrease in normal cellular glycogen, an increase in abnormal glycogen structures, glucose utilization and lactate production, which eventually results in enhanced tumour growth in xenograft models of bladder cancer. The enhanced tumour growth upon lowering AGL is found to be associated with elevated glycine synthesis through increased levels of serine hydroxymethyltransferase

2 (SHMT2). Furthermore, the effect of AGL on tumour growth is independent of its enzyme activity, indicating that AGL has an unknown non-enzymatic function [158; 159].

Most recently, the role of glycogen in cancer metastasis has been investigated for the first time by Curtis et al [160]. Ovarian cancer cells, when co-cultured with primary human cancer-associated fibroblasts (CAFs) isolated from over 100 serous ovarian cancer patients, show increased glycogen mobilization and therefore increase proliferation, invasion and metastasis. Briefly, ovarian cancer cells initially produce TGF-β1, which activates p38αMAPK signalling in neighbouring CAFs, and, in response, the CAFs secrete cytokines and chemokines (IL-6, CXCL10 and CCL5) that trigger mobilization of glycogen in cancer cells in a glycogen phosphorylase-dependent manner. Inhibition of glycogen phosphorylase reduced CAF-mediated metastatic tumour growth *in vivo*. It would be worth investigating how other components within the tumour microenvironment affect glycogen metabolism in cancer cells [160].

## 1.3 PET imaging for assessing tumour response to therapy

### 1.3.1 An introduction to PET imaging

Positron emission tomography (PET) is a functional imaging technique that enables visualization of biochemical processes in the body upon injection of a radioisotope-labelled chemical substance (1). The gamma rays used for PET imaging are produced when a positron ($\beta^+$, a positively charged electron) emitted by radionuclide meets a free electron ($e^-$), where an annihilation reaction occurs, thus leading to the production of a pair of 511 kiloelectron volt (keV) photons travelling in opposite directions. The pairs of gamma rays are detected by several rings of detectors around patients. These data are then processed using backprojection and image reconstruction algorithms to create an image map of the organ or tissue being studied. The brightness/intensity of the tissue appearing on the image reflects the amount of radionuclide accumulated in the tissue, thus indicating the level of organ or tissue function [161; 162]

The ability to measure physiological functions makes PET imaging a crucial complementary aspect to anatomical imaging modalities such as ultrasound, computed

tomography (CT) and conventional magnetic resonance imaging (MRI). In the clinic, PET imaging is often combined with CT or MRI, to provide both anatomic and molecular information [163].

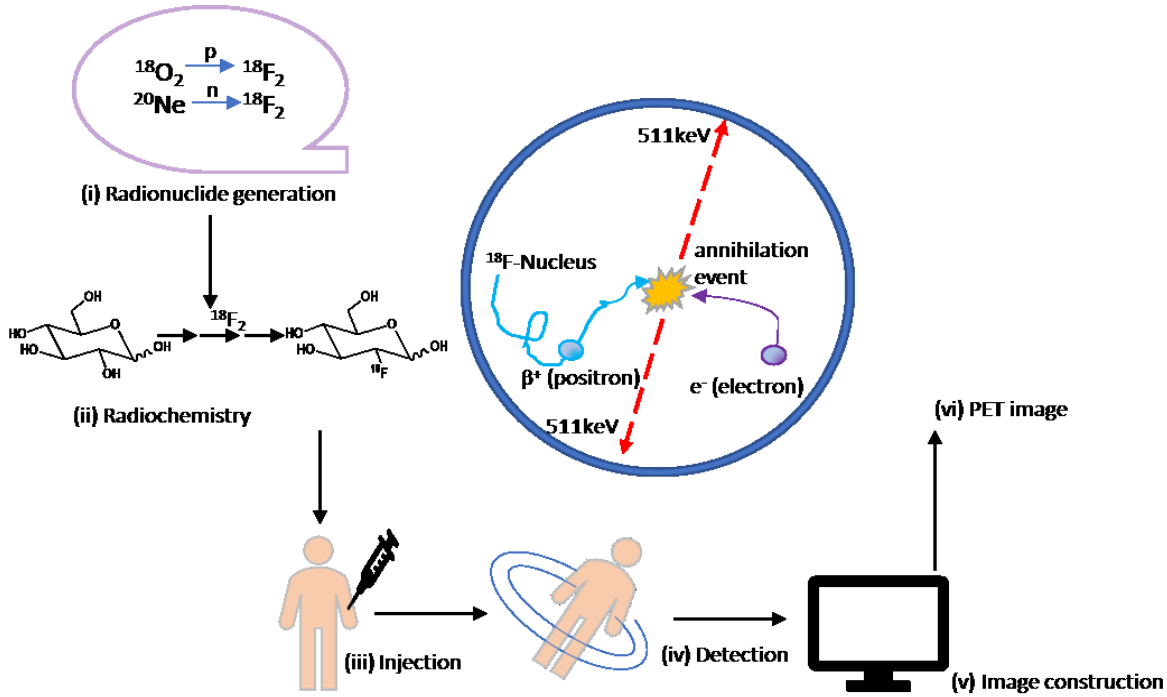


**Figure 1.10 Schematic representation of a [$^{18}$F]FDG PET image acquisition.** [Adapted from Patching et al., 2015]

(i) Radionuclide generation. The radionuclide fluorine-18 (half-life 110 minutes) is produced using a particle accelerator (cyclotron) by proton bombardment of oxygen-18 or deuteron bombardment of neon-20. (ii) Synthesis of radiolabelled molecule. Fluorine-18 is incorporated into glucose by substitution of the normal hydroxyl group at the C-2 position. (iii) Injection into a patient. A dose of [$^{18}$F]FDG in solution (typically 5 to 10 mCi or 200 to 400 MBq) is typically injected into the bloodstream of a patient who has been fasted for at least six hours. [$^{18}$F]FDG PET scan takes approximately one hour allowing the tracer to distribute to body tissues. (iv) Detection of gamma (annihilation) photons. The gamma rays are produced when a positron (β+, a positively charged electron) emitted by radionuclide meets a free electron (e-), where an annihilation reaction occurs, thus leading to the production of a pair of 511 kiloelectron volt (keV) photons travelling in opposite directions. The pairs of gamma rays are detected by several rings of detectors around patients. (v) Image construction. The locations of hundreds of thousands of coincidence events from a scanning were analysed by mathematical equations and computing. This eventually reconstructs a two- or three-dimensional image of the radiolabelled compound in body tissues.

PET imaging has been widely applied to clinical practice for diagnosis, staging and assessment of response to therapy in oncology, cardiology and neurology. The role of PET imaging in oncology has been increasingly recognized as it can functionally characterise

several cancer biological processes such as metabolic changes, cell fate/dysregulation, genome instability, angiogenesis, microenvironmental alterations and immune response [164]. PET imaging can also be used to non-invasively obtain crucial pharmacokinetic (PK) and pharmacodynamic (PD) information, therefore, its role in anticancer drug development is also increasing [165].

Since the late 1970s when the first PET instrument was introduced, large quantities of radiopharmaceuticals have been developed and used for pre-clinical research and clinical application. Each tracer primarily consists of a position-emitting radioisotope with short half-lives such as $^{11}$C (20.4 minutes), $^{18}$F (109.8 minutes), $^{64}$Cu (12.7 hours), $^{68}$Ga (67.7 minutes) and $^{89}$Zr (78.4 hours), and an analogue of biologically active component such as small molecules, peptides, antibodies and nanoparticles that can trace a specific biological process or target certain proteins [166]. The most commonly used radiotracer by far in clinical PET scanning is $^{18}$F-fluorodeoxyglucose ([$^{18}$F]FDG) which measures the dynamic changes in glucose metabolism in tumours (also known as Warburg effect) [167]. Reprogrammed metabolism is one of the remarkable hallmarks of tumours, which has received the most attention in the field of radiopharmaceutical imaging [166]. For example, two US Food and Drug Administration (FDA)-approved radiotracers, namely [$^{11}$C]choline [168] and [$^{18}$F]Fluciclovine [169], have been clinically used for diagnosis of recurrent prostate cancer in patients based on elevated levels of phospholipid metabolism and amino acid transporters, respectively. Other agents that target tumour-associated synthesis of glycogen [146] and fatty acids [170] continue to show promise in preclinical settings and clinical trials.

Another crucial application of PET imaging in clinical practice is to assess the efficacy of therapies at early phase in patients with cancer. As many anticancer drugs are designed to interrupt signal transduction pathways of cell proliferation and lead to cell death, the focus of assessing tumour response to therapy by PET imaging relies on targeting alterations involved in cell proliferation or apoptosis at early cycles of treatment. Uncontrolled cell proliferation and evasion of apoptosis are also known as the most remarkable phenotypes of tumours, therefore, imaging of cell proliferation and death could also be exploited as prognostic biomarkers or staging of tumours with various aggressiveness [166; 171; 172].

### 1.3.2 Imaging cell proliferation

Uncontrolled cell growth is perhaps the most remarkable phenotype of all types of tumours, which initiates and maintains other neoplastic characterisations. The rate of cell division is an important prognostic characteristic of malignancies, and majority of anticancer drugs are designed to inhibit cell proliferation. Therefore, on one hand, measurement of the proliferative status can provide useful information regarding the prognosis and aggressiveness of tumours, thereby guiding treatment protocols in clinical practice. On the other hand, a change in the proliferative status of a tumour during or after treatment has the potential to serve as a predictor of response and allow further tailoring of therapy. PET imaging of cell proliferation could provide a serial 3-dimentional assessment of tumour growth or regression *in vivo*, which overcomes the limitation of conventional detection strategies such as Ki67 staining that can be only used *ex vivo* in biopsy specimens [171; 172].

Nuclear DNA replication is an essential process during cell division, which requires increased substrates including nucleosides and nucleoside bases. Thymidine nucleosides, which are produced either through methylation of deoxyuridine monophosphate (dUMP) in a reaction catalysed by thymidylate synthase (TS) or through the phosphorylation of exogenous thymidine, contributes to the *de novo* and salvage pathway of DNA synthesis, respectively [173]. Over several decades, thymidine and its analogues have been radiolabelled and assessed for measuring DNA synthesis. One of the radiolabelled thymidine analogues, $^{18}$F-3'-fluoro-3-deoxy-L-thymidine ([$^{18}$F]FLT), was introduced in 1998 by Shields et al. and has been widely applied to characterise cell proliferation in many tumour types [174-179]. Upon entry into cells via the human equilibrative nucleoside transporter 1 (hENT1), FLT is phosphorylated by thymidine kinase-1 (TK1) and trapped in cells without significant incorporation into DNA. The retention of [$^{18}$F]FLT in cells has been found to be strongly associated with TK1 expression which is increased during S phase of cell cycle [180]. Although [$^{18}$F]FLT is exploited as a cell proliferation PET biomarker, it is unable to detect the *de novo* DNA synthesis pathway. This limits the use of [$^{18}$F]FLT in imaging tumours whose DNA synthesis is largely dependent on the *de novo* pathway [181]. When adopted in clinical practise, [$^{18}$F]FLT PET imaging is less efficient in detecting and staging tumours due to the low overall uptake and physiological retention in liver and bone marrow [182]. However, its

application in predicting tumour response to therapy has been thought promising as most anticancer drugs elicit inhibition of proliferation of tumour cells [177].

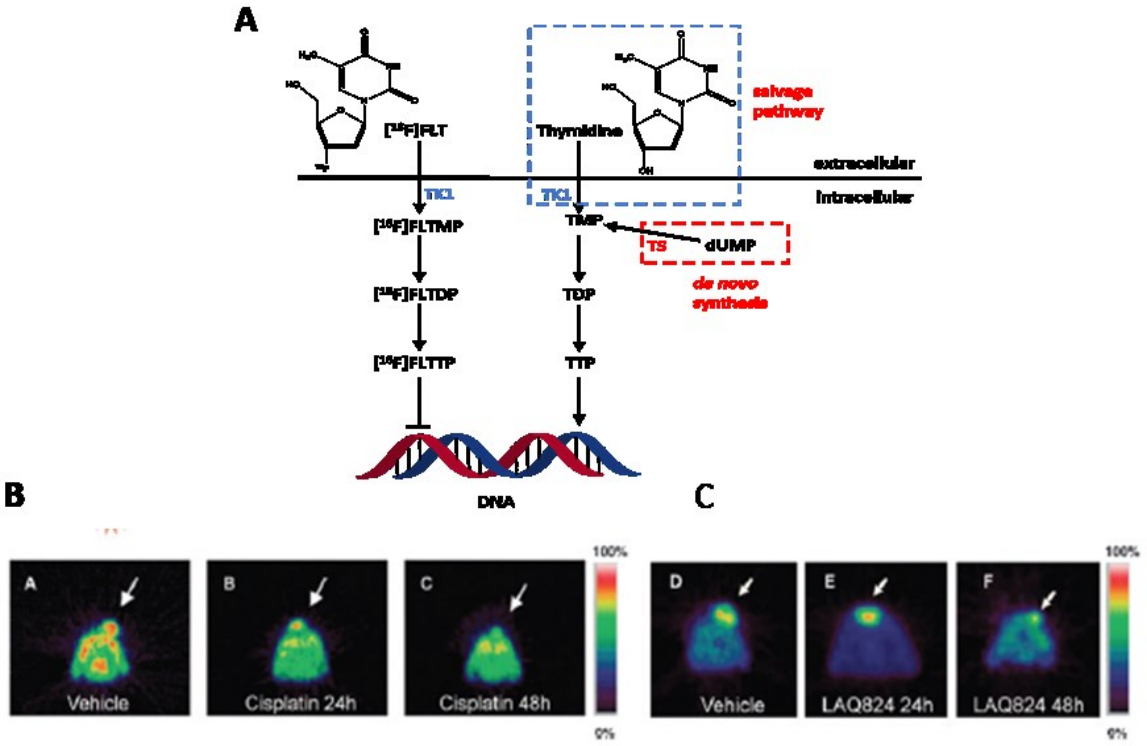


**Figure 1.11 Examples of [$^{18}$F]FLT-PET to assess anticancer treatment response in preclinical mice models.**

**A,** Uptake mechanism of thymidine and [$^{18}$F]FLT. **B,** Examples of [$^{18}$F]FLT-PET images of RIF-1 tumour-bearing mice after cisplatin treatment. Arrows, tumours. **C,** Examples of [$^{18}$F]FLT-PET images of HCT116 tumour-bearing mice after LAQ824 treatment [171; 178; 179]. Images (B and C) reproduced with permission of the rights holder, American Association for Cancer Research.

Another thymidine-based PET tracer is 1-(2'-deoxy-2'-fluoro-beta-D-arabinofuranosyl)-thymine ([$^{18}$F]FMAU), which contains the 3'-hydroxy group and can be incorporated into DNA, providing a direct measurement of DNA synthesis [183-185]. However, [$^{18}$F]FMAU is not only a substrate for TK1, but also for the mitochondrial enzyme thymidine kinase-2 (TK2), resulting in high uptake in mitochondrial of normal tissues [184]. Taken together, $^{18}$F-FLT is more desirable than [$^{18}$F]FMAU for imaging the proliferative status of solid tumours.

[$^{18}$F]FDG, the standard PET imaging tracer, can be used for indirectly tracing proliferative status of cancer cells by measuring the changes in the rate of glucose utilization as cells normally produce energy and synthesize protein in a growth-related manner. However, some

studies [186; 187] have suggested its limitation in assessing cell proliferation as changes in metabolism may lag behind the events directly involved in modulation of cell proliferation. Therefore, it is speculated that [$^{18}$F]FDG is more accurate as an indicator of cell viability [171]. In addition to increased glucose utilization, tumours with high proliferating rates contain large amounts of phospholipids, amino acids, glutamine and acetate to meet increased demands for the synthesis of lipid, protein, fatty acid and glutamine metabolism. Tracers that measure these metabolic events might be alternative tools for indirectly characterizing cancer cell proliferation [188].

Targeting transmembrane receptors such as epidermal growth factor receptor (EGFR) and human epidermal growth factor receptor 2 (HER2), or intracellular receptors such as the oestrogen receptor (ER), provides an additional opportunity to indirectly characterise cancer cell proliferation by PET imaging [189]. These receptors, which have been found overexpressed in many cancer types, initiate mitogenic signalling and promote cell growth through resultant downstream effectors [190]. Strategies for developing EGFR-based probes have been based on radiolabelling of monoclonal antibodies (mAbs), affibodies, nanobodies and small-molecule inhibitors [191]. Several attempts have been made to characterise EGFR through radiolabelling of EGF, the endogenous ligand of EGFR. However, these tracers showed poor contrast between tumour and the background due to some intrinsic drawbacks of a native ligand; for example, the co-injection of nonradioactive ligand to block EGFR in the liver may induce a biological effect and cause cell proliferation [192]. A more promising strategy is to radiolabel the clinically available mAbs for imaging EGFR such as cetuximab. Various types of radionuclides such as $^{111}$In, $^{64}$Cu, $^{89}$Zr and $^{86}$Y have been explored to label cetuximab by using DTPA or DOTA as chelate moiety; tracer retention in tumours was correlated with EGFR expression levels, however, a slow blood clearance led to poor imaging contrast at early time points post-injection. To overcome this limitation, recently, affibodies which are a class of small affinity proteins have been radiolabelled for evaluating EGFR status in tumours. It has been proved that these tracers have high affinity to EGFR and rapid clearance of unbound tracer from the circulation. Additionally, PD153035, a small-molecule inhibitor of EGFR, has been labelled by C-11 and used for assessing EGFR expression in patients with non-small-cell lung cancer (NSCLC) [193].

Similar approaches have been applied to develop HER2-based radiopharmaceuticals for characterizing HER2 expression in tumours and assessing patients' sensitivity to HER2-directed therapies [192]. PET imaging of ER is also a diagnostic tool in breast cancer patients. Uptake of the ER-specific tracer [$^{18}$F]FES has been shown positively correlated with expression of ERα in breast cancer patients [194; 195].

In summary, imaging of cellular proliferation has proved to be an effective strategy for assessing the efficacy of anticancer therapies, because it is tumour-specific and occurs at early cycle of treatment that is likely to provide earlier and definitive evidence for guiding therapy.

### 1.3.3 Imaging cell apoptosis

Programmed cell death or apoptosis is a fundamental biological process during which unwanted or damaged cells are eliminated, thus maintaining tissue homeostasis. The ability of cancer cells to evade apoptosis has been regarded as one of the hallmarks of cancer. Moreover, cell apoptosis is a common consequence of anticancer therapy and often requires monitoring to offer predictive outcome information in clinical practice [172].

Cell apoptosis is regulated by either intrinsic pathway that is strongly dependent on the release of proteins from mitochondrial or by extrinsic pathway, which is initiated upon extracellular ligands binding to cell-surface death receptors [196]. Several of these biochemical changes have been developed as potential targets for PET imaging of cell apoptosis both in pre-clinical studies and clinical trials.

Activation of caspases such as caspase-3 and caspase-7 is one of the most noticeable features of apoptosis which has been studied by several caspase-3/7 specific PET tracers, such as [$^{18}$F]WC-II-89 [197], [$^{18}$F]WC-IV-3 [198] and [$^{18}$F]ICMT-11. ICMT-11 is the most advanced for imaging activated caspase 3, and has been reported to characterise the levels of caspase 3 in lymphoma xenografts, and breast and colon models in preclinical [199-202]. As the changes in caspase 3 during cell apoptosis is transient, one of the challenges of this tracer is to determine the best time to conduct imaging following initiation of treatment [203]. A recent clinical trial shows a lack of significant changes in [$^{18}$F]ICMT imaging in patients with breast and lung cancer after treatment due to only a small proportion of apoptosis induced by first-

line chemotherapy, suggesting that therapy-induced caspase 3 activation is not an exclusive marker of response [204].

Exposure of phosphatidylserine (PS) is another common feature of cell apoptosis, which occurs within several hours upon apoptotic stimulation. Annexin V, a natural PS-binding protein, has been labelled by PET ($^{124}$I and $^{18}$F) and SPECT ($^{99m}$Tc) radionuclides and assessed for imaging tumour apoptosis in experimental and clinical settings [205; 206]. However, several limitations have been reported such as slow delivery of the tracer to the sites of interest, slow clearance from tissues resulting in high radiation doses and a lack of specificity [196]. Another similar PS-binding protein that is smaller and based on the C2A domain of synaptotagmin I shows higher affinity than annexin V for dying cells *in vitro*. [$^{99m}$Tc]C2A has been developed and used for detecting apoptosis following paclitaxel treatment in non-small cell lung carcinoma xenografts, whilst [$^{18}$F]-labelled C2A has also been developed for PET. However, poor specificity for apoptosis is a common disadvantage of these PS-based tracers, as tracer retention can also be seen in necrotic and inflamed tissue as well as platelets [207; 208].

Another class of apoptosis-based PET tracer relies on targeting the apoptotic 'membrane imprint' which includes membrane scramblase activation, irreversible membrane depolarization and permanent cellular acidification. These compounds have been shown to be selective for apoptosis as they do not cross the cell membrane of viable cells but are able to cross the cell membrane of apoptotic cells and accumulate in the cytoplasm in the early stage of the process [209]. $^{18}$F-labeled 5-fluoropentyl-2-methyl-malonic acid ([$^{18}$F]ML-10), a small peptide PET agent, has been used for clinical imaging of apoptosis [210]. The early response to radiotherapy in patients with brain tumour has been assessed by [ $^{18}$F]ML-10 in a clinical trial; a good correlation was observed between tracer retention at early timepoints of radiotherapy and late changes in tumour size as measured by MRI [211; 212]. Further investigation is needed to classify the precise molecular mechanism of this tracer.

In addition to these broad apoptotic phenotypes, cancer cells may alter specific targets along the cell death pathway to resist apoptosis. For example, proteins such as Bax or Bim that trigger intracellular apoptosis may be downregulated, and proteins such as Bcl-2 or Bcl-

XL may be overexpressed in malignant cells. These alterations might be used as potential targets for PET imaging of apoptosis [194].

### 1.3.4 Imaging cell necrosis

Recent research has identified a series of previously unrecognized regulated cell death modalities beyond apoptosis, including necroptosis, parthanatos, ferroptosis and oxytosis [213]. The development of necrosis-target PET tracers has been made to obtain potentially valuable prognostic information on tumour necrosis or targeting necrosis as an anticancer treatment approach [214].

Although necrosis was generally considered an unprogrammed form of cell death, it was recently discovered to be regulated in processes like necroptosis. Unlike tumour-suppressive apoptotic cell death, necrosis has been reported to promote cancer cell proliferation. Necrosis begins with cell swelling, resulting in cell membrane rupture and release of cellular cytoplasmic contents into the extracellular space, including release of high mobility group box 1 (HMGB1), which is a nonhistone nuclear protein that regulates gene expression and nucleosome stability and acts as a proinflammatory and tumour-promoting cytokine when released by necrotic cells. These released molecules recruit immune cells, which can evoke inflammatory reactions and thereby promote tumour progression by increasing the probability of proto-oncogenic mutation or epigenetic alterations and inducing angiogenesis, cancer cell proliferation, and invasiveness [215-217]. Moreover, the development of a necrotic core in cancer patients is correlated with increased tumour size and poor prognosis due to the emergence of chemoresistance and metastases [218].

Many efforts have been made to develop radiotracers for either imaging of necrosis or directing necrosis targeted therapy [214]. Strategies for developing necrosis-targeted tracers are currently based on targeting specific contents that are released by necrotic cells. The biomarkers that have been targeted for necrosis imaging or targeted therapy include DNA/histone H1 complex, exposed DNA, heat shock protein 90 (Hsp90), lupus-associated (La) antigen, HMGB1, fumarase and other unknown molecules [214]. Tumour necrosis treatment has been conducted in clinic in patients with advanced lung cancer by using 131–I labelled recombinant chimeric TNT monoclonal antibody ($^{131}$I-chTNT) [219]. Although several molecular probes for imaging necrosis have been synthesized and evaluated in preclinical

animal models [220-222], there are some questions remaining to be addressed prior to clinical translation, such as low probe binding affinity, poor pharmacokinetic properties and lack of clinically relevant necrosis-specific biomarker.

### 1.3.5 Imaging other cell fates in response to therapy

Autophagy is another crucial fate of cancer cells in response to various physiological stressful conditions or following treatment with pharmacological inhibitors and radiotherapy. Basal autophagy is considered a factor of cancer suppression, whereas reduced and aberrant autophagy that inhibits degradation of damaged components or proteins in oxidative-stressed cells promotes tumour development. There have been many chemotherapies such as chloroquine (CQ) and hydroxychloroquine (HCQ) that targets autophagy pathway showing promising anticancer effects in the early stages of tumorigenesis [223]. Radioisotopes have yet to be developed to specifically measure processes involved in autophagy or assess tumour response to autophagy targeted therapies.

Therapy-induced senescence is a potential strategy to treat cancer through induction of a persistent cytostatic state in tumours. Additionally, elimination of senescent cells from aging organisms has increasingly shown a potential role in alleviating age-related pathological symptoms and extending life expectancy in both preclinical and clinical settings. Both treatment scenarios are in need of an accurate tool to specifically identify and target senescent processes. To this end, PET imaging might be one of the feasible techniques that could contribute to early diagnosis of multiple senescence-related pathologies, assessment of tumour response to senescence-directed therapy and guiding senescence-targeted therapies in aging-related diseases.

## 1.4 Aim of thesis

Although significant progress has been made to understand the characteristics and functions of cellular senescence since the first observation of this phenomenon in 1961, the detection of senescent cells, especially *in vivo*, is still one of the challenges in the field due to lack of universal and specific biomarkers. Given the observation that enhanced glycogenesis is inversely correlated with proliferative rate in a variety of cancer cells, we then proposed to

detect glycogenesis by PET imaging as a biomarker for assessment of tumour response to senescence-directed therapy.

- The first aim of this thesis was to study the basal profiles of glycogenesis in a variety of cancer cells and identify crucial factors involved in tumour-associated metabolic reprogramming of glycogen so as to understand how this relates to or confounds measurement endpoints.
- Secondly, it was to assess the ability of several clinically available anticancer drugs to induce senescence *in vitro* and its interconnection with changes in glycogenesis to understand how glycogenesis could be used as an endpoint of senescence directed therapy.
- Thirdly, it was to develop novel PET imaging agents that measure glycogenesis/glycogen accumulation, as potential tools to specifically identify senescent cells driven by anticancer drugs. In parallel, an additional attempt was made to detect senescence by a novel fluorine-18 radiolabelled probe that binds to senescence-related lipofuscin accumulation *in vitro*.

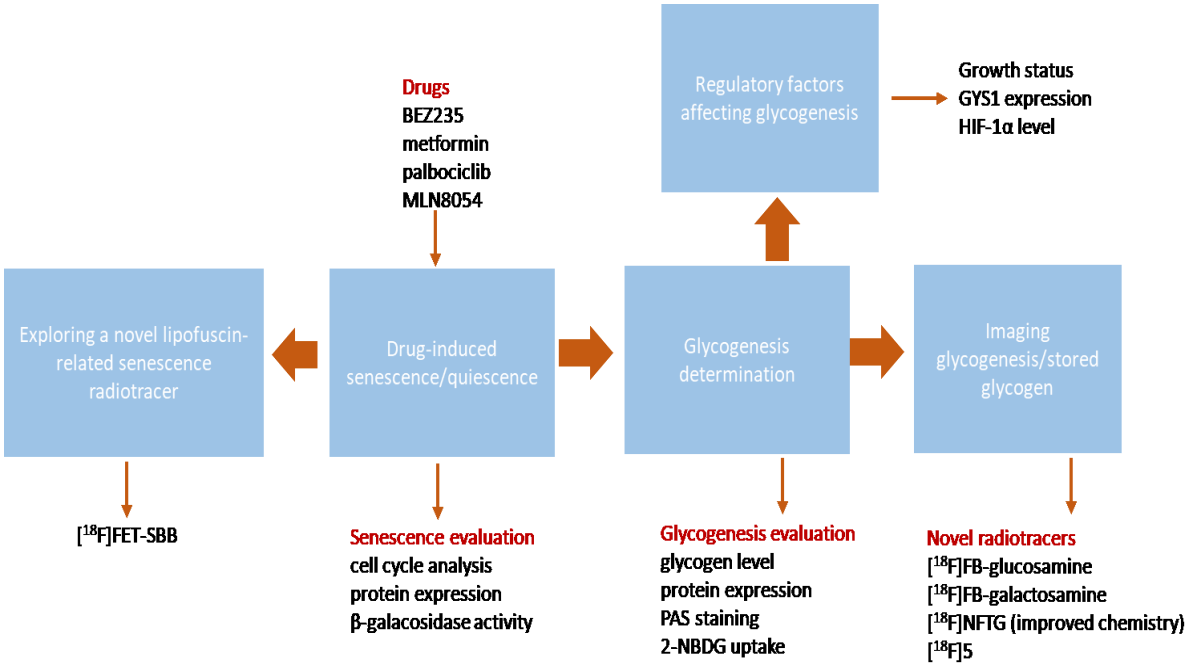


**Figure 1.12 Graphical representation summarising aims of this thesis.**

## 1.5 Layout of thesis

In order to achieve the three aims, the following workflows were set:

- In chapter 3, a comprehensive characterisation of profiles of glycogenesis was performed in a wide range of cancer cell lines harbouring various gene mutation backgrounds. A growth-related pattern of glycogenesis was assessed in cancer cells when cultured under sub-confluent and confluent conditions. The role of glycogen synthase in regulating glycogenesis within the tumour microenvironment was investigated through development of GYS1-knockdown cancer cell lines. The effect of HIF-α on glycogenesis was compared between clear cell renal cell carcinomas which constitutively express HIF-α and cancer cells whose HIF-α expression were induced by a hypoxia-mimetic, cobalt chloride ($CoCl_2$).
- In chapter 4, the ability of a series of anti-cancer drugs to induce senescence/quiescence was explored. The tested drugs include BEZ235, metformin, palbociclib and MLN8054, which target PI3K/mTOR, AMPK, CDK4/6 kinase and aurora A kinase, respectively. Several senescence-associated features were evaluated after drug treatment, including cell morphology, cell cycle assay and SA-β-gal activity. Changes in glycogenesis/glycogen accumulation in response to each treatment were determined in parallel to reveal the interconnection between senescence and glycogenesis.
- In chapter 5, several fluorine-18 radiolabelled probes were developed and assessed for their specificity to target cellular senescence and to give additional insights into how this process might be exploited for cancer imaging. Two glucosamine derivatives, namely [$^{18}$F]FB-Glucosamine and [$^{18}$F]FB-Galactosamine, were synthesised and evaluated for measuring the changes in glycogenesis, and [$^{18}$F]NFTG was used as a control tracer for glycogenesis. Next, a dual-modality imaging probe for PET and fluorescence microscopy, namely **[$^{18}$F]5**, was developed and evaluated for its specificity to bind to accumulated glycogen. Additionally, a novel radiotracer [$^{18}$F]FET-SBB, which was designed to bind to lipofuscin granules, was evaluated for use as a potential imaging agent for cellular senescence.

# Chapter 2 Materials and Methods

## 2.1 Cell culture

A wide range of cancer cell lines were chosen for this study. IGROV-1 (ovarian carcinoma; ATCC) was maintained in RPMI 1640 media (Sigma-Aldrich), supplemented with 10% foetal calf serum (FCS), 1% L-glutamine and 2% penicillin-streptomycin (Thermo Fisher). SKOV-3 (ovarian carcinoma; ATCC), MCF-7 (breast carcinoma; ATCC), T47D (breast carcinoma; ATCC), MDA-MB-231 (breast carcinoma; ATCC), HCT 116 (colorectal carcinoma; ATCC), 786-O (clear cell renal cell carcinoma; ATCC), U87 and U87 shPYGL (glioblastoma; kind gifts of Prof. Adrian Harris, University of Oxford) were cultured in DMEM media (Sigma-Aldrich) with the same supplements as described above. RCC4 plus vector alone (-pVHL, clear cell renal cell carcinoma; ECACC) and RCC4 plus VHL (+pVHL, clear cell renal cell carcinoma; ECACC) were cultured in DMEM media with 10% FCS, 1% L-glutamine and 0.5 mg/mL geneticin (G418). All cell lines were cultured at 37 °C in a humidified atmosphere containing 5% $CO_2$. All cell lines are routinely tested for mycoplasma. Cells were typically not passaged for longer than three months.

## 2.2 Compounds

BEZ235, also known as NVP-BEZ235 or Dactolisib, was purchased from Selleckchem (S1009) and dissolved as 2 mM stock solution in dimethylsulphoxide (DMSO; Sigma-Aldrich). Metformin was purchased from Selleckchem (S1950) and dissolved in PBS, as a 100 mM stock solution. Palbociclib, also known as Ibrance, was a product of Selleckchem (S1116) and prepared in DMSO, as a 2 mM stock solution. MLN8054 was purchased from Selleckchem (S1100) and made up in DMSO, as a 1 mM stock solution. Actinomycin D, also known as Dactinomycin, was purchased from Sigma-Aldrich (A1420) and dissolved as a 2 mM stock solution in DMSO. Cycloheximide was purchased from Sigma-Aldrich (C7698) and dissolved as a 1 mM stock solution in sterilized water freshly prior to use. Cobalt (II) chloride was purchased from Sigma-Aldrich (232696) and prepared in sterilized water freshly prior to use, as a 25 mM stock solution. 2-NBDG was a product of Cayman Chemical (CAYM11046-5) and dissolved as a 50 mM stock solution. Other compounds, unless indicated otherwise, were dissolved in DMSO.

## 2.3 Sulforhodamine B (SRB) Assay

### 2.3.1 Evaluation of cell tolerance to DMSO

In order to optimize experimental conditions, the tolerance limits of cells to DMSO (used to dissolve drugs) was first examined. Upon seeding in 96-well plates at appropriate densities, cells were treated with DMSO at concentrations ranging from 0.1% up to 1%. Cell viability was determined using SRB assay after 72 h of incubation with DMSO. The effect of DMSO on cell viability was evaluated by comparing the absorbance of DMSO/vehicle treated cells to the absorbance of cells that were not treated with DMSO/vehicle.

### 2.3.2 Optimization of seeding density

In order to optimize seeding density, cells were seeded in a range of different densities and allowed to attach overnight. On the next day, media were replaced with fresh ones and cells were cultured for another 72 hours. SRB assay was then performed to determine cell protein levels. The absorbance was plotted over the range of densities tested to select optimal density for each cell line.

### 2.3.3 Determination of Growth Inhibition ($GI_{50}$) of compounds

The drug concentrations for 50% of maximal inhibition of cell growth were measured using SRB assay as previously described [224]. Each cell line was seeded in 96-well plates at appropriate densities and allowed to attach overnight. Then cells were treated with vehicle or various concentrations of drugs and incubated for 72 h at 37 °C. On the day of performing the assay, cells were fixed with 10% cold TCA for 1 hour on ice and washed with running tap water. 100 µL of SRB assay solution (0.4% sulforhodamine B in 1% acetic acid solution) was added to each well of fixed cells and incubated for 30 min at room temperature. Then plates were washed with 1% acetic acid and dried. Finally, the staining reagent was dissolved in 10 mM Tris-base and the absorbance was read at a wavelength of 560 nm on a standard plate reader (Thermo). If the optical density was higher than 1, the reading was performed at 492 nm to ensure linearity of the reading. The growth inhibition curves were plotted as the percentage of control cells and $GI_{50}$ value was calculated using Graphpad Prism v8.3.1.

## 2.4 Western blotting

### 2.4.1 Sample preparation

Cells were seeded in 6-well plates, 10-cm petri dishes or 15-cm petri dishes according to desired purposes. Upon harvest, cells were washed, trypsinized and centrifuged to obtain cell pellets. Cell pellets were washed by cold PBS and frozen at -80 °C until further use. Cell pellets were lysed with radioimmunoprecipitation assay (RIPA) buffer (R0278, Sigma-Aldrich) containing protease and phosphatase inhibitors (Thermo Fisher) on ice for 30 min. Samples were then centrifuged at 15,000 × g for 5 min. Supernatant was collected and kept on ice during processing.

### 2.4.2 Protein Quantification

A 1:6 or 1:10 dilution of each whole cell lysate was prepared prior to protein quantification. Protein concentration was measured by the BCA assay (Pierce, Thermo Fisher). Bovine Serum Albumin (BSA) standard was prepared in a range of 0.1 and 0.9 mg/mL. 20 µL of standard solution and diluted cell lysate was mixed with 200 µL of BCA reagent working solution (1 part of B dilution with 50 parts of A). Plate absorbance was read at a wavelength of 560 nm using a plate reader after 30 min incubation at 37 °. Protein concentration was calculated from the BSA standard curve with multiplying dilution factor.

### 2.4.3 Immunoblotting

Equal amounts of protein (generally 6 - 20 µg per lane) were resolved on 4 - 15% mini-protein TGX gels (456-1084 or 456-1086, Bio-Rad) and run at 120 v for approximately 1 hour. In order to estimate the molecular weights of the protein bands of interest, the molecular-weight size marker (P7712S, Cell Signalling) was run on each gel. Proteins were then transferred to 0.2 µm PVDF membranes (Bio-Rad) using tank transfer system. Membranes were blocked in 5% milk in phosphate buffered saline containing 0.1% v/v tween-20 (PBST) for 1 hour at room temperature (RT) and probed for primary antibodies overnight at 4 °C or for 1 h at RT. Following three washes in PBST for 30 min (3 × 10 min), membranes were incubated with secondary HRP-conjugated mouse or rabbit antibodies (sc-2004 and sc-2005, respectively, Santa Cruz Biotechnology, 1:10000) for 1 h at RT on a rocker. Signals were visualized by chemiluminescence detection using Amersham ECL Western Blotting Detection Reagent (GE

Healthcare) and Amersham Hyperfilm (GE Healthcare). Densitometric analysis by ImageJ (NIH, Bethesda, MA, USA) was used for semi-quantification of protein expression. The relative expression of each protein was normalised to β-actin or GAPDH.

The primary antibodies used in this study included anti-Akt (4691, Cell Signalling, 1:1000), anti-p-Akt (Ser473, 4060s, Cell Signalling, 1:2000), anti-p-Akt (Thr308, 13038s, Cell Signalling, 1:1000), anti-GSK3α/β (5676s, Cell Signalling, 1:1000), anti-p-GSK3α/β (Ser21/9, 9331s, Cell Signalling, 1:1000), anti-GYS1 (3893, Cell Signalling, 1:1000), anti-GYS2 (AB83550, Abcam, 1:500), anti-pGS (Ser641, 3891, Cell Signalling, 1:1000), anti-pGS (Ser640, ab2479, Abcam, 1:1000), anti-PYGL (ab103419, Abcam, 1:500), anti-Rb (D20, 9313, Cell Signalling, 1:1000), anti-pRb (Ser807/811, 9308, Cell Signalling, 1:1000), anti-HIF-1α (D2U3T, 14179s, Cell Signalling, 1:1000), anti-HIF-2α (EPAS1, NB100-122, Novus, 1:1000), anti-GLUT2 (ab54460, Abcam, 1:500), anti-Hexokinase II (C64G5, 2867s, Cell Signalling, 1:1000), anti-cyclin D1 (sc718, Santa Cruz Biotechnology, 1:500) and anti-p21 (Waf1/Cip1, 2947, Cell Signalling, 1:1000). Anti-β-actin (ab6276, Abcam, 1:10000) or anti-GAPDH (5174s, Cell signalling, 1:1000) was used as the loading control.

### 2.5 Determination of the half-life of GYS1

Actinomycin D was dissolved in DMSO to obtain a stock solution of 2 mg/mL. Cycloheximide was freshly prepared at 1 mg/mL in deionized water. IGROV-1 cells were seeded at $1 \times 10^5$ cells/well in 6-well plates 24 h prior to treatment. 10 µL of each drug stock was added to 2 mL of media in each well of 6-well plates. Cells were incubated with actinomycin D-containing media for 6, 12, and 24 hours, or cycloheximide-containing media for 6, 12, 24, 48 and 72 hours. Cells at time 0 without drug treatment were collected as controls. All cell samples were further analysed by western blot to determine the expression levels of glycogen synthase and phospho-glycogen synthase. The amount of GYS1 was normalised to the amount of loading control β-actin at each time point. The percent remaining was calculated from the normalised protein levels at each time point relative to the time point zero. Then the half-life decay curve was derived using the one phase exponential decay model (Graphpad Prism v8.3.1).

## 2.6 Gene silencing by siRNA

Cells seeded at 2 × $10^5$ cells/well in 6-well plates were transfected by using siRNAs with two or more sequences targeting GYS1 (ON-TARGETplus siRNA reagents, Horizon) or the equivalent concentration of negative control siRNA (ON-TARGETplus non-targeting control pool). Transfection was followed as stated in manufacturer's instructions. Briefly, 5 µM stock solution of GYS1 siRNA was prepared from dilution of original solution in 1× siRNA buffer and stored at -20 °C. 6 µL of stock siRNA solution was diluted with serum-free media to a volume of 200 µL and combined with a solution of 6 µL DharmaFECT reagent and 194 µL serum-free media. After incubation for 20 minutes at room temperature, the transfection complexes, together with 1.6 mL fresh antibiotic-free complete media, were added to each well of 6-well plates. 48 or 72 h following transfection, cells were harvested and immunoblotting was performed as described in **Section 2.4**. Cell viability following siRNA transfection was determined by SRB assay.

**Table 2.1 siRNA oligonucleotides targeting GYS1.**

| Target gene | Catalogue number | Target sequence |
|---|---|---|
| GYS1 siRNA1 | J-017726-05-0002 | GGGCGAGGAGCGUAACUAA |
| GYS1 siRNA2 | J-017726-06-0002 | CAACGACGCUGUCCUCUUU |
| GYS1 siRNA3 | J-017726-07-0002 | GAAGCUUUAUGAAUCCUUA |
| GYS1 siRNA4 | J-017726-08-0002 | GAAUCGGCCUCUUCAAUAG |

Note: A = Adenine, G = Guanine, C = Cytosine and T = Thymine

## 2.7 Metabolites analysis following siRNA knockdown

IGROV-1 cells were plated in 6-well plates at 2 × $10^5$ cells/well. After 24 h, cells were transfected with siRNAs containing two gene sequences against GYS1. Non-treated and cells transfected with scrambled siRNA were used as controls. Transfection media were replaced with 2 mL of fresh test medium (Phenol- and serum-free RPMI medium containing 1% glucosamine) 72 h after transfection. Following 3 h incubation, media were collected and analysed for metabolites abundance. 0.6 mL of medium was processed by an automated

chemical analyser (Alinity ci-series, Abbott) for analysis of glucose and lactate; glutamine and glutamate were determined by commercial assay kit (GLN1-1KT, Sigma-Aldrich) according to manufacturer's instructions. Differences in metabolite concentration between time-0 and stop media were used to calculate rates of nutrient utilization and metabolites excretion, normalised to the cellular protein content of the dish.

### 2.8 Induction of hypoxia by cobalt chloride ($CoCl_2$)

Cells seeded in 6-well plates were exposed to various concentrations of $CoCl_2$ at 100, 150, 200, 250 and 300 µM for 24 h. Cell pellets were then harvested and frozen at -80 °C for further glycogen determination and immunoblotting. Cells seeded in 96-well plates and treated with the same concentrations of $CoCl_2$ were subjected to SRB assay for determination of cell viability.

### 2.9 Quantification of total glycogen level

Total cellular glycogen level was evaluated according to a modified amyloglucosidase digestion method as previously described [146; 225; 226]. Cells were each seeded at appropriate densities and allowed to attach overnight. After 24 h, cells were trypsinised, centrifuged and washed to obtain pellets. Glycogen was extracted by boiling cell pellets in 30% potassium hydroxide (KOH) for 15 min. The mixture, in the presence of 2% sodium sulfate ($Na_2SO_4$) and absolute ethanol, was kept in the fridge overnight to induce glycogen precipitation. On the next day, the mixture was centrifuged and re-incubated with 70% ethanol for 30 min to purify the precipitation. After the last centrifuge, glycogen precipitates were dissolved in deionised water to be ready for glycogen assay. Amyloglucosidase (A1602, Sigma-Aldrich) was firstly added to break down glycogen into glucose. Then the resulted glucose was measured using a Glucose (GO) assay kit (GAGO20, Sigma) according to manufacturer's instructions. Assay reagent was added to samples and incubated at 37 °C for 45 min. 12 N sulfuric acid ($H_2SO_4$) was added to terminate the reaction and absorbance was read at a wavelength of 540 nm using a standard microplate reader. Glycogen levels in unknown samples were determined based on the glycogen standard curve and normalised to total intracellular protein as measured by BCA.

## 2.10 2-NBDG fluorescence microscopy and quantification

### 2.10.1 2-NBDG fluorescence microscopy

2-NBDG fluorescence microscopy was performed according to previously described methodology [146]. Briefly, cells were each seeded in black 96-well culture plates (Corning) at appropriate densities 48 hours prior to analysis. Fresh media containing 250 µM 2-NBDG (final concentration, 0.5% DMSO) was added to cells in each well and incubated in dark for 3 hours in 37 °C incubator. Then, cells were washed with warm PBS three times. Fluorescent images were obtained at × 200 magnification using an Olympus BX51 microscope.

### 2.10.2 2-NBDG quantification

For further fluorescence quantification, following 3 hours incubation as described previously, cells placed on ice were gently washed three times with ice-cold PBS and lysed in 50 µL RIPA buffer (avoiding bubbles) for 30 min at 4 °C on a rocker in the dark. Fluorescence was measured by the fluorescence plate reader ($\lambda_{Ex}/_{Em}$=465/540nm, Infinite M200, Tecan). Protein concentration was determined by the BCA assay. The output was calculated as a percentage of relative fluorescence units (RFU), normalised to total cellular protein.

## 2.11 PAS staining

Periodic acid–Schiff (PAS) staining kit (395B, Sigma-Aldrich) was used to stain intracellular glycogen granules in a panel of cancer cell lines. The procedure was conducted following manufacturer's instructions. Briefly, cells were each seeded in 8-well chamber slides (PEZGS0816, Merck) at appropriate densities and allowed to attach overnight. On the day of staining, cells were washed once with PBS and then fixed in 100 µL of Formalin-Ethanol fixative solution for 15 min at room temperature. Formalin-Ethanol fixative solution was prepared prior to the experiment by mixing 1 mL of 37% formaldehyde solution with 9 mL of 95% ethanol. Preparation of 37% formaldehyde stock solution was conducted according to Cold Spring Harbour Protocol (formaldehyde 37% stock). After fixation, cells were washed with PBS twice and incubated in 200 µL of periodic acid solution for 5 min and rinsed with running tap water gently for 30 secs. Subsequently, cells were placed in 200 µL of Schiff's Reagent for 15 min at room temperature and rinsed gently with running tap water. Cells were finally counterstained in Hematoxylin Solution, Gill No. 3, for 1 min and rinsed in running tap

water. Images were obtained at × 100, × 200 and × 400 magnification, respectively, using an Olympus BX51 microscope (Olympus, Tokyo, Japan) with colour camera. A minimum of three fields of each condition was obtained.

α-Amylase digestion was used to verify the specificity of PAS staining to glycogen. Cells were fixed as stated above and incubated in 100 µL of α-amylase solution for 15 min at 37 °C. α-amylase was freshly prepared in PBS at a concentration of 0.5 mg/mL at 37 °C for 15 min. PAS staining was then carried out in the α-Amylase-digested cells as described above.

### 2.12 DNA cell cycle analysis by flow cytometry (FACS)

Cells were cultured and treated according to various experimental protocols. Cell pellets and media supernatant were both collected, washed and centrifuged for 5 min at 1,500 × g. Cell pellets were re-suspended in 0.5 mL of ice-cold PBS and fixed in 70% ethanol by adding dropwise, then left in 4 °C fridge for at least 12 hours. On the day of FACS analysis, samples were centrifuged for 5 min at 1,500 x g and stained in PI staining solution containing 40 µg/µL propidium iodide (PI, P4170, Sigma-Aldrich) and 0.25 mg/mL RNase A (R5503, Sigma-Aldrich) for 30 min in 37 °C water bath in the dark. DNA cell cycle analysis was then performed on a BD FACSCanto flow cytometer (BD Bioscience) or Muse Cell Analyzer. Data analysis was performed by using FlowJo.

### 2.13 Senescence-associated β-galactosidase staining (SA-β-gal)

Drug-induced senescence was examined by using the SA-β-gal staining kit (9860S, Cell Signalling) according to manufacturer's instructions. Briefly, cells were cultured and treated according to various experimental purposes in 8-well chamber slides. On the day of performing the assay, cells were fixed for 15 min at room temperature in fixation solution and gently washed with PBS three times. Then cells were incubated with β-galactosidase staining solution in 37 °C incubator for approximately 20 hours. Images were obtained at ×100, ×200 and ×400 magnification on a microscope (Olympus BX51) with a minimum of three fields for each condition. Quantification was done by counting the intensity of blue stained cells and normalising to the intensity of total cells of three independent fields by ImageJ.

### 2.14 Examination of reversibility of palbociclib-induced G0/G1 arrest

MCF-7 cells were seeded in 12-well plate at $2 \times 10^3$ cells/well 48 h prior to treatment and incubated with various concentrations of palbociclib for 24 h and 72 h. Cells were then allowed to recover for another 5 days in the absence of drug to examine reversibility. Cells constantly treated with drug were used as controls. The medium was replaced every other day during the period of the experiment, either with drug-containing media or drug-free media. Cells were collected and stained by using the Muse Count and Viability Kit (MCH100103, Merck, Germany) counted on Muse Cell Analyzer on days 0, 2, 3, 5, 7, 8 for 24 h treatment, or on days 0, 2, 5, 7, 9, 10 for 72 h treatment.

### 2.15 Colony-formation assay

For colony-formation assay, cells were seeded in 6-well plate at $1 \times 10^5$ cells/well 48 h prior to treatment and treated with drug at desired concentrations for indicated periods. At the end of treatment, cells were each re-plated at appropriate densities in 6-well plate and allowed to recover for another 10 days in drug-free media. The media were replaced every other day. On the day of performing crystal violet staining, cells were washed with PBS and stained with 0.5% crystal violet solution (C6158, Sigma-Aldrich) in 25 % methanol for 20 min. Plates were then washed, dried and imaged. For quantification, cells were de-stained with 10% acetic acid (v/v%) and the absorbance of de-stained solution was measured at 570 nm on a plate reader.

### 2.16 Determination of G6P

MCF-7 cells were treated with palbociclib, re-plated and harvested as described above. G6P measurement was conducted according to manufacturer's instructions (MAK021, Sigma-Aldrich). Briefly, G6P standard solution was prepared in water at a concentration range of 100 - 500 pmol/well. Cell pellets were homogenized in an appropriate volume of cold PBS and centrifuged at 13,000 × g for 10 min. Then the supernatant was deproteinized with a 10kDa MWCO spin filter. Samples were added to glucose-6-phosphate assay buffer to bring a final volume of 50 µL for each well. Samples were then incubated with the appropriate reaction mix for 5 min at 37 °C and measured by using a standard fluorescent plate reader

($\lambda_{Ex/Em}$=535/587nm, Infinite 200 PRO, Tecan). Data were expressed as a percentage of G6P contents (pmol) to total intracellular protein concentration as measured by BCA assay.

### 2.17 *In vitro* uptake of positron-emitting radiotracers

Cells were seeded, cultured and treated according to various experimental purposes in 6-well plates. On the day of uptake, cells were washed three times with pre-warmed PBS and incubated with 1 mL of fresh media containing approximately 0.74 MBq radiotracers (**[$^{18}$F]5**, [$^{18}$F]FET-SBB and [$^{18}$F]FpyGal for 1 h or [$^{18}$F]FB-Glucosamine, [$^{18}$F]FB-Galactosamine and [$^{18}$F]NFTG for 3 h) at 37 °C in a humidified incubator and 5% $CO_2$. At the end of incubation, cells were washed three times with ice-cold PBS and lysed in 1 mL of RIPA buffer for 10 min on ice. The radioactivity of 800 µL lysate from each sample was counted on a WIZARD2 Automatic Gamma Counter (PerkinElmer, USA). $^{18}$F-FDG was assessed separately as a metabolic control radiotracer. Data were expressed as a percentage of radioactivity incorporated into cells, normalised to total cellular protein as measured by BCA assay.

### 2.18 Evaluation of fluorine-18 radiolabelled glucosamine derivatives

#### 2.18.1 Effect of glucose on [$^{18}$F]FB-Glucosamine and [$^{18}$F]FB-Galactosamine uptake

MCF-7 cells were seeded in 6-well plates at 6 ×$10^5$ cells/well 48 hours prior to uptake. On the day of uptake, cells were washed three times with pre-warmed PBS and incubated with tracer-added DMEM medium containing a series of concentrations of glucose (0, 2.5, 5.6, and 11.1 mM) for 3 h at 37 °C in a humidified incubator and 5% $CO_2$. Radioactivity was determined as described above in **Section 2.17**.

#### 2.18.2 Direct glycogen labelling with [$^{18}$F]FB-Glucosamine and [$^{18}$F]FB-Galactosamine

MCF-7 cells were seeded in 10-cm plates at 3 × $10^6$ cells/plate 24 hours prior to uptake. Cells were incubated with 3.7 MBq radiotracer for 3 h at 37 °C in a humidified incubator and 5% $CO_2$. Cells were then washed three times with ice cold PBS and scraped into RIPA buffer for analysis of radioactivity in whole-cell lysate. Alternatively, cells were scraped into 30% KOH and heated at 95 °C for 10 min, followed by adding 2% $Na_2SO_4$ and 70% ethanol to precipitate total glycogen. The mixture was centrifuged at 1,700 × g for 10 min and cell pellets were resuspended in distilled water (total glycogen). 70% protocatechuic acid (PCA) was added and samples were centrifuged at 280 × g for 5 min. Supernatant (macro-glycogen) was collected

and pellets were resuspended in distilled water containing 30% KOH to obtain pro-glycogen. Radioactivity in pro-glycogen and macro-glycogen was measured as described in **section 2.17**. Data are presented as a percentage of radioactivity in the corresponding whole-cell lysates.

### 2.19 Evaluation of a fluorine-18 radiolabelled fluorescent chalcone

#### 2.19.1 Determination of photochemical property of compound 5

Compound **5** was freshly prepared in DMSO at the indicated concentrations of 0.01, 0.1, 1, 10 and 50 µM. Each concentration was assayed in triplicate in a 96-well dark plate using a plate reader (Infinite 200 PRO, Tecan, Switzerland). Absorption spectra were first determined, where the absorbance was plotted against the measured wavelength ranging from 380 nm to 460 nm. The wavelength of maximum absorption was used as the excitation wavelength to obtain emission (fluorescence) spectra of compound 5. The emission spectra show the relative fluorescence intensity, with the intensity plotted on the vertical axis versus wavelength on the horizontal axis.

#### 2.19.2 Fluorescence staining

At 24 h after seeding, fresh media containing 4 µM or 8 µM of compound 5 was added to cells and incubated at 37 °C for 1 h in the dark. Hoechst 33342 (2 µg/mL) was used as nuclear staining. After 1 h incubation, cells were gently washed twice with PBS and images were obtained using a standard fluorescence microscope (Olympus BX51). For glycogen digestion, fresh media containing 0.5 mg/mL of α-amylase was added to cells after the 1 h-staining. Control cells were incubated in normal media for 15 min, in the absence of α-amylase.

### 2.20 Evaluation of lipofuscin-associated radiotracer

#### 2.20.1 Determination of autofluorescence of lipofuscin

Cells were seeded and treated with palbociclib or MLN8054 at indicated concentrations for 72 h. At the end of treatment, cells were re-plated at each appropriate density on pre-coated circular coverslips placed in 12-well plates. After 24 h, cells were washed gently with PBS and fixed with 4% PFA for 5 min, in the meanwhile, a drop of DAPI solution was prepared on a rectangular coverslip. The coverslips with fixed cells were inverted allowing the cells facing down and laying over the DAPI solution. This attachment was left overnight in the dark at

room temperature. On the next day, images were obtained on a standard fluorescence microscopy under × 400 magnification.

### 2.20.2 Staining of lipofuscin by non-radioactive [$^{19}$F]FET-SBB

Cells were seeded and treated with palbociclib or MLN8054 at indicated concentrations for 72 h. At the end of treatment, cells were re-plated at appropriate densities on 8-well chamber slides and allowed to attach for 24 h. [$^{19}$F]FET-SBB was freshly prepared in 70% ethanol at a concentration of 4 mg/mL and filtered through a 0.45 µm filter prior to use. Cells were fixed in ice-cold ethanol for 5 min and incubate with [$^{19}$F]FET-SBB for 10-15 min. Then cells were quickly washed in 50% (v/v) ethanol, followed by PBS for several times. Cells were finally counterstained in Hematoxylin Solution, Gill No. 3 for 1 min and rinsed in running tap water. Images were obtained on a standard microscopy under × 400 magnification.

## 2.21 Radioactive metabolite analysis

All animal experiments were performed by licensed investigators in accordance with the United Kingdom Home Office guidance on the operation of the Animals (Scientific Procedures) Act 1986 and within guidelines for the welfare and use of animals in cancer research [227].

Non-tumour-bearing mice were injected intravenously with 3.7 MBq of [$^{18}$F]FET-SBB. At 60 min post injection, mice were exsanguinated via cardiac puncture; plasm, urine and liver were collected. Samples were analysed for radioactive metabolites by radio-HPLC (Agilent 1100 system) fitted with an online posiRAM metabolite detector (Lablogic, Sheffield, UK). An isocratic mobile phase (60% MeCN / 40% $H_2O$ / 0.1% TFA, 3 mL/min) was used in conjunction with an Agilent Zorbax XDB C18 column (250 × 9.4 mm, 5µ). The retention time of parent [$^{18}$F]FET-SBB was determined by injecting a radioactive sample onto the metabolite radio-HPLC system. The liver was excised, and a portion homogenised in ice cold MeCN (1 mL) using a Precellys tissue homogeniser fitted with the Cryolys cooling module (Stretton Scientific Ltd, Derbyshire, UK). Solid tissues and protein were pelleted by centrifugation (13,000 × g, 5 min) and the supernatant was removed and filtered (0.22 µm syringe filter) before being diluted in $H_2O$ + 0.1% TFA for radio-HPLC analysis. Urine was diluted in $H_2O$ + 0.1% TFA and filtered prior to radio-HPLC analysis. Plasma was obtained from whole blood by centrifugation (2,000 × g,

5 min) to separate the blood cells from the plasma; the plasma was removed and precipitated in ice cold MeCN (1 mL) and centrifuged (13,000 × g, 5 min) to pellet proteins. The supernatant was filtered (0.22 µm syringe filter) and diluted in $H_2O$ + 0.1% TFA for radio-HPLC analysis. The efficiency of extracting radioactivity from each plasma and liver sample was determined by counting the activity (counts per minute, CPM) in a small aliquot (20 µL) of the supernatant of a known volume and the whole protein pellet, in a λ-counter (WIZARD2 Automatic Gamma Counter, PerkinElmer, USA). Radio-HPLC chromatograms were integrated using Laura 6 software (Lablogic, Sheffield, UK).

### 2.22 Statistical analysis

Data were expressed as means ± standard deviation (SD) and statistical difference was determined by two-detailed student's t-test or ANOVA for multiple comparisons (Graphpad Prism Version8.3.1). Significant difference was defined if $p < 0.05$ (*, $p < 0.05$; **, $p < 0.01$; ***, $p < 0.001$; ****, $p < 0.0001$).

# Chapter 3 Characterisation of profiles of glycogenesis in a panel of cancer cell lines

## 3.1 Introduction

Metabolic reprogramming that provides energy and important metabolites to sustain uncontrolled tumour proliferation [147] has long been regarded as one of the crucial biomarkers of cancer cells. Of all the metabolic features, an increase in glucose uptake and glucose metabolism to lactate has received the most attention in neoplastic cells [228]. Recently, research in many cancers has uncovered changes in glycogen metabolism, which could rapidly convert into glucose to meet energy requirements of cancer proliferation [121].

High levels of glycogen have been found in several types of cancer cells such as breast, bladder, colon, glioblastoma, kidney, melanoma and ovarian [229]. Glycogen contents are thought to be inversely correlated with proliferation rate, indicating that glycogen might be utilized when needed as an energy source to sustain cancer cell proliferation, and therefore represents a novel anticancer therapeutic target. PYGL depletion, which impairs glycogen breakdown, has been found to cause a reduction in proliferation in cancer cells due to p53-dependent induction of senescence [150]. Pharmaceutical downregulation of PYGL by CP-91149 also induces the death of hepatocellular carcinoma cells though the intrinsic apoptotic pathway [230]. Despite substantial research on glycogen decomposition, less is understood on the role of glycogen synthesis within tumour microenvironment.

Therefore, this chapter explored the patterns of glycogenesis among a wide range of cancer cell lines and investigated the crucial regulatory factors responsible for cancer-associated glycogenesis. A better understanding of tumour glycogen synthesis may provide useful information about disease status in cancer, and therefore, making this pathway an effective target for anticancer therapies or a treatment response biomarker.

## 3.2 Profiles of glycogenesis in a panel of cancer cell lines

To profile the patterns of glycogen synthesis in a panel of cancer cell lines, cell lines with diverse genetic background (Table 3.1) were studied by investigating the expression and activity of glycogenesis-associated proteins, total glycogen level, in parallel with 2-NBDG and [$^{18}$F]FDG uptake biomarker profiles.

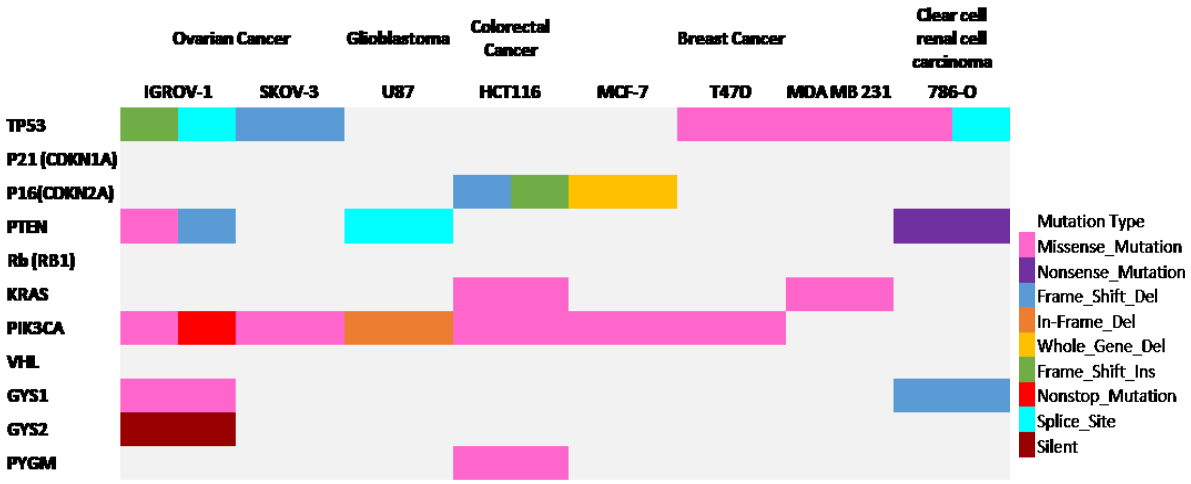


**Table 3.1 Mutated genes related to glycogenesis, senescence and PI3K pathway in the investigated cancer cell line panel.**

The information was summarized from online databases COSMIC [231] and DepMap portal [232].

### 3.2.1 Profiles of the expression and activity of glycogenesis-associated proteins

GYS is the rate-limiting enzyme of glycogen synthesis and inactivated by phosphorylation at various sites through a variety of enzymes, one of which is GSK3β, a crucial downstream effector of PI3K signalling. In order to compare the regulation of glycogenesis through PI3K pathway among all cell lines, the expression and activity of Akt, GSK3β, and GYS was examined by western blot.

The results in Figure 3.1 showed consistent expression of total Akt across the different cell lines while the phosphorylation at Serine 473 (S473) and Threonine 308 (T308) was variable. The relative phosphorylation at S473 when compared to total Akt ranged from 0.01 ± 0.02 to 1.08 ± 0.53, in which IGROV-1, 786-O and U87 cells displayed the most Akt phosphorylation. The ratio of pGSK3α/β and GSK3α/β, which indirectly reflects inactivation of this enzyme, was higher in IGROV-1, 786-O and U87 cells in comparison with SKOV-3, MCF-7 and MDA-MB-231 cells. A high expression of GYS1 was observed in IGROV-1, U87 and MCF-7 cells, while the lowest level was observed in 786-O and SKOV-3 cells. A similar trend was shown in the expression of GYS2 across the cell line panel. The investigated cell lines displayed a similar level of phospho-GYS at both Serine 640 (S640) and Serine 641 (S641) sites except in MCF-7 and MDA-MB-231 cell lines in which the signal was lower. When normalising pGS S641

to GYS1, the level ranged from 0.50 ± 0.03 in MCF-7 cell line to 3.75 ± 1.04 in SKOV-3 cells. Blotting for glycogen phosphorylase (PYGL) revealed high expressions in IGROV-1, SKOV-3 and MDA-MB-231 cell lines, low in 786-O and U87 cells, and undetectable in MCF-7 cells.

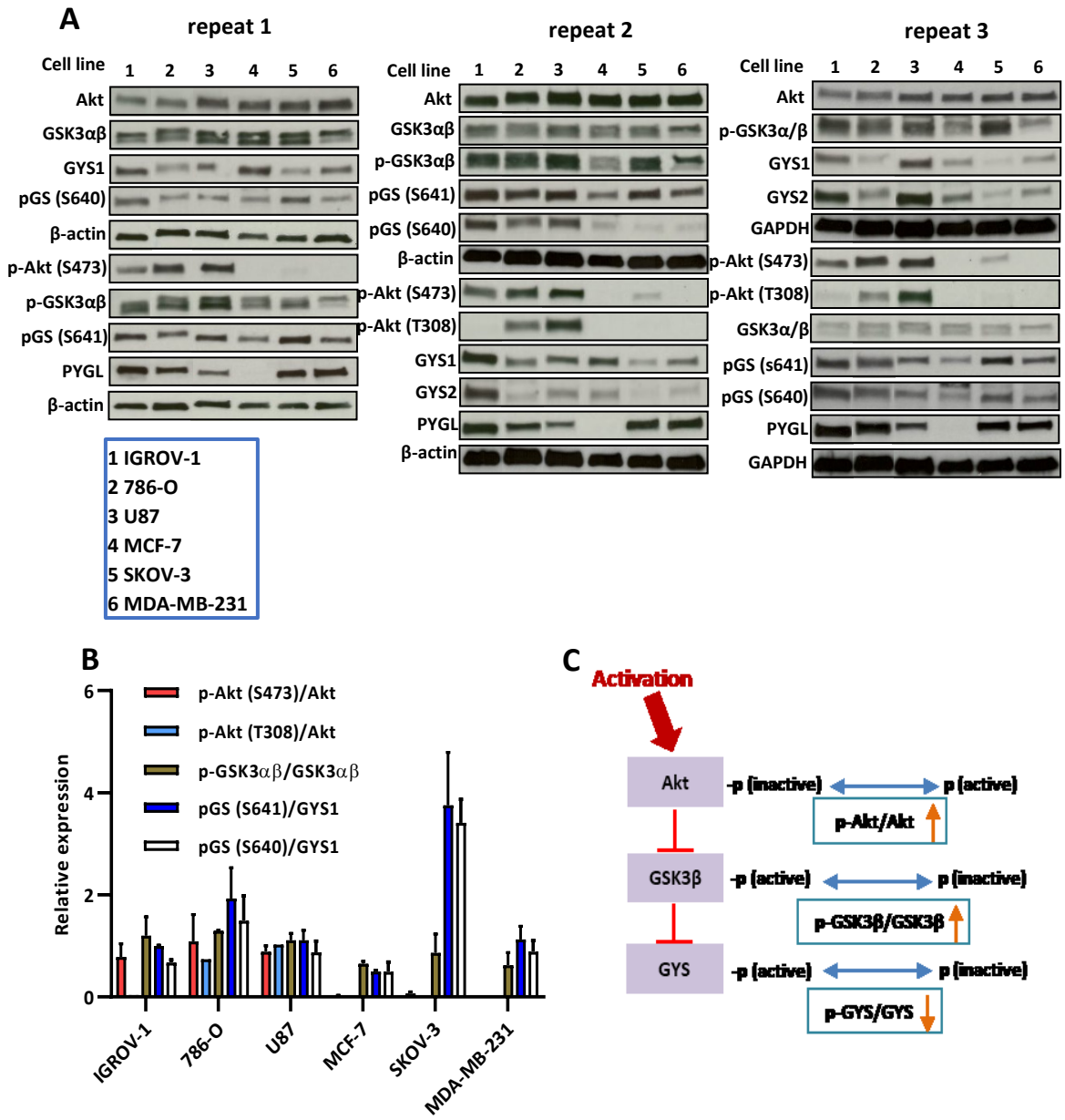


**Figure 3.1 Expression profiles of proteins regulating glycogenesis through PI3K pathway.**

**A,** Results of western blot for IGROV-1, 786-O, U87, MCF-7, SKOV-3 and MDA-MB-231 cells. Cells were seeded in 10-cm petri dish at 2 × $10^6$ cells/well and cultured for 24 h. **B,** Quantification of western blot; optical density of individual signals was normalised to β-actin or GAPDH and respective total protein as indicated. **C,** Schematic showing the regulation of Akt, GSK3β and GYS activity via activation of PI3K pathway.

### 3.2.2 Determination of total glycogen level

In order to determine glycogen contents in the same cancer cell line panel, three methods based on different mechanisms were applied, including total glycogen assay by using a modified glucose (GO) kit, 2-NBDG uptake and the chemihistological PAS staining.

**Total glycogen level assay**

Total intracellular glycogen was extracted, purified, digested to glucose by amyloglucosidase, and measured by glucose assay kit according to manufacturer's introduction. As shown in Figure 3.2, the range of total cellular glycogen was from 4.28 ± 1.37 to 40.85 ± 3.41 µg/mg protein across all cell lines, with the highest level by SKOV-3 cells. IGROV-1 had a large accumulation of glycogen at 39.31 ± 0.58 µg/mg protein. Similar low levels of glycogen were found in MCF-7, 786-O and U87 cell lines at 10.31 ± 1.33, 7.70 ± 0.85 and 4.78 ± 4.81 µg/mg protein, respectively.

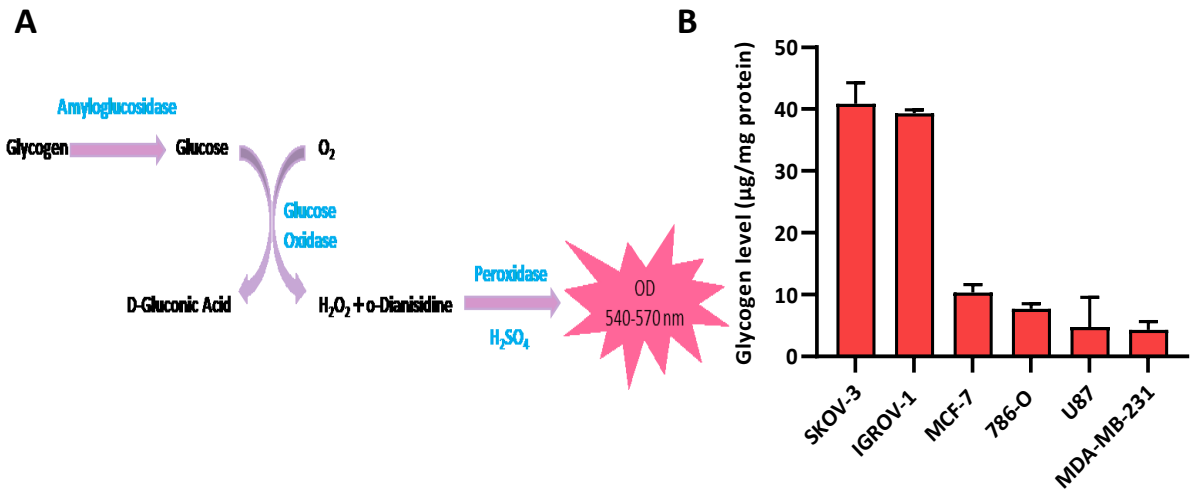


**Figure 3.2 Total intracellular glycogen level measured by glycogen assay.**

**A,** The reaction mechanism for glycogen assay. **B,** Total glycogen accumulation. Cells were seeded in 10-cm petri dish at 2 × $10^6$ cells/well and cultured for 24 h**.** Intracellular glycogen in cell pellets was measured by using GO assay kit. Data were normalised to protein concentration measured by BCA assay. Mean values ± SD (n=3).

**2-NBDG uptake**

Next, the fluorescent probe 2-NBDG was applied to record the accumulation profile of glycogen within a short period. 2-NBDG has been used to monitor glucose uptake and trace

the formation of glycogen [145]. Cells were incubated with fresh media containing 2-NBDG for 3 hours, followed by measuring fluorescence intensity at the excitation and emission wavelength of 465 and 540 nm, respectively.

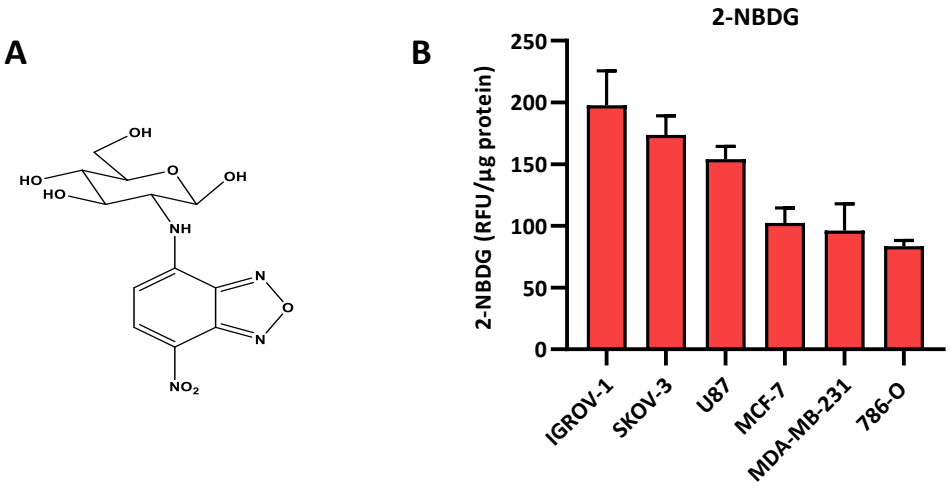


**Figure 3.3 Intracellular 2-NBDG accumulation.**

**A,** Chemical structure of 2-NBDG. **B,** 2-NBDG uptake. Cells were cultured in black 96-well plates for 24 h and incubated for another 3 h in fresh media containing 250 µM 2-NBDG. Fluorescence intensity of cell lysates was determined by using a fluorescence plate reader at $\lambda_{Ex/Em}$ = 465/540 nm. Data were expressed as a percentage of relative fluorescence units to total protein concentration measured by BCA assay. Mean values ± SD (n=3).

The highest 2-NBDG fluorescence intensity (Figure 3.3) was found in IGROV-1 and SKOV-3 cells at 197.76 ± 27.82 and 173.66 ± 15.43 RFU/µg protein, respectively, which is consistent with the results obtained from glycogen assay. MCF-7, MDA-MB-231 and 786-O cell lines had a similar low 2-NBDG uptake, at 102.51 ± 12.04, 96.11 ± 21.70 and 83.61 ±4.55 RFU/µg protein, respectively.

**PAS staining**

PAS staining is a commonly used method for histological observation of the accumulation of carbohydrate molecules such as glycogen in cells and tissues. In accordance with previous results, IGROV-1 and SKOV-3 had the largest amounts of positive-stained cells. A moderate staining was found in MCF-7, 786-O and T47D cells, whereas a weak signal was observed in HCT116 cells. Treatment of cells with α-amylase abrogated these patterns, confirming the specificity of the stain to glycogen.

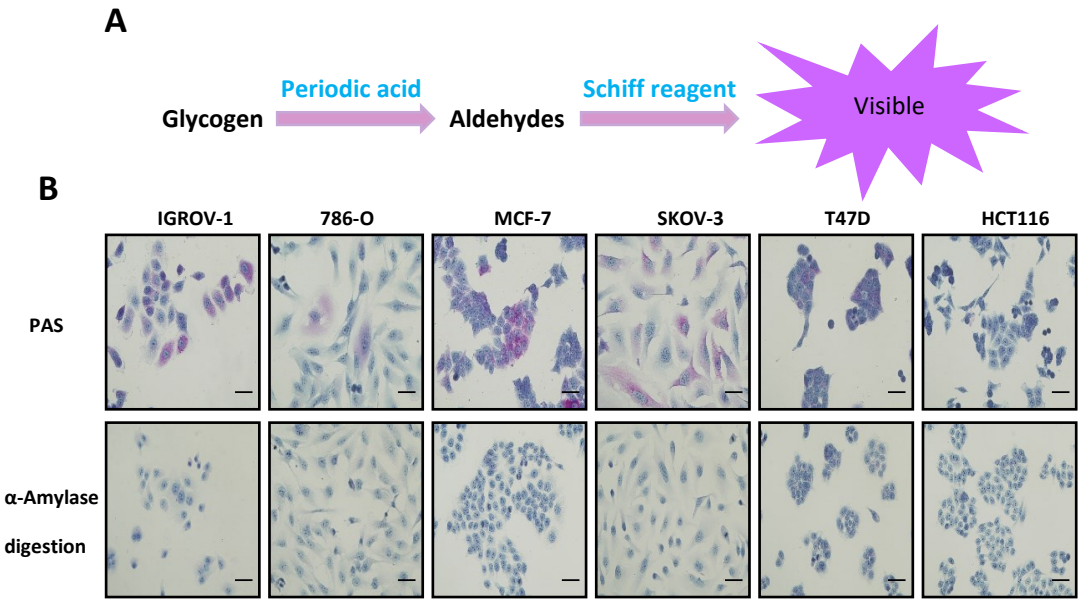


**Figure 3.4 PAS staining.**

**A,** The reaction mechanism for PAS staining. **B,** Cells were each seeded in 8-well chamber slides at appropriate densities and cultured for 24 h prior to staining. PAS staining was conducted according to manufacturer's instruction.

Collectively, despite three different approaches applied, similar patterns of glycogen accumulation were found among the investigated cancer cell lines, where two ovarian carcinoma cells SKOV-3 and IGROV-1 displayed the highest glycogen accumulation.

### 3.2.3 Determination of glucose utilization by [$^{18}$F]FDG

As glycogen accumulation is tightly associated with glucose metabolism, basal glucose utilization in the same cell line panel was then evaluated by using the standard PET radiotracer [$^{18}$F]FDG. As shown in Figure 3.5A, the retention of [$^{18}$F]FDG varied up to three fold in the range from 2.51 ± 0.13 % of incubated radioactivity dose/mg of total protein (%ID/mg) in MCF-7 cells to 6.06 ± 0.19 %ID/mg protein in U87 cells. The levels of radioactivity incorporated into cells were similar in MDA-MB-231 and SKOV-3 cells at 4.08 ± 0.18 % and 3.67 ± 0.17 %ID/mg protein, respectively. IGROV-1 and 786-O cells had lower [$^{18}$F]FDG uptake at 2.92 ± 0.10 and 2.80 ± 0.09 %ID/mg protein, respectively.

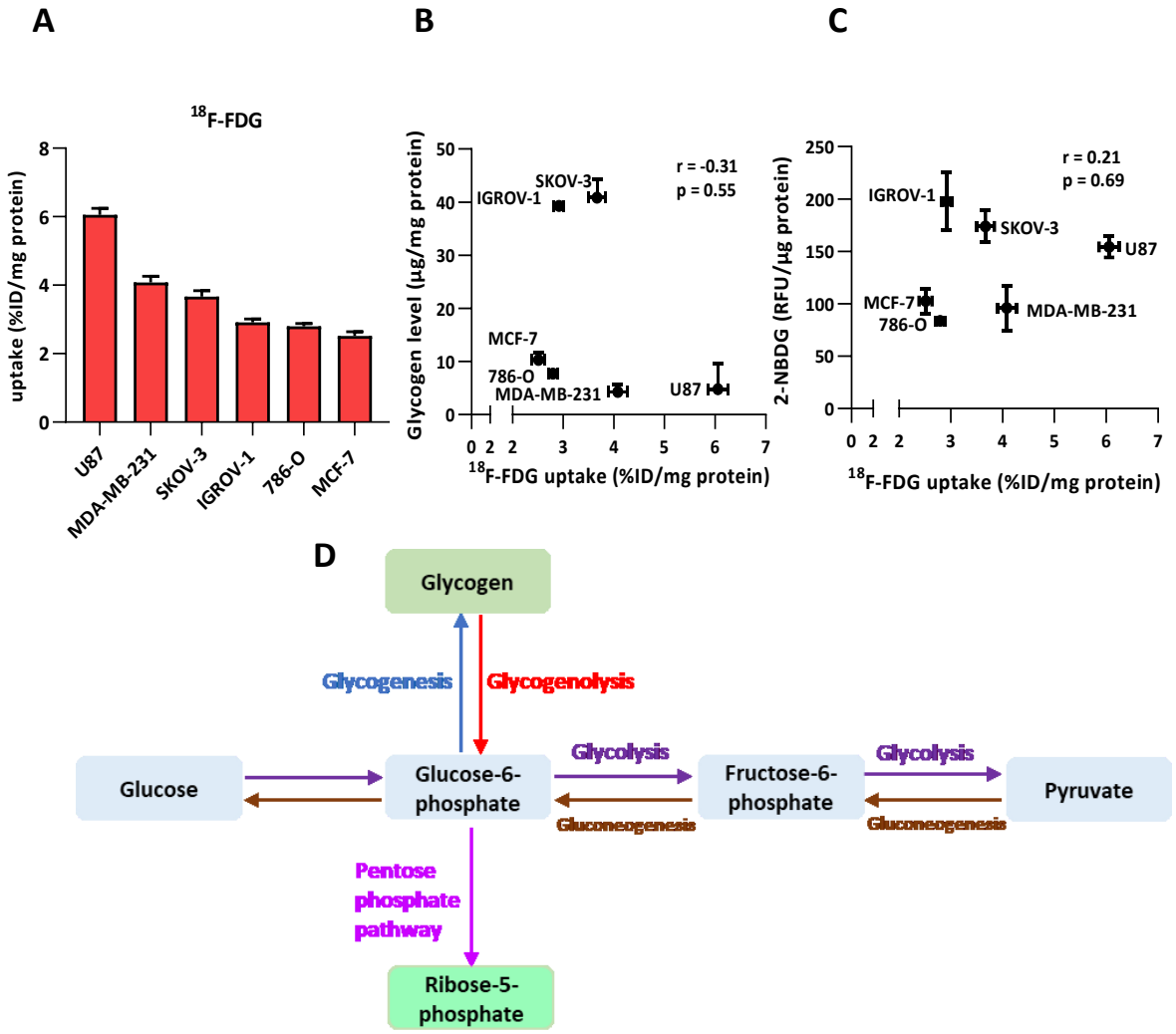


**Figure 3.5 Correlation between [$^{18}$F]FDG uptake and glycogen storage.**

**A**, Intracellular [$^{18}$F]FDG uptake. Cells were cultured in 6-well plates at 5 × $10^5$ cells/well for 24 h and incubated for 1 h with fresh media containing 0.74 MBq [$^{18}$F]FDG. Data were mean values ± SD (n=6), and expressed as % of incubated radioactivity dose, normalised to protein concentration (%ID/mg). **B and C**, Pearson correlation coefficient (r) was determined by Graphpad Prism. Scatter plot points represent independent experiments performed in triplicate. Two-tailed t test was used. **D,** Schematic showing glucose metabolism through glycolysis, glycogenesis and pentose phosphate pathway (PPP).

It was then determined whether glucose consumption as measured by [$^{18}$F]FDG is correlated with the glycogen accumulation in the tested cell lines. However, data analysis revealed that [$^{18}$F]FDG retention was not correlated with either total glycogen accumulation (r = -0.31) or dynamic glycogen mobilization as measured by 2-NBDG uptake (r = 0.21).

### 3.2.4 Discussion

Distinct profiles of glycogenesis were observed among a panel of cancer cell lines originating from different cancer types including ovarian cancer (IGROV-1 and SKOV-3), breast cancer (MCF-7 and MDA-MB-231), gliolastoma (U87) and clear cell renal cell carcinoma (786-O). GYS, as the main driver of glycogenesis, can be regulated by GSK3β, which is in turn controlled by the upstream effector Akt. In this study, most of the tested cell lines shown an Akt-GSK3β-dependent regulation of GYS1 activity except two breast cancer cells MCF-7 and MDA-MB-231. The basal GYS1 activity in the cell line panel appears to be associated with the gene mutations involved in PI3K pathway. PTEN-null cell lines including IGROV-1, U87 and 786-O showed higher phosphorylation of Akt at both phosphorylation sites, reflecting an increased Akt activity due to lack of the tumour suppressor gene PTEN. The over-activation of Akt in these cells led to increased phosphorylation of GYS3α/β that inactivates this enzyme and consistently enhanced activity of GYS1. In contrast, regulation of GYS1 activity in other tested cell lines harbouring wild-type PTEN might rely on a PI3K-AKT-independent pathway. PIK3CA-mutated MCF-7 cells exhibited only minimal AKT activation and upregulated GSK3β, which is consistent with previous observation that PIK3CA-mutations may transduce an AKT-independent signal engaging PDK1 and SGK3 [233]. Mutant KRAS in MDA-MB-231 cells possibly upregulated GSK3β, and thus facilitating the phosphorylation of GYS1. It has been found that mutant RAS-driven GSK3β transcription was dependent on MAPK signalling, which further leads to the binding of ETS transcription factors to the GSK3β promoter in pancreatic cancer [234].

Consistent with high activity of GYS1, in IGROV-1 cells there was considerable total glycogen storage and 2-NBDG uptake, which was also reported by Witney et al [146]. In contrast, in spite of low GYS1 activity, the highest glycogen content and a large accumulation of 2-NBDG was found in SKOV-3 cells, which is consistent with previous study that SKOV-3 cells had the highest level of glycogen storage in the exponential phase of growth among 58 human tumour cell lines [149]. The high glycogen level under low GYS1 activity as determined by its phosphorylation ratio was possibly due to a G6P-dependent restoration of GYS1 activity in SKOV-3 cells. Possibly, the presence of G6P, which is a crucial allosteric activator of GYS1, overcomes the enzyme inactivation caused by covalent phosphorylation, restoring full GYS1 activity. The differences of glycogen level in two breast cancer cell lines are consistent with

previous report, in which a higher amount of basal glycogen was shown by MCF-7 cells [235] when compared to MDA-MB-231 cell line.

A strong correlation (r = 0.81) between cellular glycogen level and 2-NBDG uptake was observed in this study, suggesting both measurements can be used to profile glycogen storage at the baseline. However, current data showed a moderate correlation (r = 0.54) between GYS1 activity as determined by the ratio of phospho-GYS to total GYS1 and total glycogen accumulation. One of the possible reasons is that apart from glycogen synthesis, glycogen degradation in a cell line panel also contributes to the total amount of glycogen. Moreover, western blot that measured the phosphorylation-dependent GYS1 regulation in this study might limit a comprehensive determination of GYS1 activity, as the activity of this enzyme is a complex function of the concentrations of UDP-glucose, G6P, glycogen level and its phosphorylation state [142]. Therefore, it might be more accurate if GYS1 activity is measured by a radioactivity assay based on the incorporation of [U-$^{14}$C]glucose from UDP-[U-$^{14}$C]glucose into glycogen.

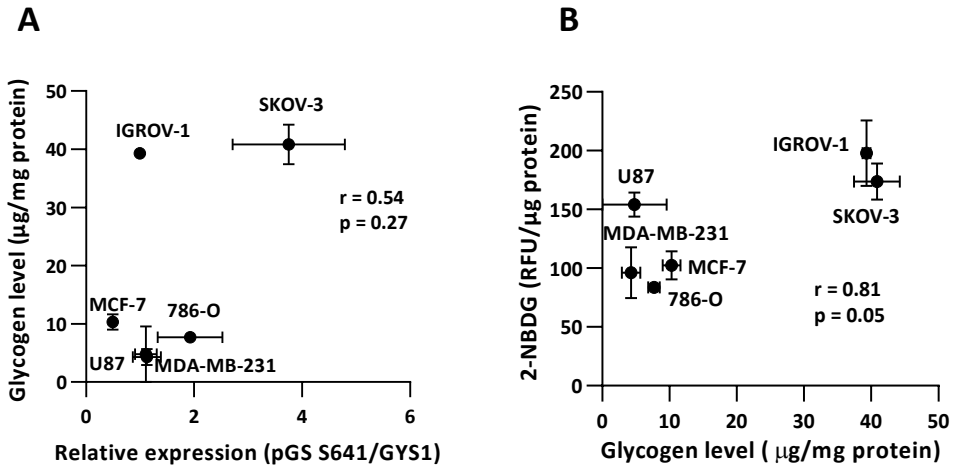


**Figure 3.6 Correlation analysis.**

Pearson correlation coefficient was determined by Graphpad Prism. Scatter plot points represent independent experiments performed in triplicate. Two-tailed t test was used. **A,** Correlation between relative protein expression (pGS S641/GYS1) and total glycogen leve. **B,** Correlation between total glycogen level and 2-NBDG uptake level.

Apart from GYS1 activity, glycogen synthesis is also dependent on the amount of glucose transported into cells. In our study, the highest [$^{18}$F]FDG was shown in U87 cell line (Figure

3.5A), which may be due to the increased activity of glucose transporter via PTEN-null-induced Akt activation in this cell line [236]. Additionally, the highest expression of hexokinase-I (HKI) mRNA was observed in U87 cell line among a panel of glioblastomas, suggesting a high basal level of HKI proteins, which could lead to high glucose uptake [236]. However, a low [$^{18}$F]FDG uptake was observed in IGROV-1 cell line (Figure 3.5A) in spite of high glycogen accumulation (Figure 3.2B) and 2-NBDG uptake (Figure 3.3B). This might be explained by the observation that IGROV-1 cells were less glycolytic/respiratory, which was attributed to a low expression of glycolysis-associated enzymes such as GLUT1, HKII when compared with another ovarian cancer cell line OC316 [237]. When comparing the two breast cancer cell lines (Figure 3.5A), more glucose uptake was observed in MDA-MB-231 which may be due to the high aggressiveness of MDA-MB-231 cells compared with the less invasive MCF-7 cells.

Furthermore, data analysis (Figure 3.5B and C) showed that there was no correlation between glucose uptake and total glycogen level among the investigated cell lines. Glucose can be metabolized in multiple pathways including glycolysis, glycogen synthesis and pentose phosphate pathway (PPP); it is normally the proliferation rate that determines the prevalent fate of glucose in cancer cells [228]. For example, extremely aggressive cancer cells dominantly utilize glucose through glycolysis for producing energy, which is the well-defined Warburg effect [228]. Therefore, glucose uptake might not be always correlated with glycogen level, and it is also important to take cell proliferative status or other factors into consideration.

In conclusion, profiles of glycogenesis varied in the tested cancer cell lines with various gene mutation background. In PTEN-null cancer cells IGROV-1, U87 and 786-O where Akt is overactivated, GYS1 activity as determined by the ratio of pGS S641 to total GYS1 appears to be regulated in an Akt-GSK3β-GYS1-related manner. However, phosphorylation is not the only means of regulating GYS1 activity in the investigated cancer cell lines. High concentrations of G6P might effectively restore GYS1 activity through activating both non-phosphorylated and phosphorylated GYS1 enzyme. Moreover, the level of glucose uptake by cells might not be positively correlated with glycogen synthesis, as cell proliferative state or cell basal metabolic status also plays a central role in determining in which way cancer cells utilize glucose.

### 3.3 Evaluation of cell growth-related patterns of glycogenesis in cancer cells

Given diverse profiles of glycogenesis in the tested cancer cell lines, it was necessary to understand how cells with different growth rates adapt their glycogenesis for survival. It has been reported that several carcinoma cells store glycogen while they are in G0/G1 growth phase (quiescence) where cell division slows. The stored glycogen could quickly supply sugar and energy for cell activity when they undergo S phase. However, it remains unclear whether this is a universal phenotype for cancer cell lines and how glycogen synthesis contributes to this elevated glycogen storage. Here, a panel of cancer cell lines were tested for cell growth status, protein expression and total glycogen level under sub-confluent and confluent conditions.

#### 3.3.1 A G0/G1 phase arrest is triggered by cell confluency

The first step was to check if cell confluence could lead to the G0/G1 cycle arrest among the tested cell lines. It was found that increased seeding density resulted in an increase in G0/G1 growth arrest across all the cell lines (Figure 3.7), characterised by flow cytometric measurements of DNA contents.

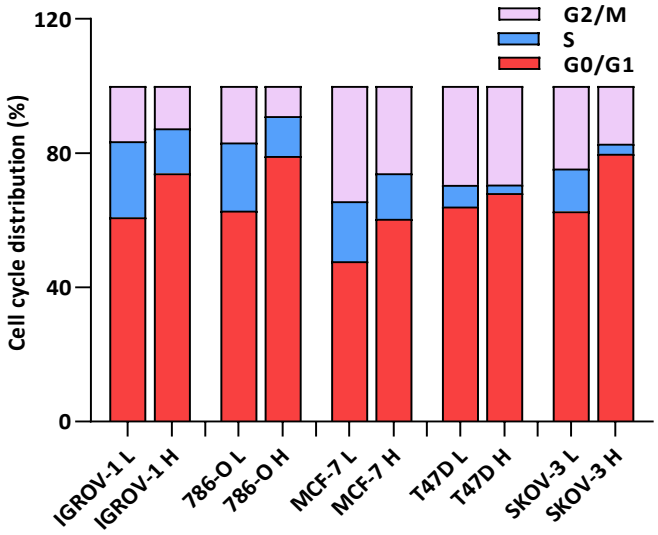


**Figure 3.7 A G0/G1 phase arrest is triggered by cell confluency.**

Cells were each seeded at appropriate seeding densities and allowed to attach for 48 hours. Cell cycle analysis was performed by FACS using PI staining.

### 3.3.2 Cell confluence facilitates the expression of glycogenesis-associated proteins

Cells were each seeded at appropriate densities and allowed to grow for 48 h before reaching sub-confluent or confluent state, respectively. As shown by western blot analysis (Figure 3.8A), increased seeding density resulted in an increase in GYS1 expression across all tested cell lines (IGROV-1, 786-O, MCF-7 and T47D) except an undetectable level in SKOV-3 cells. The most striking elevation was found in MCF-7 cells upon increased cell seeding density. A subtle elevation in the expression of phosphorylated GYS1 was shown by all cell lines except 786-O cells where there was a slight reduction. The ratio of phospho-GYS to total GYS1 decreased among all cells, with the most remarkable decrease in MCF-7 cell line, suggesting that cells under confluent condition had higher GYS1 activity. Besides, increased p21 and cyclin D1 indicated a G0/G1 phase arrest and a reduction in proliferation rate under confluent growth condition.

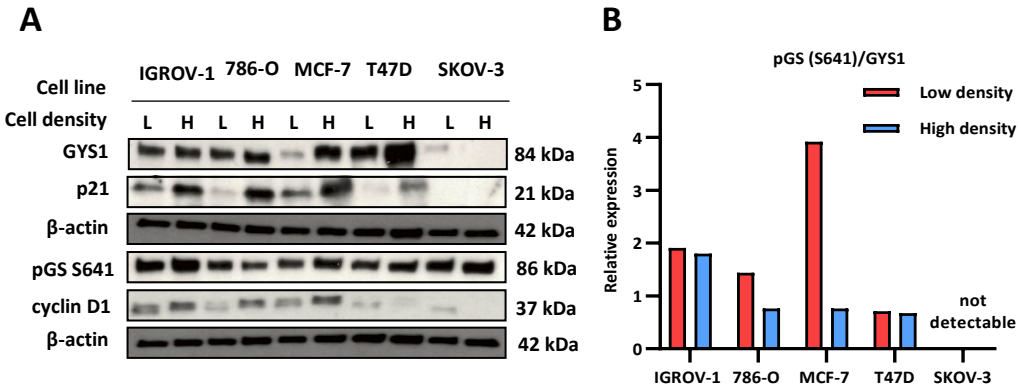


**Figure 3.8 Cell confluency facilitates the expression of glycogenesis-associated proteins.**

**A,** Results of western blot for IGROV-1, 786-O, MCF-7, T47D and SKOV-3 cells, cultured at low and high seeding density, respectively. **B,** Quantification of western blot (only one experiment was done), optical density of individual signals was normalised to β-actin. The ratio of pGS (S641) to GYS1 was determined.

### 3.3.3 Cell confluency leads to an elevation in total glycogen level

As shown in Figure 3.9, increased seeding density resulted in a dramatic elevation in glycogen contents in two cell lines, from 9.08 ± 0.47 to 32.92 ± 1.53 μg/mg protein in IGROV-1 cells, and from 27.33 ± 0.84 to 52.56 ± 2.52 μg/mg protein in SKOV-3 cells which had undetectable GYS1. MCF-7 cells that showed a striking increase in confluence-induced GYS1 expression, had an increase of glycogen level from 11.42 ± 1.38 at low density to 25.64 ± 3.04 μg/mg protein

at high density. Glycogen levels in 786-O and T47D cells remained low; there was an increase in 786-O cells from 3.54 ± 0.48 to 8.39 ± 0.08 µg/mg protein, while T47D cells had a subtle decrease from 8.71 ± 0.56 to 7.17 ± 0.90 µg/mg protein.

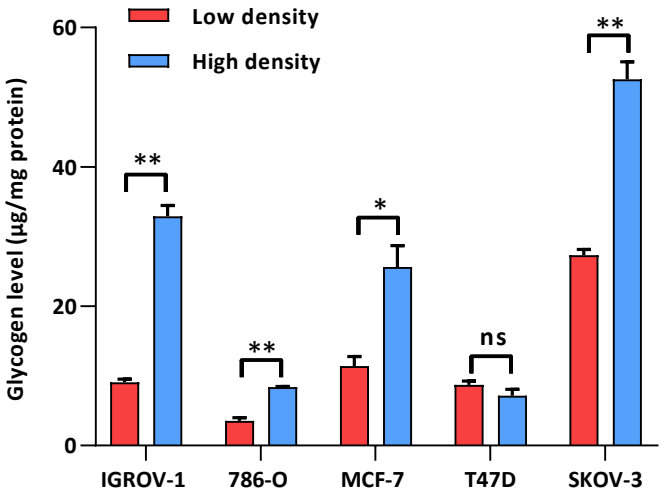


**Figure 3.9 Cell confluency leads to an elevation in total glycogen level.**

Cells were seeded and cultured as described above. Data was normalised to protein concentration measured by BCA assay. Mean values ± SD (n=3). Two-tailed t test was used (ns, no significant difference; *, $p < 0.05$; ** $p < 0.01$).

### 3.3.4 Discussion

Collectively, the data presented showed that increased seeding density *in vitro* resulted in large populations of cells in the G0/G1 cell cycle. The resulting G0/G1 phase arrest further led to elevated glycogen storage in four (IGROV-1, 786-O, MCF-7 and SKOV-3) of the five tested cell lines in a GYS1-dependent manner. This observation coincides with the findings of Rousset et al. [149] that human colorectal adenocarcinoma cell lines (HRT-18 and HRT-29) in synchronized culture exhibit a common pattern of high glycogen level in the G0/G1 phase, followed by a decreased glycogen storage during the S and G2/M phases.

The results suggest that cancer cells when entering quiescent growth arrest are prone to store glycogen via upregulation of glycogen synthesis in a GYS1-depnedent manner. The stored glycogen can be rapidly converted to glucose providing energy that is required for cell division in cycling phase.

## 3.4 Evaluation of glycogen synthase as a crucial regulator of glycogenesis in cancer cells

Although the role of GYS in glycogenesis has been well documented under physiological environment [122], it remains unclear to what extent GYS is involved in glycogen biochemistry within tumour microenvironment. Hence, the next step was to assess the effect of GYS on the biological response by targeted removal of GYS1 expression in several cancer cell lines.

### 3.4.1 Determination of half-life of glycogen synthase

To obtain a general understanding of the turnover rate of GYS1, its half-life was determined in IGROV-1 cells which previously showed a large accumulation of glycogen [146].

Here, actinomycin D and cycloheximide were used to inhibit protein synthesis through targeting RNA transcriptional and protein translational processes, respectively. Cell lysates collected at different time points after drug treatment were used for protein analysis by western blot. The amount of GYS1 was normalised to the amount of loading control β-actin at each time point. The percent remaining was calculated from the normalised protein levels at each time point relative to the zero time point, then the half-life decay curve was derived using the one phase exponential decay model (Graphpad Prism v8.3.1). The half-life of GYS1 mRNA was determined to be 2.6 hours upon transcriptional inhibition by actinomycin D.

As shown in Figure 3.10, treatment with cycloheximide during early time points (0 - 12 hours) effectively inhibited protein translation as observed by rapid reduction of GYS1 levels. However, treatment for more than 24 hours restored GYS1 expression dose-dependently. The unexpected increase might be due to the decomposition of cycloheximide in media over time. Post-translational modification of GYS1 through phosphorylation appeared not to be affected by the two inhibitors, as a subtle increase in pGS S641 was even observed after treatment.

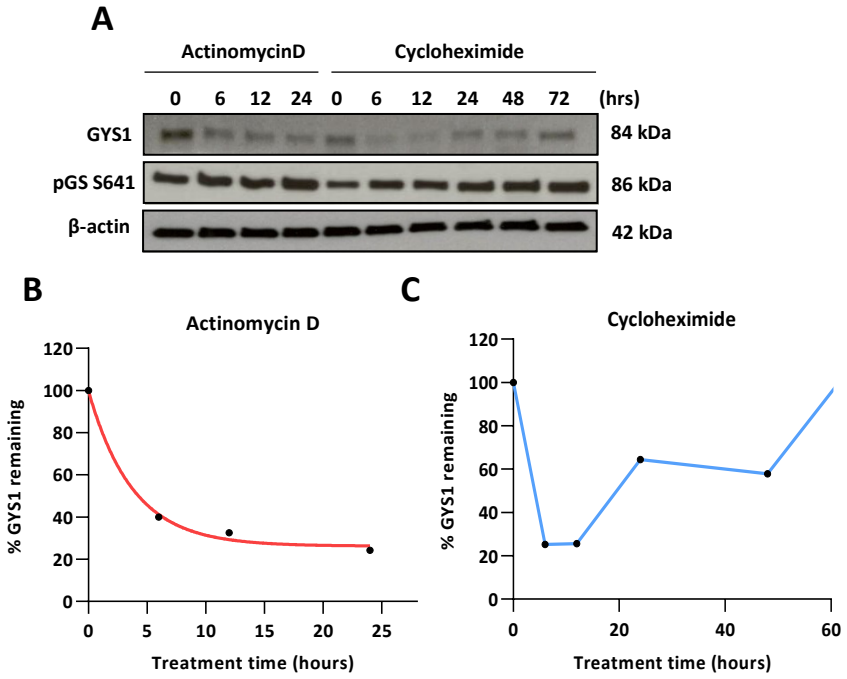


**Figure 3.10 Determination of the half-life of GYS1 protein in IGROV-1 cells.**

**A,** Western blot of GYS1 and pGS S641 expression in IGROV-1 cells in the absence or presence of actinomycin D and cycloheximide. The experiment was done only once. **B,** A One phase exponential decay model (Graphpad Prism v8.3.1) was fit to determine the half-life of GYS1 after actinomycin D treatment. **C,** Plots of the percentage of GYS1 remaining over cycloheximide treatment time.

### 3.4.2 The effects of GYS1 silencing on cell growth and glycogen accumulation

GYS1 was silenced by using small interfering RNA (siRNA). siRNA is one of the most commonly used methods to knock down a protein of interest in mammalian systems, where double strand RNA (dsRNA) induces the degradation of a cognate messenger RNA (mRNA) and thus blocks the expression of a specific target protein in a cell.

Three cancer cell lines harbouring silenced GYS1 genes were established by siRNA technique. Various siRNA sequences and siRNA concentrations were initially tested to identify one combination that produces the strongest knockdown. IGROV-1 cell line was first used because it showed high basal levels of GYS1 and large amounts of glycogen accumulation (Figure 3.2B). The optimal conditions determined were a transfection time of 72 h and a final siRNA concentration of 15 nM. As shown in Figure 3.11, greater than 90% knockdown of GYS1 was achieved in the GYS1 siRNA cells when compared to controls in IGROV-1.

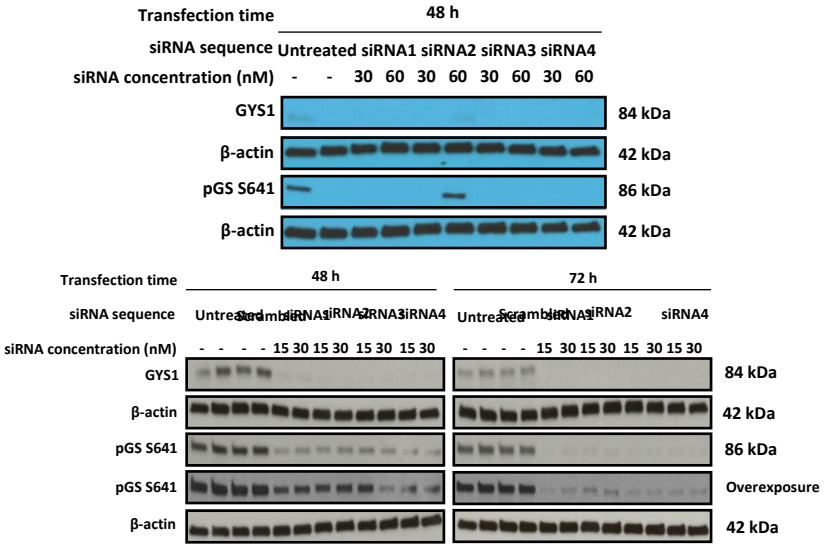


**Figure 3.11 Optimization of siRNA transfection conditions in IGROV-1 cells (two repeats).**

Untreated cells and cells transfected with scrambled siRNA were used as controls. Four different GYS1 siRNA sequences (detailed sequence information as indicated in method **Section 2.6**) were tested over the transfection period of 48 or 72 hours. Various siRNA concentrations at 15, 30 and 60 nM were compared.

To cross validate GYS1 knockdown efficiency, another two cancer cell lines 786-O and MCF-7 were then evaluated together with IGROV-1 by using the optimal experimental conditions. Western blot analysis (Figure 3.12A) revealed a remarkable inhibition on GYS1 expression in IGROV-1 and MCF-7 cells where there was greater than 90% silencing efficiency, while the knockdown efficiency was approximately 70% in 786-O cells. Expression of pGS S641 was decreased by about 50% in knockdown cells across all cell lines. The expression of PYGL remained unchanged in IGROV-1 and 786-O cells, whereas MCF-7 cells, as previously observed (Figure 3.1), had low PYGL. Interestingly, GYS1 knockdown resulted in different patterns of glycogen accumulation among the three cell lines (Figure 3.12B). In IGROV-1 cells, total glycogen level was reduced by 50% following siRNA transfection, from 42.68 ± 3.18 µg/mg protein in controls to 22.19 ± 2.05 µg/mg protein in transfected cells. Whereas total glycogen contents remained constant in MCF-7 cells between control and transfected cells, perhaps suggesting that GYS1 is not critical for glycogenesis in these latter cell lines under normoxic condition.

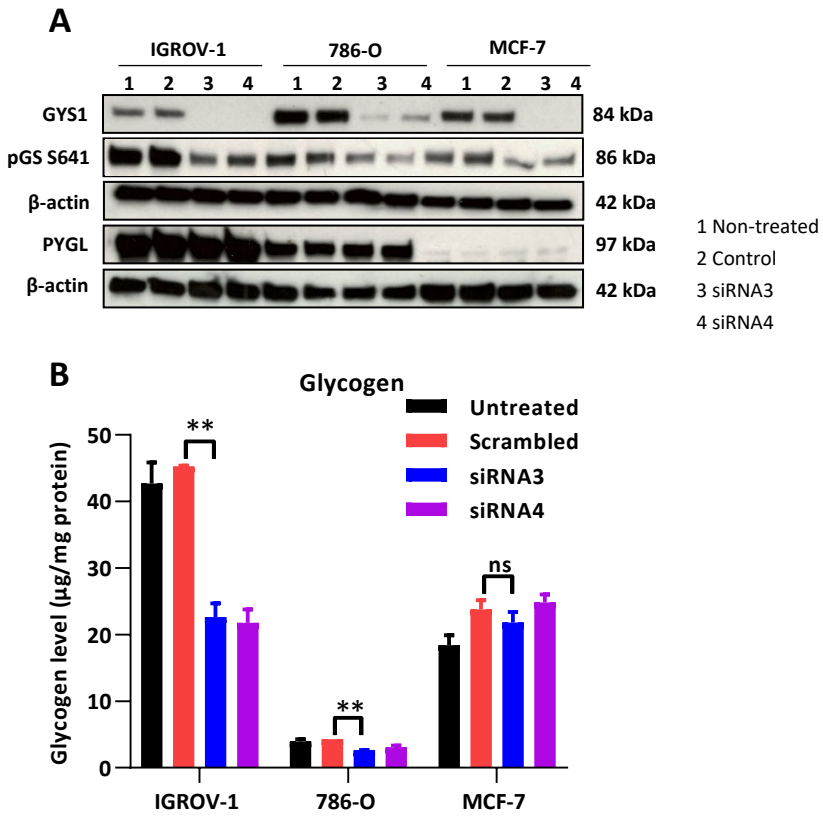


**Figure 3.12 Effect of GYS1 knockdown on total glycogen level.**

**A,** Expression of GYS1, pGS S641 and PYGL proteins following siRNA transfection. **B,** Total glycogen level following GYS1 siRNA knockdown. Mean values ± SD (n=3). Two-tailed t test was used (ns, no significant difference; **, $p < 0.01$).

Studies were further performed to see the effect of GYS1 knockdown on cell ability and other metabolic pathways in IGROV-1 cells. Cell viability determined by SRB assay was reduced by approximately 10% 72 hours after transfection compared to IGROV-1 cells transfected with control-siRNA. This suggested that GYS1 siRNA knockdown did not significantly affect cell viability in IGROV-1 cells.

Western blot analysis and glycogen assay (Figure 3.13) were repeated in IGROV-1 cells. The results confirmed a remarkable knockdown efficiency of GYS1 and a reduction in phosphorylated GYS in IGROV-1 cells, while the levels of PYGL remained constant in control and knockdown cells. Glycogen level following GYS1 knockdown was confirmed to be diminished by 50% in IGROV-1 cells, from 40.68 ± 1.62 µg/mg protein in control cells to 21.28 ± 1.40 µg/mg protein in transfected cells.

To further assess whether GYS1 knockdown might functionally affect other metabolic pathway flux, cells were cultured to confluency in media containing high glucose (11.11 mmol/L) for analysis of several metabolites. 6 hours following incubation, media were collected and analysed for glucose and glutamine consumption and the secretion of lactate and glutamate. It was found that the utilization of glucose and glutamine remained constant in control and GYS1-knockdown IGROV-1 cells, under the nutrient conditions.

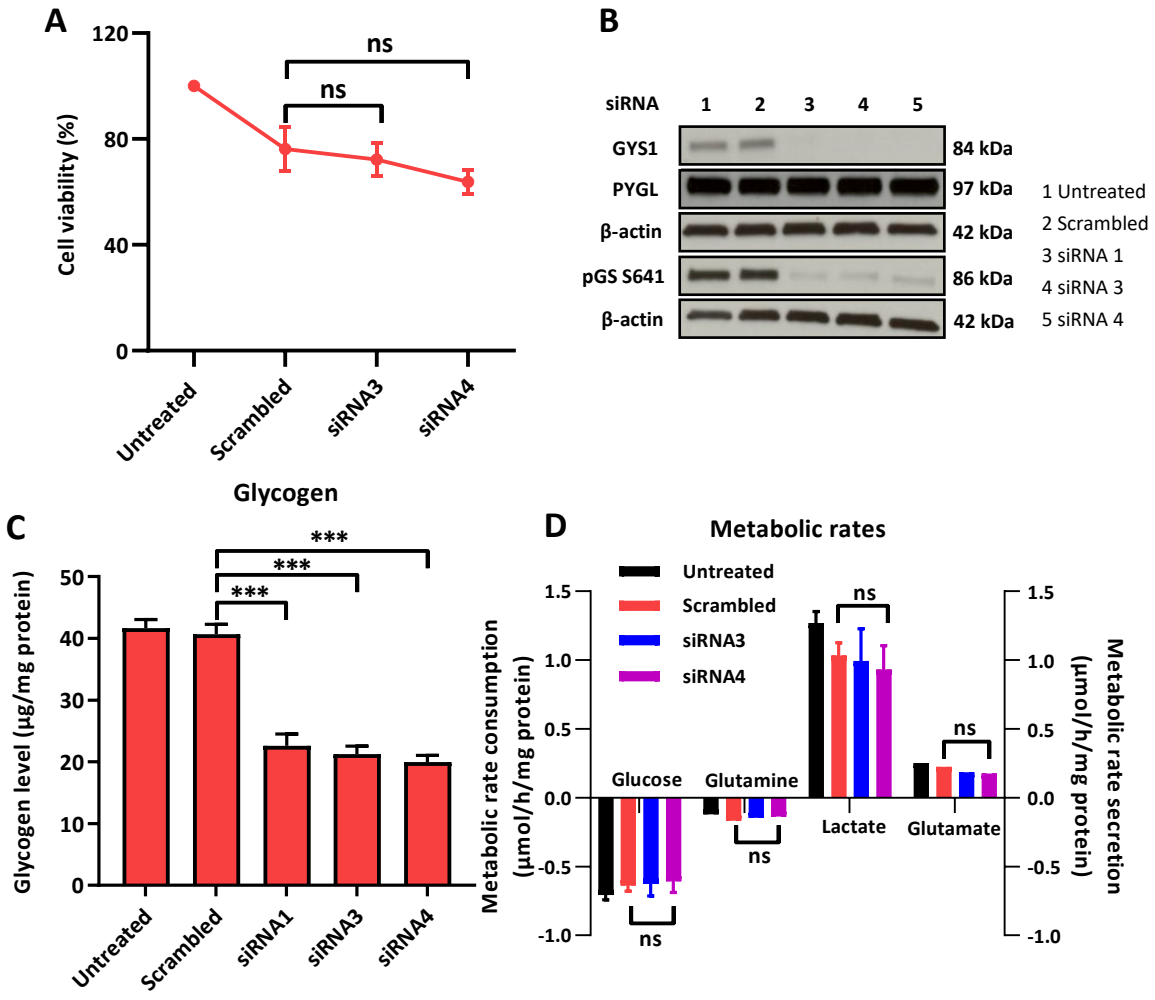


**Figure 3.13 Effects of GYS1 knockdown on cell viability, glycogen level and other metabolic pathways in IGROV-1 cells.**

**A,** The effect of GYS1 knockdown on cell viability. Mean values ± SD (n=6). **B,** The effect of GYS1 knockdown on protein expression. **C,** The effect of GYS1 knockdown on total glycogen accumulation. Mean values ± SD (n=3). **D,** Metabolic rates in GYS1-knockdown and control cells. Significant difference was defined if $p < 0.05$ (ns, no significant difference; ***, $p < 0.001$).

### 3.4.3 Discussion

The half-life of GYS1 was assessed prior to knockdown experiment. GYS1 was shown to have a half-life of 2.6 hours which was measured through inhibiting mRNA transcription by actinomycin D. The levels of phospho-GYS1, which is regulated by post-translational processes, showed no difference between control and treated cells. One study reports the GYS1 half-life of 6.0 ± 0.8 hours in rat hepatoma H4 cells after incubation with protein synthesis inhibitor, 5,6-dicoloro-1-beta-D-ribofuranosyl benzimidazole (DRB) [238].

Gene knockdown by siRNA resulted in a significant suppression in GYS1 expression as determined by western blot and a decrease in total glycogen level by 50% in IGROV-1 cells. Knockdown of GYS1, however, did not affect glycogen levels in 786-O and MCF-7 cells despite considerable gene silencing. Here, three hypotheses were posed as to why GYS1 silencing had no or little effect on the investigated biological response (glycogen accumulation):

(i) Protein depletion is different to activity inhibition and therefore despite significant inhibition of GYS1 expression, the activity of this enzyme possibly remains the same. It has been reported that protein expression level is not always correlated with the enzyme activity. In addition to phosphorylation, GYS1 activity is also regulated by an allosteric factor G6P. The presence of G6P could overcome inactivation due to phosphorylation and restore enzyme full activity.

(ii) The knockdown was not sufficient and therefore, even though GSY1 expression was substantially decreased, the function of GSY1 was not removed to an extent that biologic effects could be detected.

(iii) Cells reduce glycogen degradation to compensate for the decreased synthesis following GYS1 knockdown. Although GYS1 did not affect expression of PYGL, activity of this enzyme was not assessed in this study. It is likely that PYGL activity is decreased in response to GYS1 silencing, resulting in an inhibition on glycogen degradation. It remains to be seen if the activity of PYGL changes in response to GYS1 knockdown.

In addition to glycogen accumulation, the effect of GYS1 knockdown on cell viability and other metabolic pathways was also examined in IGROV-1 cells. Transient silencing of GYS1 did not dramatically influence cell survival, with only a 10% decrease in cell viability in knockdown

cells. Although several studies have shown an inhibition of cancer cell growth due to GYS1 knockdown, this is dependent on cell type and cellular stress condition. For example, cells under environmental conditions of nutrient limitation are more susceptible to alterations in glycogen metabolism, as glycogen is a rapid and crucial energy source in this context. Tumour cells that largely rely on glycogen mobilization for growth are possibly more sensitive to GYS1 knockdown. 18% of the total AML patient population showed an increase in the expression of GYS1, GYS2 and GBE1. And knockdown of GYS1 in KU812 cells was sufficient to reduce its growth [156]. Therefore, it would be worth assessing the function of GYS1 knockdown in cancer cells under stress conditions.

In order to understand the effect of GYS1 knockdown on metabolic pathway flux, glucose and glutamine consumption and the secretion of catabolic by-products (lactate and glutamate) were analysed. It was found that GYS1 knockdown had no effect on glycolytic flux and glutamine-glutamate cycle in IGROV-1 cells, which rules out nonspecific metabolic effects of GYS1 silencing or off-target toxicities of siRNA.

In summary, GYS1 knockdown by siRNA significantly inhibited GYS1 expression in three cell lines tested, whereas glycogen level was reduced by 50% only in IGROV-1 cells and remained unchanged in 786-O and MCF-7 cells. Further studies showed that silencing of GYS1 did not affect cell viability and other metabolic pathway flux such as glycolysis and glutamine-glutamate cycle in IGROV-1 cells. Taken together, the effect of GYS1 knockdown on related biological response such as glycogen accumulation is possibly cell type-dependent, where cancer cells are more responsive if they largely rely on glycogen metabolism for survival. Moreover, cells under stress condition, e.g. hypoxia or glucose deprivation, might be more susceptible to GYS1 inhibition, which remains to be explored.

### 3.5 Evaluation of the role of GYS1 under hypoxia in cancer cells

As the rapid and uncontrolled proliferation of tumours leads to limitations in oxygen availability and blood supply, hypoxia is a typical microenvironment feature in nearly all solid tumours [239]. Tumour hypoxia activates a signalling cascade driven by the transcription factor HIF-1 that has been recognized as the major regulator in the hypoxic responses of cells. HIF-1 belongs to the large family of basic-helix-loop-helix (bHLH) proteins and has two subunits alpha (α) and beta (β) which are similar in structure. There are more than a hundred genes reported to be regulated by HIF-1, in a promoted or repressed manner [239; 240]. Various metabolic adaptations have been found under hypoxic conditions, which enable neoplastic cells to survive. For example, most of the genes involved in glycolysis are upregulated under hypoxia through HIF-α stabilization [241]. In addition to glycolysis, cancer cells are reported to accumulate glycogen under hypoxia in a HIF-α-dependent manner, which herein prepares cells to cope with further oxygen restriction by ensuring adequate substrate supply for anaerobic glycolysis [154; 155].

Clear cell carcinoma is one of the most aggressive cancer types and historically defined by its lipid and glycogen-rich cytoplasmic deposits [242]. Alterations in the von-hippel-lindau syndrome (VHL) tumour suppressor which stabilises the HIF-α are the most striking molecular features of clear cell tumours. The significance and regulatory mechanism underlying glycogen accumulation remains undefined in this cancer type.

Additionally, depletion of GYS1 has previously been shown (**Section 3.4**) to inhibit glycogen accumulation to a lesser extent under normal culture conditions in three cancer cell lines. Therefore, it was investigated whether cells under hypoxia respond differently to GYS1 silencing in total glycogen level.

Herein, the profiles of GYS1 expression and glycogen level were assessed in clear cell renal cell carcinomas RCC4 and 786-O cells. The response of cells to GYS1 knockdown was examined in IGROV-1, MCF-7, T47D and 786-O cancer cells under hypoxic condition induced by a hypoxia-mimic agent cobalt chloride ($CoCl_2$) *in vitro*.

### 3.5.1 Glycogen accumulation in ccRCC appears to be associated with HIF-1α expression

ccRCC is a common type of kidney cancer which is characterised by high levels of glycogen storage. This subtype is the most aggressive histological type of renal cell carcinoma (RCC) and accounts for 70 – 80% of all RCC [242]. In ccRCC, the loss of pVHL function results in constitutive HIF-α activation and thus constitutive upregulation of HIF-target genes under normoxic conditions. pVHL is a component of an E3 ubiquitin ligase complex which negatively regulates the stability of HIF-α protein and its activity.

The first step was to investigate the potential role of HIF-α in glycogen accumulation using RCC4 cell line that contains constitutively stable HIF-1α and HIF-2α or 786-O cells that contains only HIF-2α. RCC4 cells where wild-type VHL was re-introduced were in parallel examined. Western blot analysis (Figure 3.14A) confirmed dramatic expression of HIF-1α and HIF-2α in RCC4 (-pVHL) cells. While the two proteins were significantly reduced in RCC (+pVHL) cells due to the re-introduction of VHL genes which leads to ubiquitination and degradation of HIF-α. As previously reported, 786-O showed high levels of HIF-2α proteins. GYS1 expression appeared to be associated with HIF-α expression in RCC4 cells, where silencing of HIF-α dramatically attenuated GYS1 expression in RRC4 (+pVHL) cells. 786-O cells exhibited the highest levels of GYS1 among the three cell lines.

As shown in Figure 3.14B, despite high levels of GYS1, 786-O cells showed the lowest accumulation of glycogen (17.67 ± 3.9 μg/mg protein), which was approximately 10-fold less than that of RCC4 cells. VHL-transfected RCC4 cells had a 30% decrease in glycogen in comparison with control cells, at 158.77 ± 22.72 μg/mg and 232.83 ± 29.24 μg/mg protein, respectively. Similar patterns of glycogen accumulation were confirmed by using PAS staining, where 786-O cells displayed the weakest positive signal, while RCC4 (-pVHL) cells had larger numbers of stained cells than RCC4 cells with VHL transfection. Taken together, although GYS1 was regulated by both HIF-1α and HIF-2α; glycogen accumulation appeared to be more dependent on GYS1 that is dominantly regulated by HIF-1α, but not HIF-2α in ccRCC under normoxia.

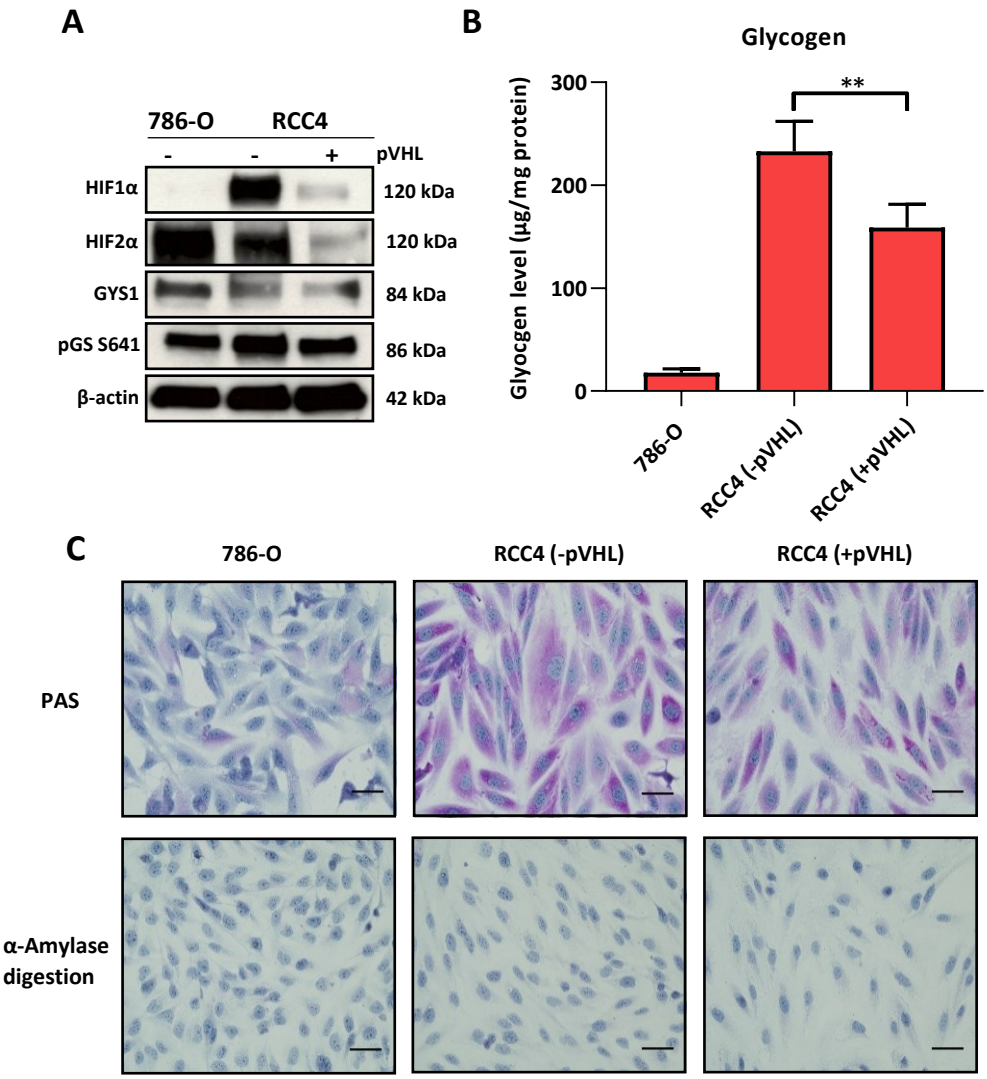


**Figure 3.14 Constitutive expression of HIF-1α in ccRCC largely increases glycogen accumulation.**

**A,** Western blot analysis for 786-O, RCC4 (-pVHL) and RCC4 (+pVHL) cells. **B,** Total glycogen assay. Mean values ± SD (n=3). **, $p < 0.001$ indicates significant difference. **C,** PAS staining. Cells were each seeded at appropriate densities in 6-well plates for western blot and glycogen assay or 8-well chamber slides for PAS staining and allowed to attach for 24 h. Scale bar = 50 µm.

### 3.5.2 Effect of $CoCl_2$ treatment on HIF-1α/HIF-2α induction and glycogen modulation

$CoCl_2$ is a commonly used chemical reagent for inducing and mimicking hypoxia in cells through activating transcription of hypoxia-regulated genes. The mechanisms of action are that $CoCl_2$ inhibits prolyl hydroxylase (PHD) enzyme though replacement of iron (Fe) with cobalt (Co), which impairs the degradation of HIF-1α through hydroxylation by PHD, and

stabilises HIF-1α expression [243]. Here, the induction of hypoxia by $CoCl_2$ was assessed in four cancer cell lines including IGROV-1, MCF-7, T47D and 786-O. Glycogen accumulation under '$CoCl_2$-induced hypoxia' condition was further evaluated by determining protein expression and total glycogen storage.

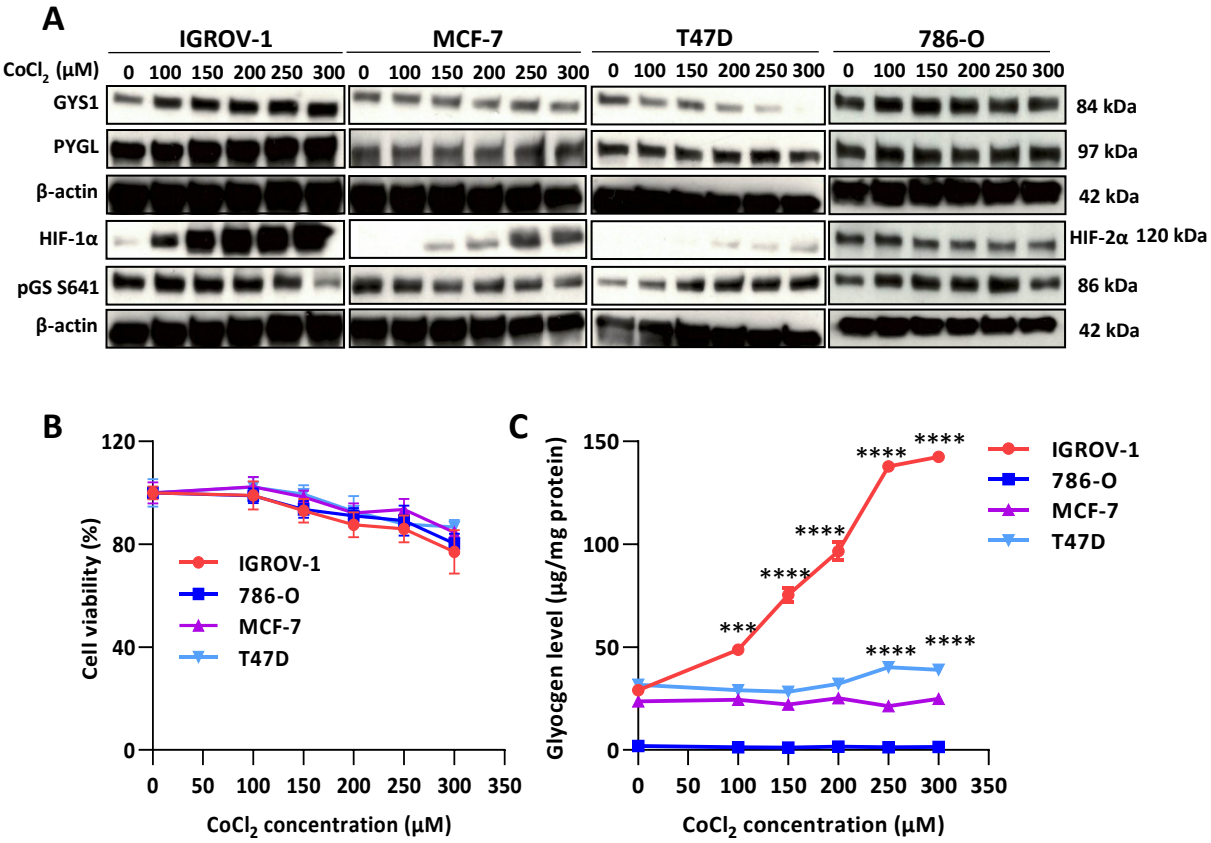


**Figure 3.15 Effect of $CoCl_2$ treatment on HIF-1α/HIF-2α induction and glycogen modulation.**

**A,** Western blot analysis for IGROV-1, MCF-7, T47D and 786-O cells. Cells were each seeded in 6-well plates at appropriate densities and exposed to various concentrations of $CoCl_2$ for 24 h. **B,** Cell viability in response to $CoCl_2$ treatment measured by SRB assay. Mean values ± SD (n=6). **C,** Total glycogen accumulation measured by glycogen assay following 24 h-$CoCl_2$ treatment.

Cell viability was firstly tested in the investigated cells to choose appropriate concentration ranges of $CoCl_2$ for further studies. It was shown in Figure 3.15B that $CoCl_2$ at indicated concentrations ranging from 100 - 300 µM did not cause significant cell toxicity among all cell lines. Western blot analysis (Figure 3.15A) was performed to determine the effect of $CoCl_2$ treatment on HIF-1α/HIF-2α expression, as well as proteins involved in glycogenesis signalling cascade. Treatment with $CoCl_2$ for 24 h remarkably and dose-

dependently induced an increase in HIF-1α expression in IGROV-1, MCF-7 and T47D cell lines, whereas 786-O cells that constitutively overexpress HIF-2α showed a slight reduction in HIF-2α after $CoCl_2$ treatment. Expression of glycogenesis-associated proteins differed among the cell lines in response to $CoCl_2$ treatment. IGROV-1 showed a nicely dose-dependent elevation in GYS1 activity as observed by increased GYS1 level and decreased phosphorylation of GYS1. In contrast, GYS1 activity was reduced in T47D cells and remained unchanged in MCF-7 and 786-O cells upon $CoCl_2$ treatment. PYGL expression was unchanged following $CoCl_2$ treatment across all cell lines.

Regarding glycogen accumulation (Figure 3.15C), increased GYS1 activity subsequent to $CoCl_2$ treatment in IGROV-1 cells contributed to a dose-dependent elevation in glycogen storage, where there was an approximately 5-fold increase from 29.02 ± 0.10 μg/mg protein in control cells to 142.55 ± 0.10 μg/mg protein in cells treated with 300 μM $CoCl_2$. Whereas MCF-7 and 786-O cells displayed constant glycogen levels in control and treated cells, which is consistent with the findings of unchanged GYS1 activity in the two cell lines. Interestingly, although there was a remarkable inhibition in GYS1 activity in T47D cells, total glycogen level was slightly increased at high concentrations of $CoCl_2$ at 250 and 300 μM.

### 3.5.3 Knockdown of GYS1 under hypoxia induces a dramatic decrease in glycogen level

Several papers have reported that knockdown of GYS1 attenuated hypoxia-induced glycogen accumulation, but only with a subtle inhibition in glycogen level in cells under normoxia. Similar results were observed in **Section 3.2**, where two of the three tested cell lines showed no changes in glycogen level upon GYS1 silencing under normal culturing conditions that contain an adequate oxygen supply. Therefore, it was investigated if GYS1 knockdown would result in more profound changes in glycogen storage under hypoxia condition induced by $CoCl_2$ *in vitro* in the four cell lines tested.

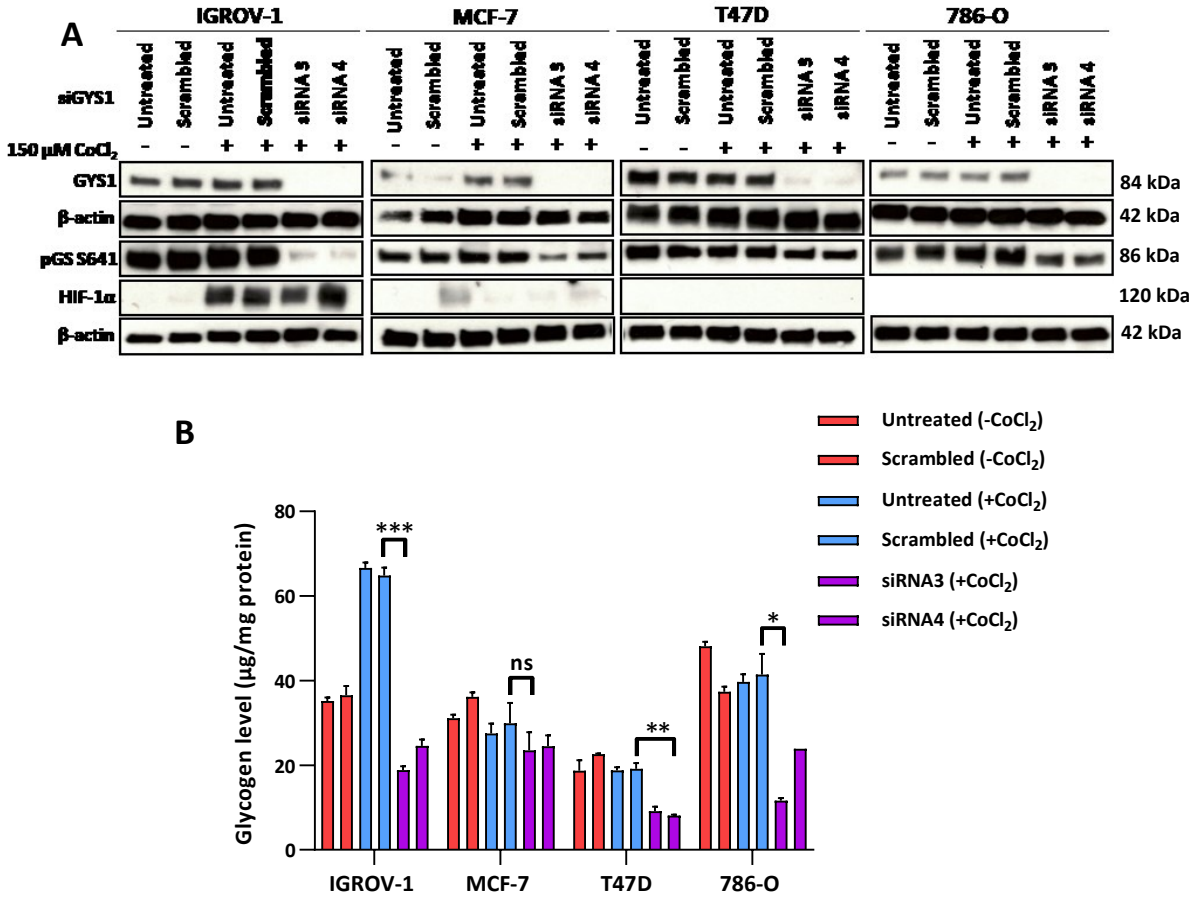


**Figure 3.16 Effect of GYS1 knockdown on glycogen accumulation under $CoCl_2$-induced hypoxia.**

**A,** Western blot analysis for IGROV-1, MCF-7, T47D and 786-O cells. **B,** Total glycogen level. Cells were seeded and transfected by using siRNAs with two sequences targeting GYS1 or scrambled siRNA. 72 h following transfection, cells were incubated with 150 µM $CoCl_2$ for another 24 h. At the end of treatment, cells were collected and analysed for protein expression by western lot and glycogen level by glycogen assay. * $p < 0.05$, ** $p < 0.01$ and *** $p < 0.001$ indicate significant difference from the value measured in the scrambled control group.

IGROV-1 and MCF-7 cells showed an increase in GYS1 expression when treated with 150 µM $CoCl_2$ compared to cells in the absence of $CoCl_2$, whereas in response to $CoCl_2$the level of GYS1 remained unchanged or a subtle decrease in 786-O and T47D cells, respectively. GYS1 expression remained low in siRNA treated cells among the four cell lines under $CoCl_2$-induced hypoxic condition.

The patterns of glycogen accumulation in IGROV-1 cells were in accordance with the levels of GYS1 expression, where $CoCl_2$-mediated GYS1 increase significantly resulted in a two-

fold increase in glycogen storage and GYS1 silencing correspondingly reduced glycogen level by around 70%. GYS1-knockdown under $CoCl_2$-induced hypoxia contributed to a 50% decrease in total glycogen accumulation in T47D and 786-O cells, while MCF-7 cells had a decrease to a lesser extent.

Taken together, we found that in IGROV-1 cells, there was a HIF-1α-mediated induction of GYS1 under hypoxia, which accordingly promoted total glycogen accumulation. Knockdown of GYS1 largely reduced hypoxia-induced glycogen storage in IGROV-1. Although MCF-7, T47D and 786-O showed no difference in glycogen level upon $CoCl_2$ treatment, knockdown of GYS1 under $CoCl_2$-induced hypoxia attenuated glycogen accumulation, suggesting that GYS1 contributes to glycogen accumulation across these cancer cell lines, although its regulation is not necessarily HIFα-dependent.

### 3.5.4 Discussion

ccRCC, which is one of the most aggressive subtypes of RCC, is characterised by high levels of glycogen storage and lipid deposition. The regulation of lipid deposition in ccRCC has recently been explored [244], where constitutive activation of HIF-α directly suppresses carnitine palmitoyltransferase 1A (CPT1A) which is the rate-limiting component of mitochondrial long chain fatty acid transport, thus reducing fatty acid transport into the mitochondrial and forcing fatty acids to lipid droplets for storage. The referenced study [244] highlights the importance of altered lipid metabolism in contributing to ccRCC and suggests that targeting lipid metabolism may be a new approach for therapeutic intervention in renal cancer. However, the significance of glycogen accumulation in ccRCC tumorigenesis is poor understood.

Here, we showed that re-expression of VHL in RCC4 cell line resulted in a degradation of HIF-1α and HIF-2α, a reduction in GYS1 level and an inhibition in the accumulation of glycogen, suggesting that HIF-α-mediated GYS1 induction correlates with a significant glycogen accumulation in RCC4 cells. However, another ccRCC cell line 786-O, despite significant expression of HIF-2α and GYS1, produced small amounts of glycogen. A similar pattern was observed by Pelletier et al. [235], where RCC4 cells had about 30 times higher glycogen accumulation than 786-O cells. Further silencing of HIF-2α in 786-O (+pVHL) cells reduced glycogen expression slightly, but not significantly. Although the exact reason remains

unclear, they suggested that HIF-2α could be involved but does not predominate in regulation of glycogen in ccRCC cells. Additionally, the inconsistency between levels of GYS1 and glycogen accumulation in 786-O cells might be explained by the fact that a large amount of GYS1 expression is not always correlated with high GYS1 activity. One study has found that HIF-α expression during hypoxia in mouse myotubes and hepatocytes results in increased total GYS1 activity without altering the ratio of phospho-GYS and total GYS1 [154].

The effect of knockdown of GYS1 on glycogen accumulation was further assessed under $CoCl_2$-induced hypoxia condition in four cancer cell lines. Although HIF-1α was dose-dependently induced by $CoCl_2$ in most of the cell lines, it was only in IGROV-1 cells that an increase in GYS1 activity and glycogen storage was observed, suggesting that HIF-α-mediated changes in glycogenesis is cell type-dependent under hypoxic condition *in vitro*. Knockdown of GYS1 under $CoCl_2$-induced hypoxia suppressed glycogen accumulation among all the tested cell lines with various degrees, with the most significant reduction observed in IGROV-1 cells. Combining with the data observed under normoxia, it may suggest that induction of GYS1 and glycogen storage is an adaptive response of cancer cells perhaps to meet altered energy requirements under hypoxia. The stored glycogen then can be rapidly metabolized to glucose for energy production and supporting cell proliferation under more severe stress conditions, such as hypoxia or glucose deprivation. Collectively, these observations indicate a potential role of GYS1 as a target for therapeutic intervention in cancer.

## 3.6 Discussion

The increased glycogen accumulation in several solid tumours together with the growth-related pattern of glycogen storage makes glycogen metabolism an attractive target for anticancer therapy and a potential biomarker for assessing the response of tumours to treatment. This chapter explored the significance and regulation of glycogenesis within tumour microenvironment.

GYS1, which is the rate-limiting enzyme of glycogen synthesis, was shown to be regulated in a Akt-GSK3β-dependent manner via PI3K signalling cascade in most of the investigated cell lines, particularly in cells harbouring PTEN mutation such as IGROV-1, 786-O and U87 where Akt is overactivated due to PTEN loss. As acute inactivation of PTEN can lead to senescence in a p53-dependent manner [245], the enhanced GYS1 activity as observed might be a downstream effector of senescence but independent of the PI3K pathway. GYS1 activity, as determined by the ratio of phospho-GYS to total GYS1, showed a weak correlation with total glycogen storage in several cancer cells, suggesting that apart from posttranslational modifications of GYS1 enzyme by phosphorylation, the allosteric activator G6P might play a crucial role in regulating GYS1 activity in tumours. Although glucose uptake is thought to be associated with glycogenesis, we found a lack of correlation between [$^{18}$F]FDG uptake and total glycogen level among the investigated cancer cell lines. Possibly, the amount of glucose that is converted into glycogen rather than metabolised through glycolytic or PPP pathway is highly dependent on the proliferation rate of tumours and stress conditions of tumour environment. For example, aggressive tumour cells are prone to utilize glucose through the glycolytic pathway as an adaptation to altered requirement for energy [228].

Furthermore, a cell growth-related pattern of glycogen accumulation was confirmed in IGROV-1, 786-O, MCF-7 and SKOV-3 cells in a GYS1-dependent manner, where cell confluency contributed to a G0/G1 cycle arrest, elevated GYS1 expression and in turn increased glycogen accumulation. The inverse correlation between proliferation rate and glycogen content indicated that glycogen is consumed to sustain cancer cell growth which might be provided as a potential target for anticancer treatment. Furthermore, it is of great interests to identify this unique pattern as a useful biomarker for assessing anticancer therapies that lead to changes in cell proliferative rate.

In order to identify the significance of GYS1 within tumour microenvironment, the relationship between GYS1 knockdown, cell viability and glycogen accumulation was evaluated across several cancer cell lines *in vitro*. Knockdown of GYS1 effectively inhibited GYS1 protein expression and resulted in a 50% decrease of total glycogen level in IGROV-1 cells, but no inhibition on cell viability. It remains unclear why another two cell lines showed no difference in glycogen accumulation upon GYS1 knockdown, however, several papers reported that knockdown of GYS1 attenuated hypoxia-induced glycogen accumulation, but only with a subtle inhibition in glycogen level in cancer cells under normoxia. Consistently, we then found that glycogen accumulation was suppressed in response to GYS1 silencing under $CoCl_2$-induced hypoxia in four cell lines. Further work is needed to understand the molecular mechanism underlying this response and to investigate the potential role of GYS1 as a target for anticancer therapies.

Furthermore, it was observed that ccRCC cells significantly accumulate glycogen under normoxia in a GYS1-dependent manner mediated by HIF-α due to the defect of VHL gene. HIF-1α, but not HIF-2α, was shown to play a dominant role in regulating glycogen storage in ccRCC cells. Recent studies have identified HIF control of fatty acid metabolism as essential for ccRCC tumorigenesis, it is also worth investigating to what extent glycogen is involved in pathological features of ccRCC.

# Chapter 4 Evaluation of diverse anti-cancer drugs on modulating senescence/quiescence and glycogenesis

The role of senescence in suppressing tumour progression and as a determinant of the outcome of conventional anticancer therapies have indicated that pro-senescence therapies could be an alternative strategy for treating cancer [246]. Senescent tumour cells can be efficiently eliminated by immune cells, resulting in efficient tumour suppression, which might provide a useful approach for the chronic management of some cancers. Several drugs have shown inhibitory effect against tumorigenesis via inducing cell senescence, however, an effective approach to assess cell response to pro-senescence therapies remains less explored.

One of the potential strategies is to develop radiopharmaceuticals for non-invasively tracing senescent cells through measuring one or more senescence-associated features. Given the fact that glycogen is accumulated when cancer cells undergo the G0/G1 cycle arrest, we hypothesized that elevated glycogenesis/glycogen would be an effective biomarker of chemotherapy-induced quiescence/senescence in neoplastic cells. Tracing changes in glycogenesis/glycogen by a specific PET tracer might provide opportunities to evaluate the outcomes of pro-senescence therapies in patients.

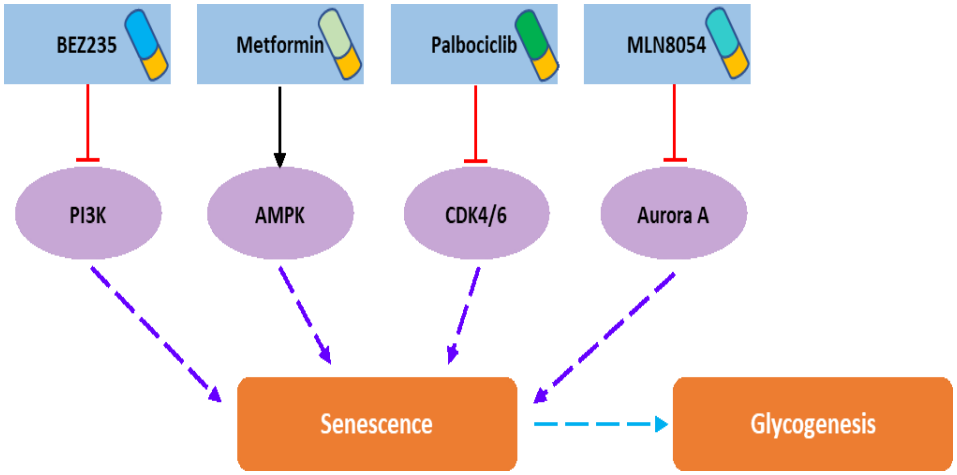


**Figure 4.1 Summary of the downstream targets of the four tested drugs.**

BEZ235 is a PI3K/mTOR dual inhibitor. The mechanism of action of metformin is to activate AMPK enzyme. Inhibition of CDK4/6 activity is responsible for the anticancer effect of palbociclib. MLN8054 inhibits cell proliferation via suppressing aurora A kinase activity.

With the intention to identify drugs that could effectively trigger cancer senescence and monitor their biological activity, we proposed to assess four commercially available drugs which are thought to engage cell cycle regulation via targeting diverse signalling cascades including PI3K, AMPK, CDK4/6 and Aurora A kinase. A wide range of cancer cell lines were tested for cell viability, cell cycle status, senescence induction and glycogen alterations upon *in vitro* treatment by the investigated drugs.

## 4.1 Targeting PI3K pathway as a regulator of senescence/quiescence and glycogenesis in a panel of cancer cell lines

### 4.1.1 Introduction

PI3K pathway is a crucial intracellular signal transduction system that tightly controls many aspects of cellular function such as metabolism, proliferation and cell survival [247]. The PI3K pathway is highly conserved and can be activated by several signals, including growth factors, cytokines and hormones. Upon stimulation, receptor tyrosine kinases (RTKs) undergo dimerization and cross-phosphorylation of tyrosine residues in the intracellular domains, which allows PI3K enzyme bound via their regulatory subunit or adapter molecules such as the insulin receptor substrate (IRS) proteins. Activated PI3K further triggers the production of the second messenger phosphatidylinositol 3,4,5-trisphosphates (PIP3) via phosphorylation of phosphatidylinositol 4,5-bisphosphate (PIP2). The PIP3 usually serves as membrane docking lipids for proteins that contain pleckstrin homology (PH) domains, including Akt and its upstream activator PDK1, thus eventually causing the activation of many downstream signal cascades [248; 249].

Deregulation of PI3K pathway frequently occurs in many types of cancer due to activating mutations in upstream regulators such as human epidermal growth factor receptor 2 (HER2) and epidermal growth factor receptor (EGFR), loss of PTEN or selective mutations of PIK3CA (p110α) [250]. Abnormalities in PI3K pathway is associated with the resistance of some cancer cells to conventional chemotherapy *in vitro* and *in vivo* [251]. This link between activation of PI3K pathway and cancer makes this pathway an attractive target for therapeutic strategies.

NVP-BEZ235, also known as Dactolisib, is one of the PI3K inhibitors currently in phase I/II clinical trials for advanced solid tumours such as colorectal, breast, renal and non-small cell

lung carcinoma [252]. The mechanism of action of BEZ235 is to inhibit the catalytic activity of PI3K and mTOR via reversibly binding to the ATP-binding sites of kinases [253]. Multiple studies have shown that BEZ235 exerts antiproliferative activities through inducing cell cytotoxicity, G0/G1 cycle arrest and cell autophagy. BEZ235 has also been reported to sensitize radiotherapy by downregulating the activity of DNA-dependent protein kinase in irradiated human cancer cells [254].

Additionally, over-activation of PI3K pathway in cancer is thought to be a barrier to cellular senescence through inhibition of several CDK inhibitors such as p16, p21, p27 and p53. Several studies have shown that pharmaceutical inhibition of PI3K signalling leads to increased expression of CDK inhibitors responsible for senescence [255]. One study found that expression of a constitutively activated forkhead box proteins (FOXO), which is a downstream factor of PI3K, rapidly triggered senescence [256]. These observations suggest pharmaceutical downregulation of PI3K pathway might trigger cancer senescence, thereby contributing to suppressing tumour proliferation.

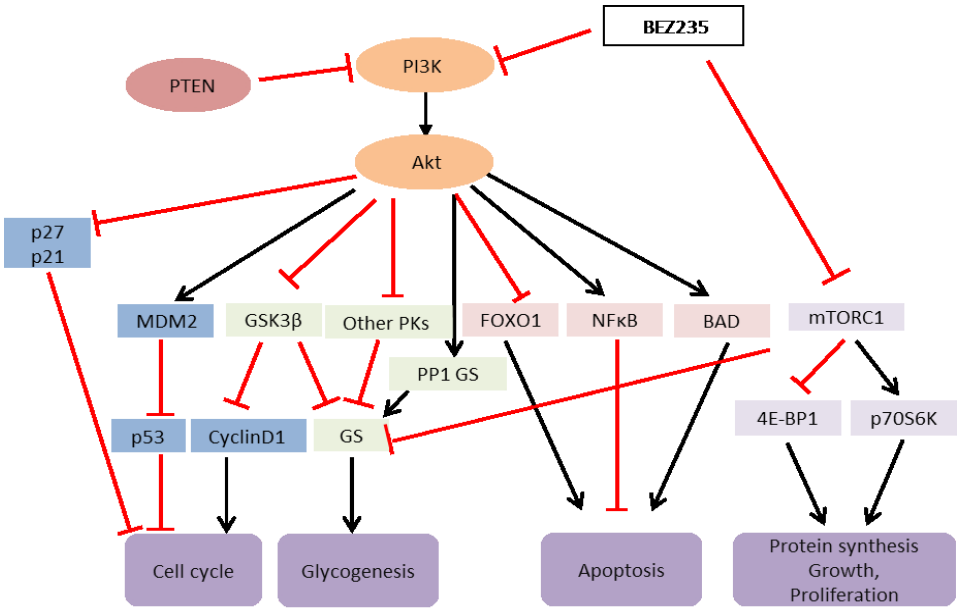


**Figure 4.2 The mechanism of action of BEZ235 via PI3K pathway.**

BEZ235 is a dual PI3K/mTOR inhibitor that inhibit the catalytic activity of PI3K and mTOR via reversibly binding to the ATP-binding sites of kinases. [Adapted from Liu et al., 2009]

It has also been reported that dysregulated metabolism in cancer cells is highly linked to aberrant PI3K/AKT pathway. For example, the activity of AKT has been found to be associated with translocation of hexokinase I/II (HKI/II) to the mitochondrial outer membrane [257], GLUT1 expression and translocation of GLUT-1 and GLUT-4 to cell membrane. Glycogen synthase, as the driving enzyme of glycogenesis, is phosphorylated at several sites by GSK3β which is one of the main downstream effectors of PI3K/AKT signalling.

Therefore, the aim of this section was to investigate whether BE235 could induce senescence and its link to modulation of glycogenesis in a panel of cancer cell lines.

### 4.1.2 Selection of responsive cell lines for further investigation

**BEZ235 inhibits cell growth in a panel of cancer cell lines**

In order to optimize experimental conditions, the tolerance limits of cells to DMSO was first examined, and the growth properties of each cell line was characterized in 96-well plates over 72 hours.

A series of DMSO concentrations ranging from 0.1% to 1% (v/v) were tested in IGROV-1 and MDA-MB-231 cells (Figure 4.3C). Cells displayed no observable toxic effects when DMSO was used between 0.1% and 0.6%, suggesting the tolerable concentrations of DMSO < 0.6%. Next, a range of cell numbers from $2 \times 10^3$ to $2 \times 10^4$ cells/well were seeded and cultured in 96-well plates for 72 hours. The growth curve (Figure 4.3D) revealed that the seeding densities of $5 \times 10^3$ and $1.5 \times 10^4$ cells/well appropriately led to cell growth at exponential and stationary phase, respectively. Collectively, final concentration of DMSO was controlled below 0.6% in media, and the two seeding densities were chosen to compare the effect of BEZ235 on inhibiting cell proliferation under different growth conditions.

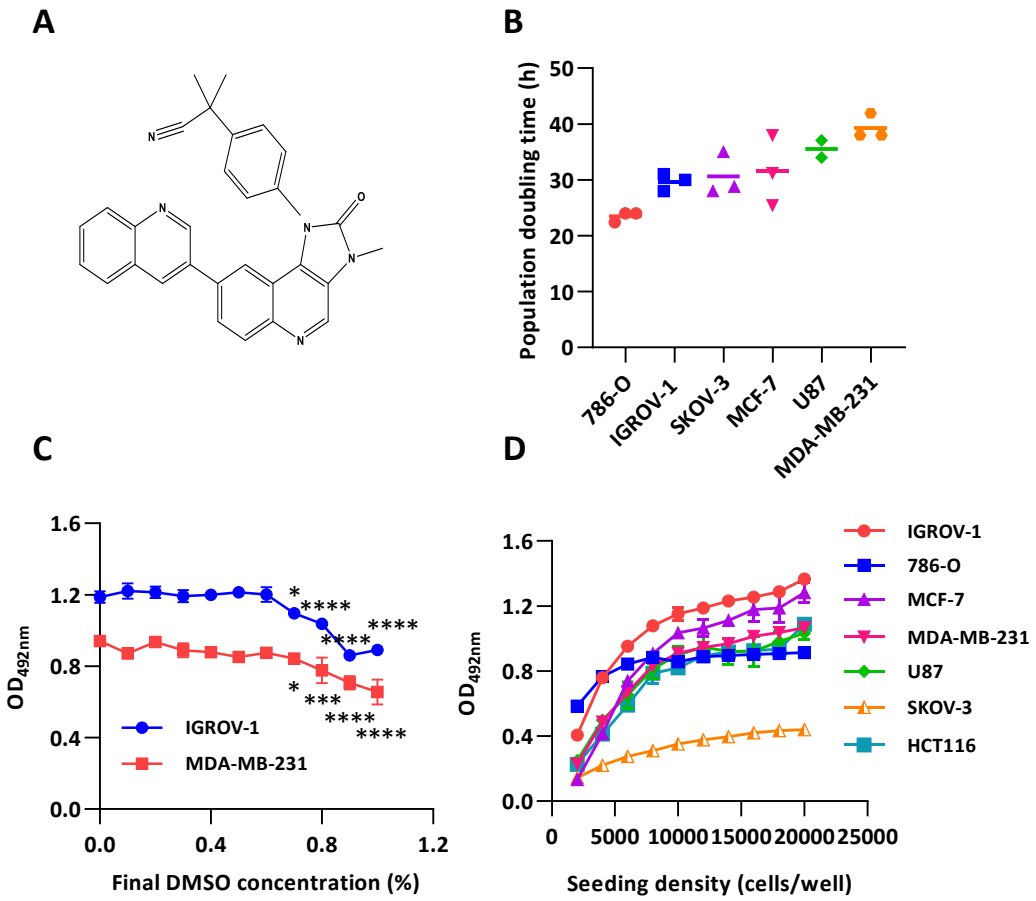


**Figure 4.3 Optimization of DMSO concentration and cell seeding density.**

**A,** Chemical structure of BEZ235. **B,** Population doubling time (PDT) of cell lines in hours. PDT were summarized from online source (Cellosaurus). **C,** The effect of DMSO concentration on cell viability in IGROV-1 and MDA-MB-231 cells. Mean values ± SD (n=3). *p < 0.05, *** p < 0.001 and **** p < 0.0001 indicate significant difference from the value measured in control intreated group. **D,** Growth curves of a panel of cancer cell lines. Mean values ± SD (n=3).

Next, to screen for responsive cell lines, we tested the effect of BEZ235 in a comprehensive panel of tumour cell lines with various gene mutation background (Table 3.1). The $GI_{50}$ value was determined by using a 72 h-SRB growth assay with continuous drug exposure. This treatment duration was based on the fact that a 72 h time point allowed more than two doublings of most of the investigated cell lines (doubling time was summarized from Cellosaurus, as shown in Figure 4.3B).

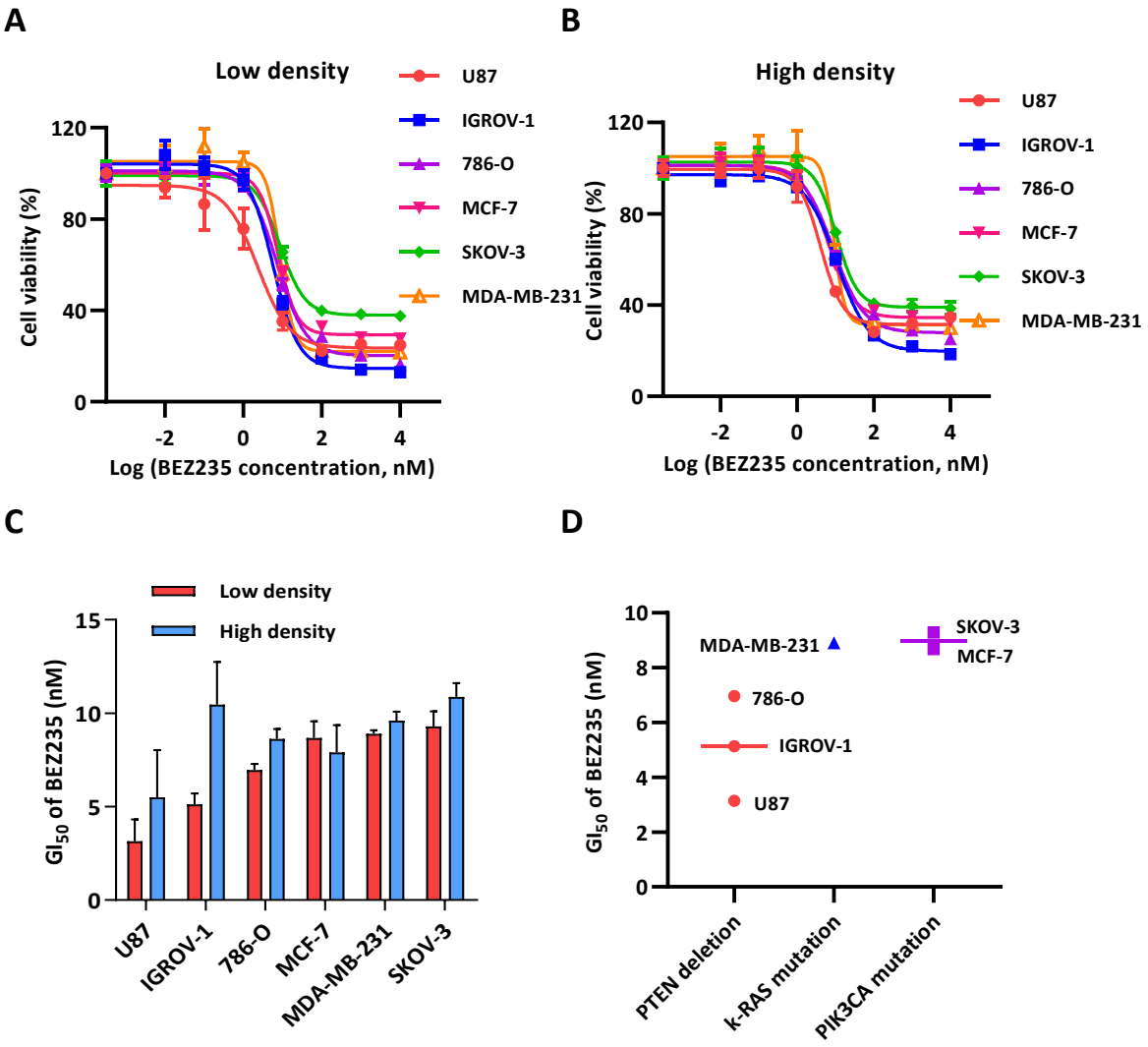


**Figure 4.4 $GI_{50}$ determination for BEZ235 in a panel of cancer cell lines.**

**A,** Dose response curve of each cell line at low seeding density ($5 \times 10^3$ cells/well) following 72 h-treatment. **B,** Dose response curve of each cell line at high seeding density ($1.5 \times 10^4$ cells/well) following 72 h-treatment. **C,** $GI_{50}$ values in tested cell lines at two seeding densities. Mean values ± SD (n=3). **D,** Median $GI_{50}$ of cell lines grouped by gene mutation type.

As shown in Figure 4.4, five cancer cell lines displayed near-equivalent response to BEZ235 treatment under sub-confluent and confluent conditions, with the exemption of IGROV-1 cells that showed approximately two-fold increase in $GI_{50}$ value from low to high seeding density, at 5.13 ± 0.33 nM and 10.46 ± 1.32 nM, respectively. When cultured at exponential growth phase, cell lines with PTEN deletion including U87, IGROV-1 and 786-O were more sensitive to BEZ235, with the $GI_{50}$ of 3.15 ± 0.67 nM, 5.13 ± 0.33 nM and 6.96 ± 0.19 nM, respectively. A lower sensitivity was found in two PI3KCA mutated cell lines MCF-7

and SKOV-3, whose $GI_{50}$ was 8.68 ± 0.52 nM and 9.29 ± 0.47 nM, respectively. MDA-MB-231 had a $GI_{50}$ of 8.89 ± 0.11 nM at low seeding density and 9.61 ± 0.27 nM at high sending density.

**BEZ235 has distinct effects on PI3K/Akt signalling**

To obtain a preliminary view of how BEZ235 influences PI3K pathway, we next examined the expression profiles of several downstream factors involved in this pathway, including proteins that regulate cell cycle progression and glycogenesis.

Cells seeded at low and high densities in 6-well plates were exposed to a single concentration of BEZ235 at 250 nM for 24 h. Cells incubated with vehicle-containing media (final DMSO concentration: 0.5%) were used as controls. It was found that initial seeding density had negligible impact on expression profiles of the investigated proteins upon BEZ235 treatment, which is consistent with the fact observed in $GI_{50}$ assay that there was near-equivalent drug response under sub-confluent and confluent conditions in all cell lines.

As shown in Figure 4.5A, Akt phosphorylation at serine 473 residue, which directly reflects the activation of PI3K, was remarkably supressed by 250 nM of BEZ235, except MCF-7 and MDA-MB-231 cells in which no phospho-Akt could be detected. BEZ235 at 250 nM appeared to cause a subtle increase in pGSK3αβ/GSK3αβ ratio (Figure 4.5B) across all tested cell lines, suggesting an inhibition of GSK3αβ activity by BEZ235. Surprisingly, the expression of pGS S641, which is the inactive form of GYS1, was elevated in all the investigated cell lines following treatment. In addition to the glycogenesis pathway, the effect of BEZ235 on glycogen degradation was also examined by measuring the expression of PYGL which catalyses the rate-limiting step of glycogenolysis. The differences in PYGL level were unremarkable between control and BEZ235-treated cells across all cell lines. P21 expression, as one of the important biomarkers of quiescence/senescence, was only increased in U87 cells upon treatment, while the other cell lines showed an unchanged or decreased p21 level. Taken together, while BEZ235 treatment led to an efficient Akt inhibition in all cell lines tested, its effect on downstream targets including GSK3αβ, GYS1 and p21 varied, and inconsistent with regulation of the investigated glycogenesis enzymes.

A

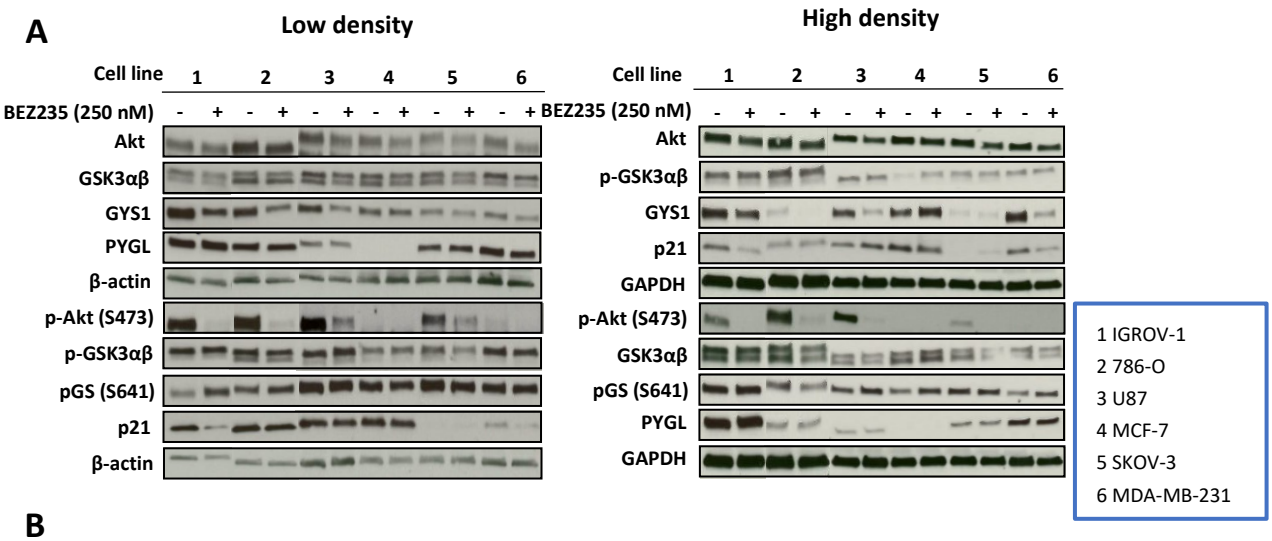


B

| Cell line | Relative to each control | | | | | | | | | |
|---|---|---|---|---|---|---|---|---|---|---|
| | pAkt (S473)/Akt | | pGSK3αβ/GSK3αβ | | pGS (S641)/GYS1 | | PYGL | | P21 | |
| | Low | High | Low | High | Low | High | Low | High | Low | High |
| IGROV-1 | 0 | 0.11 | 1.84 | 1.09 | 8.43 | 1.53 | 1.26 | 1.03 | 0.15 | 0.3 |
| 786-O | 0 | 0.12 | 0.65 | 1.15 | 2.11 | 8.38 | 1.40 | 1.03 | 0.92 | 1.25 |
| U87 | 0.06 | 0.03 | 1.43 | 1.25 | 2.05 | 5.93 | 0.78 | 0.78 | 0.71 | 1.53 |
| MCF-7 | 0 | 0 | 1.69 | 3.28 | 1.57 | 1.08 | 0 | 0 | 1.02 | 0.84 |
| SKOV-3 | 0.19 | 0 | 0.77 | 2.94 | 1.03 | 1.14 | 1.10 | 1.00 | 1.05 | 7.8 |
| MDA-MB-231 | 0 | 0 | 1.06 | 0.77 | 1.57 | 8.69 | 0.84 | 1.08 | 0.44 | 0.42 |

C

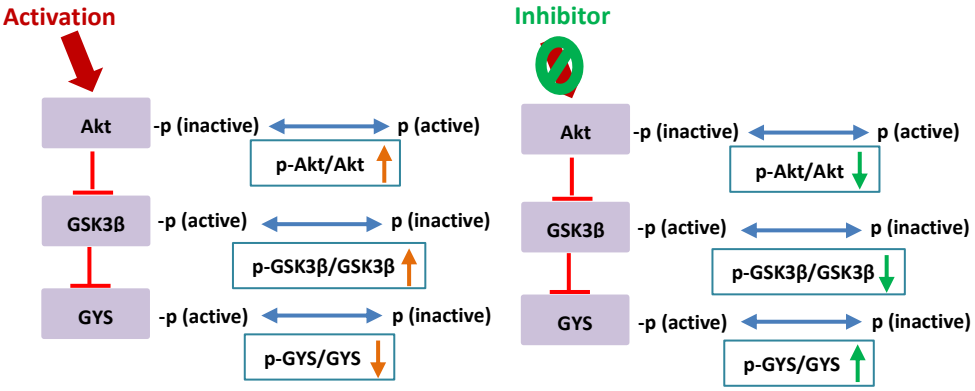


**Figure 4.5 The effects of BEZ235 on phosphorylation of Akt and its downstream targets involved in regulation of cell cycle and glycogenesis.**

**A,** Results of western blot after 24 h-BEZ235 treatment in a cell line panel at low seeding density ($1 \times 10^5$ cells/well) and high seeding density ($1 \times 10^6$ cells/well), respectively. **B,** Semi-quantification of western blot results by using ImageJ. Protein expression was normalised to β-actin or GAPDH and respective control. **C,** Schematic showing the regulation of Akt, GSK3β and GYS activity via activation or inhibition of PI3K pathway.

**BEZ235 leads to distinct changes in total glycogen accumulation**

Total glycogen level was next determined to identify cell lines that are suitable for studying the effects of BEZ235 on glycogenesis regulation. Consistent with previous results, cell lines including SKOV-3, IGROV-1 and MCF-7 displayed the highest basal glycogen contents (Figure 4.6). When exposed to 250 nM BEZ235, 786-O and SKOV-3 cell lines showed profound elevation of total glycogen storage under both seeding densities, with the most remarkable increase observed in SKOV-3 cells from 52.42 in controls to 147.75 µg/mg protein at 250 nM BEZ235 at low seeding density, and 37.58 to 100.59 µg/mg protein (control vs. 250 nM BEZ235) at high seeding density. A subtle increase was found in MDA-MB-231 cells following BEZ235 treatment, from 2.38 to 4.92 µg/mg protein at low density, and 0.66 to 8.15 µg/mg protein under the confluent condition. In contrast to upregulation of glycogen contents, 250 nM BEZ235 resulted in decreased glycogen in U87 and MCF-7 cell lines. IGROV-1 cells growing at low density showed an increase in glycogen level from 9.86 in control cells to 22.65 µg/mg protein after treatment, whereas there was a subtle decrease under confluent condition from 29.80 to 25.24 µg/mg protein (control vs. 250 nM BEZ235).

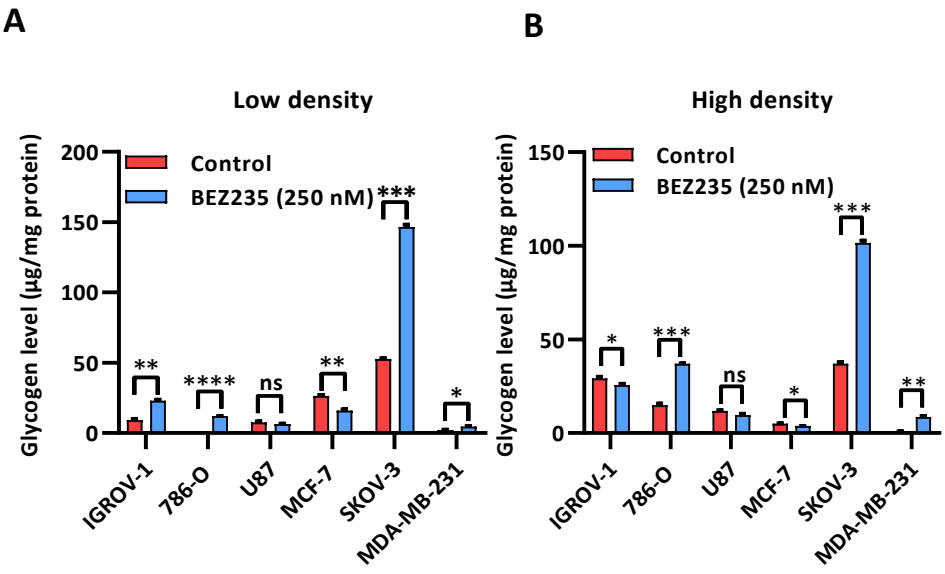


**Figure 4.6 The effects of BEZ235 on total intracellular glycogen accumulation.**

**A,** Changes of glycogen level upon BEZ235 treatment in a panel of cancer cell lines when seeded at low seeding density ($1 \times 10^5$ cells/well). **B,** Changes of glycogen level at high seeding density ($1 \times 10^6$ cells/well). Glycogen was digested to glucose by amyloglucosidase and measured by GO kit. Glycogen level was normalised to total protein concentration as measured by BCA assay. * $p < 0.05$, ** $p < 0.01$, *** $p < 0.001$ and $p < 0.0001$ indicate significant difference from the value measured in control untreated group.

### 4.1.3 Further investigation in four representative cell lines

U87, MCF-7, 786-O and SKOV-3 cells were chosen as representative cell lines for further investigation. This was based on the observations that U87 was the most responsive cell line to BEZ235 as shown by the lowest $GI_{50}$ of 3.15 ± 0.67 nM. As BEZ235 has been shown to strikingly suppress the proliferation of MCF-7 cells, we then tested whether one of the mechanisms could be associated with senescence. 786-O and SKOV-3 cells were used because preliminary data showed an increase in glycogen accumulation upon treatment, which was partially in support of our hypothesis that drug-induced senescence triggers an elevation of glycogenesis.

**BEZ235 induces a G0/G1 cycle arrest in four representative cell lines**

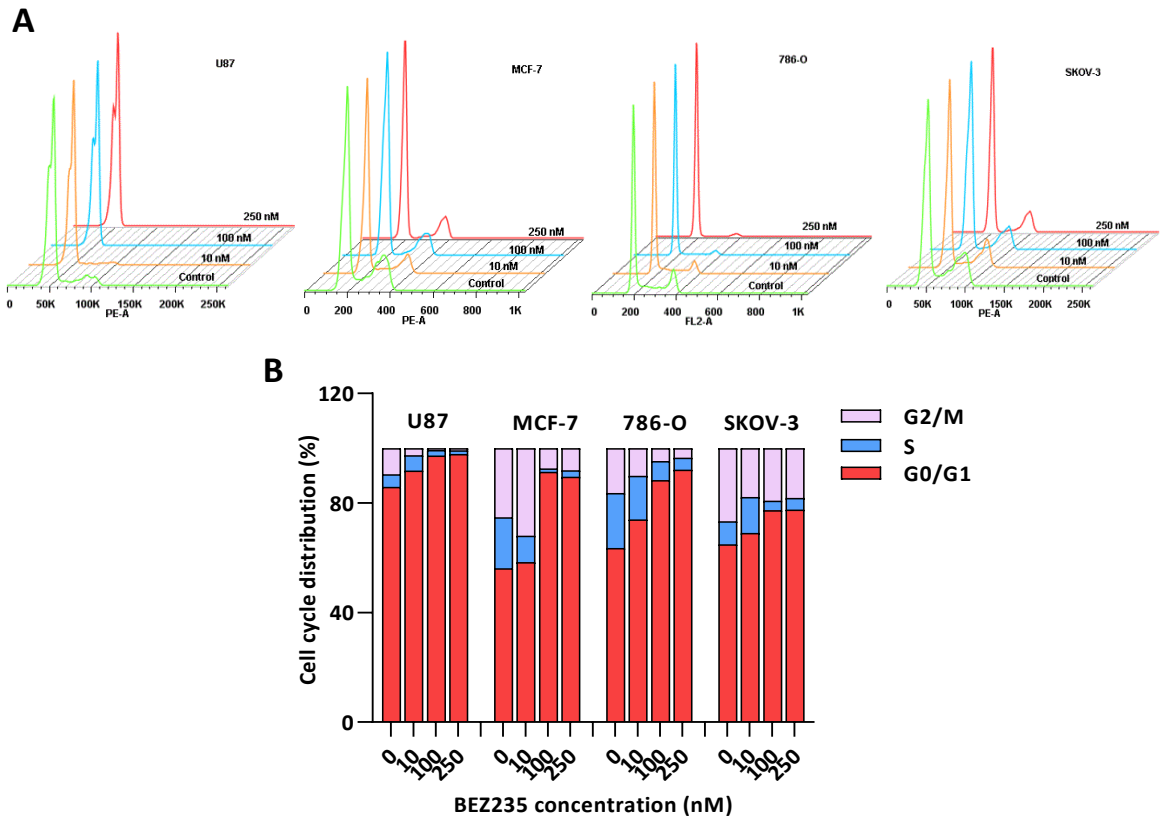


**Figure 4.7 BEZ235 effectively leads to a G0/G1 cycle arrest.**

**A,** Representative histograms of cell cycle analysis in U87, MCF-7, 786-O and SKOV-3 cells. **B,** The percentage of cells in G0/G1, S and G2/M phase. Data was analysed by FlowJo software.

Cell cycle analysis was performed by flow cytometry using PI staining in U87, MCF-7, 786-O and MCF-7 cell lines. It was shown (Figure 4.7) that BEZ235 led to a remarkable G0/G1 phase arrest in all cells in a dose-dependent manner after 24 hours of treatment. The most profound increase was found in MCF-7 cells, from 56.1% of cells in G0/G1 phase in untreated cells to 89.5% in treated cells. Similar trend was observed in 786-O cells that BEZ235 led to an elevation in total numbers of cells in G0/G1 phase, from 63.5% in control cells to 92.1% in treated cells (250 nM BEZ235). In SKOV-3 cells, BEZ235 at indicated concentrations resulted in a moderate increase, which was from 64.9% in control cells to 69.0%, 77.3% and 77.6% at 10 nM, 100 nM and 250 nM BEZ235, respectively. Although 250 nM BEZ235 yielded in the greatest proportion of cells in G0/G1 phase (97.8%), most U87 cells were in G0/G1 phase at baseline with a percentage of 85.9%.

**BEZ235 has little or no effect on SA-β-gal activity in the four cell lines**

To further evaluate whether BEZ235-mediated G0/G1 arrest is associated with senescence, SA-β-gal staining was carried out in the four cell lines (Figure 4.8). A subtle increase in the numbers of positive stained cells was observed in 786-O and SKOV-3 cells following 24 hours of BEZ235 treatment at indicated concentrations. In contrast, the proportion of blue stained cells remained low and unchanged in U87 and MCF-7 cells after treatment when seeded at low density. Under confluent condition, a strong signal was even seen in untreated U87 and MCF-7 cells, which reflected one of the limitations of SA-β-gal staining that cell confluency might lead to false-positive results.

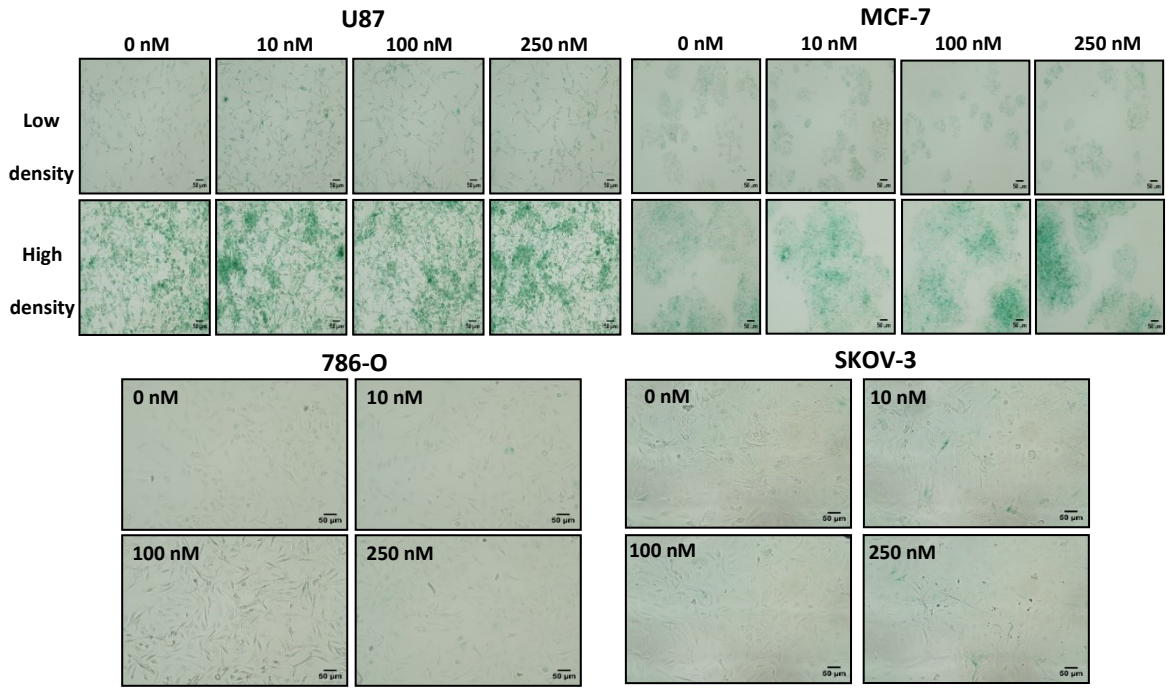


**Figure 4.8 BEZ235 has little or no effects on SA-β-gal activity in the four cell lines.**

U87 and MCF-7 cells were seeded at two densities, while 786-O and SKOV-3 cells were seeded only at low density. SA-β-gal staining was performed according to manufacturer's instruction after 24 hours of BEZ235 treatment. Images were obtained under × 400 magnification on a standard microscope. Scale bar = 50 µm.

### BEZ235 inhibits Akt and GYS1 activity

While BEZ235 appeared to barely induce senescence as measured by SA-β-gal staining in the four cell lines tested, we still examined whether the inhibtor has effects on the downstream targets of PI3K pathway that could regulate cell growth and glycogen metabolism.

Western blot analysis (Figure 4.9) revealed that all cells exposed to BEZ235 for 24 h displayed considerably declined levels of Ser473-P-Akt in a dose-dependent manner, among which BEZ235 at 100 and 250 nM completely blocked Akt phosphorylation in most of the cell lines. GSK3αβ plays a pivotal role not only in inhibition of glycogen synthase, but also controlling cell metabolism, differentiation and immunity. Here, pGSK3αβ/GSK3αβ ratio remained unchanged or slightly increased in all cell lines despite the remarkable inhibition of Akt by BEZ235. The ratio of pGS S641 to GYS1 was dramatically increased in the four investigated cell lines, suggesting inhibition of this enzyme by BEZ235. Cells exposed to BEZ235 did not change the levels of PYGL protein across all cell lines. Taken together, although

suppression of Akt by BEZ235 has little effect on its downstream factor GSK3αβ, the activity of GYS1 was diminished in all tested cell lines, indicating that BEZ235 might mediate GSY1 activity via regulation of other enzymes rather than through GSK3αβ.

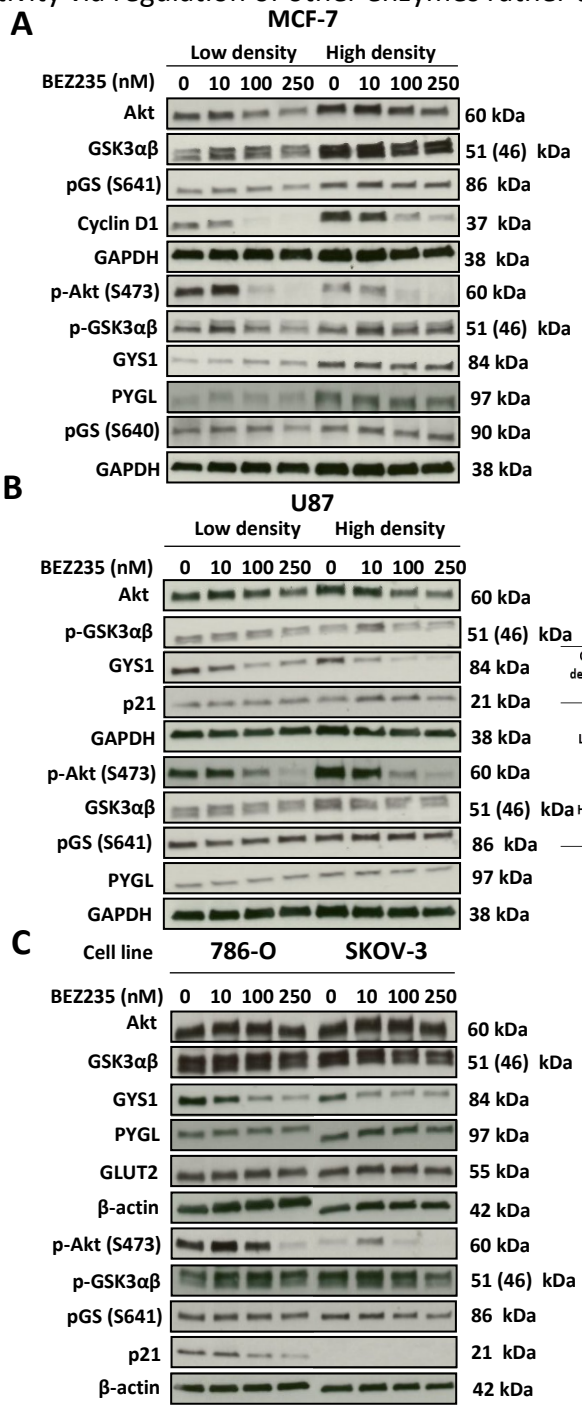


| MCF-7 | | | | | | | | |
|---|---|---|---|---|---|---|---|---|
| BEZ235 (nM) | Relative to each control | | | | | | | |
| | pAkt (S473)/Akt | | pGSK3αβ/GSK3αβ | | pGS (S641)/GYS1 | | PYGL | |
| | Low | High | Low | High | Low | High | Low | High |
| 0 | 1.00 | 1.00 | 1.00 | 1.00 | 1.00 | 1.00 | 1.00 | 1.00 |
| 10 | 1.14 | 0.84 | 0.75 | 1.38 | 1.23 | 1.25 | 1.61 | 1.05 |
| 100 | 0.24 | 0.28 | 0.49 | 1.33 | 0.80 | 1.38 | 1.26 | 0.83 |
| 250 | 0.05 | 0.13 | 0.44 | 1.40 | 0.58 | 1.25 | 1.21 | 1.14 |

| U87 | | | | | | |
|---|---|---|---|---|---|---|
| Cell density | BEZ235 (nM) | Relative to each control | | | | |
| | | pAkt (S473)/Akt | pGSK3αβ/GSK3αβ | pGS (S641)/GYS1 | PYGL | P21 |
| Low | 0 | 1.00 | 1.00 | 1.00 | 1.00 | 1.00 |
| | 10 | 0.85±0.11 | 1.21±0.18 | 1.34±0.67 | 0.84±0.79 | 1.35 |
| | 100 | 0.25±0.18 | 1.09±0.42 | 4.11±0.50 | 0.83±0.67 | 1.44 |
| | 250 | 0.10±0.03 | 1.12±0.47 | 2.65±0.27 | 1.07±0.91 | 1.41 |
| High | 0 | 1.00 | 1.00 | 1.00 | 1.00 | 1.00 |
| | 10 | 0.69±0.01 | 0.91±0.08 | 1.61±0.28 | 1.13±0.10 | 1.77 |
| | 100 | 0.23±0.11 | 1.03±0.07 | 5.46±0.83 | 0.84±1.00 | 1.62 |
| | 250 | 0.01±0.07 | 1.65±0.17 | 4.48±0.06 | 0.78±1.05 | 1.04 |

| Cell line | BEZ235 (nM) | Relative to each control | | | | |
|---|---|---|---|---|---|---|
| | | pAkt (S473)/Akt | pGSK3αβ/GSK3αβ | pGS (S641)/GYS1 | PYGL | P21 |
| 786-O | 0 | 1.00 | 1.00 | 1.00 | 1.00 | 1.00 |
| | 10 | 1.17±0.34 | 1.59±0.36 | 1.32±0.64 | 0.76 | 0.85 |
| | 100 | 0.39±0.37 | 0.97±0.24 | 4.31±0.21 | 0.66 | 0.41 |
| | 250 | 0.11±0.04 | 1.58±0.18 | 3.83±1.40 | 0.70 | 0.23 |
| SKOV-3 | 0 | 1.00 | 1.00 | 1.00 | 1.00 | |
| | 10 | 0.65±0.07 | 1.18±0.46 | 1.99±0.81 | 0.96 | Not |
| | 100 | 0.32±0.23 | 1.19±0.31 | 2.31±0.37 | 0.90 | detectable |
| | 250 | 0.11±0.04 | 1.27±0.37 | 2.20±0.34 | 0.75 | |

**Figure 4.9 BEZ235 inhibits the activity of Akt and GYS1 in the four cell lines tested.**

**A**, Representative blots and semi-quantification of western blot in U87 cells at low and high seeding density. **B**, Representative blots and semi-quantification of western blot in MCF-7 cells at low and high seeding density. **C**, Representative blots and semi-quantification of western blot in 786-O and SKOV-3 cells. Quantification was done by normalisation of protein expression to β-actin or GAPDH, and respective vehicle control.

**BEZ235 has distinct effects on total glycogen accumulation**

Having found a reduced GYS1 activity, we further tested total intracellular glycogen accumulation after 24 hours of BEZ235 treatment in the four cell lines. As shown in Figure 4.10, U87 cells showed decreased glycogen level under confluent condition from 111.58 µg/mg protein to 68.18 µg/mg protein (control vs. 250 nM BEZ235), while cells under sub-confluent condition showed constantly low glycogen contents. In MCF-7 cells, treatment with BEZ235 led to a subtle decrease in total intracellular glycogen under both growth conditions, from 5.35 ± 0.46 to 0.90 ± 0.95 µg/mg protein (control vs. 250 nM) at low density, and from 30.70 ± 8.70 to 23.24 ± 2.62 µg/mg protein (control vs. 250 nM) at high seeding density. In contrast, BEZ235 at indicated concentrations induced a significant and dose-dependent glycogen elevation in 786-O and SKOV-3 cells, with the most pronounced increase observed in SKOV-3 cells from 29.60 ± 1.34 µg/mg protein in vehicle-treated cells to 121.26 ± 10.10 µg/mg protein in cells treated with 250 nM BE235.

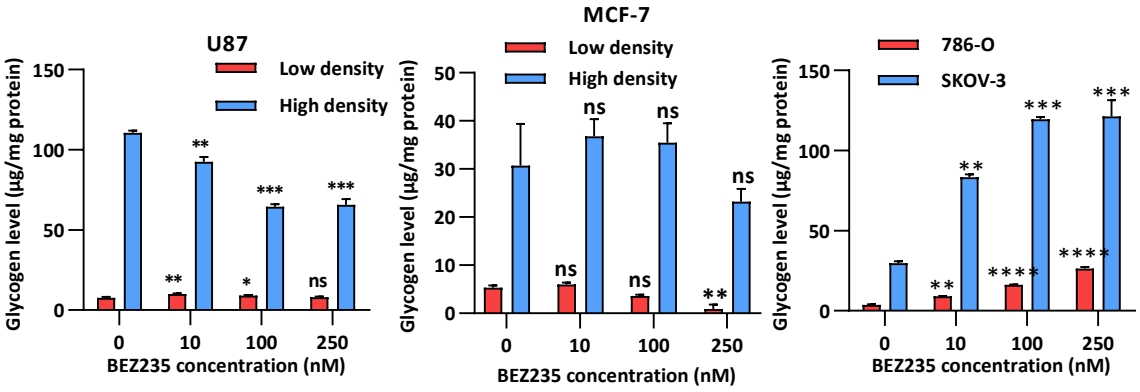


**Figure 4.10 BEZ235 has diverse effects on total glycogen accumulation in U87, MCF-7, 786-O and SKOV-3 cells.**

Cells were treated with BEZ235 at indicated concentrations for 24 h prior to glycogen assay. Significant difference was described as * $p < 0.05$, ** $p < 0.01$, *** $p < 0.001$ and **** $p < 0.0001$.

**BEZ235 inhibits glucose uptake measured by [$^{18}$F]FDG**

The effect of BEZ235 on glucose utilization was then assessed by using the standard radiotracer [$^{18}$F]FDG, as it might explain why cells have diverse profiles of glycogen metabolism. The results of *in vitro* uptake (Figure 4.11) showed that BEZ235 at indicated concentrations substantially impaired [$^{18}$F]FDG uptake across all cell lines. This inhibition was

in a dose-dependent manner at the low concentration ranges of BEZ235 (0-100 nM), with a plateau level observed at 100 nM across all cells. Despite similar patterns observed, the retention of radioactivity was higher in U87 cells when cultured at high density compared to low density at each drug concentration accordingly. [$^{18}$F]FDG uptake was reduced by almost 50% in 786-O cells when treated with 100 nM BEZ235 (10.94% ± 0.29% ID/mg protein) in comparison with control cells (20.85% ± 0.80% ID/mg protein). More significantly, BEZ235 at 100 nM resulted in a corresponding 3.4-fold reduction in [$^{18}$F]FDG uptake in SKOV-3 cells when compared with cells incubated in the absence of BEZ235 (9.13% ± 0.07% ID/mg protein, respectively).

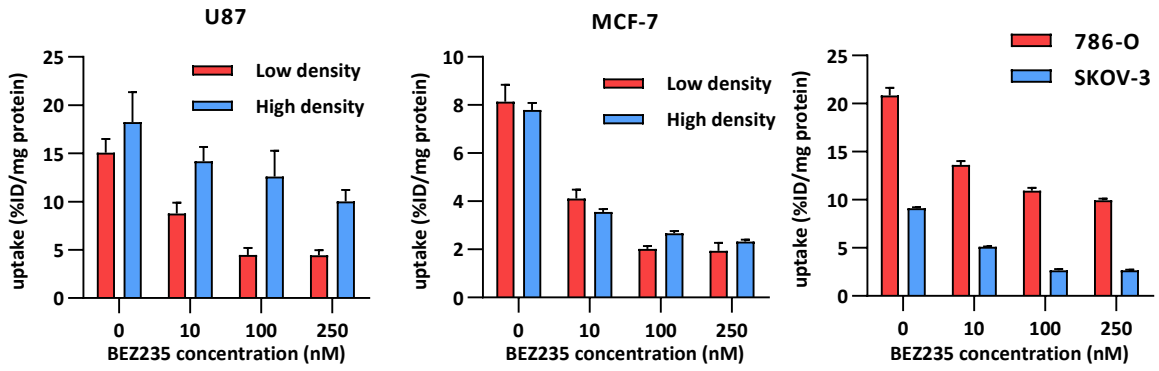


| One-way ANOVO Multiple Comparison Test | Summary |
|---|---|
| U87-L 0 vs U87-L 10 | **** |
| U87-L 0 vs U87-L 100 | **** |
| U87-L 0 vs U87-L 250 | **** |
| U87-H 0 vs U87-L 10 | ** |
| U87-H 0 vs U87-H 100 | *** |
| U87-H 0 vs U87-H 250 | **** |

**Figure 4.11 The effects of BEZ235 on [$^{18}$F]FDG uptake.**

Following 24 h BEZ235 treatment, cells were incubated with fresh media containing 0.74 MBq [$^{18}$F]FDG for 1 h. Mean values ± SD (n=6). Statistically significant difference was analysed by one-way ANOVO test and compared to respective control: $^{**}$ $P < 0.01$, $^{***}$ $P < 0.001$, $^{****}$ $P < 0.0001$.

### 4.1.4 Discussion

PI3K pathway is responsible for many cell cascades such as cell growth, proliferation and apoptosis [258]. As mentioned, PI3K signalling also plays a crucial role in regulation of GYS

activity. Therefore, inhibition of PI3K by BEZ235 provides the possibility to investigate how glycogenesis is modulated when cells stop dividing.

The calculated $GI_{50}$ values of BEZ235 (Figure 4.4) were in a low nanomolar range across all tested cancer cell lines including U87, IGROV-1, 786-O, MDA-MB-231, SKOV-3 and MCF-7, suggesting a profound effect of BEZ235 on inhibiting cell progression. Among them, the growth of tumour cells with PTEN null (U87, IGROV-1 and 786-O) was more effectively inhibited by the inhibitor. Consistent with previous studies, triple-negative breast cancer cell line MDA-MB-231 with k-RAS mutation was less sensitive to BEZ235. This might because ERK pathway in the presence of excessive k-RAS expression may partially compensate for the diminished activity of PI3K/AKT upon BEZ235 treatment [247]. Additionally, MCF-7 and SKOV-3 cells harbouring PI3KCA mutation responded moderately to BEZ235 treatment; it is possible that these mutations do not interfere with the ATP pocket, in which the drug reversibly binds.

Furthermore, by western blotting it was shown that BEZ235 effectively inhibited the phosphorylation of Akt at S473, particularly in the most sensitive cell lines (IGROV-1, 786-O and U87). A consistent decrease in GYS1 activity was observed in the cell line panel. Nevertheless, the GSK3αβ activity was slightly decreased as shown by increased pGSK3αβ/GSK3αβ ratio or remained unchanged in several cell lines. These observations revealed a contradictory regulation mechanism of Akt on GYS1 activity through Akt/GSK3αβ/GYS1 signalling cascade. The possible reason might be distinct from Akt; GSK3αβ is subjected to multiple regulatory mechanisms such as multiple kinases. For example, cAMP-dependent protein kinase A (PKA) also controls the activity of GSK3 in mammalian cells in parallel. More specifically, PKA associates with, phosphorylase and inactivates both isoforms of GSK3 [259; 260]. Consistently, dramatically increased phosphorylation of GYS1 by BE235 might also be explained by cAMP-dependent PKA cascade, as this is another well-established mechanism responsible for GYS1 phosphorylation in addition to GSK3-mediated regulation [142]. As discussed in **Chapter 3** that intracellular G6P level is a crucial regulator of GYS1 activity, it is inferred that BEZ235-induced inhibition of GYS1 could partially be a result of decreased G6P concentration in the investigated cancer cells. Although the effect of BEZ235 on G6P level remains unclear, other PI3K/mTOR inhibitors such as Gedatolisib (PKI-587) have been found to decrease the concentration of G6P in a non-small cell lung cancer cell line H1975 [261; 262]. Consistently, the presented observation, which is the reduction of [$^{18}$F]FDG

uptake following BEZ235 treatment in U87, MCF-7, 786-O and SKOV-3 cells, was indirectly in support of the hypothesis.

Consistent with the decreased GYS1 activity, the total intracellular glycogen level was reduced following BEZ235 treatment in U87, IGROV-1 and MCF-7 cells, whereas the inhibitor caused an elevation in glycogen accumulation in 786-O and SKOV-3 cells. The increased glycogen contents appeared to preliminarily fulfil the hypothesis that enhanced glycogenesis is a potential biomarker of drug-induced senescence. Therefore, further evaluation was conducted to assess whether BEZ235 induces senescence and how this is linked to glycogenesis modulation in the representative cell lines.

BEZ235 treatment resulted in a robust G0/G1 growth arrest in a dose-dependent manner across U87, MCF-7, 786-O and SKOV-3 cells. Similar results have been previously reported that BEZ235 suppresses tumour proliferation through triggering cell cycle arrest [263]. Use of β-galactosidase assay, which is a routinely used biomarker of senescence, however, showed no signs of senescence induction upon BEZ235 treatment. The low β-galactosidase activity, together with an unchanged p21 level measured by western blot, suggested that cell cycle arrest mediated by BEZ235 is a reversible event (also termed quiescence), but not irreversible (senescence). Although BEZ235 appeared not to trigger senescence in this study, several studies have shown that BEZ235 radiosensitizes several cancer cells such as non-small-cell lung carcinoma, prostate cancer and a U87-tumour bearing mice model [254; 264; 265] through induction of senescence. The increased cellular radiosensitivity by BEZ235 is associated with downregulation of DNA-PK, which in turn impairs DNA damage repair via the non-homologous end joining (NHEJ) pathway.

Further studies were carried out to explore how glycogenesis is modulated upon inhibition of PI3K/AKt pathway by BEZ235, as it remains unclear to what extent pharmacological targeting of PI3K pathway would impact glycogen accumulation. Western blot analysis confirmed that BEZ235 dose-dependently inhibited the phosphorylation of Akt at S473 site and the activity of GYS1 across the four cell lines. Consistent with decreased GYS1 activity, U87 and MCF-7 cells displayed reduced total glycogen accumulation, whereas there was an increase in 786-O and SKOV-3 cells. The reason why PI3K-mediated GYS1 inhibition by BEZ235 did not translate into glycogen level in 786-O and SKOV-3 cells remains unclear. One

of the possibilities could be the relative contributions of GYS1 and PYGL on glycogen level in the two cell lines, as shown in Figure 4.9C, subtle decrease of PYGL in 786-O and SKOV-3 might largely impair glycogen degradation which overwhelm any negative effects on glycogen synthesis associated with decreased GYS1 activity following BEZ235 treatment. Besides, expression of endogenous HIF-α, in 786-O cell line [244] induced by VHL defects (Section 3.5) and in SKOV-3 cells triggered by Rab25 expression [266; 267], might sensitize glycogen synthesis in an insulin-dependent manner. It has been found that HIF-α impacts insulin signalling pathway and further other genes involved in metabolic events such as glycolysis and lipid metabolism [268] In pancreatic cancer cell line MiaPaCa2. Although insulin-induced IR expression is independent of HIF-α, the gene is still required for insulin to increase HK-II and VEGF expression, which further contributes to metabolic regulation [269; 270]. Here, 786-O and SKOV-3 cells harbouring HIF-α genes might be more sensitive to insulin-induced glycogen synthesis directly via glucose in comparison with HIF-null cells (U87 and MCF-7). Another explanation for the enhanced glycogen level under decreased GYS1 activity condition was perhaps a consequence of increased gluconeogenesis via PI3K pathway that provides substrates for glycogenesis. Gluconeogenesis is, to some extent, regarded as the reverse reaction of glycogenesis, which results in the generation of glucose from smaller carbon substrates such as lactate or amino acids [271; 272]. The rate of gluconeogenesis is majorly controlled by the action of three key enzymes, including phosphoenolpyruvate carboxykinase (PEPCK) which converts oxaloacetate to phosphoenolpyrute, fructose 1,6-bisphosphatase (FBPase) which converts fructose 1,6-bisphosphate to fructose 6-phosphate, and glucose-6-phasphatase (G6Pase) which turns glucose-6-phasphate to glucose [271]. Among them, FBPase is the rate-limiting enzyme that is regulated through signal transduction by cAMP and its phosphorylation [271]. Although it remains unknown whether the activity of FBPase is upregulated in 786-O and SKOV-3 under BEZ235 treatment, FBPase activity has been found to be positively correlated with the expression of HIF-α in clear cell renal cell carcinomas [273]. Possibly, HIF-α expression in 786-O and SKOV-3 cells enhances the activity of FBPase, which further contributes to the conversion of fructose 1,6-biophoaphate to fructose 6-phosphate, eventually leading to increased G6P level. This elevated G6P via gluconeogenesis in 786-O and SKOV-3 cells then flux into glycogen; while in the other cells as discussed above G6P level is reduced and not available for fluxing into glycogen.

Concerning other metabolic processes, glucose consumption measured by [$^{18}$F]FDG uptake was strikingly reduced upon BEZ235 treatment. This response may be due to a BEZ235-mediated inhibition on the activity or translocation of glucose transporter and hexokinase, which in turn suppresses glucose uptake.

In summary, BEZ235 effectively inhibited cell proliferation, G0/G1 cell cycle arrest, and triggered distinct alterations in GYS1 activity as measured by western blot and total glycogen level in the tested cancer cell line panel in a lineage specific. Additionally, BEZ235 inhibited [$^{18}$F]FDG uptake in a dose-dependent manner, suggesting that inhibition of PI3K by BEZ235 plays a crucial role in regulating metabolic changes.

## 4.2 Targeting AMPK pathway as a regulator of senescence/quiescence and glycogenesis in a panel of cancer cell lines

### 4.2.1 Introduction

Metformin (1,1-dimethylbiguanide), which was initially used as an anti-type II diabetes drug, exerts functions through decreasing hepatic glucose production and intestinal glucose absorption, and improving insulin sensitivity by increasing peripheral glucose uptake and utilization. It has been found that patients with type II diabetes when treated with metformin have a reduction in cancer incidence and cancer-related mortality [274] compared to those treated with other antidiabetic agents. The inhibitory effects of metformin on tumours are increasingly being explored as a therapeutic option for a variety of cancer types [275].

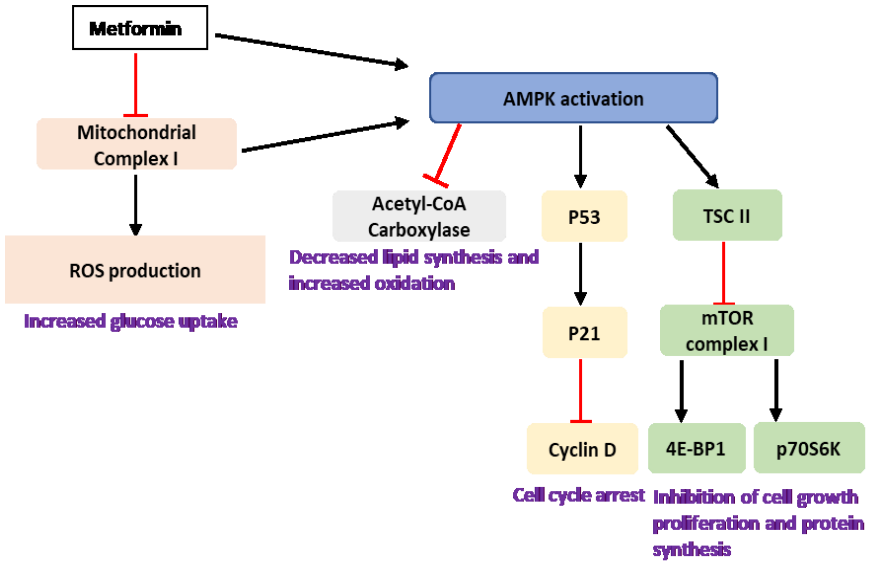


**Figure 4.12 The mechanisms of anticancer action of metformin.**

The molecular mechanisms of metformin involve both indirect and direct effects. The indirect functions are regulated in an insulin-dependent manner, which results in reduced circulating insulin levels and the neoplastic cell proliferation via insulin/IGF-1 pathway. The direct regulation is through activation of AMPK, which facilitates catabolic pathways such as glucose uptake from circulation and fatty acid oxidation to generate more ATP, and inhibits anabolic pathways that utilize energy. [Adapted from Andrzejewski., et al]

The molecular mechanisms of action of metformin is believed to involve both indirect and direct effects [276]. The indirect functions, which are regulated in an insulin-dependent manner, reduce circulating insulin levels, thus reducing the neoplastic cells proliferation via insulin/IGF-1 pathway. Direct regulation starts with inhibition of mitochondrial complex I,

which in turn results in decreased ratio of ATP to AMP [277]. To maintain cellular hemeostasis in response to reduced ATP/AMP, AMPK, as one of the master regulators of cellular metabolism, gets activated and facilitates catabolic pathways such as glucose uptake from circulation and fatty acid oxidation to generate more ATP, and inhibit anabolic pathways that utilize energy. AMPK activation inhibits the mTOR pathway via phosphorylation of TSC1/2, which leads to inhibition on cell cycle progression, cell proliferation and protein synthesis. Metformin-mediated AMPK activation also inhibits acetyl-CoA carboxylase (ACC) and fatty acid synthase (FASN), thereby preventing lipid synthesis. Besides, AMPK activation in response to metformin also results in increased activity of p53 that promotes cell apoptosis, autophagy and cell cycle arrest [278]. Most recently, it has been found that metformin also exerts anti-inflammatory and anti-angiogenic effects by decreasing the production of inflammatory factors, including tumour necrosis factor alpha (TNFα), IL-6 and IL-1β, and inhibiting NF-kB and HIF-1α which in turn suppresses the production of vascular endothelial growth factor (VEGF) [279].

The effects of metformin on inducing cellular senescence has been controversial. Although one study has shown that low doses of metformin induced senescence in liver cancer cells in a p53-dependent manner [280], most of the studies reported negative regulation of metformin on senescence [281-283]. For example, Moiseeva et al. reported an inhibition of senescence-associated secretory phenotype by metformin via IKK/NF-kB activation [281].

Considering AMPK as a crucial sensor of cellular metabolism, we speculated that metformin would also affect glycogen metabolism when AMPK is activated. The AMPK-dependent regulation of glycogen has long been a paradox [284]. Glycogen synthase has been found to be inhibited via the acute activation of AMPK, which results in glycogen degradation in skeletal muscle cells [285]. However, the chronic activation of AMPK by 5-aminoimidazole-4-carboxamide ribonucleoside (AICAR) has been shown to facilitate glucose uptake and lead to muscle glycogen synthesis [286]. Accordingly, the constitutive activation of AMPK via mutations in the γ2 and γ3 subunits has been associated with glycogen storage in the skeletal and cardiac muscles of pigs and mice [287]. It is, therefore, of great interest to explore how glycogen metabolism is regulated in tumours in response to metformin treatment.

Here, we evaluated the effects of metformin on cell growth inhibition, cell cycle arrest and senescence induction in several cancer cell lines and explored how glycogen metabolism changes in response to treatment.

### 4.2.2 Growth inhibition of metformin in a panel of cancer cell lines

Metformin-induced growth inhibition was studied across the same cell line panel under the same growth conditions as for BEZ235 treatment. Metformin significantly inhibited the proliferation of U87, MDA-MB-231, MCF-7 and IGROV-1 cells, particularly in cells when grown at high density. SKOV-3 and 786-O cells had a poorer response to metformin under both growth conditions, whose $GI_{50}$ was 18.18 ± 3.61 mM at low density and 22.57 ± 5.73 mM at high density in SKOV-3 cells, 24.91 ± 1.66 mM and 34.23 ± 2.78 mM in 786-O cells at each seeding density, respectively.

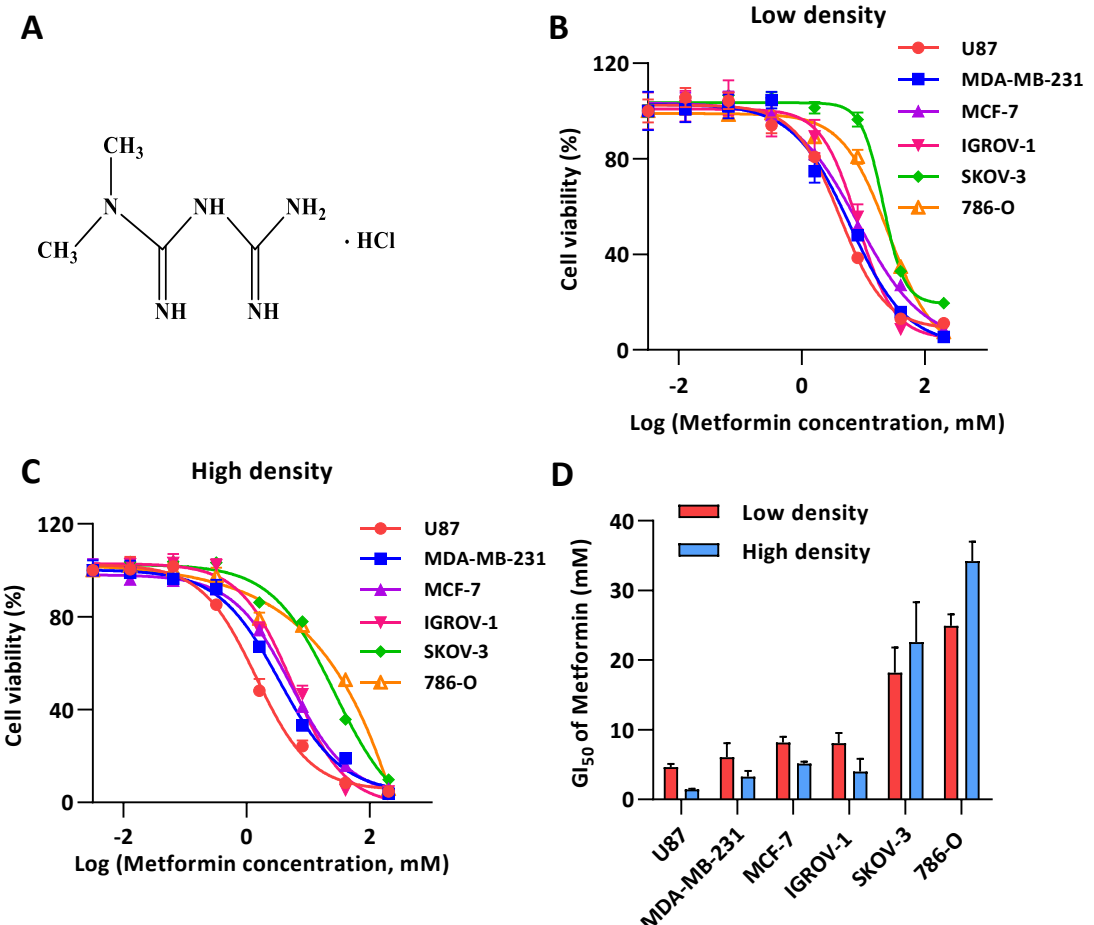


**Figure 4.13 $GI_{50}$ determination for metformin in a panel of cancer cell lines.**

**A,** Chemical structure of metformin. **B,** Representative dose response curve of each cell line at low seeding density ($5 \times 10^3$ cell/well). **C,** Representative dose response curve of each cell line at high seeding density ($1.5 \times 10^4$ cells/well). Each dose response curve was an example from three independent experiments which were performed in triplicates. **D,** Average $GI_{50}$ values in tested cell lines. Mean values ± SD (n=3).

### 4.2.3 Metformin at a high concentration induces a G0/G1 cycle arrest and subtly increases β-galactosidase activity in MCF-7 cell line

MCF-7 cell line was further studied because of its high sensitivity to metformin as shown in initial $GI_{50}$ assay. Here, to determine whether metformin could trigger cell senescence, cell cycle analysis and SA-β-gal staining were performed. Metformin at 50 mM induced a G0/G1 cycle arrest (Figure 4.14). Consistently, metformin dose-dependently increased the total numbers of SA-β-gal blue-stained MCF-7 cells (Figure 4.15), with the most remarkable increase observed in cells treated with 50 mM metformin.

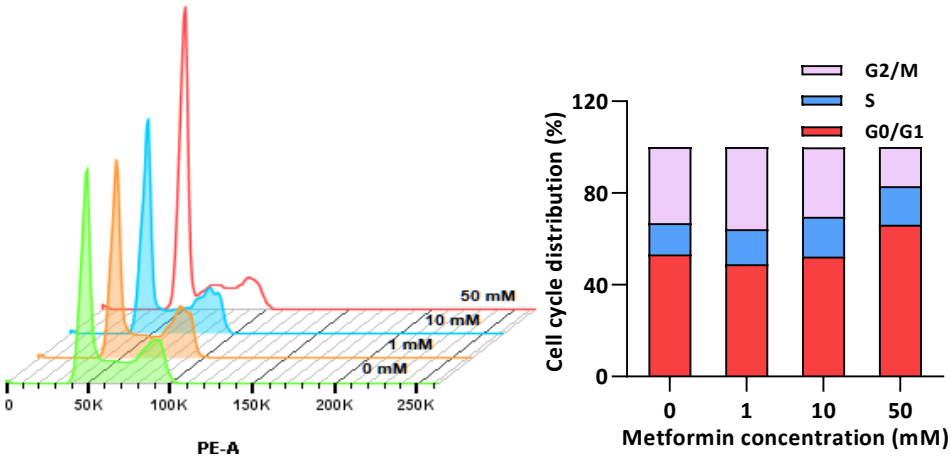


**Figure 4.14 The effects of metformin on cell cycle modulation**.

Cells were treated with metformin for 24 h. Cell cycle analysis was performed by FACS using PI staining.

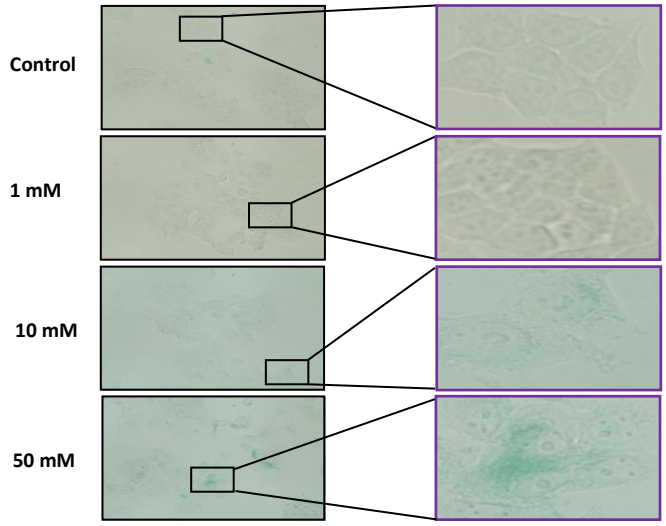


**Figure 4.15 Metformin slightly induces an increase in SA-β-gal activity in MCF-7 cells after 24 hours of metformin treatment.**

Images were obtained under × 400 magnification on a standard microscope.

### 4.2.4 Metformin reduces glycogen accumulation in a GYS1-independent manner

It was then investigated, whether metformin has effects on modulation of glycogen mobilization. As shown in Figure 4.16A, an approximately 10-fold reduction in glycogen was found following exposure of MCF-7 cells to 10 mM metformin, in comparison with vehicle-treated cells (28.46 ± 3.31 μg/mg protein in control vs. 2.38 ± 2.11 μg/mg protein at 10 mM). However, a higher concentration of metformin at 50 mM led to a subtle increase in glycogen to 9.89 ± 8.63 μg/mg protein. A similar pattern was observed in another breast cancer cell line MDA-MB-231 (Figure 4.16B), where low concentrations of metformin inhibited glycogen storage, from 3.09 ± 4.19 in control cells to 0.05 ± 0.01 μg/mg protein at 10 mM metformin, while 50 mM slightly increased glycogen to 1.08 ± 1.15 μg/mg protein cells. 2-NBDG fluorescence microscopy was further carried out to complement with glycogen assay in profiling dynamic glycogen mobilization during a shorter period (3 hours). Consistently, metformin was found to subtly decrease 2-NBDG fluorescence intensity in MCF-7 cells in a dose-dependent manner.

To explore how metformin regulates glucose consumption, *in vitro* [$^{18}$F]FDG uptake was assessed in MCF-7 cells following treatment (Figure 4.16C). In contrast to decreased glycogen contents, the inhibitor substantially promoted [$^{18}$F]FDG retention in MCF-7 cells, with the highest accumulation observed at 10 mM metformin. A reduction in uptake was observed in cells treated with 50 mM metformin, compare to that at 10 mM.

Taken together, although metformin facilitated glucose uptake as determined by [$^{18}$F]FDG in MCF-7 cells, glycogen accumulation was significantly suppressed by metformin at concentrations < 10 mM.

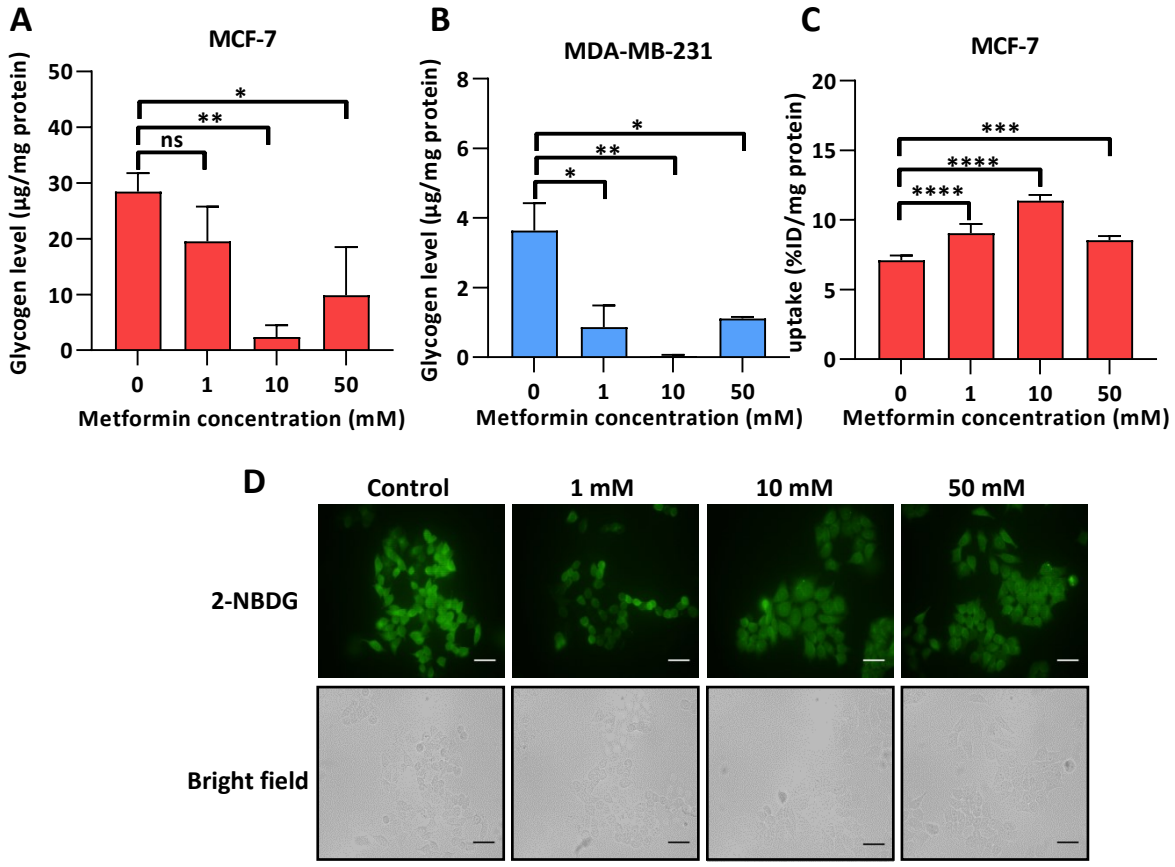


**Figure 4.16 Metformin diminishes glycogen accumulation and facilitates glucose uptake in MCF-7 cells.**

**A,** Total glycogen level in MCF-7 cells. **B,** Total glycogen level in MDA-MB-231 cells. Mean values ± SD (n=3). **C,** *In vitro* $^{18}$F-FDG uptake in MCF-7 cells. Mean values ± SD (n=6). Statistically significant difference was analysed and compared to untreated control group: * $p < 0.05$, ** $p < 0.01$, *** $p < 0.001$, **** $p < 0.0001$. **D,** Intracellular 2-NBDG uptake in MCF-7 cells. Cells were treated with metformin for 24 h at indicated concentrations prior to various assays. Scale bar = 50 µm.

To further examine the mechanism underlying decreased glycogen storage, western blot analysis was performed to check protein expression upon metformin treatment. Western blot analysis revealed an elevation of total GYS1 levels in MCF-7 and MDA-MB-231 cells when treated with metformin < 10 mM, whereas GYS1 expression was inhibited by a higher dose of metformin at 50 mM. The level of phospho-GYS1 was initially decreased at low drug concentrations (<10 mM), followed by an increase at 50 mM of metformin. GYS1 activity as determined by the ratio of phospho-GYS1 to total GYS1 was significantly increased in both cells when treated with 1 and 10 mM of metformin, while metformin at 50 mM led to a lower

increase in GYS1 activity when compared to low concentrations. Besides, metformin did not affect the levels of PYGL.

Two cell cycle-related proteins p21 and cyclin D1 were also determined. Metformin at 50 mM effectively increased p21 expression in MCF-7 cells, while cyclin D1 level was significantly reduced when treated with 10 mM and 50 mM metformin. In contrast, MDA-MB-231 showed no changes in the expression of p21 and cyclin D1 proteins between control and treated cells.

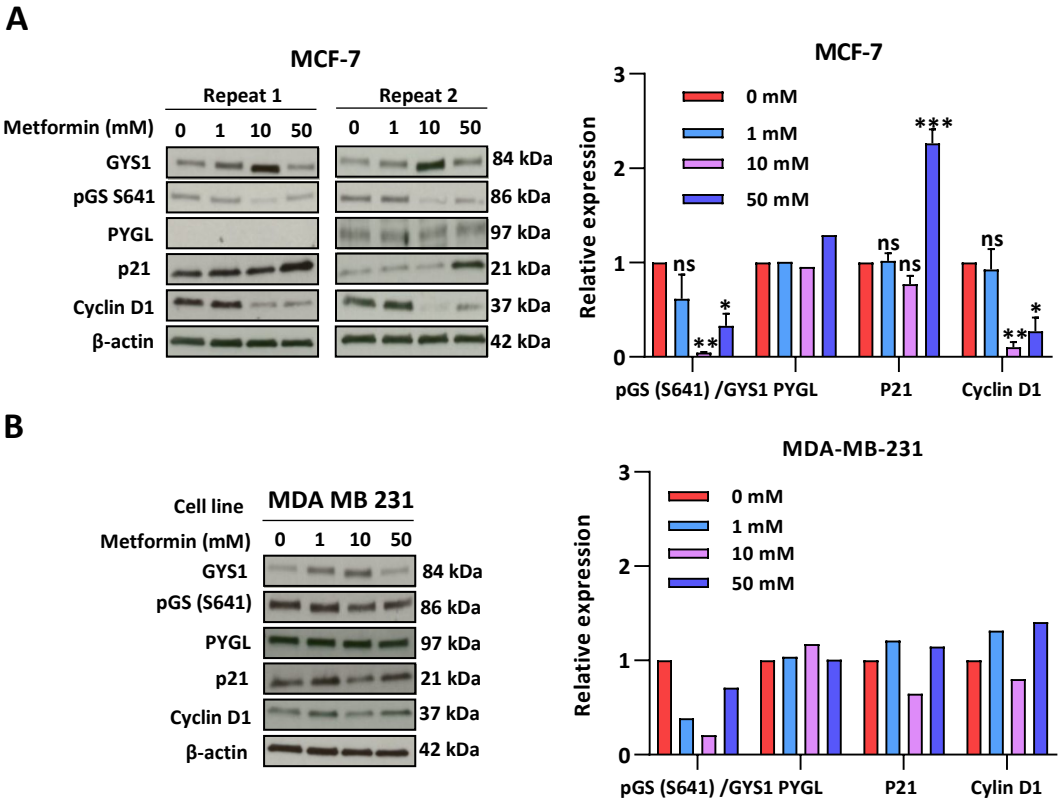


**Figure 4.17 Metformin decreases GYS1 activity determined by western blot.**

**A,** Western blot for MCF-7 cells and quantification by using ImageJ. **B,** Western blot for MDA-MB-231 cells and quantification by using ImageJ (one experiment). Optical density of individual signals was normalised to β-actin and respective control as indicated. * $p < 0.05$, ** $p < 0.01$ and *** $p < 0.001$ indicate significant difference from the value measured in control untreated group.

### 4.2.5 Metformin also facilitates glycogen degradation

Having found a lack of correlation between total glycogen accumulation and GYS1 activity, we attempted to understand whether metformin acts as a positive regulator of glycogen breakdown that results in substantial reduction in glycogen contents despite an increased

GYS1 activity. To this end, the study was carried out on a genetically modified U87 cell line which harbours PYGL deletion by shRNA and its parental cell line U87 shCtrl [150] (both cell lines were kind gifts of Prof. Adrian Harris, University of Oxford).

The growth inhibition by metformin was first compared between the two cell lines. $GI_{50}$ assay (Figure 4.18) showed that cells with PYGL knockdown displayed less sensitivity to metformin treatment when grown under exponential growth phase, with $GI_{50}$ value of 7.21 ± 0.95 mM in U87 shCtrl and 13.22 ± 1.09 mM in U87 shPYGL cells, respectively. Both cells showed higher sensitivity to metformin when seeded at high density.

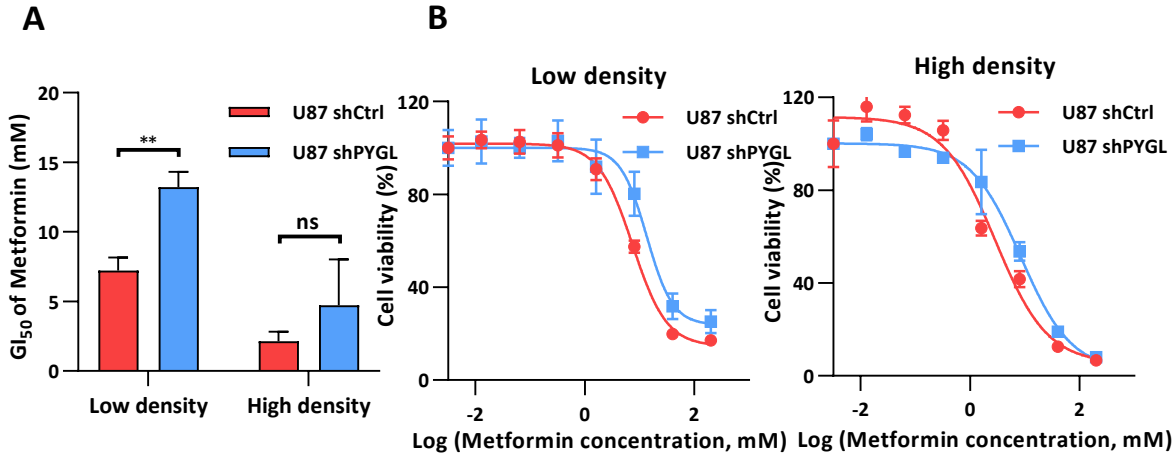


**Figure 4.18 Comparison of $GI_{50}$ values between U87 shCtrl and U87 shPYGL cells.**

**A,** $GI_{50}$ values in the two cell lines. Mean values ± SD (n=3). Significant difference is defined by ** $p < 0.01$. **B,** Representative dose response curve at low ($5 \times 10^3$ cell/well) and high seeding density ($1.5 \times 10^4$ cells/well), respectively. Each dose response curve was an example from three independent experiments which were performed in triplicates.

Western blot analysis (Figure 4.19A) showed a 70% PYGL knockdown in PYGL shRNA cells in comparison with controls. Upon low-concentration metformin treatment, PYGL expression was increased in both empty control vector and PYGL knockdown cells. Metformin at 1 and 10 mM induced an increase in GYS1 activity as determined by a decreased ratio of phospho-GYS1 to GYS1 in both cell lines, which is consistent with previous observations for MCF-7 and MDA-MB-231 cells. P21 was subtly increased in both cell lines, whereas total cyclin D1 was inhibited by metformin. Hexokinase, which phosphorylates glucose to produce G6P, was increased in control cells following low concentrations of metformin, while the expression was slightly decreased in PYGL-knockdown U87 cells.

Total intracellular glycogen level was then evaluated by using glycogen assay. PYGL silencing resulted in a corresponding 4-fold increase in basal glycogen storage when compared to parental cell line, at 56.41 ± 1.60 µg/mg protein and 14.50 ± 2.57 µg/mg protein, respectively. Exposure of cells to metformin for 24 hours induced a dose-dependent inhibition of total glycogen contents in both cell lines.

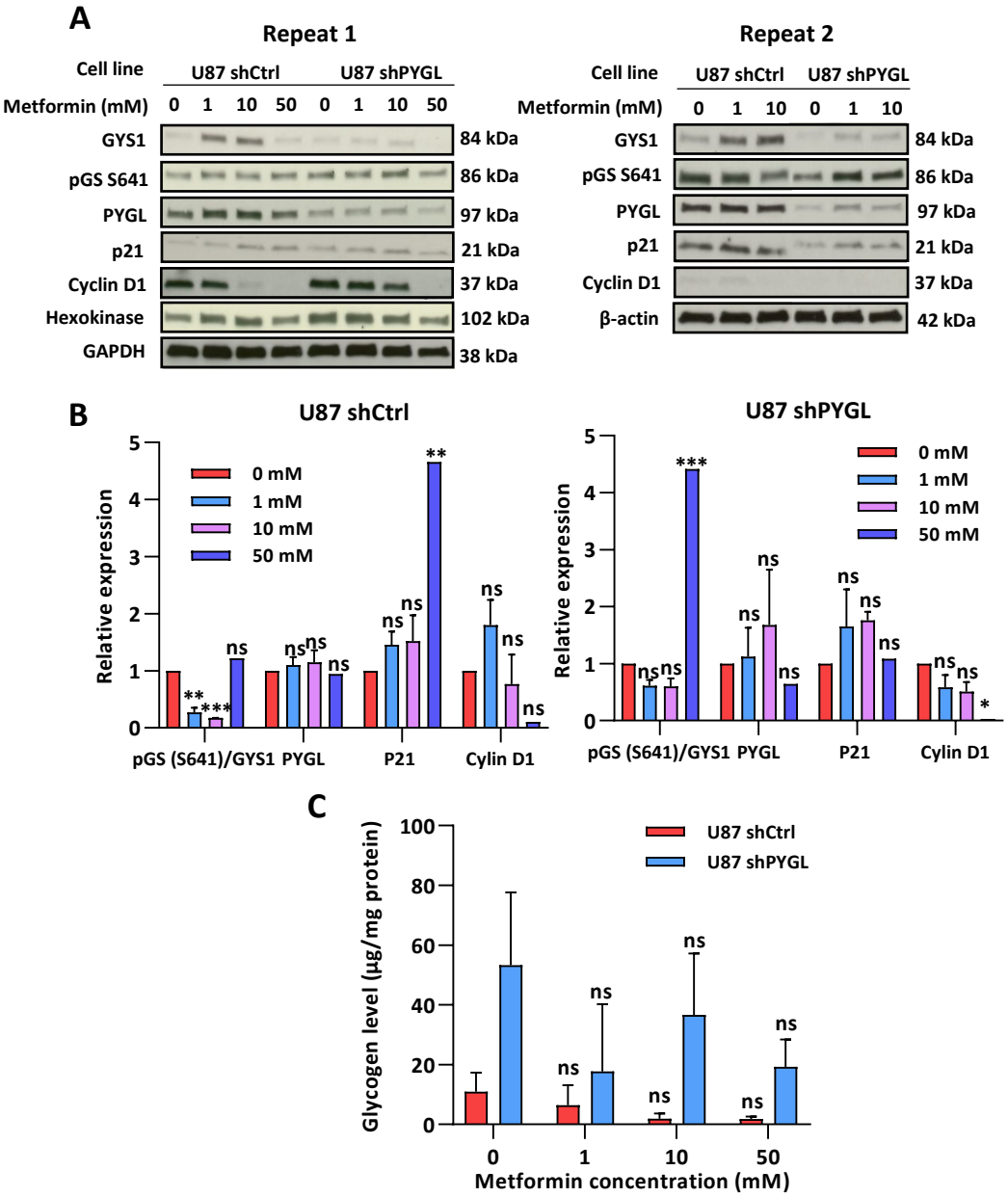


**Figure 4.19 The effects of metformin on glycogen metabolism in U87 shCtrl and U87 shPYGL cell lines.**

**A,** Western blots for the two cell lines. **B,** Quantification of western blot, optical density was normalized to GAPDH or β-actin and respective control by using ImageJ. **C,** Total glycogen level following metformin treatment. Statistically significant difference is defined by * $p < 0.05$, ** $p < 0.01$ and *** $p < 0.001$.

Collectively, metformin < 10 mM dose-dependently increased GYS1 activity and total PYGL expression in both cell lines regardless of PYGL status, suggesting that metformin might facilitate both synthesis and degradation of glycogen. The total glycogen level as determined by glycogen assay was slightly decreased in both cell lines, possibly resulting from the difference in the rate of glycogenesis and glycogenolysis.

### 4.2.6 Discussion

In this section, we sought to explore if metformin could induce senescence-related growth arrest, and how this is related to glycogenesis in several cancer cells *in vitro*. It was shown that cell lines including U87, MDA-MB-231, MCF-7 and IGROV-1 displayed more profound response to metformin compared to SKOV-3 and 786-O cells. Interestingly, all tested cells when cultured under confluent condition with low proliferation rate showed higher sensitivities to metformin in comparison with cells under sub-confluent condition. This observation is, however, contradictory to documented evidence that majority of treatment strategies, including chemotherapy and targeted therapies, target the bulk of the tumour with a proliferative phenotype, whereas slow-cycling cancer cells may be left unchanged. Lower sensitivity of slow-cycling cells has been regarded as one of the leading causes of treatment resistance in cancer cells which eventually trigger cancer relapse [288-290]. Given the fact that metformin alters mitochondrial substrate utilization and re-route metabolic flux, it is possible that sensitivity of cancer cells to metformin is largely associated with cellular energy homeostasis and metabolic features. Proliferative cancer cells shift their metabolism toward aerobic glycolysis (Warburg effect) to rapidly produce ATP which is required for uncontrolled cell division and biomass accumulation, whereas slow-cycling cells under confluent condition have been shown to feature a high level of oxidative phosphorylation [291]. Cancer cells that have a high reliance on oxidative phosphorylation as a source of ATP are thought to be more sensitive to metformin treatment because mitochondrial respiration is rapidly diminished upon the direct inhibition of mitochondrial complex I by metformin [276]. Metformin-mediated targeting of slow-cycling cells might be a way to relieve multidrug resistance caused by tumour heterogeneity, thereby serving as a combination treatment with other drugs for anti-cancer therapies. With regards to U87 cells, we originally hypothesized that cells with

PYGL knockdown would show a higher sensitivity to metformin due to lack of flexibility to efficiently fulfil glycolysis. However, $GI_{50}$ assay revealed a weaker response of U87 shPYGL cells to metformin in comparison with parental U87 shCtrl cells.

One of the aims of this section by using metformin is to test if this drug could trigger cellular senescence in tumour cells *in vitro*, which might serve as an alternative mechanism of action of metformin as an anti-cancer drug. However, it seems that metformin at concentration <10 nM, which is the commonly used concentration range of metformin *in vitro*, did not induce cellular senescence in MCF-7 cells, as shown by unchanged p21 levels and the absence of SA-β-gal activity. A higher concentration of metformin (50 mM), despite slightly increasing SA-β-gal activity, might be an off-target effect of metformin in this context. In one single study, the exact mechanism by which metformin triggered senescence in hepatoma cells is not clear, but it appears to be associated with p53 stabilization that is regulated by AMPK through relieving the inhibitory effect of SIRT1 on p53 acetylation [280].

Next, the study was focused on understanding of how metformin alters the metabolic features of cancer cells. Direct inhibition of mitochondrial complex I by metformin in cells decreases the proton gradient and mitochondrial oxygen consumption rate, diminishes tricarboxylic acid cycle (TCA) activity and metabolites, and eventually leads to decreased cellular ATP levels [274]. Cancer cells compensate for these metformin-mediated effects by increasing glucose uptake and glycolysis, and switching to glutamine utilization, as a way of refuelling the TCA and providing biosynthetic intermediates for lipid production required to synthesize membranes. In agreement with these facts, there was an increased glucose uptake determined by [$^{18}$F]FDG in MCF-7 cells upon metformin treatment (<10 mM) and elevated hexokinase expression in both parental U87 and U87 cells with PYGL deletion. Similarly, it has been reported that treatment of HCC cells with metformin also results in intracellular accumulation of [$^{18}$F]FDG both *in vitro* (3.5 fold) and *in vivo* (5 fold), via a process that leads to decreased G6Pase expression and is controlled by the AMPK-Akt-4EBP1 pathway and FOXO1 transcriptional factor [292].

Although several studies have indicated that glycogen metabolism in hepatic cells are affected by metformin [293], this link is less understood in cancer cells. It was found that exposure of cancer cells to low doses of metformin (<10 mM) significantly increased the

expression of total GYS1 as well as a subtle decrease in phospho-GYS at Ser641 site. This trend, however, is not consistent with the observation that AMPK inactivates GYS1 by phosphorylation of this enzyme. It is likely that metformin favourably phosphorylates GYS1 at Ser7 site, but not Ser641 measured in this study [294]. Total glycogen accumulation was dramatically reduced upon metformin-mediated AMPK activation. Otto et al. [295] has reported that low and clinically relevant concentrations of metformin inhibits glycogen synthesis and gluconeogenesis in rat hepatocytes possibly through suppressing the respiratory chain as the two events are energy-demanding processes. In addition to affect glycogenesis, metformin possibly facilitates glycogen degradation as increased PYGL was observed in this study, which might lead to a reduction in the accumulation of glycogen.

To summarize, it was shown that metformin effectively inhibited proliferation of a wide range of cancer cells, confirming its role on tumour inhibition. Metformin treatment in MCF-7 cells facilitated glucose uptake and suppressed glycogen accumulation possibly through upregulation of glycogen degradation. These observations are in support of the fact that metformin upregulates AMPK, leading to metabolic changes in cells via facilitating catabolic pathways and inhibiting anabolic events.

## 4.3 Targeting CDK4/6 as a regulator of senescence/quiescence and glycogenesis in ER-positive cancer cell lines

### 4.3.1 Introduction

The aberration in cell cycle signalling, including upregulation of positive regulatory proteins (cyclins and CDKs) or downregulation of negative regulatory proteins (p16, Rb and p53), is a key hallmark of cancer cells, resulting in uncontrolled cellular proliferation and tumorigenesis [296]. Development of cell cycle inhibitors has long been an effective approach for anticancer therapies, among which selective CDK4/6 inhibitors such as palbociclib, ribociclib and abemaciclib have shown promising pre-clinical and clinical effects against a wide range of solid tumours [297].

Palbociclib was the first FDA-approved CDK4/6 inhibitor in 2015 and has been used for the first-line treatment of ER-positive, HER2-negative advanced breast cancer in combination with anti-estrogen therapy [298]. Palbociclib inactivates CDK4/6-cyclin D1 complex and reduces the phosphorylation of Rb protein. The decreased phospho-Rb in turn inhibits the release of E2F transcription factors from pRb-E2F complex, hence leading to the block of S-phase entry and inhibition of cell proliferation. It is noted that cancer cells with upregulated CDK4/6 pathway through loss of p16 or increased cyclin D1 expression are more sensitive to palbociclib treatment [299; 300]. In general, Rb expression may serve as a promising biomarker for either selecting patients that most likely benefit from palbociclib treatment or predicting treatment efficacy [301], although palbociclib sometimes shows activity in a small group of Rb-negative models [302].

Palbociclib is currently in phase III clinical trials with a therapeutic schedule of three consecutive weeks at a dose of 125 mg daily and one week off, in combination with endocrine therapy. Pharmacokinetic studies have revealed a rapid absorption of palbociclib, where detectable plasma concentrations of palbociclib were observed at one hour following oral administration in patients. A 26-hour half-life of palbociclib warrants the use of once-daily dosing [303-305]. Despite these promising clinical advances with palbociclib therapy, studies are needed to identify the patients who would receive the greatest benefit, evaluate possible combination treatments and diminish acquired resistance. Another aspect that requires

further investigation relates to developing accurate and appropriate biomarkers for assessment of therapeutic efficacy of palbociclib.

In this study, we examined if senescence induction could be one of the mechanisms responsible for the anticancer effects of palbociclib, and how this is related to glycogen regulation in sensitive cancer cells. To this end, two ER-positive breast cancer cell lines were assessed for cell proliferation, senescence induction, and glycogen metabolism under palbociclib treatment *in vitro.*

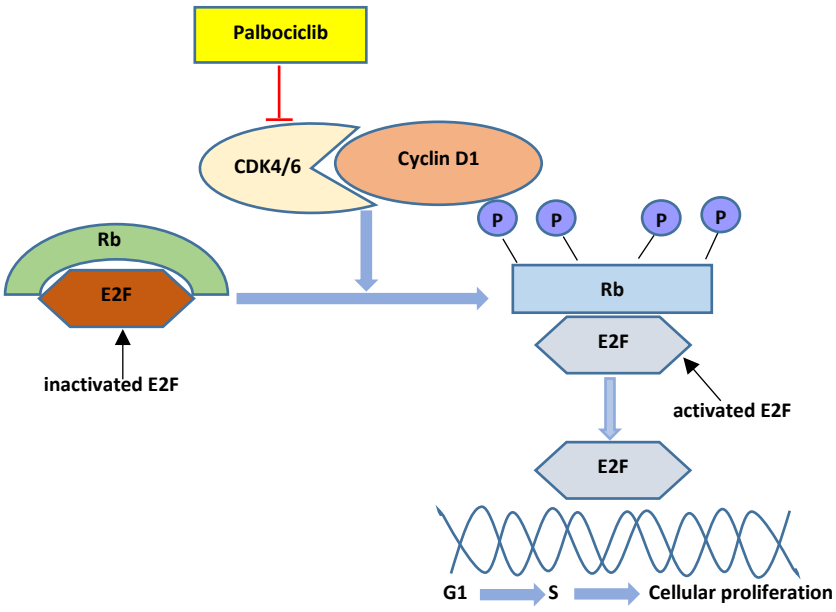


**Figure 4.20 The mechanism of action of palbociclib.**

Palbociclib induces a G0/G1 phase arrest via inactivation of CDK4/6-cyclin D1 complex and subsequent elevation of the activity of Rb, eventually leading to inhibition of the release of E2F transcription factors from pRb-E2F complex and blockage of S phase transition. [Adapted from Clark et al., 2016]

### 4.3.2 Palbociclib dose-dependently induces an irreversible G0/G1 cycle arrest

**Palbociclib effectively inhibits cell growth and causes a G0/G1 cycle arrest in two ER-positive cancer cell lines**

The growth-inhibitory potential of palbociclib was assessed in two ER-positive breast cancer cell lines MCF-7 and T47D (Figure 4.21). Both cell lines displayed high sensitivities to palbociclib treatment, with a $GI_{50}$ value of 1.42 ± 0.43 µM in MCF-7 and 7.54 ± 0.63 µM in T47D cells, respectively.

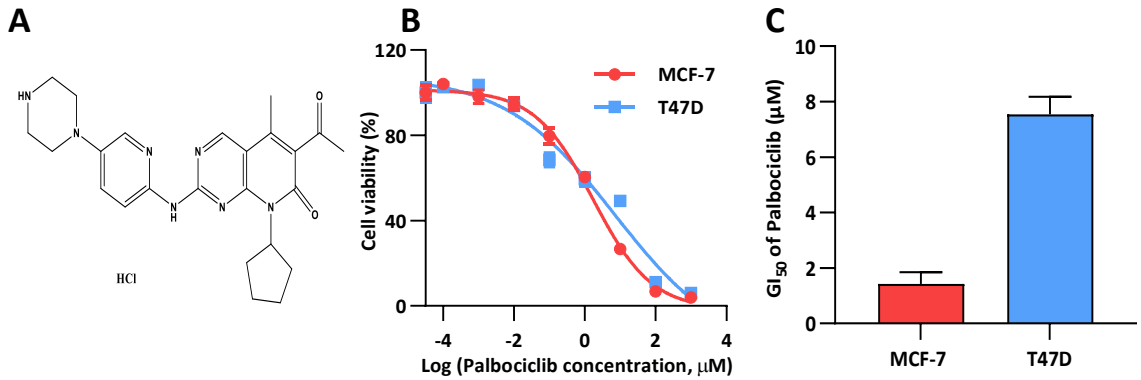


**Figure 4.21 $GI_{50}$ determination for palboiclib in two ER-positive cancer cell lines.**

**A,** Chemical structure of palbociclib. **B,** Representative dose response curve of each cell line. Cells were seeded at each appropriate density 24 h prior to treatment and incubated with palbociclib at indicated concentrations for 72 h. **C,** Average $GI_{50}$ values in MCF-7 and T47D. Mean values ± SD (n=3).

The molecular targets of palbociclib were then examined in the two cell lines by western blotting (Figure 4.22). Exposure of MCF-7 and T47D cells to palbociclib for 24 h and 72 h resulted in a dose-dependent inhibition of Rb phosphorylation as well as decrease in total Rb levels that has been previously observed in other tumour types [306; 307]. Although the mechanism of the inhibitory effect of palbociclib on total Rb level is not clear, cancer cell retention of a functional Rb protein is essential for response to palbociclib. Cyclin D1 was increased after treatment with 0.1 and 1 µM of palbociclib, followed by a substantial reduction at 10 µM. Bollard [308] and Comstock [297] et al. observed a similar increase in cyclin D1 levels in hepatocellular and prostate cancer cell lines following palbociclib treatment. By applying co-immunoprecipitation analyses, they suggested that elevated cyclin D1 might be due to a stabilization of the inactive cyclin D1-CDK4/6 complex which in turn leads to attenuation of the turnover of cyclin D1 by palbociclib. Another tumour suppressor protein p21 was dose-dependently increased in MCF-7 cells in response to palbociclib, whereas the expression in T47D cells was remarkably inhibited. LC3B-II, a standard marker for autophagosomes, was dose-dependently increased in MCF-7 cells, suggesting that palbociclib might also trigger autophagy as a stress response.

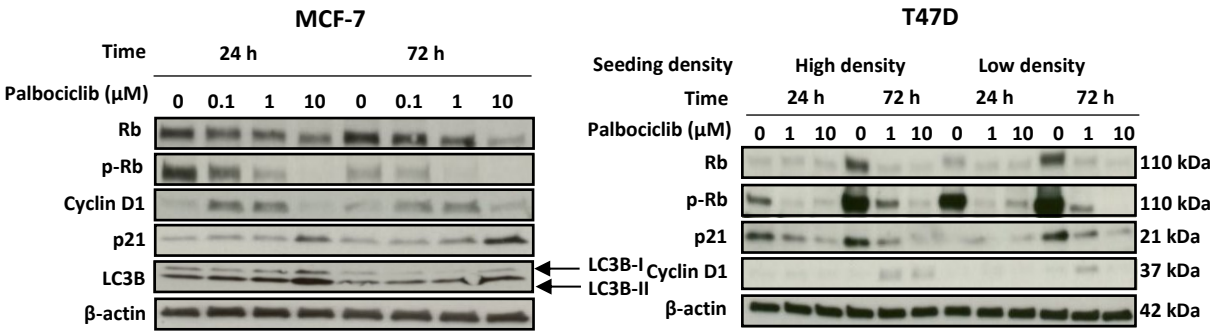


**Figure 4.22 Western blot for MCF-7 and T47D cells following palbociclib treatment.**

Cells were each seeded at appropriate densities and treated with palbociclib at indicated concentrations for 24 h and 72 h. β-actin was used as a loading control.

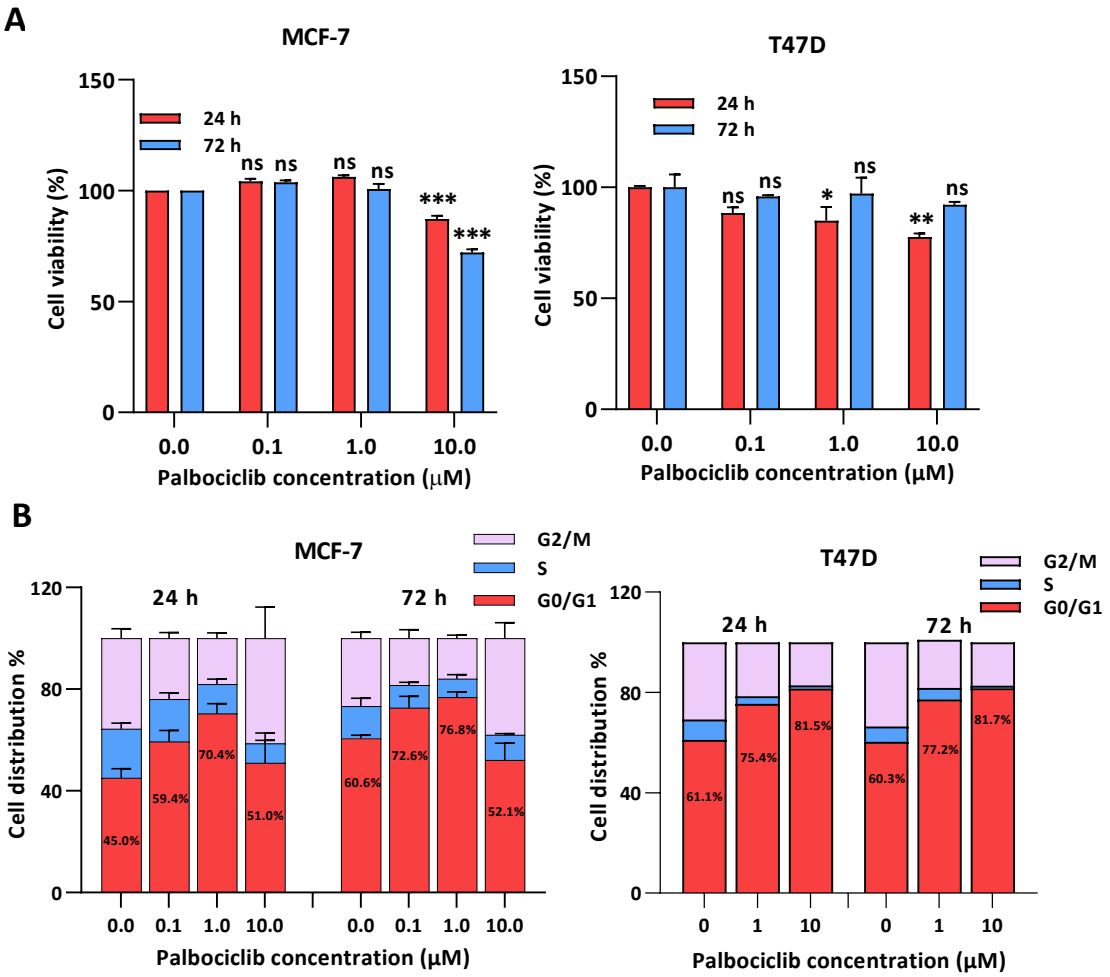


**Figure 4.23 The effects of palbociclib on cell viability and cell cycle arrest in MCF-7 and T47D cells.**

**A,** Cell viability was assessed by using Muse Cell Analyzer. Statistically significant difference is described by * $p < 0.05$, ** $p < 0.01$ and *** $p < 0.001$. **B,** Cell cycle analysis was performed on FACS. Mean values ± SD (n=3).

Next, the effects of palbociclib on cell cycle arrest were evaluated by flow cytometry. As shown in Figure 4.23, there was a dose-dependent G0/G1 cycle arrest in MCF-7 cells when exposed to low concentrations of palbociclib at 0.1 and 1 µM, whereas 10 µM palbociclib led to a decrease in cell numbers in G0/G1 phase, which was possibly because different cell fates including apoptosis and autophagy were triggered by high-dose of drug. In T47D cells, palbociclib led to a dose-dependent G0/G1 cycle arrest at 24 h and 72 h post-treatment.

**Palbociclib-mediated G0/G1 arrest is irreversible**

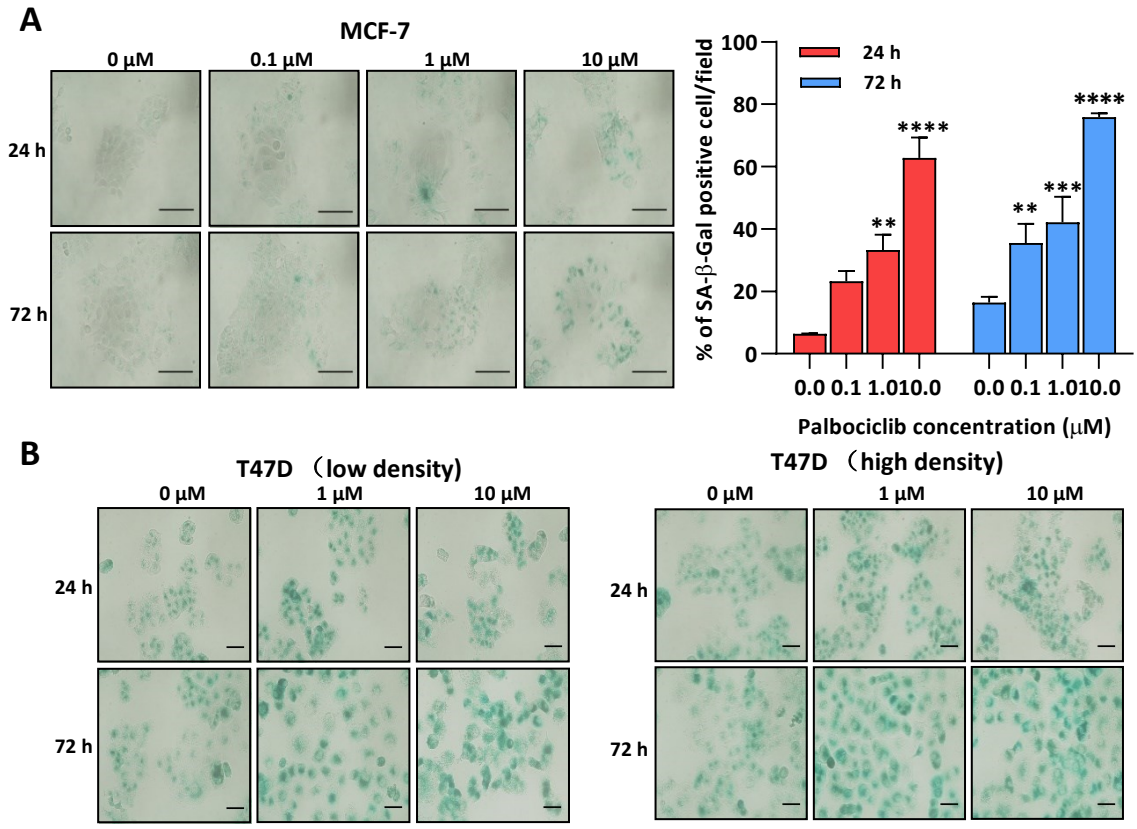


**Figure 4.24 Palbociclib induces positive SA-β-gal staining in MCF-7 cells.**

**A,** Representative images and quantification of SA-β-gal staining for MCF-7 cells. ** $p < 0.01$, *** $p < 0.001$ and *** $p < 0.0001$ indicate significant difference from the value measured in control untreated group. **B,** Representative images for T47D cells. After treatment, cells were stained by using SA-β-gal staining kit (Cell Signalling Technology) for 18 - 24 h. Images were acquired at × 400 magnification. Quantification was done by measuring the intensity of blue staining and normalised to the intensity of total cells by ImageJ. Mean values ± SD (n=3). Scale bar = 50 µm.

To test if palbociclib-mediated G0/G1 cycle arrest is associated with senescence, we evaluated the activity of SA-β-Gal after 24 h- and 72 h-exposure of MCF-7 or T47D cells to

palbociclib. As shown in Figure 4.24, MCF-7 cells showed a dose-dependent increase in total numbers of positive-stained cells. There was a remarkable increase in the percentage of positive stained cells, from 6.42 % ± 0.05 % in non-treated cells to 62.78% ± 4.61% in cells treated with 10 μM palbociclib 24 h post-palbociclib treatment. A more profound elevation was observed after a long-term treatment for 72 h, from 16.38% ± 1.09% in control cells to 75.87% ± 0.72% at 10 μM palbociclib. However, an unexpected positive staining was found in negative control T47D cells, which limited the use of SA-β-gal staining as a detection of senescence in this cell line. Besides, there was a flat and enlarged morphology in both cell lines after palbociclib treatment.

It has been well-documented that cell cycle arrest can be reversible (quiescence) or irreversible (senescence). To further examine for reversibility of palbociclib-mediated G0/G1 arrest and distinguish senescence from quiescence, cells were pre-treated with palbociclib (1 and 10 μM) for 24 or 72 hours to arrest them and cultured for another 5 days in the absence of palbociclib (Figure 4.25B).

Figure 4.25 showed that withdrawal of 1 μM of palbociclib immediately caused re-entry of cell cycle of large numbers of MCF-7 cells, whereas cells when pre-treated with a higher concentration of palbociclib at 10 μM were unable to recover from cell cycle arrest in drug-free media. SA-β-gal staining confirmed that 10 μM palbociclib triggered senescence in MCF-7 cells as there was a constant number of cells positive for staining following withdrawal of the drug and removal of a lower dose of palbcociclib dramatically reduced SA-β-gal positive staining. Consistently, crystal violet staining revealed a dramatic reduction in the numbers of colonies that formed after removal of 10 μM palbociclb; however, there was still some growth at lower dose of palbociclib (1 μM). Taken together, these results indicated that while palbociclib may induce an irreversible cell cycle arrest or senescence, this may be dose- and time-dependent.

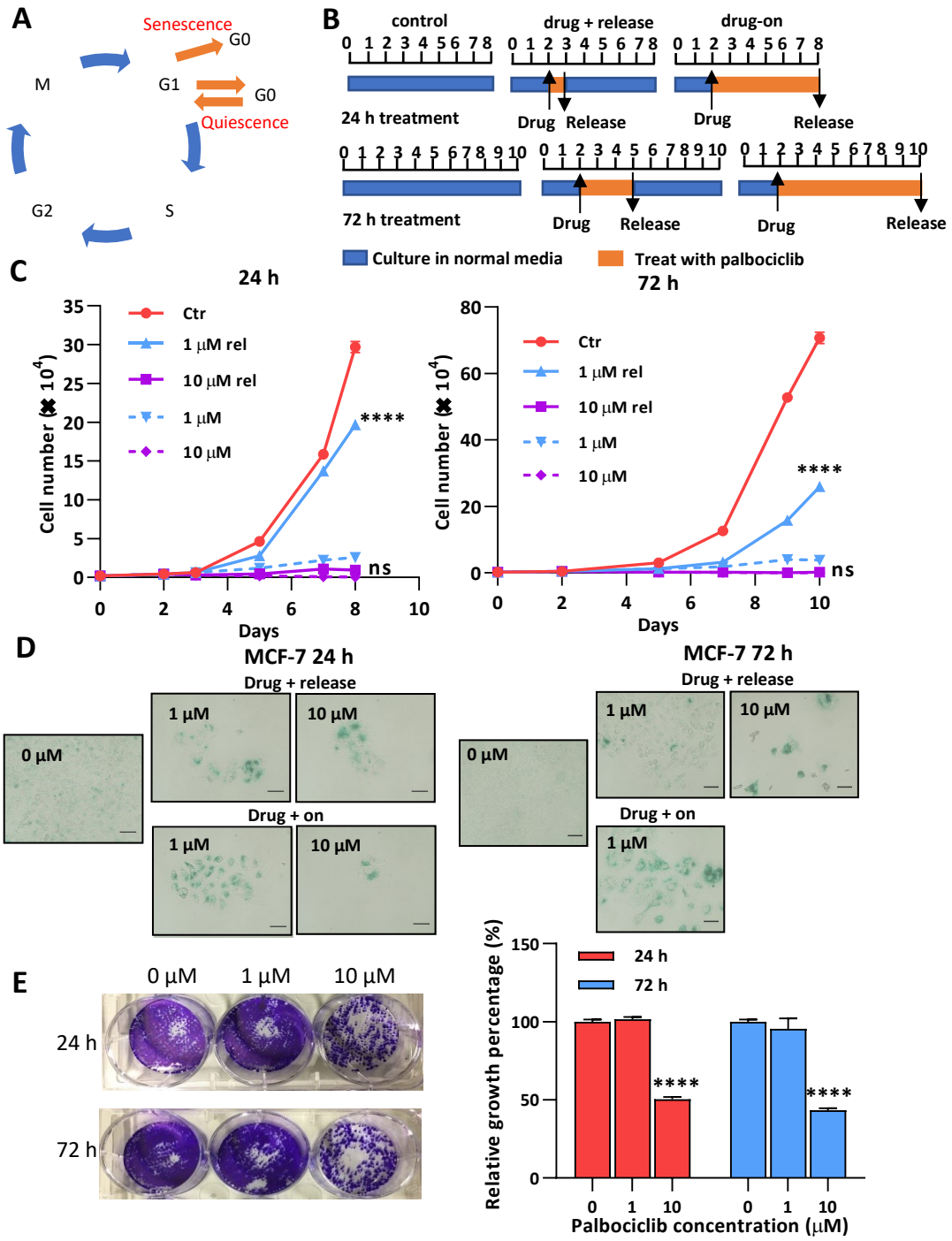


**Figure 4.25 Evaluation of reversibility of palbociclib-mediated G0/G1 cycle arrest in MCF-7 cells.**

Cells were treated with DMSO (Ctr) or palbociclib (1 μM and 10 μM) for 24 h and 72 h, and allowed to recover (rel) for another 5 days in the absence of drug. **A,** Schematic showing cell cycle arrest through senescence and quiescence. **B,** Schematic showing treatment strategy. **C,** Cell numbers counted by Muse Cell Analyzer. Statistically significant difference is analysed and compared to the value measured on the day of drug withdrawal (**** $p < 0.0001$). **D,** SA-β-gal staining. **E,** Crystal violet staining. At the end of treatment, cells were each re-plated at appropriate densities in 6-well plate and allowed to recover for another 10 days in drug-free media. The media were replaced every other day. Crystal violet staining was performed as described in Method. Significant difference is compared to control untreated group.

**Senescence-like phenotype is reinforced after enrichment of viable cells following palbociclib treatment**

To exclude dead cells from palbociclib treatment and effectively accumulate senescent cells at 24 h and 72 h after treatment, MCF-7 and T47D cells were collected by excluding floating cells and re-plated at identical cell number; culturing for another 24 h in the absence of drug. It was confirmed by western blot analysis (Figure 4.26B) that there was a dose-dependent inhibition of phosphorylation of Rb protein and an increase in levels of p21 and cyclin D1 in MCF-7 cells. A similar trend was observed in T47D cells except the expression of p21 decreased upon treatment.

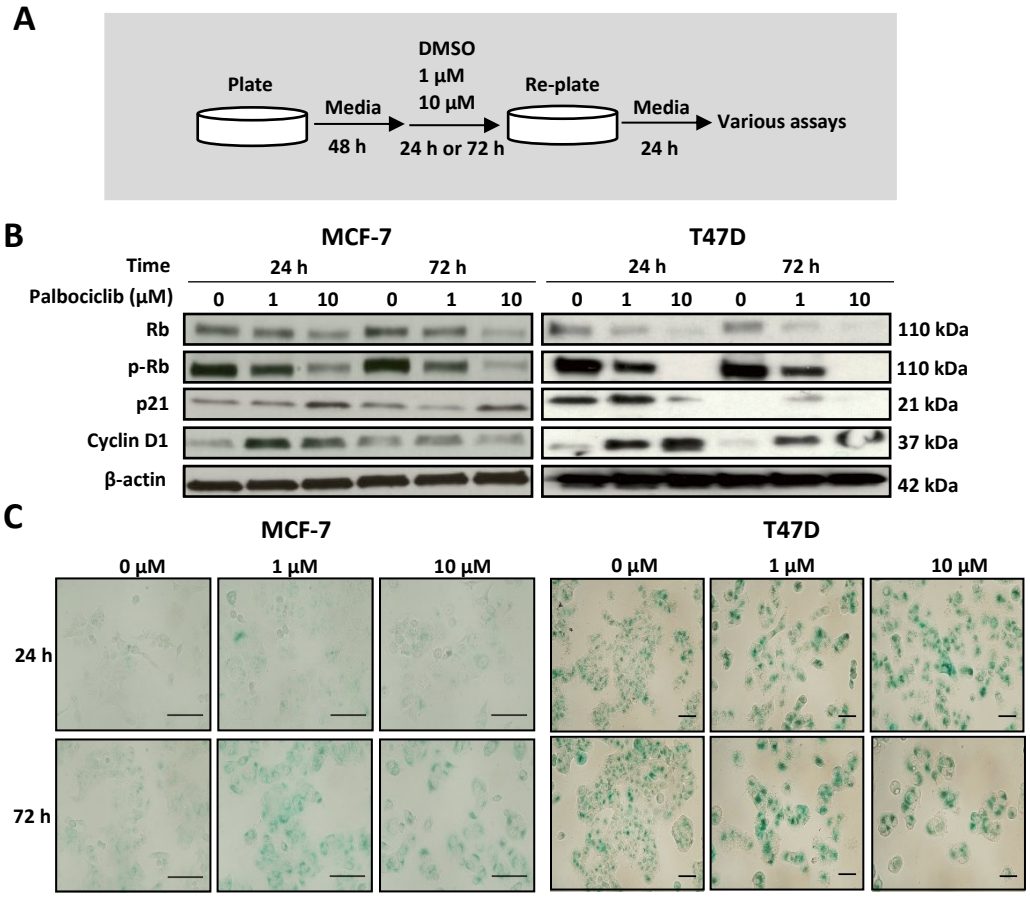


**Figure 4.26 Evaluation of a cell re-plating model to effectively accumulate palbociclib-induced senescence cells.**

**A,** Schematic showing the strategy of cell re-plating after palbociclib treatment. **B,** Results of western blot for MCF-7 and T47D cells. **C,** SA-β-gal staining. Scale bar = 50 µm.

Cell cycle analysis revealed a more remarkable G0/G1 arrest in both cell lines when compared with previous observations (Figure 4.23) in which the assay was immediately conducted after 24 h- and 72 h-treatment. Besides, the strategy of re-plating cells resulted in a more dramatic increase in total numbers of SA-β-gal positive cells in MCF-7 cells. SA-β-gal still failed to work in T47D cells as a strong positive stain was shown in non-treated cells.

Taken together, cells when treated and re-plated in this manner displayed a more significant senescence-like phenotype compared to the normal treatment strategy where the assays were immediately performed after treatment.

### 4.3.3 Palbociclib causes an increase in total glycogen storage

Having found a dose-dependent senescence-like phenotype, we then tested our hypothesis that glycogenesis might be positively regulated and used as a potential biomarker of palbociclib-induced senescence in responsive ER-positive breast cancer cell lines. To this end, we examined the accumulation of glycogen in MCF-7 and T47D cells by using a glycogen assay and PAS staining. All assays, unless indicated otherwise, were carried out in re-plated cells as described above.

The glycogen assay was performed to examine total intracellular glycogen accumulation following palbociclib treatment. A significant increase in glycogen storage was observed in MCF-7 cells when exposed to palbociclib at concentrations of 1 and 10 μM. After 24 h, glycogen level was increased from 29.3 ± 7.4 μg/mg protein in control cells to 71.2 ± 4.9 μg/mg protein at 10 μM palbociclib. Long-term treatment (72 h) at 10 μM increased glycogen level to 72.4 ± 6.3 μg/mg protein in comparison with 41.1 ± 1.0 μg/mg protein in vehicle-treated cells. In T47D cells, palbociclib treatment had less impact on glycogen accumulation, where there was only a subtle increase at 72 h post-treatment. Of note, baseline glycogen was already high in T47D cells.

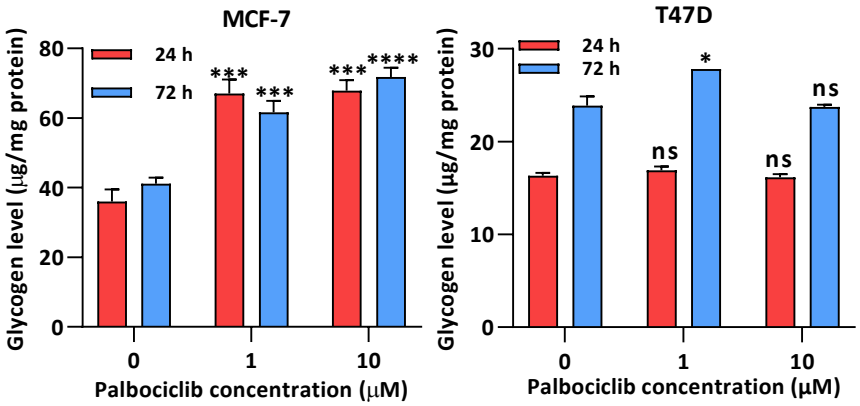


**Figure 4.27 Total intracellular glycogen level following palbociclib treatment in MCF-7 and T47D cells.**

Cells were each seeded at appropriate densities and treated with palbociclib at indicated concentrations for 24 h and 72 h. Cells were then re-plated and cultured in drug-free media for 24 h, followed by the glycogen assay. Significantly significant difference is compared to control untreated group: * $p < 0.05$, *** $p < 0.001$ and **** $p < 0.0001$.

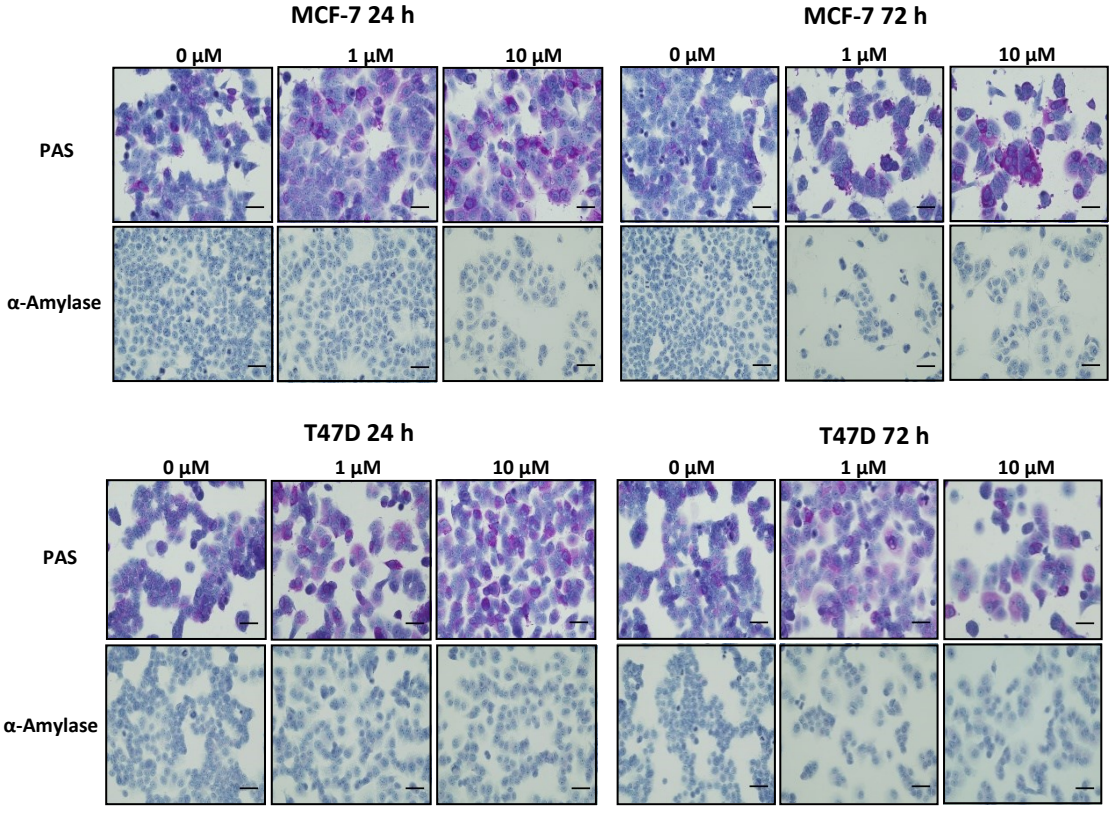


**Figure 4.28 PAS staining in MCF-7 and T47D cells following palbociclib treatment.**

Cells were treated and re-plated as indicated in Figure 4.27. PAS staining was conducted according to manufacturer's instruction. Scale bar = 50 µm.

PAS staining was then performed to localize glycogen in MCF-7 and T47D cells after palbociclib treatment. Cells with α-amylase digestion were used as controls. Consistently, there was a remarkable increase in total numbers of positive-stained MCF-7 cells upon treatment. In T47D cells, the total number of PAS stained cells remained constant between control and treated cells

### 4.3.4 Elevated G6P level is associated with palbociclib-induced glycogen accumulation

To further investigate the mechanisms underlying enhanced glycogen storage following palbociclib treatment, the expression profiles of proteins involved in glycogen metabolism signalling were examined. Upon palbociclib inhibition, the expression of GYS1 and phospho-GYS was less affected in T47D cells, which is consistent with previous observation of subtle changes in glycogen level in this cell line. Palbociclib dramatically reduced total GYS1 level and increased the expression of pGS S641 in MCF-7 cells, thus resulting in a decreased GYS1 activity as determined by the ratio of pGS S641 to total GYS1. PYGL, which is the rate-limiting enzyme of glycogen degradation, together with its inactive form phospho-PYGL (Serine 15) was found slightly decreased in treated MCF-7 cells.

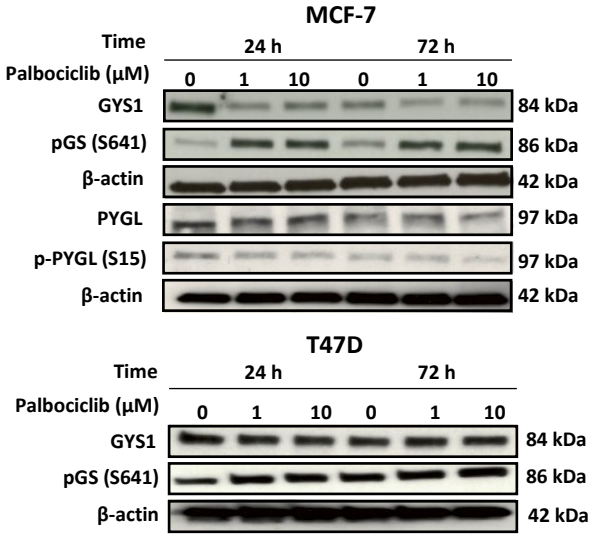


**Figure 4.29 The effect of palbociclib on regulating the expression of glycogen-associated proteins in MCF-7 and T47D cells.**

Cells were each seeded at appropriate densities and treated with palbociclib at indicated concentrations for 24 h and 72 h. Cells were then re-plated and cultured in drug-free media for 24 h, followed by western blot analysis.

Collectively, the decreased GYS1 activity as determined by the ratio of phospho-GYS to total GYS1 appeared was opposed to the accumulation of glycogen in response to palbociclib in MCF-7 cells. As discussed in **Chapter 3**, in addition to phosphorylation, GYS1 activity is positively regulated by G6P. We therefore assessed initially if palbociclib altered G6P concentrations in MCF-7 cells. Exposure of MCF-7 cells to palbociclib resulted in a dose-dependent increase of G6P level, with a more significant elevation observed after 72-h treatment. Taken together, our results suggest that increased G6P levels upon palbociclib treatment might upregulate glycogen accumulation based on two distinct mechanisms. One is that G6P itself, as an important substrate of glycogenesis, simply fluxed into glycogen, contributing to increased glycogen level, while another possibility is that allosteric regulation of GYS1 by G6P rapidly restored GYS1 activity in MCF-7 cells.

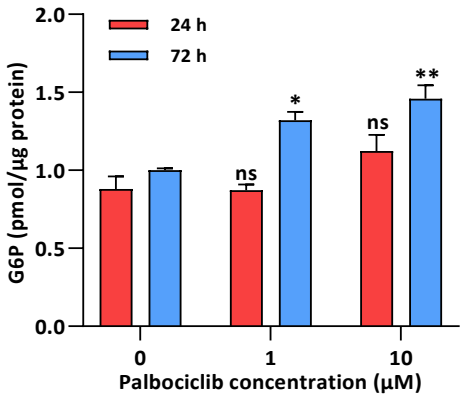


**Figure 4.30 Palbociclib increases G6P level in MCF-7 cells.**

Cells were seeded and treated with palbociclib for 24 h and 72 h, re-plated and recovered in drug-free media for 24 h. G6P concentration in cell lysates was measured by using a commercial kit according to manufacturer's instruction. * $p < 0.05$ and ** $p < 0.01$ indicate significant difference from the value measured on control untreated group.

### 4.3.5 The effect of palbociclib on glucose utilization

The effect of palbociclib on glucose utilization was accordingly assessed in MCF-7 cells by using the standard radiotracer [$^{18}$F]FDG. The uptake of [$^{18}$F]FDG was significantly diminished in response to 24-h treatment at the indicate concentrations, whereas no remarkable changes in radioactivity retention was seen in MCF-7 cells after a longer-term treatment (72 h).

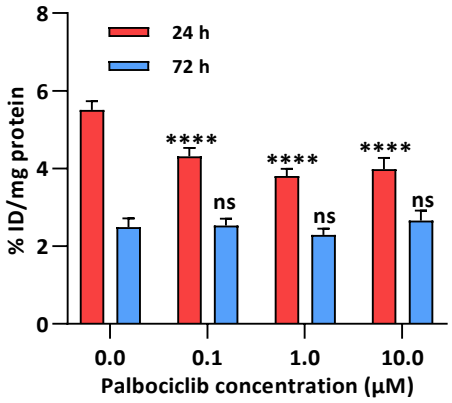


**Figure 4.31 The effect of palbociclib on glucose utilization measured by [$^{18}$F]FDG uptake.**

Cells were prepared as described above. On the day of uptake, cells were incubated with fresh DMEM media containing 0.74 MBq [$^{18}$F]FDG for 1 h at 37 °C in a humidified atmosphere of 5% $CO_2$. Mean values ± SD (n=6). Significant difference is compared to control group and described by **** $p < 0.0001$.

### 4.3.6 Discussion

With the intention of exploring glycogenesis as a potential biomarker for assessing tumour response to senescence-directed anticancer therapies, in this section, a CDK4/6 inhibitor palbociclib was examined in two ER-positive breast cancer cell lines. It was found that palbociclib induced a senescence-like phenotype in MCF-7 cells as characterised by an irreversible G0/G1 phase arrest, positive SA-β-gal staining, and increased p21 expression. Besides, a dose-dependent elevation in glycogen accumulation was observed in MCF-7 cells after palbociclib treatment, which was possibly due to increased glycogenesis in a GYS1-dependent manner mediated by G6P. Although SA-β-gal failed to characterise senescence in T47D cells, a senescence-like morphology with enlarged cell size and flattened cell shape was observed in this cell line following palbociclib treatment. Unlike MCF-7 cells, palbociclib led to unremarkable changes in glycogen in T47D cells. This perhaps means that glycogenesis as biomarker of senescence is not generic.

Palbociclib was shown to effectively inhibit cell growth of MCF-7 and T47D through induction of the G0/G1 phase arrest. The proliferation of hormone receptor-positive breast cancer is thought to highly dependent on CDK4/6 activity. Inactivation of CDK4/6-cyclin D1 by palbociclib suppresses cell progression from the G1 phase to the S phase via inhibition of the

release of E2F from Rb [300]. The sensitivity of cells to palbociclib is associated with the status of Rb protein expression, where Rb-negative cancer cells are prone to be resistant to palbociclib and are characterised, apart from loss of Rb, by an upregulation of p16 and no appreciable cyclin D1 protein expression.

Various types of cell fates, including reversible G0/G1 phase arrest (quiescence), senescence, autophagy and cell death were induced by palbociclib in this study in a time- and dose-dependent manner, suggesting that palbociclib elicits multiple downstream signalling cascades to exert its anticancer effect [309; 310]. One study has indicated that the regulation of MDM2 and the expression of ATRX determines the choice between quiescence and senescence in response to CDK4/6 inhibition. MDM2 turnover, which is dependent on its E3 ligase activity and expression of ATRX, is required for palbcoiclib-induced senescence. While failure to reduce MDM2 does not prevent palbociclib-mediated reversible cell cycle arrest (quiescence), it inhibits cells entering the more stable senescent state [311]. The inability of T47D cells to engage classical senescence/glycogenesis following palbociclib in this study may be due in part to non-functional p53 status (harbouring the highly expressed MDM2 p57 protein), compared to MCF-7 cells (functional p53; expression of the less abundant MDM2 p90 protein [312]. Consistent with this, MCF-7 was found to be strongly arrested under quiescence by CDK4 inhibitors, whilst decreased MDM2 levels, to some extent, triggered the conversion of cell response from quiescence to senescence [311]. Apart from quiescence and senescence, palbociclib at a high dose also triggers cellular autophagy as characterised by increased expression of autophagy protein LC3B-II, which has been found to be associated with palbociclib-induced ROS production. Furthermore, it has been reported that combination of autophagy and CDK4/6 inhibitors induces irreversible growth inhibition and senescence *in vitro*, and diminishes growth of cell and patient-derived xenograft tumours *in vivo*, providing the basis for utilizing autophagy inhibitor to combat cell resistance to cell-cycle-targeted therapies, such as CDK4/6 inhibitors [310].

Palbociclib is thought to exert two pro-senescence effects on cancer cells. The well-established one is that through inhibition of CDK4/6, the tumour suppressor RB1 is maintained in an active hypophosphorylated form, which arrests cells in the G0/G1 phase of the cell cycle. Another attempt to understand the molecular mechanism of palbociclib-induced senescence was made by Miettinen et al. in 2018 [313]. Using mass spectrometry-

based cellular thermal shift assay (MS-CeTSA), also known as thermal proteome profiling, the group identified the proteasome as a novel downstream target for palbociclib in breast cancer cells. To elaborate, proteasome is activated by palbociclib through decreasing its binding to the proteasome inhibitor ECM29, which in turn causes stress resulting from increased proteolysis, thereby leading to the reduction in cancer cell proliferation and the induction of a senescence-like state [313; 314].

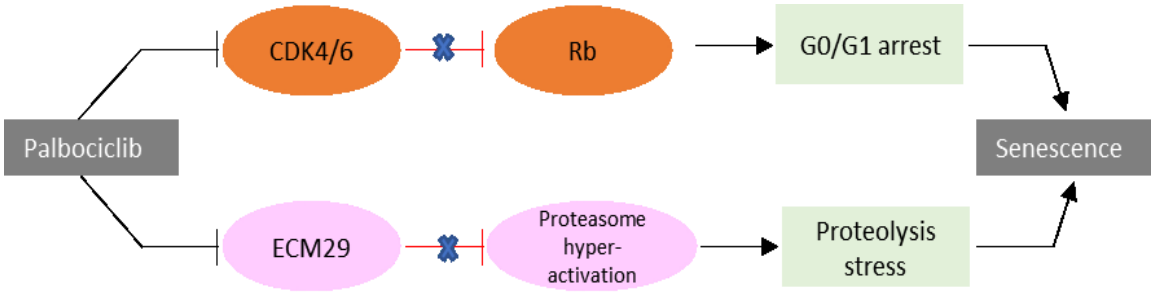


**Figure 4.32 Effects of palbociclib on senescence induction.**

Palbociclib exhibits two pro-senescence effects on cancer cells. Palbociclib inhibits the activity of CDK4/6-cylin D1 complex, which in turn makes Rb an active hypophosphorylated form, eventually resulting in G0/G1 phase arrest. Palbociclib also activates the proteasome through decreasing its binding to the proteasome inhibitor ECM29, which subsequently causes stress resulting from increased proteolysis. Together, these two effects cause a senescence response in cancer cells. [Adapted from Oliveira et al., 2018]

The interface of cell-cycle regulatory factors with metabolism is close but complex and varied. For example, cyclin D1 has been shown to act in a transcriptional role to coordinate metabolism and mitochondrial function. For example, CDK4/6 plays a crucial role in controlling glucose metabolism, Franco et al. [315] revealed that inhibition of CDK4/6 by palbociclib increases oxidative phosphorylation through a pathway involving the Rb tumour suppressor and mTOR activation. It remains to be understood how glycogen metabolism is modulated upon palbociclib treatment, and if this can serve as a reliable biomarker for palbociclib-induced senescence. In order to maximally accumulate palbociclib-mediated senescent cells, MCF-7 cells following palbociclib treatment were re-plated in identical numbers and allowed to recover for 24 h in drug-free media. This re-plating strategy was shown to increase the total number of senescent cells as characterised by enhanced SA-β-gal activity. Glycogen storage was dose-dependently increased in MCF-7 cells at 24 h and 72 h post-treatment, suggesting that cells store glycogen when entering cell cycle arrest. This is

consistent with previous observation in **Chapter 3** that glycogen level is positively correlated with cell populations in the G0/G1 phase. GYS1, which is the rate-limiting enzyme for glycogen synthesis, was dramatically inactivated via phosphorylation. The mechanism of enhanced GYS1 phosphorylation is unclear, however, it might be due to the activation of kinases by palbociclib that catalyse GYS1 phosphorylation at Ser641 site. For example, AMPK, which phosphorylates GYS1 at multiple sites, has been found to be activated in a CDK4/6-independent manner in hepatocellular carcinoma [316]. Additionally, palbociclib has been found to dose-dependently inhibit phosphorylation of AKT S473 and in turn moderately increases GSK3β activity [309] in several lung cancer cells. This might subsequently result in the inactivation of GYS1 through increased phosphorylation of this enzyme. Upregulation of GSK3β upon palbociclib treatment has also been seen in MiaPaCa-2 pancreatic cancer cells through PI3K/AKT signalling [317].

A lack of correlation between total glycogen level and GYS1 activity determined by the ratio of phosphorylation to total expression evoked exploration of allosteric activation of GYS1 by G6P. A dose-dependent elevation in G6P was shown in MCF-7 cells, with the most striking increase observed at 72 h post-treatment. It is unclear to what extent a G6P-dependent GYS1 activation occurs. Increased levels of G6P might rapidly restore GYS1 activity, thereby enhancing glycogen storage (or simply providing increased substrate for glycogenesis). The hypothesis should be checked by measuring GYS1 activity using a radioactivity assay based on the incorporation of [U-$^{14}$C]glucose from UDP-[U-$^{14}$C]glucose into glycogen. In contrast, alterations in GYS1 expression and glycogen accumulation were unremarkable in T47D cells in response to palbociclib treatment despite a G0/G1 phase arrest and senescence-like flattened morphology.

In summary, treatment with palbociclib at doses of 1 μM or less resulted in reversible G0/G1 arrest, while only chronic treatment (72 h) at higher dose (10 μM) contributed to senescent inhibition of growth in MCF-7 cells. Moreover, our results show that CDK4/6 inhibition by palbociclib promoted glycogen synthesis and subsequently induced accumulation of glycogen in a dose-dependent manner in ER-positive breast cancer MCF-7 cells. This effect was possibly due to an increased GYS1 activity which was perhaps partly regulated by the allosteric activator G6P, but not dephosphorylation-dependent activation. Further studies were conducted in **Chapter 5** to explore if this palbociclib-mediated changes

in glycogenesis could be detected by PET imaging agents. However, the cell lines specific nature of changes in glycogenesis limits it use as a biomarker.

## 4.4 Targeting Aurora A kinase as a regulator of senescence/quiescence and glycogenesis in cancer cells

### 4.4.1 Introduction

Genomic instability is a crucial characteristic of most cancer cells, which is closely controlled by DNA damage checkpoint, DNA repair machinery and mitotic checkpoint. Many mitotic regulators are aberrantly expressed in tumour cells, herein making them potential and useful therapeutic targets. Aurora A is such a mitotic kinase that regulates multiple steps of mitotic, including centrosome duplication, formation of a bipolar mitotic spindle and chromosome alignment on the mitotic spindle [318]. Overexpression of aurora A is thought to contribute to tumour initiation and progression among a wide range of cancer types [319]. Emerging data have indicated that loss of function or inhibition of aurora A results in aberrant mitosis, leading to cell cycle arrest and apoptosis. These findings have inspired numerous drug discovery efforts in investigation of clinically useful inhibitors of aurora A kinase for cancer therapy.

MLN8054, a selective inhibitor of aurora A kinase, has been used in trials treating several cancer types including colorectal, breast, bladder and pancreatic tumours. MLN8054 treatment results in G2/M arrest, spindle defects and anti-proliferative effects in multiple cultured human tumour cell lines. Although senescence is classically defined as an irreversible cell cycle arrest in G0/G1 phase, recently, several studies have shown that senescence program can be also launched after G2 arrest [320].

In this study, we sought to examine the ability of MLN8054 to induce senescence in cultured tumour cells and characterise the profiles of glycogenesis under treatment conditions.

### 4.4.2 Growth inhibition of MLN8054 in HCT116 and MCF-7 cells

The inhibitory effect of MLN8054 on cell proliferation was tested on HCT116 and MCF-7 cells. HCT116 cells showed a higher sensitivity ($GI_{50}$ = 16.32 ± 0.1 µM) in response to MLN8054 in comparison with MCF-7 cells where there was only a 50% inhibition of cell growth at the maximal drug concentration (Figure 4.33). Therefore, subsequent experiments were mainly carried out by using HCT116 cells due to its high sensitivity to MLN8054.

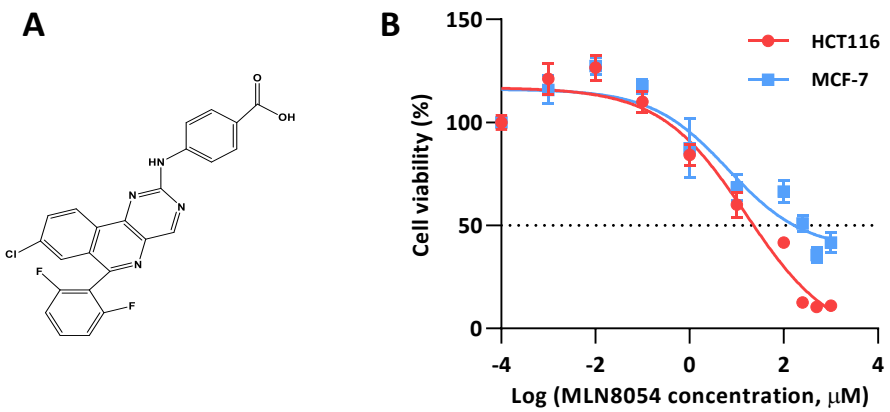


**Figure 4.33 $GI_{50}$ determination for MLN8054 in HCT116 and MCF-7 cells.**

**A,** Chemical structure of MLN8054. **B,** Representative dose response curves. Mean values ± SD (n = 6).

### 4.4.3 The effect of MLN8054 on cell cycle arrest and senescence induction

Cell cycle analysis (Figure 4.34A) showed a dose-dependent increase in G2/M cycle arrest in HCT116 cells upon MLN8054 treatment over the periods of 24 h, 48 h and 72 h. Incubation with varying concentrations of MLN8054 for 24 h, 48 h and 72 h dose-dependently induced an increase in total numbers of β-galactosidase stained HCT116 cells, as shown in Figure 4.34B. The effect was more pronounced at 72 h post-treatment (63.52 ± 2.49 % at 1 µM, 75.54 ± 2.12 % at 4 µM vs. 17.21 ± 3.78% of SA-β-gal positive cells in untreated cells).

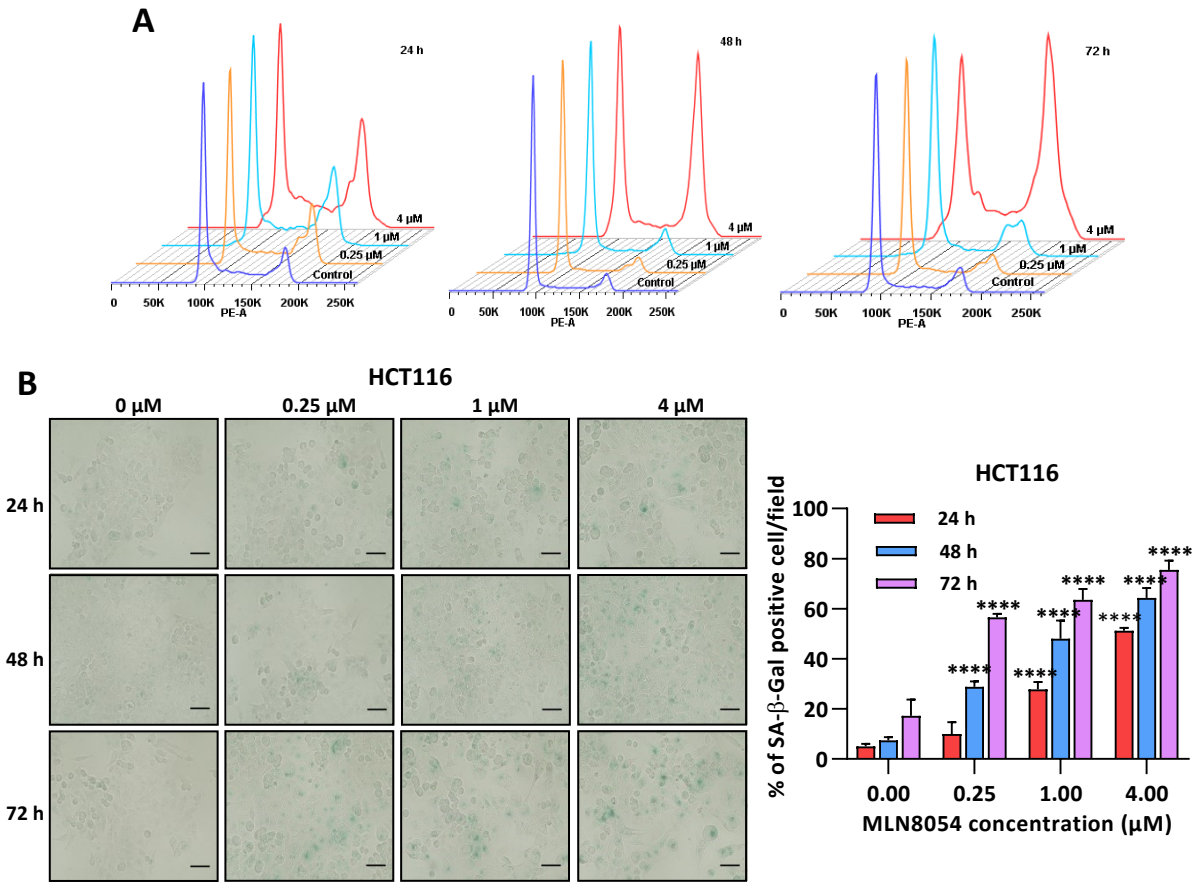


**Figure 4.34 MLN8054 induces a G2/M cycle arrest and a SA-β-gal positive staining in HCT116 cells.**

**A,** Cell cycle analysis by FACS. Cells were each seeded at appropriate densities and treated with MLN8054 at indicated concentrations for 24 h, 48 h and 72 h. Cells were then collected, stained by PI reagent and analysed by FACS. **B,** SA-β-gal staining following 24 h, 48 h and 72 h MLN8054 treatment. Scale bar = 50 µm. Quantification was performed by counting the intensity of blue stained cells, normalised to total cell numbers. Three independent fields for each condition were obtained and quantified. **** $p < 0.0001$ indicates significant difference from the value measured in control untreated group.

### 4.4.4 MLN8054-induced a G2/M phase arrest is reversible in HCT116 cells

To test whether the G2/M phase arrest is quiescence or senescence, HCT116 cells were re-plated at 24 h, 48 h and 72 post-treatment and allowed to recover for 24 h in drug-free media. HCT116 cells were then assessed for its reversibility by SA-β-gal assay. Exposure of treated cells in drug-free media for 24 h abrogated SA-β-gal staining in HCT116 cells, indicating that MLN8054-induced G2/M arrest is reversible and associated with quiescence, but not senescence.

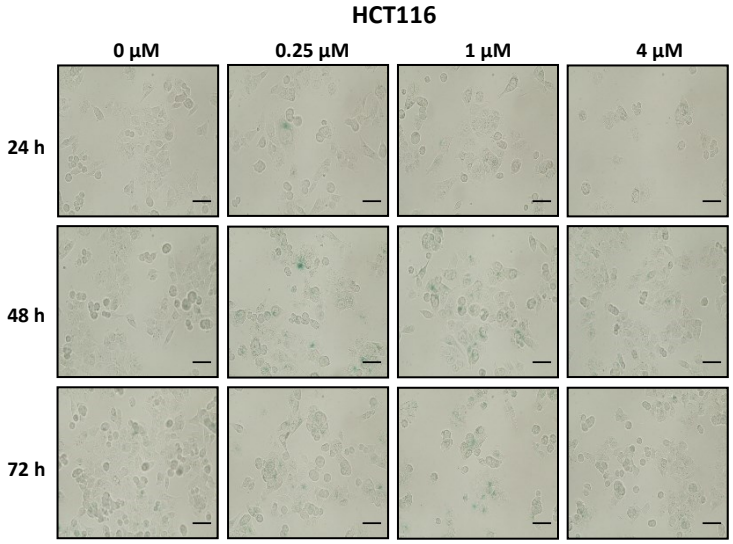


**Figure 4.35 SA-β-gal staining in MLN8054-treated HCT116 cells.**

Cells were re-plated at 24 h, 48 h and 72 h post-treatment and allowed to recover in drug-free media for 24 h. SA-β-gal staining was then performed as described. Scale bar = 50 μm.

### 4.4.5 The effect of MLN8054 on glycogenesis

Next, the response of HCT116 and MCF-7 cells to MLN8054 treatment was evaluated for changes in glycogen metabolism, by determining proteins involved in glycogen signalling and total intracellular glycogen level. Western blot analysis (Figure 4.36A) showed a dose-dependent inhibition of GYS1 activity as measured by an increased ratio of pGS S641 to GYS1 after MLN8054 treatment for 24 h, 48 h and 72 h in both cell lines. Cell cycle biomarkers, p21 and cyclin D1, were dose-dependently increased in MCF-7 cells, with the most remarkable increase observed after a 72-h treatment. MLN8054 induced a similar dose-dependent increase in p21 expression in HCT116 cells during the treatment periods of 24 h, 48 h and 72 h.

As shown in Figure 4.36B, a dose-dependent increase in total glycogen level was observed when HCT116 cells were exposed to MLN8054 for 48 h and 72 h, while a short-term treatment 24 h did not change total glycogen storage. The increase was more profound at 72 h post-treatment, from 1.59 ± 0.10 μg/mg protein in untreated cells to 7.40 ± 0.44 μg/mg protein at 4 μM. In contrast, a higher basal level of glycogen was observed in untreated MCF-7 cells, which is consistent with previous observations. Interestingly, MLN8054 at low concentrations

(0.25 and 1 μM) caused an elevation in glycogen content in MCF-7 cells, with a massive reduction observed at a higher drug dose, perhaps related to cell death. The same pattern of glycogen changes was found in MCF-7 cells across all treatment conditions (at 24 h, 48 h and 72 h), with the most alterations observed at 72 h.

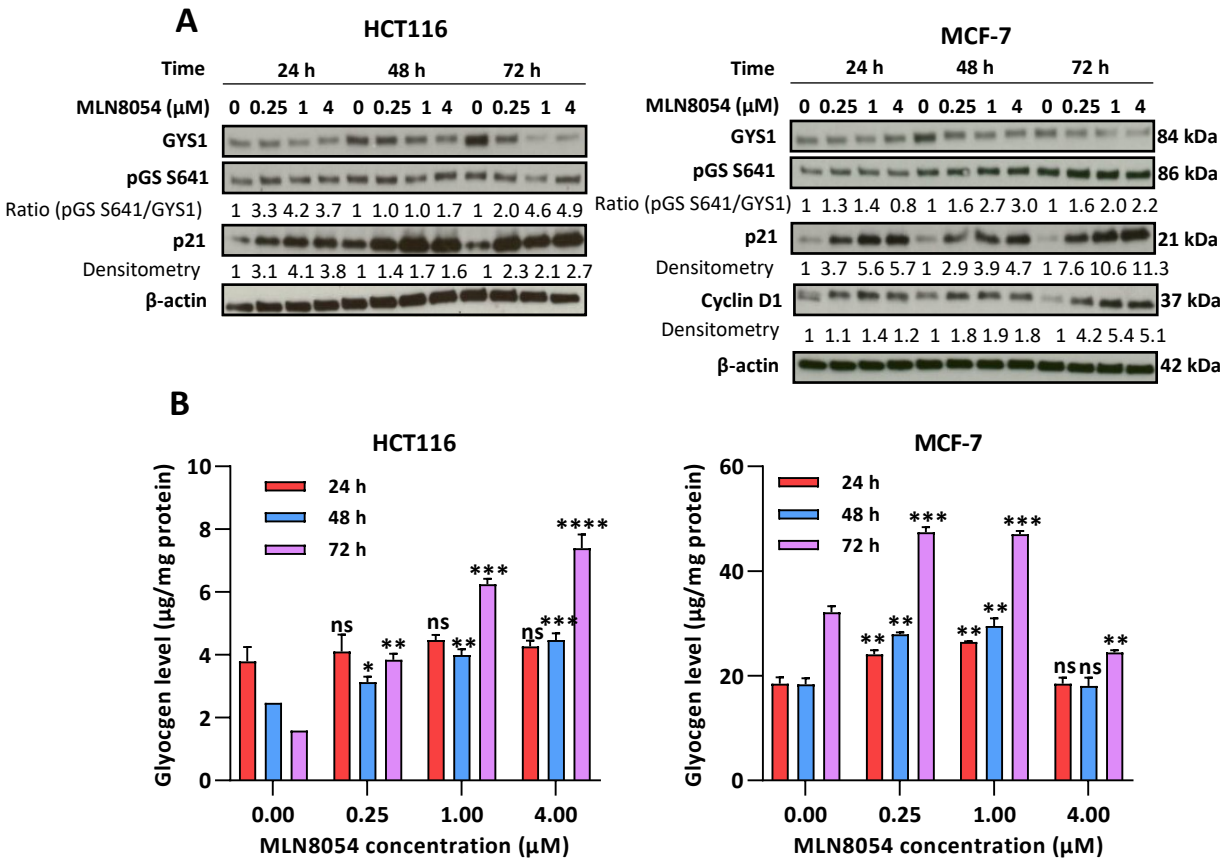


**Figure 4.36 The effect of MLN8054 on glycogen accumulation in HCT116 and MCF-7 cells.**

**A,** Results of western blot for MLN8054-treated HCT116 and MCF-7 cells. Semi-quantification of blots was done by using ImageJ. **B,** Total intracellular glycogen contents after MLN8054 treatment. Significant difference is described by ** $p < 0.01$, *** $p < 0.001$ and **** $p < 0.0001$.

### 4.4.6 Discussion

In summary, we demonstrate that MLN8054 possessed anti-tumour activity in HCT116, a colorectal cancer cell line, through inhibiting *in vitro* proliferation and inducing quiescent G2/M accumulation. A dose-dependent accumulation of glycogen was observed in HCT116 cells at 72 h post-treatment.

Aurora A kinase is frequently overexpressed in a range of cancer types, including breast, colorectal, ovarian and hepatocellular carcinoma. Upregulation of aurora A kinase has been

linked to centrosome amplification, aneuploidy and chromosome instability. MLN8054, a small-molecule inhibitor, shows selectively inhibitory effect against aurora A kinase and exerts anticancer activity against human tumour xenografts [318]. The anti-tumour effect of MLN8054 is majorly via induction of cell death. Here, we confirmed that MLN8054 had an antiproliferative effect on HCT116 cells and inhibited cells from progression through mitosis, thereby resulting in cell death and the G2/M phase arrest. The action of mechanism of MLN8054 is thought to be through development of abnormally formed monopolar, bipolar, or multipolar mitotic spindles, often with unseparated centrosomes. Monopolar and multipolar spindles may resolve to form bipolar spindles or may die directly from defective mitoses. Aurora A inhibition leads to chromosome congression defects at metaphase, lagging chromosomes in anaphase, and telophase chromatin bridges, resulting in aneuploid cells and eventually cell death [321].

In addition to cell apoptosis, several studies have shown that MLN8054 exerts anti-cancer effect via triggering irreversible G2/M cycle arrest (senescence). Cellular senescence was originally defined as an irreversible arrest in the G0/G1 phase of the cell cycle through inactivation of cyclin D1-CDK4/6 and cyclin E1-CDK2 complexes that positively regulate G1/S phase progression. Recently, the idea that senescence could also be induced during a prolonged G2 arrest emerged after the discovery that p21 is also involved in the G2/M checkpoint regulation. Although the mechanisms underlying MLN8054-induced senescence remains unclear, it is possibly regulated via the p53-p21-Rb axis by MLN8054-induced inhibition of aurora A kinase. It was shown that p53 is stabilised and upregulated following MLN8054 treatment, which might trigger the onset of senescence. To answer these questions, it would be useful to assay for senescence in both p53-null and p53 wild-type cancer cell lines upon MLN8054 treatment. Furthermore, p53/p21-dependent irreversible cell cycle exit in G2 has been shown to be associated with down-regulation of both cyclin 1 and cyclin B1, and accumulation of non-phosphorylated Rb family pocket proteins [322]. Possibly, the role of p21 in G2 arrest is also associated with inactivation of cyclin B1-CDK1 complexes in the nucleus, thereby preventing mitotic entry [323].

Although senescence-associated β-gal staining was observed in HCT116 cells after 24 h-, 48 h- and 72 h-treatment, re-incubation with drug-free media abrogated the positive stain, indicating that the G2/M cycle arrest induced by MLN8054 under the indicated conditions is

a quiescent state, but not irreversible senescence. It is likely that HCT116 cells are prone to enter senescent state only when under chronic MLN8054 treatment.

The role of aurora A kinase plays in controlling metabolic signalling pathways in tumours is less understood. One study has reported that polyploidy tumour cells induced by aurora kinases inhibitors (MK-0547 and ZM447439) had higher level of glycolytic metabolism than untreated acute myeloid leukemia (AML) [324]. Combined treatment with 2DG could sensitise the anti-proliferative effect of aurora A kinase in the same cancer cell line [324]. However, little is known about how aurora A kinase inhibitor would regulate glycogen metabolism. Here, it was shown that MLN8054 facilitated glycogen accumulation in a dose-dependent manner in HCT116 cells despite decreased GYS1 activity as characterised by the ratio of phosphorylation to total expression. Xu et al. [325] found that during metabolic stress, aurora A overexpression suppressed GSK3β activity in breast cancer cell lines, suggesting a connection between the two enzymes. Possibly, inhibition of aurora A kinase by MLN8054 somewhat increases GSK3β activity, which in turn leads to down-regulation of GYS1.

# Chapter 5 Evaluation of novel PET imaging agents for detecting drug-induced senescence/quiescence

## 5.1 Introduction

Drugs that induce senescence have shown significant benefits as anticancer reagents. In addition, pro-senescence and anti-senescence (senolytic) therapies are showing promising roles in preclinical mouse models, with potential application in the clinic for delaying physical dysfunction and extending lifespan [326].

Although many studies have reported the role of senescence in translational medicine, approaches to identify and target senescent cells remain challenging and less explored, particularly the *in vivo* detection. PET imaging has its unique advantages of high specificity and minimally invasive measurement of changes involved in biological processes. This chapter therefore aimed to assess radiopharmaceuticals for PET imaging to specifically identify senescent cells, with the potential of aiding the assessment of senescence-directed therapies.

Having observed an increase in glycogenesis and glycogen accumulation following palbociclib treatment, we herein proposed to develop PET radiotracers to measure changes in glycogenesis or stored glycogen as a useful tool for tracing senescent cells. Additionally, a novel tracer, which was designed to measure senescence-mediated accumulation of lipofuscin, was studied in parallel to expand the available library of radiopharmaceuticals that could accurately detect senescent cells.

## 5.2 Evaluation of fluorine-18 radiolabelled glucosamine analogues as PET probes for targeting glycogenesis

A glucosamine-derived PET radiotracer namely N-(methyl-(2-[$^{18}$F]fluoroethyl)-1H-[1,2,3]triazole-4-yl)glucosamine ([$^{18}$F]NFTG) was previously developed by our group and briefly tested for measuring glycogenesis in tumour cells *in vitro* and in tumour-bearing mice *in vivo* [146; 327]. The putative mechanism of action was based on the enzymatic incorporation of [$^{18}$F]NFTG into the granules of glycogen catalysed by glycogen synthase (GYS). Thus, GYS enzyme activity formed the basis of PET signal attributed to [$^{18}$F]NFTG

accumulation. Despite a promising role in imaging glycogenesis, [$^{18}$F]NFTG is disadvantaged by a complex radiosynthesis and purification.

Here, the synthesis of two analogues of [$^{18}$F]NFTG, namely N-(4-[$^{18}$F]fluorobenzyl)glucosamine ([$^{18}$F]FB-glucosamine) and N-(4-[$^{18}$F]fluorobenzyl) galactosamine ([$^{18}$F]FB-galactosamine), was attempted and evaluated with the aim of being used to specifically target glycogenesis. Additional attempt was made to produce [$^{18}$F]NFTG through an improved synthetic method; the product of this new synthetic route was also evaluated.

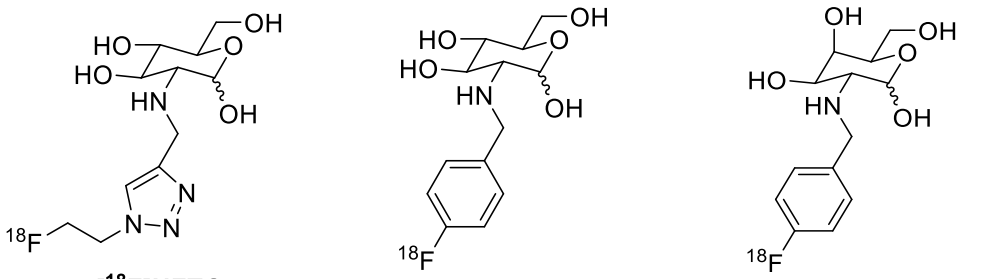


**Figure 5.1 Chemical structures of fluorine-18 radiolabelled glucosamine analogues for detecting glycogenesis.**

### 5.2.1 Evaluation of specificity of [$^{18}$F]FB-glucosamine and [$^{18}$F]FB-galactosamine to glycogenesis *in vitro*

Glucosamine is an essential substrate of glycosylated proteins and lipids and has been labelled with various radioisotopes such as fluorine-18 ($^{18}$F), gallium-68 ($^{68}$Ga) and technetium-99m ($^{99m}$Tc) for tumour imaging [328; 329]. Chemical synthesis of [$^{18}$F]FB-glucosamine and [$^{18}$F]FB-galactosamine was done by Dr. Louis Allott and Dr. Diana Brickute. Briefly, the two tracers were synthesized by replacing the N-substituted [$^{18}$F]fluoroethyltriazole of [$^{18}$F]NFTG with a [$^{18}$F]fluorobenzyl ([$^{18}$F]FB) group. Compared to [$^{18}$F]fluoroethyltriazole, the enhanced lipophilicity of the [$^{18}$F]FB-moiety allowed purification of the two novel compounds by C18 preparative HPLC using a biocompatible solvent system.

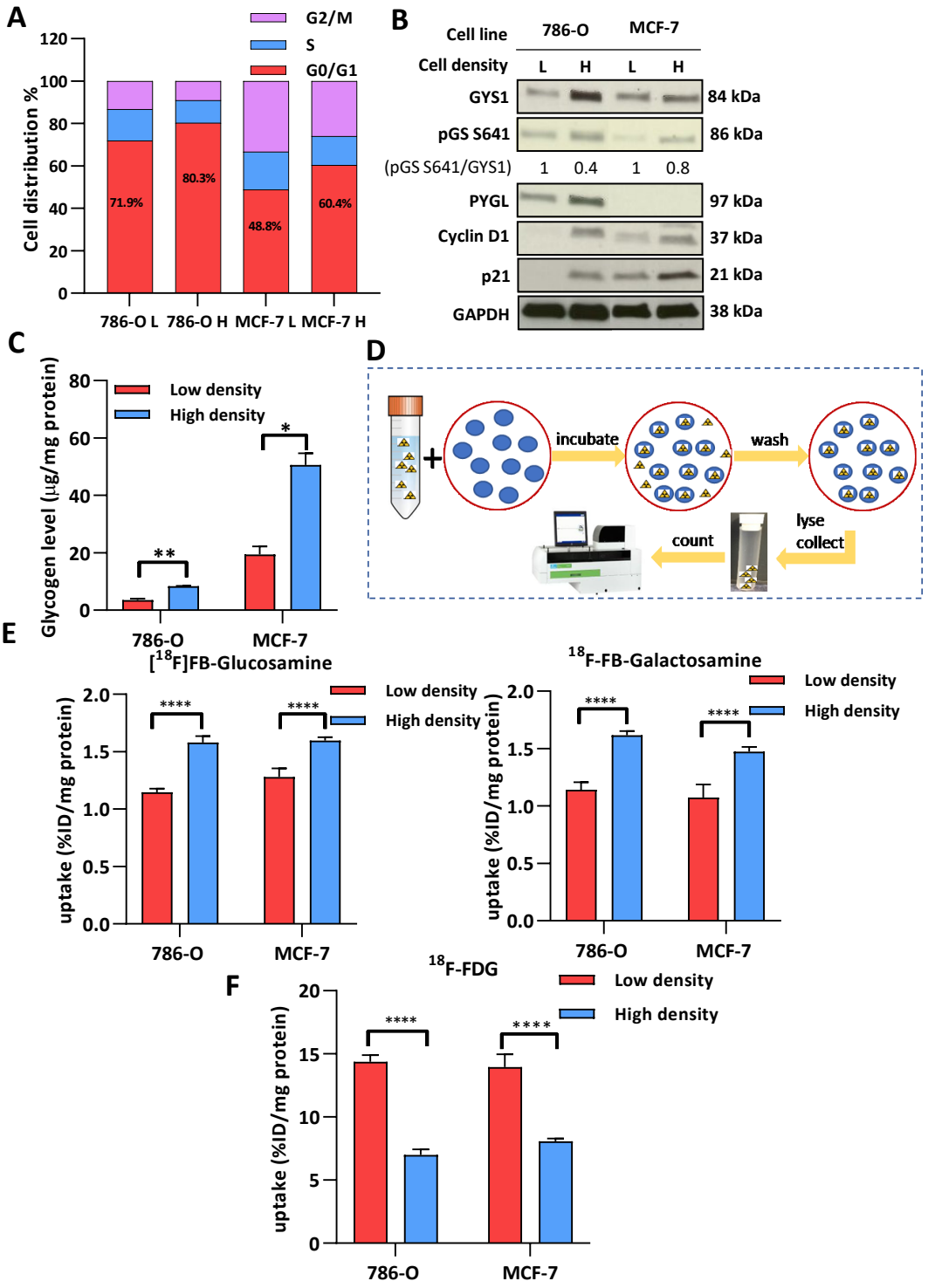


**Figure 5.2 Cell confluency facilitates the uptake of [$^{18}$F]FB-glucosamine and [$^{18}$F]FB-galactosamine *in vitro* in 786-O and MCF-7 cells.**

Cells were each seeded at appropriate densities and allowed to attach for 48 h. **A,** Cell cycle analysis by flow cytometry using PI staining. **B,** Western blot analysis. **C,** Total glycogen level was measured by glycogen assay. **D,** Schematic showing *in vitro* radiotracer uptake experiment. **E,** *In vitro* [$^{18}$F]FB-Glu and [$^{18}$F]FB-Gal uptake (3 h incubation). **F,** *In vitro* [$^{18}$F]FDG uptake (3 h incubation). Mean values ± SD (n=6). Significant difference is described by **** $p < 0.0001$.

In order to examine the specificity of the two novel tracers, *in vitro* uptake was performed in 786-O and MCF-7 cells, where changes in glycogenesis had been observed in a cell growth-dependent manner (**Section 3.3**). Cell cycle analysis (Figure 5.2A) confirmed a G0/G1 phase arrest, as well as increased expression of cyclin D1 and p21 (Figure 5.2B) induced by cell confluency in 786-O and MCF-7 cells. Elevated GYS1 activity and glycogen accumulation were also observed in both cells when seeded at high density, particularly in MCF-7 cells with an approximately 2.5-fold increase in total glycogen accumulation (Figure 5.2C).

It was then tested whether the two probes are capable of differentiating glycogen changes resulting from the increased seeding density (quiescence). As shown in Figure 5.2E, there was increased uptake of [$^{18}$F]FB-glucosamine and [$^{18}$F]FB-galactosamine under confluent condition in both cell lines in comparison with sub-confluent condition. However, the difference in tracer uptake did not reflect the marked differences in either GYS1 activity or glycogen level between 786-O and MCF-7 cells. By comparison, the uptake of [$^{18}$F]FDG (Figure 5.2F), which measures glucose utilization, was remarkably reduced in cells when seeded at high density, suggesting that glucose consumption was dramatically decreased in cells entering the non-cycling phase under confluent condition. GYS1 expression or activity, detectable by pGS S641/GYS1 alone appears to have limited value, and together with the decreased [$^{18}$F]FDG (and increased G6P in earlier work) data, suggests a potentially important role of intracellular G6P, e.g. via gluconeogenesis would have been worth elaborating further as influencing glycogenesis.

It is known that glucose is an effective regulator of glycogen synthesis under physiological condition as it provides substrates for glycogen formation. In order to examine if the rate of uptake was affected by external glucose level, various concentrations of glucose were added to radioactivity-containing media. The differences of tracer retention were unremarkable in MCF-7 cells when incubated with different concentrations of glucose.

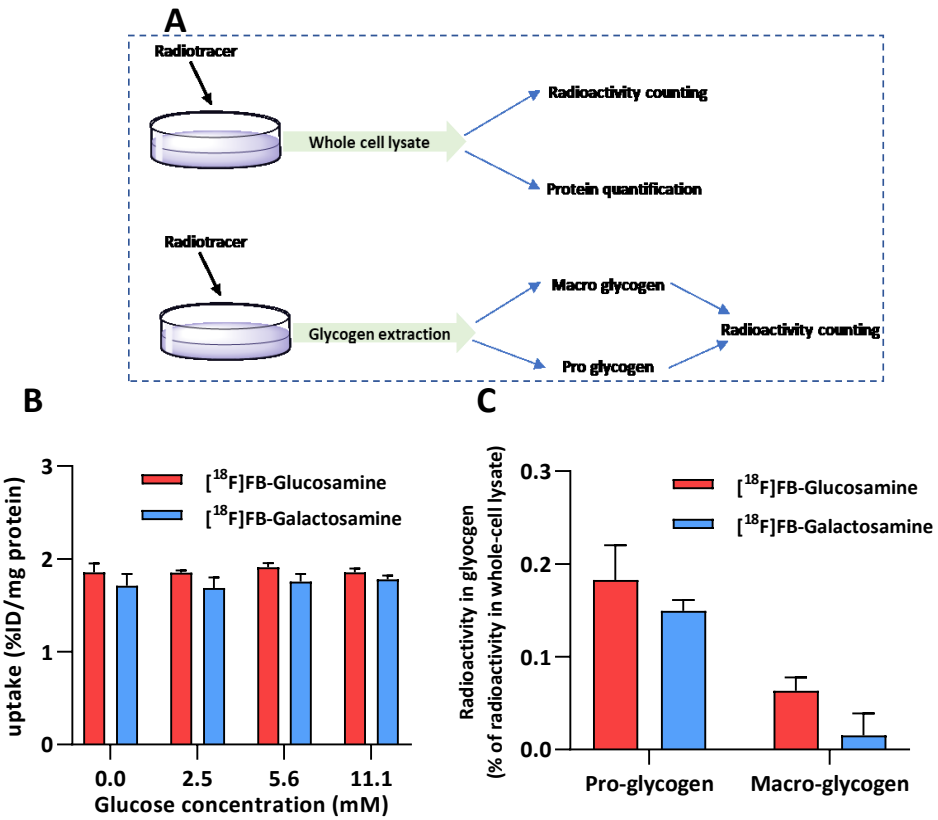


**Figure 5.3 Evaluation of specificity of [$^{18}$F]FB-glucosamine and [$^{18}$F]FB-galactosamine to glycogenesis *in vitro*.**

**A,** Schematic showing the strategy of direct radiolabelling of glycogen. Briefly, cells were incubated with 7.4 MBq radiotracer for 3 h at 37 °C in a humidified condition of 5% $CO_2$. Cells were then washed three times with cold PBS and scraped into RIPA buffer for analysis of radioactivity in whole-cell lysate, or scraped into 30% potassium hydroxide, 70% ethanol for obtaining whole-cell lysate and total glycogen, respectively. Radioactivity in pro-glycogen and macro-glycogen was measured as described. Data were presented as a percentage of radioactivity in the corresponding whole-cell lysates. **B,** The effect of extracellular glucose on tracer uptake. Cells were incubated with tracer-added DMEM medium containing a series of concentrations of glucose for 3 h. **C,** Direct labelling of glycogen by the two tracers.

To directly evaluate tracer specificity, radioactivity incorporated into glycogen granules was measured by extracting pro-glycogen and macro-glycogen following tracer incubation. As shown in Figure 5.3, the percentage of radioactivity incorporated into pro-glycogen and macro-glycogen was low in MCF-7 cells, at around 0.20% and 0.10%, respectively; in contrast, the level for [$^{18}$F]NFTG was reported to be 69.2% ± 2.3% in pro-glycogen [146].

Taken together, although [$^{18}$F]FB-glucosamine and [$^{18}$F]FB-galactosamine shared similar structures to [$^{18}$F]NFTG, the two tracers did not show the same specificity to glycogenesis.

### 5.2.2 Evaluation of a 'new' [$^{18}$F]NFTG for targeting palbociclib-induced glycogenesis

To reduce instability of product, the attempt was then made to synthesize [$^{18}$F]NFTG by an improved radiolabelling strategy by Dr. Louis Allott and Dr. Diana Brickute, in which the radiosynthesis of copper catalysed azide-alkyne cycloaddition (CuAAC) "click" chemistry was automated in the GE FASTLab$^{TM}$ platform. [$^{18}$F]NFTG uptake in 786-O and MCF-7 cells (Figure 5.4A) under sub-confluent and confluent conditions were performed to compare with the findings of [$^{18}$F]FB-glucosamine and [$^{18}$F]FB-galactosamine. The uptake of [$^{18}$F]NFTG was significantly increased in cells under confluent condition in both cell lines. Moreover, tracer uptake was higher in MCF-7 cells in comparison with 786-O cells, which reflects the differences of glycogen between the two cell lines as measured by glycogen assay.

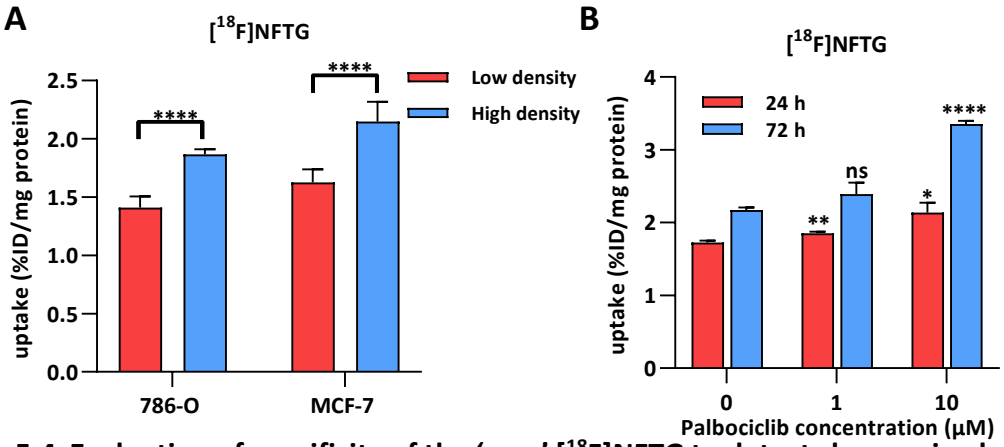


**Figure 5.4 Evaluation of specificity of the 'new' [$^{18}$F]NFTG to detect changes in glycogenesis *in vitro.***

**A,** *In vitro* uptake of [$^{18}$F]NFTG in 786-O and MCF-7 cells, cultured under sub-confluent and confluent conditions. **B,** *In vitro* uptake of [$^{18}$F]NFTG in palbociclib-treated MCF-7 cells. On the day of uptake, cells were incubated with fresh DMEM media containing 0.74 MBq [$^{18}$F]NFTG for 1 h at 37 °C in a humidified atmosphere of 5% $CO_2$. Mean values ± SD (n=6). Significant difference is described by * $p < 0.05$, ** $p < 0.01$ and **** $p < 0.0001$.

The ability of [$^{18}$F]NFTG to distinguish varying degrees of glycogenesis was then assessed in palbociclib-treated MCF-7 cells that has shown a dose-dependent increase in glycogenesis. As shown in Figure 5.4B, the uptake was dose- and time-dependently elevated in MCF-7 cells after palbociclib treatment, with the most striking increase observed after long-term treatment at 72 h (2.17 ± 0.09 %ID/ mg protein in control cells vs. 3.36 ± 0.10 %ID/mg protein at 10 µM palbociclib).

### 5.2.3 Discussion

Glucosamine is an amino sugar and convers naturally to glucosamine-6-phosphate that serves as the chemical precursor of all nitrogen-containing sugars, as well as glycosylated proteins and lipids. Glucosamine derivatives when radiolabelled by $^{18}F$, $^{68}Ga$ and $^{99m}Tc$ have been evaluated as novel candidates for PET/SPECT imaging agents [328; 329].

Several $^{18}F$-labelled glucosamine derivatives have been previously synthesized and their abilities to target tumour cells assessed [326]. Among them, [$^{18}F$]NFTG showed high *in vitro* and *in vivo* specificity to glycogenesis. Although the exact mechanism of [$^{18}F$]NFTG accumulation remains unclear, it has been reported that [$^{18}F$]NFTG retains the α-proton which is required for the initial flux into newly formed glycogen, analogous to 2-NBDG [145; 146]. To overcome the limitation present in [$^{18}F$]NFTG synthesis, the attempt was made by our chemists to synthesize two analogues of [$^{18}F$]NFTG through attaching [$^{18}F$]fluorobenzyl ([$^{18}F$]FB) group to the glucosamine or galactosamine, producing [$^{18}F$]FB-glucosamine or [$^{18}F$]FB-galactosamine, respectively. Despite a more clinically translatable synthetic route, [$^{18}F$]FB-glucosamine and [$^{18}F$]FB-galactosamine showed poorer specificities to glycogenesis in comparison with [$^{18}F$]NFTG, as shown by low incorporation of radioactivity into newly-formed glycogen granules.

In parallel, [$^{18}F$]NFTG was synthesised using an improved method and assessed for its ability to selectively detect the changes of glycogenesis in response to palbociclib-mediated senescence/quiescence. The uptake of [$^{18}F$]NFTG was profoundly increased in MCF-7 cells in a dose-dependent manner, with the most dramatic accumulation seen in cells that have shown senescence-like phenotypes - treatment with 10 μM of palbociclib for 72 h. Despite promising results, several limitations and challenges remained for using this tracer as an imaging biomarker of senescence in clinical settings.

(i) Although [$^{18}F$]NFTG largely accumulated in senescent cells induced by palbociclib, there were still some increases in quiescent cells (at low doses of palbociclib), indicating that this tracer might not be efficient in differentiating changes in glycogenesis induced by quiescence and senescence.

(ii) The putative mechanism of action of [$^{18}F$]NFTG was based on the enzymatic incorporation of [$^{18}F$]NFTG into the granules of glycogen by glycogen synthase

[146]. Thus, GYS1 enzyme activity formed the basis of PET signal attributed to [$^{18}$F]NFTG accumulation. Changes in glycogenesis following palbociclib treatment however was found to be associated with levels or G6P-dependent activation of GYS1 activity, but not dependent on phosphorylation/dephosphorylation regulation. It is not clear if [$^{18}$F]NFTG could accurately sense this type of changes in glycogenesis, as so far the reported applications of [$^{18}$F]NFTG were made based on phosphorylation-dependent regulation of GYS1 and glycogenesis.

(iii) Detection of glycogenesis, which is a dynamic process regulated by different enzymes and signalling pathways, appears to be difficult. In addition to the complicated regulatory mechanisms, levels of enzymes /proteins and glycogen at baseline are very different in various cell lines.

(iv) Although the synthetic route was improved through automating the radiosynthesis of CuAAC “click” chemistry, the purification of [$^{18}$F]NFTG still remains challenging and not compatible with the requirements of GMP production for clinical use.

## 5.3 Evaluation of a fluorine-18 radiolabelled fluorescent chalcone for detecting glycogen

In addition to glycogenesis, we extended our interests to explore a novel tracer measuring stored glycogen granules. To this end, we proposed a dual-modality (fluorescence/PET) fluorine-18 radiolabelled molecule based on the structure of a previously reported molecule (namely CDg4). CDg4 was developed by Lee et al. [330] as a fluorescent probe based on the chalcone pharmacophore for *in vitro* imaging of mouse embryonic stem cells. This compound was hypothesized to bind to the unique secondary structure of glycogen α (1 → 6) in embryonic stem cell colonies. In this section, the ability of fluorescent probe **5** and fluorine-18 radiolabelled **[$^{18}$F]5** to specifically detect stored glycogen was assessed using fluorescence microscopy and *in vitro* radioactivity uptake.

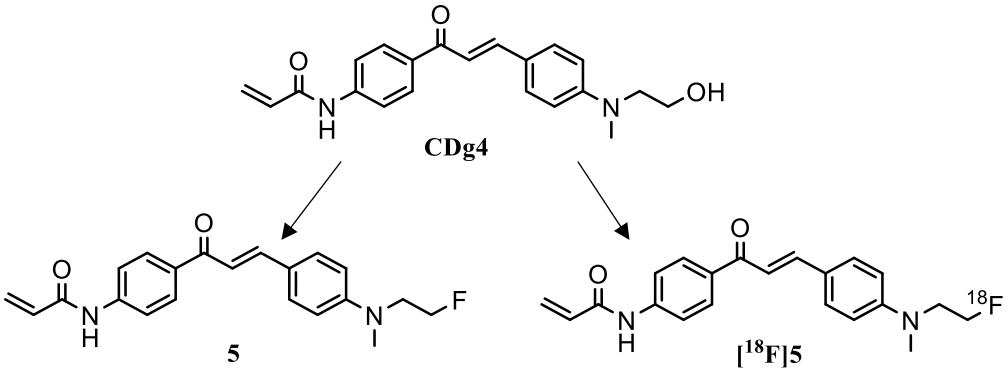


**Figure 5.5** Chemical structures of **5** and **[$^{18}$F]5** based on the previously published CDg4.

### 5.3.1 Development of dual-modality fluorescence/PET chalcones

The design and synthesis of fluorescent probe **5** and fluorine-18 radiolabelled **[$^{18}$F]5** is described in detail elsewhere [331]. Briefly, the terminal hydroxyl group of CDg4 was replaced by a fluorine atom which not only maintains the fluorescence property, but also ensured the simple fluorine-18 radiochemistry. The non-radioactive fluorine-19 derivative (**5**) was synthesized for use as a fluorescent probe as well as a high-performance liquid chromatography (HPLC) reference standard for radiochemistry development. As shown in Figure 5.6, the photochemical properties (excitation: $\lambda_{ex}$ and emission: $\lambda_{em}$) of **5** were determined to be $\lambda_{ex}$ = 420 nm/$\lambda_{em}$ = 550 nm by UV-Vis and fluorescence spectroscopy. **[$^{18}$F]5** was synthesized in a three-step radiosynthesis in 170 min with a non-decay corrected

radiochemical yield (RCY n.d.c) of 5.1 ± 0.9% (n=4) and a molar activity ($A_m$) of 7.6 GBq/µmol. The $LogD_{7.5}$ of **[$^{18}$F]5** was determined to be 1.03 ± 0.37 using the shake-flask method.

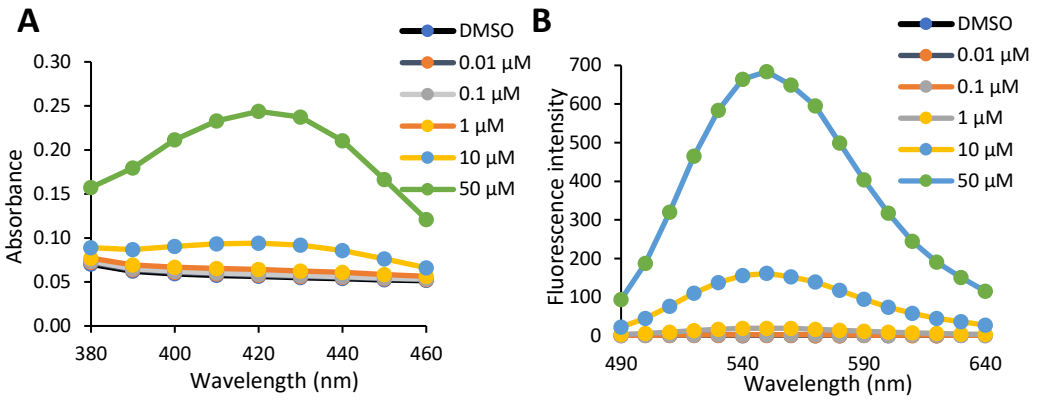


**Figure 5.6 Spectra for compound 5.**

**A,** Excitation $\lambda_{ex}$ = 420 nm. **B,** Emission $\lambda_{em}$ = 550 nm. Compound 5 was dissolved in DMSO at the indicated concentrations of 0.01, 0.1, 1, 10 and 50 µM. Each condition was assayed in triplicate in 96-well dark plates using a standard plate reader (Infinite 200 PRO, Tecan). Absorption spectra was obtained using the wavelength ranging from 380 and 460 nm. The wavelength of maximum absorption was further used to determine the fluorescence spectra of compound 5.

### 5.3.2 Evaluation of specificity of fluorescent probe (5) to cellular stored glycogen

To assess the ability to bind glycogen, compound **5** was evaluated by fluorescence microscopy in a panel of cancer cell lines (IGORV-1, HCT116, MCF-7 and T47D) with different glycogen level (Figure 5.7B). Compared to the other three tested cell lines, HCT116 had the lowest accumulation of glycogen which was used as a negative control.

A concentration-dependent increase of fluorescent intensity was observed among the four cell lines (Figure 5.7C). However, 4 µM was thought to be a more appropriate concentration to compare the staining specificity of compound **5** across the cell line panel. At a higher concentration of 8 µM, there might be other non-specific binding due to a high accumulation of this compound within cells over a short period of 1 h. Of all the four cell lines, IGROV-1 showed the most fluorescent intensity at a concentration of 4 µM of compound **5**, while HCT116 cells exhibited the least fluorescence accumulation. The two cell lines were further chosen to study the specificity of compound 5 to glycogen following α-amylase incubation. The intensity of green fluorescence produced by **5** was diminished in both cells

when treated with α-amylase to digest carbohydrate polymers, suggesting a specific binding to glycogen-related macromolecules by **5.**

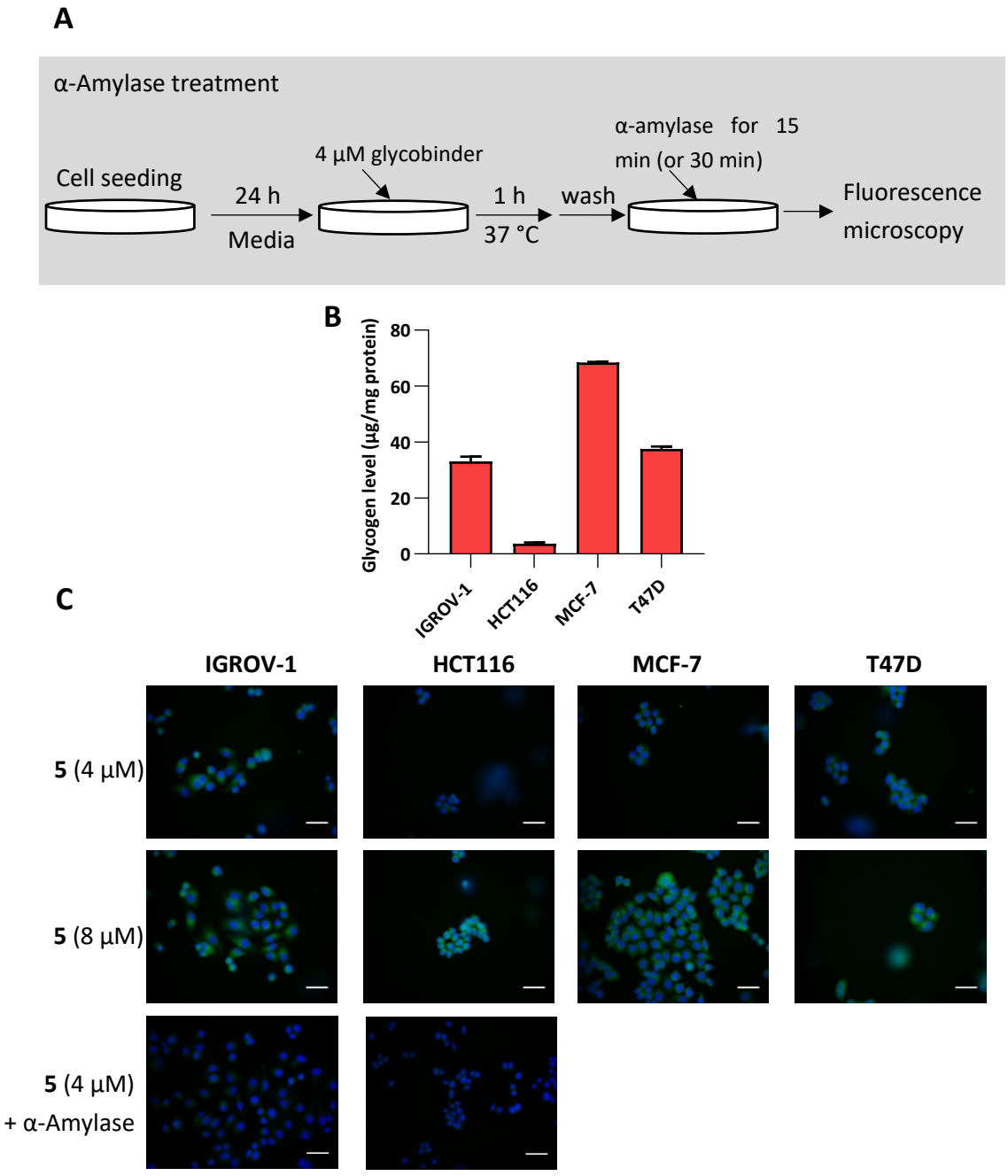


**Figure 5.7 Fluorescence microscopy of compound 5 (green fluorescence), nuclear staining (blue fluorescence) in four cancer cell lines.**

**A,** Schematic showing α-amylase treatment. **B,** Total glycogen level. **C,** Fluorescence microscopy. Cells were incubated with two concentrations (4 and 8 µM) of compound **5** for 1 h at 37 °C in dark. IGROV-1 and HCT116 cells treated with α-Amylase to digest carbohydrates were also assessed. Images were obtained under 400 × magnification. Scale bar = 50 µm.

### 5.3.3 *In vitro* cell uptake of [$^{18}$F]5

To further test the ability of **[$^{18}$F]5** to bind to glycogen granules, a panel of 11 cancer cell lines was used. The total glycogen level was first determined among the cell line panel using a modified GO assay kit (Figrue 5.8A). Consistent with previous observations, RCC4 (-pVHL), RCC4 (+pVHL) and U87 shPYGL cells displayed the most accumulation of glycogen, whereas lower levels were seen in 786-O, MDA-MB-231 and HCT116 cell lines.

As shown in Figure 5.8B, the radiotracer uptake was much higher in 786-O, MCF-7, T47D and HCT116 cells (24.98 ± 1.43, 21.02 ± 1.61, 15.73 ± 1.23 and 15.80 ± 0.61 %ID/mg protein, respectively) when compared to the remaining cell lines which had an average uptake of 11.01 ± 0.62 %ID/mg protein. It was expected that **[$^{18}$F]5** uptake would correlate with total glycogen level, however, despite stark differences in uptake in some cell lines, no correlation ($R^2$=0.03) with total glycogen was observed (Figure 5.8C).

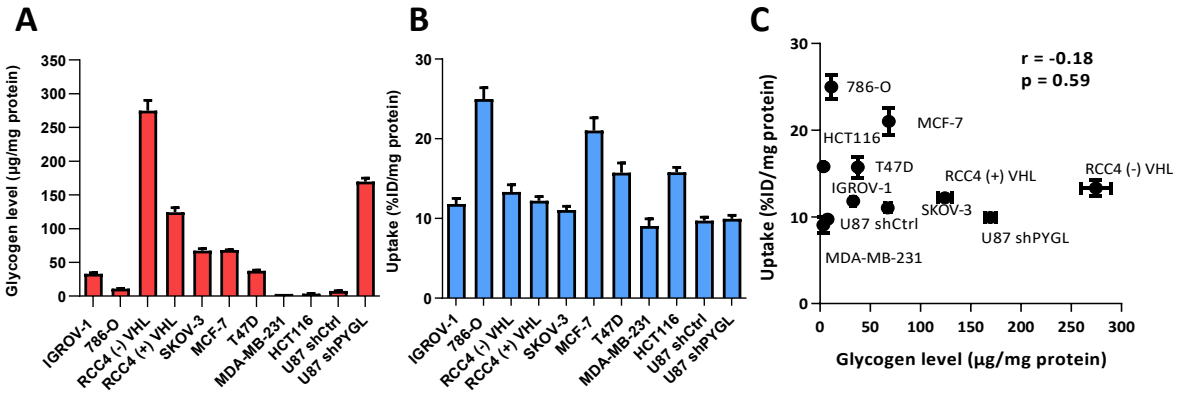


**Figure 5.8 Correlation of [$^{18}$F]5 uptake to total glycogen level among a panel of cancer cell lines.**

**A,** Total intracellular glycogen level. Cells were each seeded at an appropriate density in 6-well plates and allowed to attach overnight. After 24 hours, cells were collected and subjected to glycogen assay by using a modified GO assay kit. Mean values ± SD (n=3). **B,** *In vitro* [$^{18}$F]5 uptake. Cells under the same culturing conditions were incubated with fresh DMEM media containing 0.74 MBq **[$^{18}$F]5** for 1 h at 37 °C in a humidified atmosphere of 5% $CO_2$. Mean values ± SD (n=6). **C,** Pearson correlation coefficient (r) was determined by Graphpad Prism. Scatter plot points represent independent experimens perfomred in triplicate. Two-tailed t test was used.

### 5.3.4 Discussion

In this section, two analogues of CDg4 were developed and investigated for use as a dual-modality fluorescence/PET probe measuring stored glycogen in a panel of cancer cell lines.

Fluorescent probe **5** was observed to accumulate in glycogen-containing cells by fluorescence microscopy, and the signal was diminished by enzymatic digestion of carbohydrates using α-amylase. However, there was no correlation between total glycogen level and *in vitro* uptake of **[$^{18}$F]5** in the investigated cancer cell lines.

In addition to [$^{18}$F]NFTG, which was thought to measure GYS activity, we sought to develop PET imaging agents that could directly measure total stored glycogen. Lee et al. [330] reported the successful use of a chalcone-based fluorescent probe (CDg4) for *in vitro* staining mouse embryonic stem cells (mESC). Further studies found that CDg4 uniquely responded to glycogen in a dose-dependent manner with a maximal 66-fold fluorescence increase; in contrast, CDg4 showed no response to dextran, amylose, dermatan sulphate, hyaluronic acid and heparin, which are structurally similar carbohydrate polymers to glycogen. The specific staining of CDg4 to glycogen was speculated to rely on the unique secondary structure of α (1 → 6) of glycogen. Based on the chemical structure of CDg4, fluorescent probe **5** and fluorine-18 radiolabelled **[$^{18}$F]5** were synthesised by Dr. Louis Allott and Dr. Diana Brickute [331] with the aim of using as a dual-modality fluorescence/PET probe in tumour cells.

The photochemical properties of compound **5** were determined to be $\lambda_{ex}$ = 420 nm/$\lambda_{em}$ = 550 nm, which is similar to that of CDg4 ($\lambda_{ex}$ = 430 nm/$\lambda_{em}$ = 560 nm), indicating that replacing the hydroxyl group with fluorine had minimal effect on fluorescence property. It was found that the intensity of green fluorescence produced by compound **5** was correlated with the levels of total stored glycogen among four representative cancer cell lines. Furthermore, the amylase treatment dramatically reduced the fluorescence intensity of IGROV-1 and HCT116 cells stained by compound **5**, indicating that the molecular binding target of compound **5** might be carbohydrate polymers.

The promising results obtained from fluorescence microscopy warranted the *in vitro* assessment of radiolabelled **[$^{18}$F]5** to measure stored glycogen in a panel of 11 cancer cell lines. *In vitro* uptake of **[$^{18}$F]5** was high in all cell lines (>10% ID/mg protein), with the highest accumulation observed in 786-O, MCF-7, T47D and HCT116 cells showing 1.4 - 2.3 fold higher accumulation. Although the mechanism of uptake of **[$^{18}$F]5** remains unclear, it was hypothesized to be via passive diffusion due to its slightly lipophilic property (LogD7.5 = 1.03 ± 0.37). However, correlation analysis found that there was no correlation between total

glycogen level and tracer retention across the cell lines tested. The differences in **[$^{18}$F]5** uptake between cell lines might be based on a non-specific mechanism, which may be explained by the formation of covalent bonds between **[$^{18}$F]5** and cellular components (e.g. proteins, biomolecules).

Collectively, although qualitative fluorescence microscopy showed the accumulation of compound **5** in cells which exhibited high levels of stored glycogen, radiotracer uptake did not produce comparable results. The so-called "mass effect" might be one of the causes of the difference in the *in vitro* performance of **5** and **[$^{18}$F]5.** The quantity of compound **5** which was used at 4 µM and 8 µM as a fluorescent probe was approximately 40- and 80-fold higher than the radiotracer uptake experiment where **[$^{18}$F]5** was used at ca 100 nM (0.74 MBq at 1 mL, molar activity of 7.6 MBq/nmol). A higher concentration of compound **5** may have been sufficient to overcome non-specific reactivity towards cellular components and hence exerted desired effects. A study on EGFR inhibitors has indicated a similar "mass effect", where drugs when used at high doses result in effective response despite many being substrates of permeability glycoprotein (P-gp) [332].

## 5.4 Evaluation of a novel PET radiotracer for detecting lipofuscin accumulated in senescence

### 5.4.1 Introduction

The presence of lipofuscin, an aggregate of oxidized proteins, lipids and metals, has been observed in various types of senescent cells [44; 333], making it a potential biomarker of cellular senescence. Although the mechanism for the formation of lipofuscin has not been identified, reactive oxygen species (ROS) produced during senescence is thought to have an influence. Increased ROS levels result in the carbonylation of several protein residues such as proline, threonine, lysine and arginine, in the presence of metal. These carbonyl residues are further converted to Schiff bases via reacting with amino groups and promote protein aggregation. The insoluble lipofuscin is eventually formed by cross-linking the protein aggregates with sugars and lipids [46]. Lipofuscin can be visualized by fluorescence microscopy based on its natural feature of autofluorescence and stained by histochemical stain [334; 335].

Sudan Black B (SBB), which is a lipophilic histochemical stain, has been commonly used for identification of lipofuscin [335]. SBB staining is an easy and rapid method that provides reliable and reproducible results when used in various settings. SBB is applicable for both *in vitro* cell studies and *in situ* in fresh-frozen or archival (formalin fixed-paraffin embedded, FFPE) tissues. The application of SBB in specific recognition of senescent cells has been reported through staining lipofuscin granules [335]. To improve the sensitivity and specificity of SBB, Salmonowicz et al. developed a biotin-linked SBB derivative for the antibody-enhanced detection of lipofuscin, which has been commercialized and known as SenTraGor™ [336].

Despite the various methods applied, detection of lipofuscin *in vivo* has yet to be reported. Radiotracer imaging techniques have shown great promise for the non-invasive detection of a series of biological processes *in vivo*. Therefore, we proposed a fluorine-18 radiolabelled molecule [$^{18}$F]FET-SBB and its non-radioactive compound [$^{19}$F]FET-SBB based on the structure of SBB for use as specific imaging agents targeting lipofuscin.

### 5.4.2 Development of SBB derivatives

The design and synthesis of [$^{19}$F]FET-SBB and fluorine-18 radiolabelled [$^{18}$F]FET-SBB is described in detail elsewhere (Brickute and Allott et al, publication in preparation). [$^{18}$F]FET-SBB was synthesized in 120 min with a non-decay corrected radiochemical yield (RCY n.d.c) of 5%. The $LogD_{7.5}$ of [$^{18}$F]FET-SBB was determined to be 1.57 ± 0.18 (n=3) using the shake-flask method.

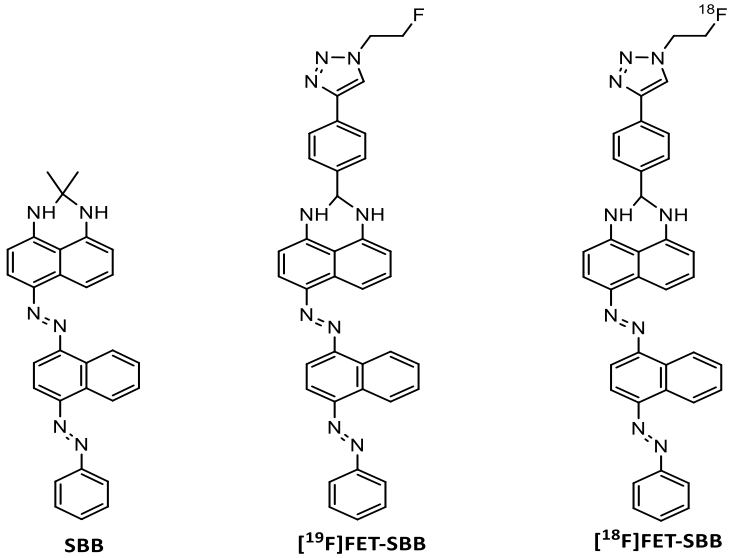


**Figure 5.9 Chemical structures of [$^{19}$F]FET-SBB and [$^{18}$F]FET-SBB based on SBB.**

### 5.4.3 Determination of autofluorescence of lipofuscin in drug-induced senescence

Next, the levels of lipofuscin in palbociclib- and MLN8054-treated cells were determined using fluorescence microscopy based on lipofuscin's autofluorescence. The effects of the two drugs on induction of senescence/quiescence have been assessed in **Chapter 4**. In brief, palbociclib was shown to effectively arrest cell growth in G0/G1 phase of cell cycle in MCF-7 cell line, with senescence-like phenotypes observed at 72 h post-treatment (10 µM of palbociclib). T47D cells also entered G0/G1 phase arrest in response to palbcocilib and dose-dependently exhibited senescence-like cell morphology. In contrast, although a G2/M cycle arrest was induced by MLN8054 in HCT116 cells, this effect was shown to be reversible, but not an irreversible senescence arrest. MCF-7 cells showed no response to MLN8054 treatment under the indicated treatment conditions.

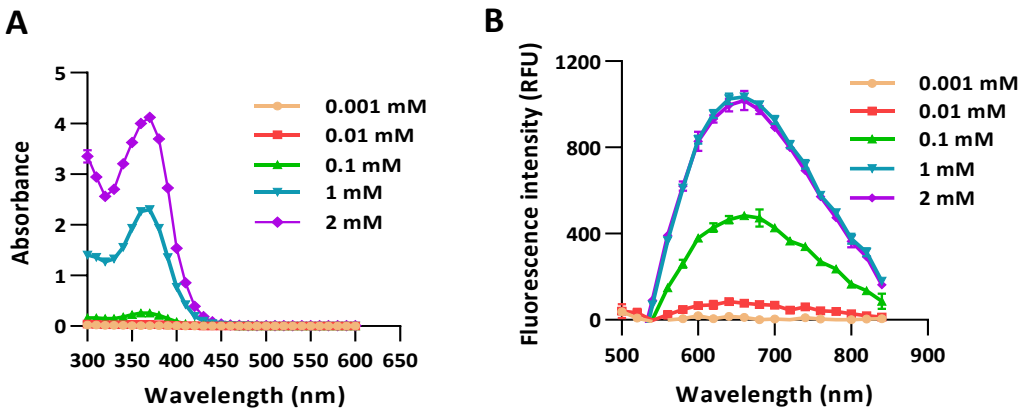


**Figure 5.10 Spectra for palbociclib.**

**A,** Excitation $\lambda_{ex}$ = 365 nm. **B,** Emission $\lambda_{em}$ = 660 nm. Palbociclib was freshly dissolved in DMSO at indicated concentrations. Each condition was assayed in triplicate in 96-well dark plates using a standard plate reader (Infinite 200 PRO, Tecan). Absorption spectra was obtained using the wavelength ranging from 300 and 600 nm. The wavelength of maximum absorption was further used to determine the fluorescence spectra of palbociclib.

The optimal fluorescent channels for detecting lipofuscin are FITC ($\lambda_{ex}$ = 488 nm and $\lambda_{em}$ = 509 nm) or TRICT channel ($\lambda_{ex}$ = 535 nm and $\lambda_{em}$ = 572 nm). Palbociclib exhibits intrinsic fluorescence and therefore it was important to rule out any overlap of its excitation and emission spectra with the autofluorescence of lipofuscin. The photochemical properties of palbociclib (Figure 5.10) were determined by UV-Vis ($\lambda_{ex}$) and fluorescence spectroscopy ($\lambda_{em}$). Palbociclib showed an optimal photochemical characteristic ($\lambda_{ex}$ = 365 nm and $\lambda_{em}$ = 660 nm) which did not overlap with lipofuscin.

As shown in Figure 5.11A and B, an increased intensity of lipofuscin autofluorescence was observed in MCF-7 and T47D cells following palbociclib treatment in a dose-dependent manner. In contrast, MLN8054 did not result in the formation of lipofuscin, as shown by the absence of green fluorescence in HCT116 and MCF-7 cells (Figure 5.11 C and D).

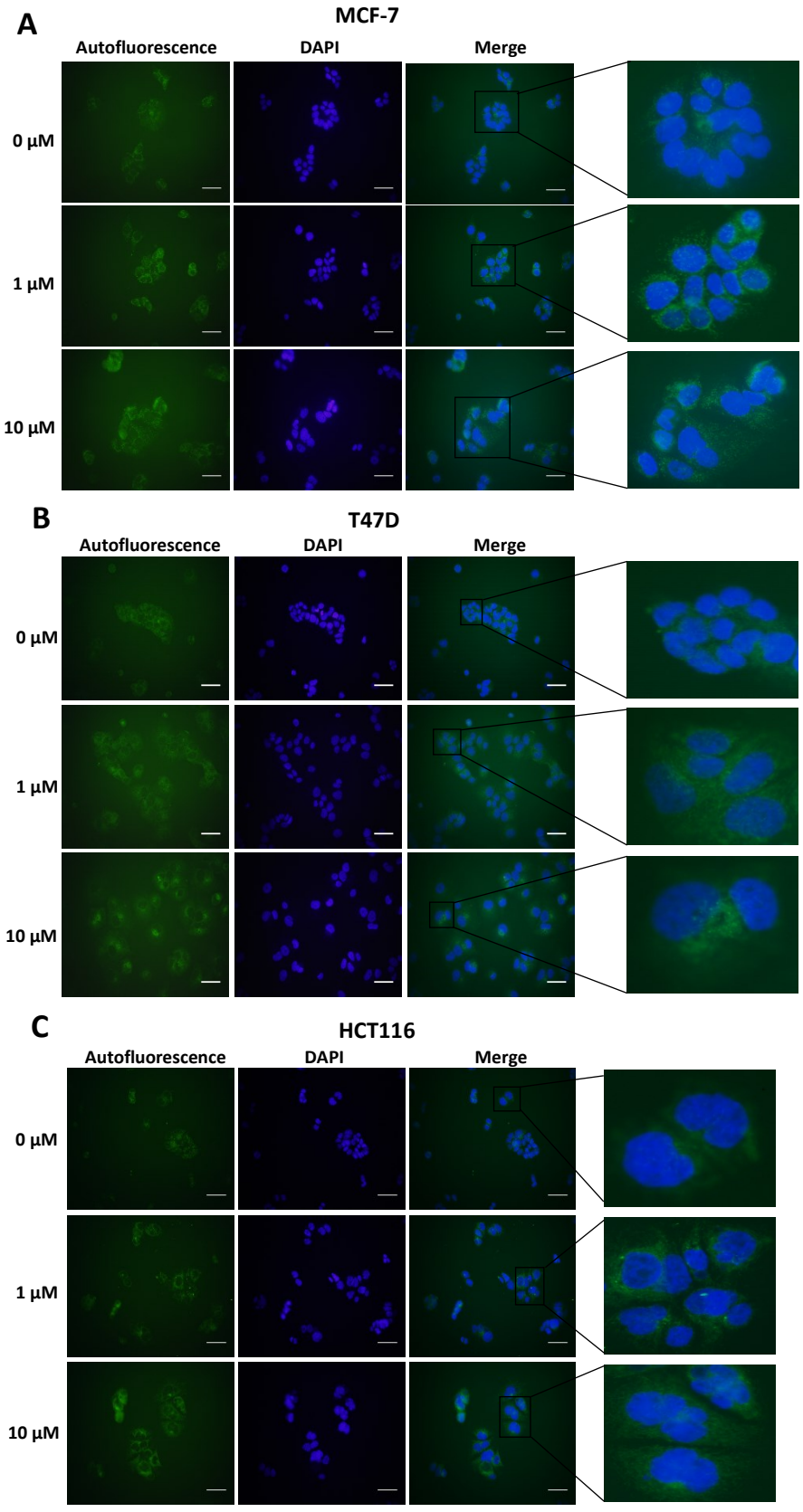
A
MCF-7
Autofluorescence
DAPI
Merge
0 µM
1 µM
10 µM
B
T47D
Autofluorescence
DAPI
Merge
0 µM
1 µM
10 µM
C
HCT116
Autofluorescence
DAPI
Merge
0 µM
1 µM
10 µM

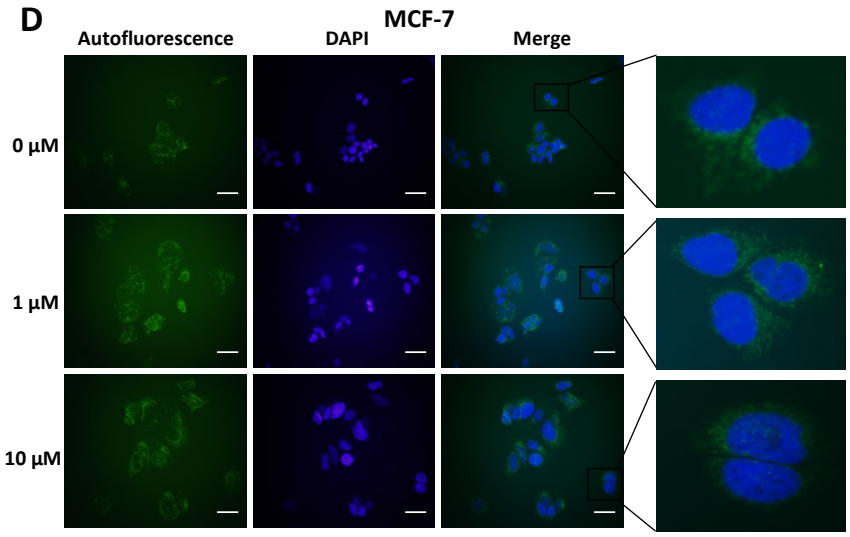


**Figure 5.11 Autofluorescence of lipofuscin in cancer cells following palbociclib and MLN8054 treatment.**

Representative images of autofluorescence of lipofuscin in MCF-7 **(A)** and T47D **(B)** cells following palbociclib treatment, and in HCT116 **(C)** and MCF-7 **(D)** cells following MLN8054 treatment. Briefly, cells were treated with palbociclib or MLN8054 at indicated concentrations for 72 h and then re-plated in 8-well chamber slides at each appropriate seeding density. After 24 h, cells were fixed with 4% PFA for 15 min and incubated with DAPI overnight. Images were obtained on a standard fluorescence microscopy under × 400 magnification. Scale bar = 50 µm. The green colour represents lipofuscin's autofluorescence and the blue colour represents cell nuclei stained by DAPI.

### 5.4.4 Evaluation of specific staining of lipofuscin by non-radioactive [$^{19}$F]FET-SBB

Next, non-radioactive [$^{19}$F]FET-SBB was used as an *in vitro* stain to determine if the compound bound to lipofuscin aggregates. Palbociclib dose-dependently resulted in accumulation of perinuclear and cytoplasmic aggregates in MCF-7 and T47D cells (Figure 5.12 A and B), which were accordingly stained by [$^{19}$F]FET-SBB as blue-dark granules. MLN8054, however, did not lead to the similar aggregates stained by [$^{19}$F]FET-SBB (Figure 5.12 C and D). These data are consistent with the pattern of lipofuscin's autofluorescence, suggesting the specific staining of lipofuscin by [$^{19}$F]FET-SBB in palbociclib-induced senescent cells. The mechanism of how [$^{19}$F]FET-SBB binds to lipofuscin remains unclear, it is likely to work in the same way as SBB via interacting with the lipid compartment of lipofuscin due to its high lipophilicity [335; 337]. The promising results of [$^{19}$F]FET-SBB warranted further investigation of the radiolabelled [$^{18}$F]FET-SBB as a imaging probe for senescence-associated lipofuscin accumulation.

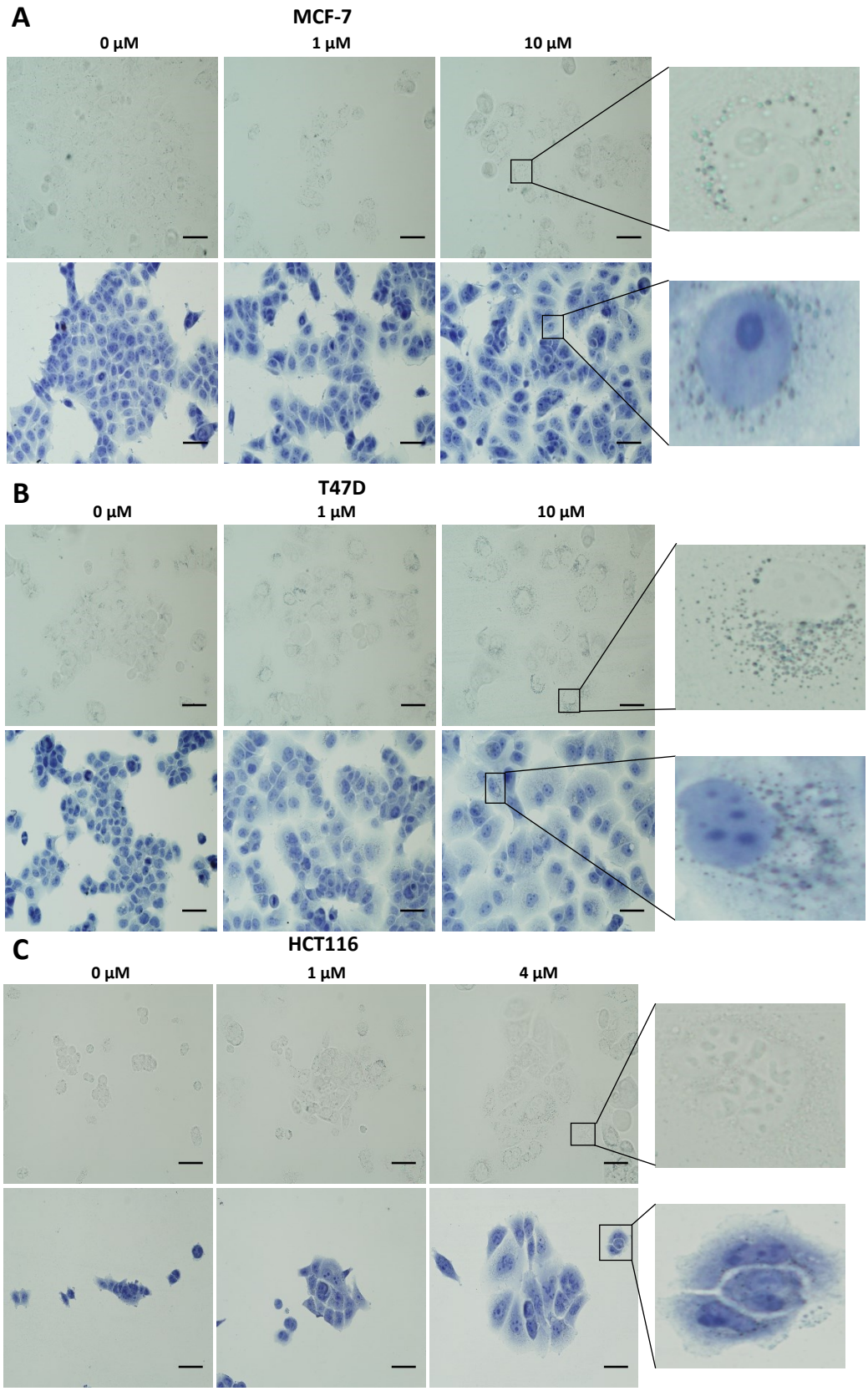
A
MCF-7
0 µM
1 µM
10 µM
B
T47D
0 µM
1 µM
10 µM
C
HCT116
0 µM
1 µM
4 µM

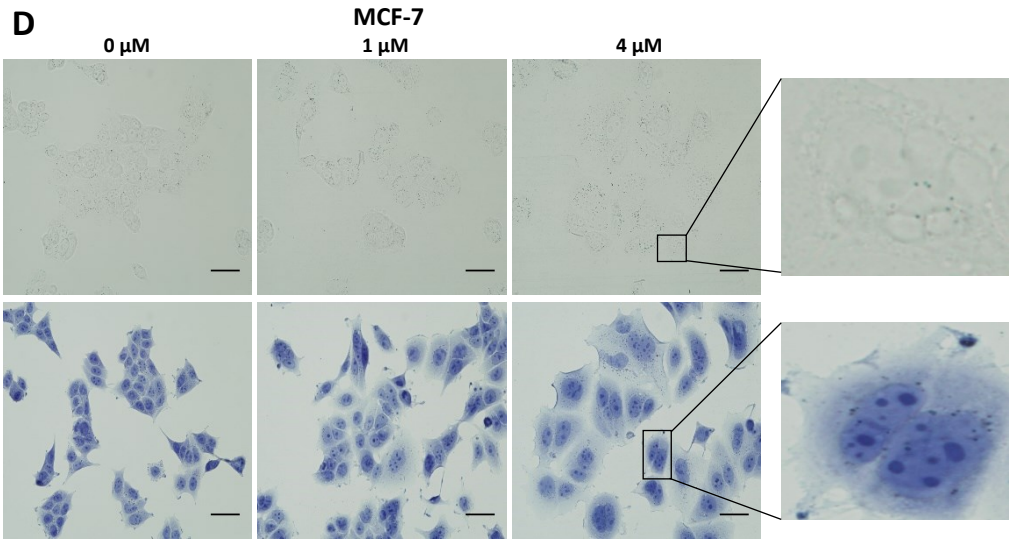


**Figure 5.12 [$^{19}$F]FET-SBB staining in cancer cells following palbociclib and MLN8054 treatment.**

Representative images of FET-SBB staining in MCF-7 **(A)** and T47D **(B)** cells following palbociclib treatment, and in HCT116 **(C)** and MCF-7 **(D)** cells following MLN8054 treatment. Briefly, cells were treated with palbociclib or MLN8054 at indicated concentrations for 72 h and re-plated in 8-well chamber slides at appropriate seeding density. After 24 h, cells were fixed in ice-cold methanol for 5 min and incubated with FET-SBB solution for 10 min. Cells were quickly washed in 50% (v/v) ethanol, followed by PBS 3 tines. Cells were finally counterstained in Hematoxylin Solution, Gill No. 3, for 1 min and rinsed in running tap water. Images were obtained on a standard microscopy under 400 × magnification. Scale bar = 50 µm. FET-SBB perinuclear accumulation as dark blue - black granules. Upper images, FET-SBB stain alone; Lower images: FET-SBB stain followed by hematoxylin counterstain

### 5.4.5 *In vitro* uptake of [$^{18}$F]FET-SBB

As show in Figure 5.13A, tracer retention was significantly increased in T47D cells following palbociclib treatment, from 7.40 ± 0.58 %ID/mg protein in control cells to 9.44 ± 0.43 %ID/mg protein at 1 µM palbociclib and 8.38 ± 0.30 %ID/mg protein at 10 µM palbociclib. Unexpectedly, the uptake of [$^{18}$F]FET-SBB decreased from 8.21 ± 0.73 % ID/mg protein in untreated cells to 6.27 ± 0.30 %ID/mg protein in palbociclib-treated (10 µM) MCF-7 cells. In accordance with [$^{19}$F]FET-SBB staining, MLN8054 did not cause changes in the levels of [$^{18}$F]FET-SBB retention in HCT116 and MCF-7 cells despite a high uptake overall (Figure 5.13B).

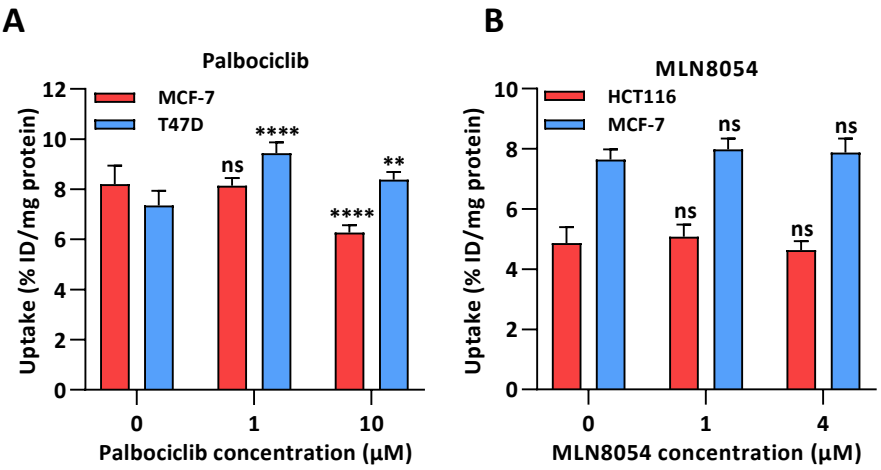


**Figure 5.13 *In vitro* uptake of [$^{18}$F]FET-SBB in cancer cells pre-treated with palbociclib (A) and MLN8054 (B).**

Cells were pre-treated as previously described and re-plated at each appropriate density in 6-well plates 24 h prior to uptake. On the day of uptake, cells were incubated with fresh media containing 0.74 MBq [$^{18}$F]FET-SBB for 1 h at 37 ℃ in a humidified condition of 5% $CO_2$. The radioactivity of 200 µL lysate was counted on a WIZARD2 Automatic Gamma Counter. Data was expressed as a percentage of radioactivity incorporated into cells, normalised to total cellular protein as measured by BCA assay. Mean values ± SD (n=6; **, $P < 0.01$; ****, $P < 0.0001$).

### 5.4.6 Validation of specificity of [$^{18}$F]FET-SBB in more *in vitro* senescent models

In order to cross validate the specificity of [$^{18}$F]FET-SBB to detect senescence-associated accumulation of lipofuscin, two experimental settings of senescence were conducted in parallel assessed in collaboration with Prof. Jesus Gil's group at Imperial College London.

Cellular senescence was triggered by either oncogenic RAS in normal fibroblasts or 0.5 µM palbociclib in a liver carcinoma cell line (SK-HEP-1) over a period of 9 days. IMR90 human primary fibroblasts were infected with a vector expressing an ER:RAS fusion, where H-RAS$^{G12V}$ is fused to a mutant form of the estrogen receptor (ER) ligand binding domain. Activation of RAS upon 4-hydroxy-tamoxifen (4-OHT) treatment caused IMR90 ER:RAS cells to undergo senescence, serving as an optimal tool to study senescence [338]. A senescence-like phenotype was confirmed by using SA-β-gal staining, in which greater than 90% of cells showed positive response to SA-β-gal under both conditions (Figure 5.14A).

To assess the accumulation of lipofuscin, a commercially available kit SenTraGor$^{TM}$, involving a biotin-linked SBB, was used in both cellular settings (Figure 5.14B). Senescent

fibroblasts induced by RAS exhibited a 1.2-fold increase in the intensity of positive-stained cells by SenTraGor™, whereas palbociclib-treated SK-HEP-1 cells showed no changes in cell intensity stained by SenTraGor™ when compared to control cells.

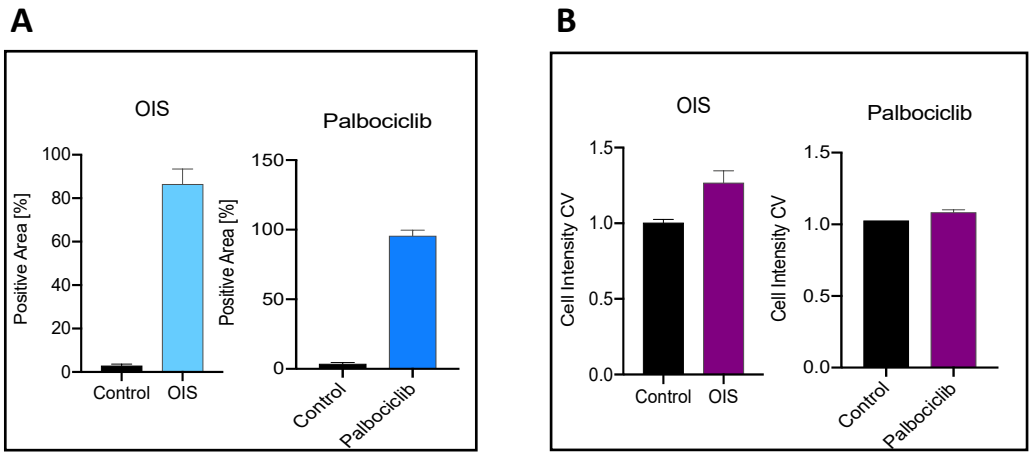


**Figure 5.14 Evaluation of SA-β-gal activity and lipofuscin accumulation in senescent fibroblasts induced by RAS oncogene and palbociclib-treated SK-HEP-1 cells.**

**A,** Percentage of the positive area of stained cells by SA-β-gal. **B,** Cell intensity of stained cells by sentragor (SBB analogue conjugated with biotin). Prior to SA-β-gal and sentragor assay, ER:RAS cells were treated with 4-hydroxytamoxifen (4OHT) for 9 days in OIS model, while SK-HEP-1 cancer cells were treated with 0.5 µM of palbcociclib for 9 days. (in collaboration with Prof. Jesus Gil and Dr. Verena Wagner)

We next examined the accumulation of [$^{18}$F]FET-SBB under oncogenic RAS/palbociclib induction conditions in the two cell lines (Figure 5.15A). Following RAS induction, uptake of [$^{18}$F]FET-SBB remained unchanged when compared to control cells (5.59 ± 0.23 %ID/mg protein in RAS-induced cells vs. 5.22 ± 0.53 %ID/mg protein in controls). In comparison, palbociclib significantly reduced the retention of radioactivity in SK-HEP-1 cells, from 4.06 ± 0.15 %ID/mg protein in untreated cells to 1.85 ± 0.12 %ID/protein in treated cells ($p < 0.0001$).

By comparison, the uptake of [$^{18}$F]FpyGal [339], a recently emerging senescence-specific PET probe that measures the activity of β-galactosidase, was increased in both cell lines despite the low uptake overall (Figure 5.15B). In RAS-induced fibroblasts, [$^{18}$F]FpyGal retention was dramatically increased from 0.38 ± 0.09 %ID/mg protein in controls to 0.60 ± 0.03 %ID/mg protein ($p < 0.001$). Palbociclib treatment increased the uptake of [$^{18}$F]FpyGal to a lesser extent, from 0.18 ± 0.04 %ID/mg protein in untreated cells to 0.22 ± 0.02 %ID/mg protein in treated cells ($p < 0.05$).

The standard radiotracer [$^{18}$F]FDG was, in parallel, used for assessing the rate of glucose utilization in the tested cell lines (Figure 5.15C). [$^{18}$F]FDG cell uptake in RAS-induced fibroblasts at 60 min was 8.25 ± 0.66 %ID/mg protein, 1.7-fold higher than controls (4.75 ± 0.12 %ID/mg protein; $p < 0.0001$). In contrast, [$^{18}$F]FDG uptake was 2.8-fold lower in palbociclib-treated versus vehicle-control cells, at 6.51 ± 0.35 %ID/mg protein and 18.41 ± 0.79 %ID/mg protein, respectively ($p < 0.0001$).

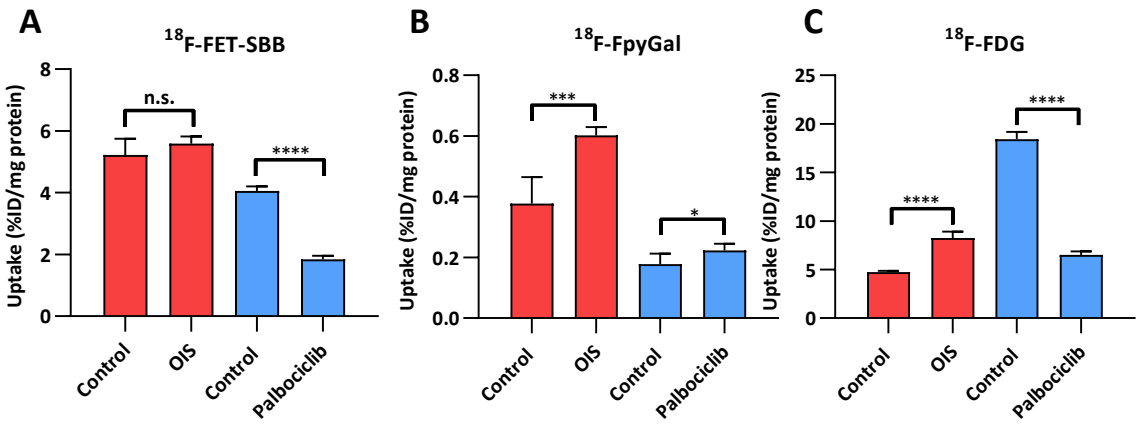


**Figure 5.15 *In vitro* cell uptake of [$^{18}$F]FET-SBB (A), [$^{18}$F]FpyGal (B), and [$^{18}$F]FDG (C) in oncogene-induced senescence (OIS) and palbociclib-induced senescence.**

Prior to uptake, ER:RAS cells were treated with 4-hydroxytamoxifen (4OHT) for 9 days in OIS model, while SK-HEP-1 cancer cells were treated with 0.5 µM of palbcociclib for 9 days. On the day of uptake, cells were incubated with fresh media containing 0.74 MBq radiotracer ([$^{18}$F]FET-SBB, [$^{18}$F]FpyGal or [$^{18}$F]FDG) for 1 h at 37℃ in a humidified atmosphere of 5% $CO_2$. Mean values ± SD (n=6). Two-tailed, unpaired, Student's t-tests were used to determine statistically significant differences between control and treated group in GraphPad Prism v.8.3.1 (* $P < 0.05$, *** $P < 0.001$, **** $P < 0.0001$).

### 5.4.7 *In vivo* metabolite analysis

To understand the *in vivo* metabolic profiles of [$^{18}$F]FET-SBB, metabolites in the liver, plasma and urine were determined by radio-HPLC at 60 min post-injection. As shown in Figure 5.16, [$^{18}$F]FET-SBB showed good stability (>95%) in the liver and plasma at 60 min after injection, with only the peaks of parent compound detectable. Only two polar metabolites were seen in urine, however, the quantity of radioactivity was very low.

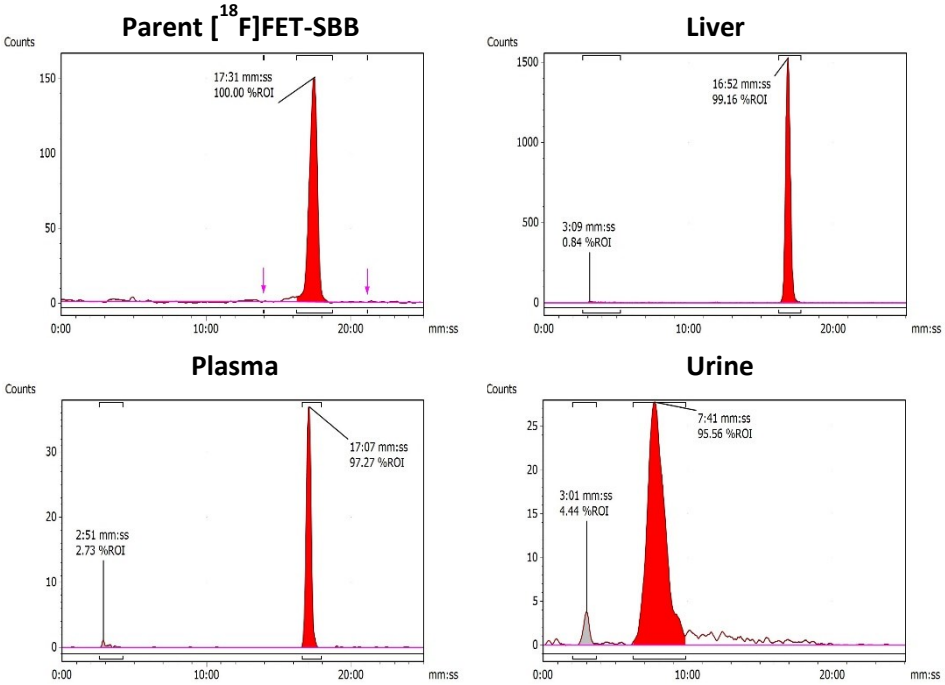


**Figure 5.16** ***In vivo*** **metabolic stability of [$^{19}$F]FET-SBB in liver, plasma and urine.**

Representative radio-chromatograms of parent [$^{18}$F]FET-SBB ($t_R$ = 17:31 min:sec) and metabolites extracted from liver, plasma and urine at 60 min p.i.; efficiencies of radioactivity extraction from liver and plasma were 76.9 ± 5.5 and 77.6 ± 6.9% of total radioactivity, respectively**.**

### 5.4.8 Discussion

The aim of this section was to develop a fluorine-18 radiolabelled compound ([$^{18}$F]FET-SBB) measuring the accumulation of lipofuscin as a potential biomarker of cellular senescence. Reference compound [$^{19}$F]FET-SBB was successfully synthesised and assessed for its staining specificity to lipofuscin in cell-based studies. The fluorine-18 radiolabelled [$^{18}$F]FET-SBB was synthesized in a RCY n.d.c of 5%. [$^{18}$F]FET-SBB cell uptake was broadly evaluated in several *in vitro* cell models, and compared to a recently reported senescence-associated radiotracer [$^{18}$F]Fpy-Gal and the clinically standard tracer [$^{18}$F]FDG, for the detection of cellular senescence.

Lipofuscin, which is an aggregate of oxidized proteins, lipids and metals, is increasingly being used as a biomarker of aging and cellular senescence. Effective identification of senescent cells, through the measurement of lipofuscin accumulation, would provide valuable insights into senescent features, allowing the assessment of cell response to

senescence-directing anticancer therapies at an early stage and the planning of clinical strategies to eliminate senescent cells in pathological settings. There have been so far considerable efforts to develop methods to measure lipofuscin, however, none is suitable for *in vivo* application. Therefore, we developed the first radiolabelled derivative of SBB to utilise the unparalleled sensitivity of PET for the detection and quantification of lipofuscin in senescent cells.

Cancer cells that were pre-treated with palbociclib or MLN8054 were used as cell models to evaluate [$^{18}$F]FET-SBB and non-radioactive [$^{19}$F]FET-SBB. Previous results in **Chapter 4** have shown senescence-like phenotypes present in MCF-7 and T47D cells in response to palbociclib, whereas MLN8054-mediated G2/M growth arrest was reversible quiescence, but not senescence in HCT116 cell line. Consistently, a dose-dependent accumulation of peri-nuclear and cytoplasmic aggregates was seen in MCF-7 and T47D cells following palbociclib treatment, as characterised by enhanced green autofluorescence and positive stain by non-radioactive [$^{19}$F]FET-SBB as blue-dark granules; while there were no similar patterns observed in HCT116 and MCF-7 cells upon MLN8054 inhibition.

In accordance with the findings of lipofuscin's autofluorescence and [$^{19}$F]FET-SBB staining, [$^{18}$F]FET-SBB uptake was significantly increased in palbociclib-treated T47D cells, but remained unchanged in HCT116 and MCF-7 cells following MLN8054 treatment. An unexpected trend was observed in MCF-7 cells, where the radioactivity retention was profoundly decreased in response to palbociclib. One explanation for the reduced uptake of [$^{18}$F]FET-SBB in MCF-7 cells may be the possibility that palbociclib facilitates the expression of efflux transporters, resulting in rapidly efflux of [$^{18}$F]FET-SBB in this cell line. Several types of imaging agents such as quinoline or quinazoline-based tracers have been found to be effluxed by members of the ATP binding cassette transporter (ABC transporters) [340]. Although there is no direct evidence highlighting the regulatory effect of palbociclib on the expression or function of ABC transporters, palbociclib has been found to be substrate of permeability protein (P-gp) and breast cancer resistance protein (BCRP) at the blood-brain barrier level [341]. An additional explanation is that palbociclib-mediated autophagy might partially contribute to the decreased tracer uptake in MCF-7 cells. In addition to senescence, palbociclib at a high dose (10 μM) also triggered cell autophagy in MCF-7 cells, as shown by increased expression of LC3B-II, which is a standard marker for autophagosomes (Figure

4.22). Levels of P-gp have been found positively correlated with LC3B expression in tumour samples from colorectal cancer patients, indicating that efflux transporters might be upregulated under cell autophagy [342; 343]. Further studies utilising ABC transporter inhibitors may be explored to verify this hypothesis.

In order to validate the feasibility of [$^{18}$F]FET-SBB to target senescence-associated lipofuscin accumulation, *in vitro* tracer uptake was assessed in two additional experimental models of cellular senescence, which were induced by oncogenic RAS or palbociclib used at a clinically-relevant concentration. Ectopic expression of oncogenes such as RAS or BRAF has been shown to induce senescence in multiple cell types such as fibroblasts, melanocytes, hepatocytes or different epithelial cells [11]. As expected, RAS triggered senescence in fibroblasts, as characterised by increased SA-β-gal activity, with a small increase in lipofuscin accumulation determined by SenTraGor$^{TM}$. Consistently, the uptake of [$^{18}$F]FpyGal, which measures SA-β-gal activity, was dramatically increased in OIS cells, while the changes in [$^{18}$F]FET-SBB retention showed no significant difference despite a subtle increase. Elevated [$^{18}$F]FDG uptake in OIS might also be indicative of senescence, as increased glucose utilization is found to be a feature of cellular senescence [344; 345]. In a similar model of oncogenic RAS-driven senescence in human fibroblasts, retinoblastoma protein (Rb) was responsible for increased glycolysis and subsequent mitochondrial OXPHOS activities through upregulating a series of glycolytic genes at the mRNA levels [68].

Additionally, palbociclib was used at a clinically relevant concentration of 0.5 μM to induce senescence in a liver carcinoma cell line SK-HEP-1 during a period of 9 days. Greater than 90% of SK-HEP-1 cells were positively stained by SA-β-gal after palbociclib treatment, however, no stain was observed by SenTraGor$^{TM}$, suggesting that chronic senescence induced by a low dose of palbociclib enhanced SA-β-gal activity, but did not result in the formation of lipofuscin. *In vitro* uptake confirmed a similar trend that [$^{18}$F]FpyGal retention had a significant increase, while [$^{18}$F]FET-SBB was largely reduced upon palbociclib treatment. The decreased [$^{18}$F]FET-SBB retention in treated cells, as discussed, might be a result of palbociclib-mediated upregulation of efflux transporters, thus leading to rapidly efflux of the tracer.

It remains unclear why not all senescent cells in this study accumulated lipofuscin. The formation of lipofuscin is initiated by high levels of ROS [46], so it is likely that only senescent

cells harbouring increased ROS are prone to accumulate lipofuscin. In addition, the presence of lipofuscin during senescence might be transient and temporal as senescence is now recognized as a dynamic multistep process [73; 346].

In conclusion, this section demonstrates in preclinical models of senescence, that a novel PET radiotracer and its non-radioactive derivative are sensitive to the accumulation of lipofuscin. Lipofuscin appears to label senescent cells at baseline but this is not the same with drug treatment. A difference between lipofuscin autofluorescence, [$^{19}$F]FET-SBB staining and [$^{18}$F]FET-SBB uptake is possibly due to efflux mechanism of the radiotracer, however, this hypothesis requires further testing of a metabolically stable radiotracer.

# Chapter 6 Summary and prospects

## 6.1 Summary of work

In this thesis, three principal aims were proposed and investigated. First, to characterise the profiles of glycogenesis/glycogen storage in a variety of cancer cell lines and identify crucial factors engaging tumour-associated reprogramming of glycogen metabolism. Secondly, to investigate the effect of distinct anticancer drugs on senescence/quiescence induction and its link to glycogenesis/glycogen alterations. Thirdly, to assess the ability of several novel radiotracers to detect cellular senescence, based on measurement of glycogenesis and lipofuscin.

Since the observation in 1961 by Hayflick and his colleagues [1; 2], that normal human fibroblasts have limited proliferation and irreversibly enter cell cycle arrest, many attempts have been made to understand the characteristics and function of senescent cells. In the field of oncology, drugs that could trigger senescence have been implicated as crucial anticancer treatments either alone or in combination with currently used cancer therapies. The need for specifically identifying senescent cells has become urgent, not only because this would help better understand the theory of senescence, but also guide the evolving field of pro-senescent or anti-senescent therapies. Therefore, it is important to investigate accurate biomarkers for cellular senescence and correspondingly develop specific tools to identify senescent cells with the potential of clinical translation. In this thesis, the feasibility of using glycogenesis/stored glycogen alongside lipofuscin accumulation as potential imaging biomarkers of drug-induced cancer senescence has been described, and characterisation of tumour-associated reprogramming of glycogen metabolism reported on the side.

**Profiles of glycogenesis in a variety of cancer cells**

Glycogenesis is regulated by a series of enzymes, among which GYS1 plays a dominant role under physiological conditions. This thesis demonstrated distinct profiles of glycogenesis in different cancer cell lines and the trend appears to be associated with gene mutations and baseline protein/enzyme expression in the investigated cell lines. Our results revealed an Akt-GSK3β-dependent regulation of basal GYS1 activity through PI3K pathway in PTEN-null cancer cell lines including 786-O, IGROV-1 and U87. While other PTEN wild-type cancer cell lines

might regulate the GYS1 activity in a PI3K-AKT-independent pathway. For example, mutant KRAS in MDA-MB-231 cells possibly upregulates GSK3β, and thus leads to the phosphorylation of GYS1 which inactivates the protein [234].

Throughout the thesis, there was a lack of correlation between GYS1 activity (as determined by the ratio of phosphorylation to total expression) and total glycogen accumulation under several conditions. One of the possibilities would be that apart from phosphorylation/dephosphorylation, allosteric activator G6P plays a crucial role in rapid restoration of GYS1 activity. Intracellular G6P level in this context is determined by either the rate of glucose uptake or the conversion via gluconeogenesis. Additionally, the total level of accumulated glycogen is a consequence of both glycogenesis and glycogen degradation, in which the relative contributions of the two events would lead to different levels of glycogen accumulation.

Moreover, a unique pattern of tumour glycogen metabolism was confirmed, which is cancer cells store glycogen while they are in a non-cycling phase such as the G0/G1 cycle arrest [146; 149]. The enhanced glycogen accumulation resulted in part from an increase in glycogen synthesis that was driven by increased GYS1 activity, as characterised by decreased phosphorylation of this enzyme. Further studies on the biological effects of GYS1 showed that knockdown of GYS1 by siRNA decreased total glycogen accumulation by 50% in the most responsive cell line IGROV-1, but it did not affect cell viability. In parallel, GYS1 silencing did not affect other metabolic pathway flux such as glycolysis and glutamine-glutamate cycle in IGROV-1 cells, which rules out the possibility of compensatory supplies of glycogen formation under GYS1 silencing. In comparison, cancer cells under hypoxic condition were more susceptible to GYS1 knockdown, as total glycogen level was diminished more significantly in not only IGROV-1 cells, but also 786-O and T47D cell lines. Clear cell renal carcinoma cell lines, which are characterised by high levels of glycogen storage, were shown to upregulate glycogen accumulation through a HIF-1α-GYS1-dependent manner, but less dependent on HIF-2α levels.

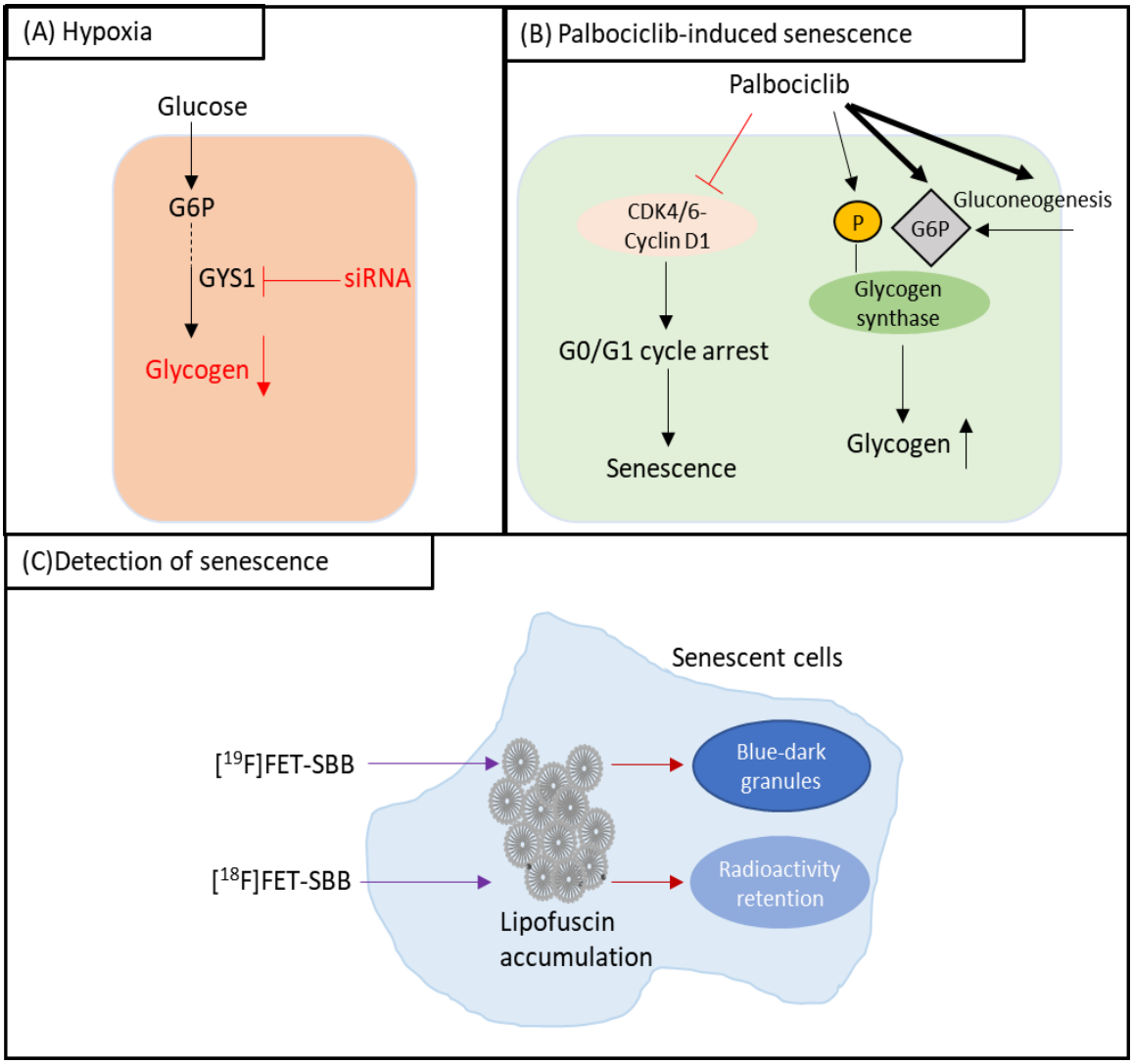


**Figure 6.1 Graphical summary of this thesis.**

**A,** Knockdown of GYS1 by siRNA significantly attenuated GYS1 accumulation under hypoxia condition in cancer cells. **B,** Palbociclib induced senescence-like phenotypes in breast cancer cell lines and elevated glycogen synthesis through G6P-dependent activation of GYS1 enzyme. **C,** Accumulation of lipofuscin in senescent cells was stained by [$^{19}$F]FET-SBB as dark-blue granules and in correlation with the retention of [$^{18}$F]FET-SBB. G6P, glucose-6 phosphate; GYS1, glycogen synthase 1.

### Evaluation of distinct anticancer drugs to induce senescence

Cancer cell senescence that is induced by pharmacological interventions has been increasingly regarded as an alternative or adjuvant treatment strategy for several types of tumours, particularly cancer cells that have developed resistance to pro-apoptotic therapies. This thesis demonstrated diverse mechanisms for senescence engagement and signalling by different

anticancer drugs. Four anticancer drugs targeting diverse downstream factors were assessed in this study for their abilities to induce cellular senescence. BEZ235, which is a PI3K/mTOR dual inhibitor, showed inhibitory effects on cell growth in a variety of cancer cell lines and resulted in a G0/G1 phase arrest. However, it turned out that BEZ235-mediated cell cycle arrest was not associated with cellular senescence in U87, MCF-7, 786-O and SKOV-3 cell lines, as shown by an absence of SA-β-gal staining and unchanged p21 expression. Next, an AMPK activator, metformin, was found to cause a weak signal of SA-β-gal staining at low doses (< 10 mM) in MCF-7 cells, whereas high-concentration metformin led to cell death, despite more profound SA-β-gal staining. Palbociclib, a drug used in clinical trials for the treatment of patients with ER-positive, HER2-negative breast cancer, was shown to induce a senescence-like phenotype in MCF-7 and T47D cells under certain treatment conditions, as shown by an irreversible G0/G1 phase arrest, enlarged cell size and flattened cell shape, increased SA-β-gal activity and p21 expression. In addition to G0/G1 phase, we also investigated whether cells under G2/M phase arrest could transit to senescent state. To this end, MLN8054, an aurora kinase inhibitor, was assessed. In response to MLN8054, although HCT116 showed an increased SA-β-gal activity, reversibility experiments revealed that cells under MLN8054-mediated G2/M arrest could re-enter the cell cycle in the absence of the drug, suggesting a quiescent growth arrest, but not senescence. Collectively, palbociclib was the only drug tested in this study that could lead to senescence-like phenotypes *in vitro*, which warrants the further use of palbociclib-treated cell models for radiotracer evaluation.

**Exploration of changes in glycogenesis in response to drug treatment**

Given the fact that glycogen accumulates in cancer cells under non-proliferating phase, attempts were made to explore glycogenesis as a biomarker of cancer senescence induced by chemotherapies. Senescence, relative to quiescence, appears to be associated with glycogenesis; although the latter can also occasionally be associated with glycogenesis. We found that there was a significant increase in glycogen levels in MCF-7 cells upon palbociclib treatment. Increased glycogen accumulation was perhaps in part a result of enhanced glycogen synthesis driven by GYS1 that was upregulated by the allosteric activator G6P, but not phosphorylation-dependent regulation; or by increased G6P *per se* via increased gluconeogenesis. By comparison, profiles of glycogenesis following treatment of three other tested drugs were determined, where enhanced glycogen storage was also observed in SKOV-

3 and 786-O cells in response to BEZ235 as well as in HCT116 and MCF-7 cells under long-term MLN8054 treatment.

**Assessment of novel radiotracers to specifically detect drug-induced senescence**

The diversity and extent of senescence means that, of the tracers examined in this thesis, none was completely robust for measurement of senescence. The second-generation glucosamine-based PET radiotracers, [$^{18}$F]FB-Glucosamine and [$^{18}$F]FB-Galactosamine, were developed based on the structure of [$^{18}$F]NFTG, which has been successfully used for targeting glycogenesis *in vitro* and *in vivo*. However, we found a lack of specificity of the second-generation tracers to glycogenesis, as shown by low incorporation of radioactivity into glycogen granules extracted from cell lysates following tracer incubation. [$^{18}$F]NFTG was applied to assess senescence-associated glycogenesis in palbociclib-treated cells. The uptake of [$^{18}$F]NFTG was increased in MCF-7 cells in response to palbociclib, however, the tracer failed to distinguish the difference in glycogenesis between quiescence and senescence states. Additionally, the challenging purification of [$^{18}$F]NFTG negates the use of this compound for further in *vivo* evaluation.

In parallel, we proposed a dual-modality (fluorescence/PET) fluorine-18 radiolabelled molecule based upon the structure of a previously reported molecule (namely CDg4) to determine the levels of stored glycogen. Fluorescent probe **5** was observed to accumulate in glycogen-containing cells by fluorescence microscopy, and the signal was diminished by enzymatic digestion of carbohydrates using α-amylase. However, there was no correlation between total glycogen level and *in vitro* uptake of **[$^{18}$F]5** in the investigated cancer cell lines.

The attempt was further made to develop a lipofuscin-based PET imaging agent for specifically targeting drug-induced senescence, as lipofuscin is being exploited as a promising biomarker of cellular senescence. [$^{18}$F]FET-SBB and its non-radioactive [$^{19}$F]FET-SBB were developed based upon the structure of SBB which is a routinely used to stain for detecting the accumulation of lipofuscin. [$^{19}$F]FET-SBB accumulated in senescent MCF-7 and T47D cells induced by palbociclib, which was in correlation with lipofuscin content determined by fluorescence microscopy. The radioactive [$^{18}$F]FET-SBB followed the same trend in T47D cells after palbociclib treatment; however, an unexpected decrease in uptake was observed in senescent MCF-7 cells. Regardless, the absence of any trend in MLN8054 treated cells, where

no lipofuscin was detected by autofluorescence, gives encouragement that [$^{18}$F]FET-SBB may trace lipofuscin deposits. The metabolic analysis of [$^{18}$F]FET-SBB showed largely intact parent radiotracer at 60 min p.i., which encourages further evaluation of [$^{18}$F]FET-SBB in animals bearing senescent tissues. Potential substrate specificity for ABC transporters requires elaboration in the future.

## 6.2 Prospects

### The role of allosteric activation of GYS1 in tumour glycogenesis

The activity of GYS1 is regulated by dephosphorylation and by the allosteric stimulator G6P. Due to the complex interplay between multiple phosphorylation sites and allosteric effectors, the relative importance of these two regulatory mechanisms in controlling GYS1 is not established. Most recently, Bouskila et al. [347] found that allosteric activation of GYS1 is the primary mechanism by which insulin facilitates the accumulation of muscle glycogen. A similar finding was observed in hepatocytes that allosteric activation of GYS2 by G6P plays a key role in regulating hepatic glycogen synthesis [348]. Using both mutagenesis and intein-mediated phospho-peptide ligation experiments, residues including Arg583 and Arg587 were found to be required for activation of GYS2 by G6P [132].

Although the understanding of G6P-mediated GYS activity has been largely improved in muscle and liver tissues, it remains unclear to what extent this regulatory mechanism contributes to the reprogramming of glycogen synthesis in cancer. In this thesis, GYS1 activity was assessed mainly based on phospho-dependent mechanism, where the ratio of phosphorylated GYS1 to total GYS1 level was determined using western blot analysis. Among several cases, phospho-mediated GYS1 activity did not always reflect the changes in glycogenesis or glycogen storage, suggesting an additional regulation by G6P could be possible.

In addition to our observed evidence, current hypothesis proposed that allosteric activation of GYS1 might play a crucial role in tumours is based on the upregulated glucose utilisation, thereby resulting in high levels of G6P. Possibly, G6P concentration increases as a result of glucose uptake within tumour environment and in turn stimulates allosteric

activation of GYS, eventually resulting in an increase in glycogen synthesis. The allosteric activation of GYS does not require permanently elevated levels of G6P [349]. Moreover, the literature indicates that addition of G6P to either phosphorylated or unphosphorylated enzyme could generate a high-activity state, suggesting that the presence of G6P could overcome inactivation due to phosphorylation and can restore full enzyme activity [142].

**Glycogenesis – a new target for cancer therapy?**

The evidence that glycogen metabolism is reprogrammed in cancer cells indicates that targeting of glycogen metabolism could be a new strategy for cancer treatment [121; 129]. Several efforts have been undertaken to identify inhibitors of glycogenesis for cancer therapy, however, there are so far no specific inhibitors or activators developed for GYS. Current approach to target this pathway is through indirectly regulating GSK3β [350] and AMPK [351], which are two major kinases involved in GYS phosphorylation and thus inactivation. Due to the multi-faced and complex functions of these kinases, these drugs might pose off-target effects and poor selectivity to glycogenesis pathway.

A further approach is to targeting glycogenesis as a combinational strategy for anticancer therapy. For example, bevacizumab treatment as an angiogenic therapy in U87MG xenograft model also induces hypoxia within tumour microenvironment and eventually causes an adaptive response of cancer cell through consuming glycogen as an energy source [150]. Given the observation that glycogen accumulates under hypoxia conditions as a survival mechanism of cancer cell, a combinational therapy of targeting glycogenesis together with bevacizumab treatment could provide superior treatment efficacy. Cancer cells affected by nutrient stress are prone to consume glycogen as a major energy source and a survival mechanism. Blocking glycogenesis or glycogenolysis in these cells that undergo drug-induced acute stress condition could provide synergy as anticancer-treatment. Additionally, as reported in this thesis, as drug-induced quiescent/senescent cells largely accumulate glycogen, it might be an additional opportunity for treating tumours to combine treatment of glycogenesis with drugs that have arrested cells in a non-proliferating phase.

**Enhanced glycogenesis represents an important metabolic feature of senescence**

Enhanced glycogen synthesis was observed in senescent cells induced by palbociclib in this thesis, and the underlying mechanism by which glycogen was accumulated requires further investigation. As several senescence-associated alterations occur in cellular lysosome, the accumulated glycogen granules might also be presented in lysosome. Under physiological condition, glycogen has shown to deposit in lysosome and degraded by α-1,4-Glucosidase (GAA), which is referred to as glycogen autophagy [141]. Despite being largely accumulated, the role of the glycogen particle as the stored form of efficient energy in senescence needs to be clarified.

**Emerging strategies to identify senescent cells**

Although there have been a wide range of characteristics used for characterising cellular senescence, currently no single marker is absolutely specificity for senescent cells. Several factors that determine the specificity of each marker include cell type, tissues, organismal development stage and species. Therefore, Gorgoulis et al. [326] most recently proposed a multi-marker approach, combining broader and more specific markers for more robust detection of senescent cells *in situ*. Briefly, two of the most common phenotypes including SA-β-gal activity and lipofuscin accumulation are assessed. Further verification is conducted by co-staining with other markers frequently observed such as upregulated $p16^{INK4A}$ and $p21^{WAF1/Cip1}$ or downregulated proliferation markers and lamin B1. Thirdly, markers for specific types of senescence such as SASP or DNA damage and DDR should be identified within various senescence contexts. This approach might lead to the recognition of senescent cells with highest accuracy, which could also be used to evaluate the efficacy of senolytic therapies.

A potential approach is to identify specific transcriptome signature of cellular senescence by gene-sequencing and bioinformatics modelling analysis. These core transcriptome signatures cannot only help identify senescent cells, but also discriminate among different senescence programs. However, in order to establish reliable profiles of gene expression related to senescence, a wide range of senescent cell models need to be developed and assessed [352; 353].

It is of great importance to develop specific panels of markers for each senescence subtype, as it will guide the evolving field of senotherapy and senescence-related anticancer therapies.

**The potential role of PET imaging in studying senescence**

The work in this thesis contributes to the progression of knowledge regarding the development of PET imaging agents that could be translated into the clinical setting for detection of senescence resulting from anticancer chemotherapies. PET radiotracers can provide important information on the dynamics of cancer biology, which allows for early measurement of tumour biochemical changes in response to therapy. Future development of senescence-specific tracers would benefit from the better understanding of theories of cellular senescence and characterization of the cellular and molecular signatures of senescence. In addition to assessment of cancer therapy, radiotracers that specifically identify senescent cells might have potential applications in directing or monitoring senotherapies in age-related diseases.

## Reference


1. Hayflick L. (1961). The limited in vitro lifetime of human diploid cell strains. *Experimental Cell Research,* 25: 585-621.
2. Hayflick L., & P.S. M. (1965). The serial cultivation of human diploid cell strains. *Experimental Cell Research* 37: 614-636.
3. Tan F.C., Hutchison E.R., Eitan E., & Mattson M.P. (2014). Are there roles for brain cell senescence in aging and neurodegenerative disorders? *Biogerontology,* 15: 643-660.
4. Harley C.B., Futcher A.B., & Greider C.W. (1990). Telomeres shorten during ageing of human fibroblasts. *Nature,* 345(6274): 458-460.
5. d'Adda di Fagagna F., Teo S.H., & Jackson S.P. (2004). Functional links between telomeres and proteins of the DNA-damage response. *Genes Dev,* 18(15): 1781-1799.
6. d'Adda di Fagagna F., Reaper P.M., Clay-Farrace L., Fiegler H., Carr P., Von Zglinicki T., et al. (2003). A DNA damage checkpoint response in telomere-initiated senescence. *Nature,* 426(6963): 194-198.
7. Collins K., & Mitchell J.R. (2002). Telomerase in the human organism. *Oncogene,* 21(4): 564-579.
8. Chen Q.M., Prowse K.R., Tu V.C., Purdom S., & Linskens M.H. (2001). Uncoupling the senescent phenotype from telomere shortening in hydrogen peroxide-treated fibroblasts. *Experimental Cell Research,* 265(2): 294-303.
9. d'Adda di Fagagna F. (2008). Living on a break: cellular senescence as a DNA-damage response. *Nature Reviews: Cancer,* 8(7): 512-522.
10. Fumagalli M., Rossiello F., Clerici M., Barozzi S., Cittaro D., Kaplunov J.M., et al. (2012). Telomeric DNA damage is irreparable and causes persistent DNA-damage-response activation. *Nature Cell Biology,* 14(4): 355-365.
11. Bringold F., & Serrano M. (2000). Tumor suppressors and oncogenes in cellular senescence. *Experimental Gerontology,* 35(3): 317-329.
12. Serrano M., Lin A.W., McCurrach M.E., Beach D., & Lowe S.W. (1997). Oncogenic ras provokes premature cell senescence associated with accumulation of p53 and p16INK4a. *Cell,* 88(5): 593-602.
13. Mooi W.J., & Peeper D.S. (2006). Oncogene-induced cell senescence--halting on the road to cancer. *New England Journal of Medicine,* 355(10): 1037-1046.

14. Courtois-Cox S., Jones S.L., & Cichowski K. (2008). Many roads lead to oncogene-induced senescence. *Oncogene,* 27(20): 2801-2809.
15. Dimauro T., & David G. (2010). Ras-induced senescence and its physiological relevance in cancer. *Current Cancer Drug Targets,* 10(8): 869-876.
16. Patil P., Falabella M., Saeed A., Lee D., Kaufman B., Shiva S., et al. (2019). Oxidative stress-induced senescence markedly increases disc cell bioenergetics. *Mechanisms of Ageing and Development,* 180: 97-106.
17. Coluzzi E., Leone S., & Sgura A. (2019). Oxidative Stress Induces Telomere Dysfunction and Senescence by Replication Fork Arrest. *Cells,* 8(1): 19-43.
18. Harman D. (1956). Aging: a theory based on free radical and radiation chemistry. *Journal of Gerontology,* 11(3): 298-300.
19. Zhu M.J., Wang X., Shi L., Liang L.Y., & Wang Y. (2018). Senescence, oxidative stress and mitochondria dysfunction. *Medical Research and Innovations,* 2(4): 1-5.
20. Liguori I., Russo G., Curcio F., Bulli G., Aran L., Della-Morte D., et al. (2018). Oxidative stress, aging, and diseases. *Clinical Interventions in Aging,* 13: 757-772.
21. Correia-Melo C., Marques F.D., Anderson R., Hewitt G., Hewitt R., Cole J., et al. (2016). Mitochondria are required for pro-ageing features of the senescent phenotype. *EMBO Journal,* 35(7): 724-742.
22. Wiley C.D., Velarde M.C., Lecot P., Liu S., Sarnoski E.A., Freund A., et al. (2016). Mitochondrial Dysfunction Induces Senescence with a Distinct Secretory Phenotype. *Cell Metabolism,* 23(2): 303-314.
23. Campisi J., & d'Adda di Fagagna F. (2007). Cellular senescence: when bad things happen to good cells. *Nature Reviews: Molecular Cell Biology,* 8(9): 729-740.
24. Collado M., Blasco M.A., & Serrano M. (2007). Cellular senescence in cancer and aging. *Cell,* 130(2): 223-233.
25. Sherr C.J., & McCormick F. (2002). The RB and p53 pathways in cancer. *Cancer Cell,* 2(2): 103-112.
26. Gil J., & Peters G. (2006). Regulation of the INK4b-ARF-INK4a tumour suppressor locus: all for one or one for all. *Nature Reviews: Molecular Cell Biology,* 7(9): 667-677.
27. Sharpless N.E. (2005). INK4a/ARF: a multifunctional tumor suppressor locus. *Mutation Research,* 576(1-2): 22-38.

28. Narita M., Nũnez S., Heard E., Narita M., Lin A.W., Hearn S.A., et al. (2003). Rb-mediated heterochromatin formation and silencing of E2F target genes during cellular senescence. *Cell,* 113(6): 703-716.
29. Macaluso M., Montanari M., & Giordano A. (2006). Rb family proteins as modulators of gene expression and new aspects regarding the interaction with chromatin remodeling enzymes. *Oncogene,* 25(38): 5263-5267.
30. Cao X., & Li M. (2015). A New Pathway for Senescence Regulation. *Genomics, Proteomics & Bioinformatics,* 13(6): 333-335.
31. Kang C., Xu Q., Martin T.D., Li M.Z., Demaria M., Aron L., et al. (2015). The DNA damage response induces inflammation and senescence by inhibiting autophagy of GATA4. *Science,* 349(6255): aaa5612.
32. Hernandez-Segura A., Nehme J., & Demaria M. (2018). Hallmarks of Cellular Senescence. *Trends in Cell Biology,* 28(6): 436-453.
33. Beauséjour C.M., Krtolica A., Galimi F., Narita M., Lowe S.W., Yaswen P., et al. (2003). Reversal of human cellular senescence: roles of the p53 and p16 pathways. *EMBO Journal,* 22(16): 4212-4222.
34. Childs B.G., Baker D.J., Kirkland J.L., Campisi J., & van Deursen J.M. (2014). Senescence and apoptosis: dueling or complementary cell fates? *EMBO Rep,* 15(11): 1139-1153.
35. Sanders Y.Y., Liu H., Zhang X., Hecker L., Bernard K., Desai L., et al. (2013). Histone modifications in senescence-associated resistance to apoptosis by oxidative stress. *Redox Biol,* 1(1): 8-16.
36. Yosef R., Pilpel N., Tokarsky-Amiel R., Biran A., Ovadya Y., Cohen S., et al. (2016). Directed elimination of senescent cells by inhibition of BCL-W and BCL-XL. *Nat Commun,* 7: 11190.
37. Baar M.P., Brandt R.M.C., Putavet D.A., Klein J.D.D., Derks K.W.J., Bourgeois B.R.M., et al. (2017). Targeted Apoptosis of Senescent Cells Restores Tissue Homeostasis in Response to Chemotoxicity and Aging. *Cell,* 169(1): 132-147.e116.
38. Yosef R., Pilpel N., Papismadov N., Gal H., Ovadya Y., Vadai E., et al. (2017). p21 maintains senescent cell viability under persistent DNA damage response by restraining JNK and caspase signaling. *EMBO Journal,* 36(15): 2280-2295.

39. Rippe C., Blimline M., Magerko K.A., Lawson B.R., LaRocca T.J., Donato A.J., et al. (2012). MicroRNA changes in human arterial endothelial cells with senescence: relation to apoptosis, eNOS and inflammation. *Experimental Gerontology,* 47(1): 45-51.
40. Matsushita H., Chang E., Glassford A.J., Cooke J.P., Chiu C.P., & Tsao P.S. (2001). eNOS activity is reduced in senescent human endothelial cells: Preservation by hTERT immortalization. *Circulation Research,* 89(9): 793-798.
41. Kurz D.J., Decary S., Hong Y., & Erusalimsky J.D. (2000). Senescence-associated (beta)-galactosidase reflects an increase in lysosomal mass during replicative ageing of human endothelial cells. *Journal of Cell Science,* 113 ( Pt 20): 3613-3622.
42. Lee B.Y., Han J.A., Im J.S., Morrone A., Johung K., Goodwin E.C., et al. (2006). Senescence-associated beta-galactosidase is lysosomal beta-galactosidase. *Aging Cell,* 5(2): 187-195.
43. Hildebrand D.G., Lehle S., Borst A., Haferkamp S., Essmann F., & Schulze-Osthoff K. (2013). α-Fucosidase as a novel convenient biomarker for cellular senescence. *Cell Cycle,* 12(12): 1922-1927.
44. Georgakopoulou E.A., Tsimaratou K., Evangelou K., Fernandez Marcos P.J., Zoumpourlis V., Trougakos I.P., et al. (2013). Specific lipofuscin staining as a novel biomarker to detect replicative and stress-induced senescence. A method applicable in cryo-preserved and archival tissues. *Aging,* 5(1): 37-50.
45. von Zglinicki T., Saretzki G., Döcke W., & Lotze C. (1995). Mild hyperoxia shortens telomeres and inhibits proliferation of fibroblasts: a model for senescence? *Experimental Cell Research,* 220(1): 186-193.
46. Nyström T. (2005). Role of oxidative carbonylation in protein quality control and senescence. *EMBO Journal,* 24(7): 1311-1317.
47. Evangelou K., Lougiakis N., Rizou S.V., Kotsinas A., Kletsas D., Muñoz-Espín D., et al. (2017). Robust, universal biomarker assay to detect senescent cells in biological specimens. *Aging Cell,* 16(1): 192-197.
48. Hernandez-Segura A., de Jong T.V., Melov S., Guryev V., Campisi J., & Demaria M. (2017). Unmasking Transcriptional Heterogeneity in Senescent Cells. *Current Biology,* 27(17): 2652-2660.e2654.
49. Sadaie M., Salama R., Carroll T., Tomimatsu K., Chandra T., Young A.R., et al. (2013). Redistribution of the Lamin B1 genomic binding profile affects rearrangement of

heterochromatic domains and SAHF formation during senescence. *Genes Dev,* 27(16): 1800-1808.

50. Shimi T., Butin-Israeli V., Adam S.A., Hamanaka R.B., Goldman A.E., Lucas C.A., et al. (2011). The role of nuclear lamin B1 in cell proliferation and senescence. *Genes Dev,* 25(24): 2579-2593.
51. Dreesen O., Chojnowski A., Ong P.F., Zhao T.Y., Common J.E., Lunny D., et al. (2013). Lamin B1 fluctuations have differential effects on cellular proliferation and senescence. *Journal of Cell Biology,* 200(5): 605-617.
52. Ivanov A., Pawlikowski J., Manoharan I., van Tuyn J., Nelson D.M., Rai T.S., et al. (2013). Lysosome-mediated processing of chromatin in senescence. *Journal of Cell Biology,* 202(1): 129-143.
53. Salama R., Sadaie M., Hoare M., & Narita M. (2014). Cellular senescence and its effector programs. *Genes Dev,* 28(2): 99-114.
54. Lopes-Paciencia S., Saint-Germain E., Rowell M.C., Ruiz A.F., Kalegari P., & Ferbeyre G. (2019). The senescence-associated secretory phenotype and its regulation. *Cytokine,* 117: 15-22.
55. Coppé J.P., Patil C.K., Rodier F., Sun Y., Muñoz D.P., Goldstein J., et al. (2008). Senescence-associated secretory phenotypes reveal cell-nonautonomous functions of oncogenic RAS and the p53 tumor suppressor. *PLoS Biology,* 6(12): 2853-2868.
56. Borodkina A.V., Deryabin P.I., Giukova A.A., & Nikolsky N.N. (2018). "Social Life" of Senescent Cells: What Is SASP and Why Study It? *Acta Naturae,* 10(1): 4-14.
57. Kuilman T., Michaloglou C., Vredeveld L.C., Douma S., van Doorn R., Desmet C.J., et al. (2008). Oncogene-induced senescence relayed by an interleukin-dependent inflammatory network. *Cell,* 133(6): 1019-1031.
58. Takahashi A., Imai Y., Yamakoshi K., Kuninaka S., Ohtani N., Yoshimoto S., et al. (2012). DNA damage signaling triggers degradation of histone methyltransferases through APC/C(Cdh1) in senescent cells. *Molecular Cell,* 45(1): 123-131.
59. Hayakawa T., Iwai M., Aoki S., Takimoto K., Maruyama M., Maruyama W., et al. (2015). SIRT1 suppresses the senescence-associated secretory phenotype through epigenetic gene regulation. *PloS One,* 10(1): e0116480.

60. Chen H., Ruiz P.D., McKimpson W.M., Novikov L., Kitsis R.N., & Gamble M.J. (2015). MacroH2A1 and ATM Play Opposing Roles in Paracrine Senescence and the Senescence-Associated Secretory Phenotype. *Molecular Cell,* 59(5): 719-731.
61. Contrepois K., Coudereau C., Benayoun B.A., Schuler N., Roux P.F., Bischof O., et al. (2017). Histone variant H2A.J accumulates in senescent cells and promotes inflammatory gene expression. *Nat Commun,* 8: 14995.
62. Laberge R.M., Sun Y., Orjalo A.V., Patil C.K., Freund A., Zhou L., et al. (2015). MTOR regulates the pro-tumorigenic senescence-associated secretory phenotype by promoting IL1A translation. *Nature Cell Biology,* 17(8): 1049-1061.
63. Herranz N., Gallage S., Mellone M., Wuestefeld T., Klotz S., Hanley C.J., et al. (2015). mTOR regulates MAPKAPK2 translation to control the senescence-associated secretory phenotype. *Nature Cell Biology,* 17(9): 1205-1217.
64. Acosta J.C., O'Loghlen A., Banito A., Guijarro M.V., Augert A., Raguz S., et al. (2008). Chemokine signaling via the CXCR2 receptor reinforces senescence. *Cell,* 133(6): 1006-1018.
65. Adams P.D. (2009). Healing and hurting: molecular mechanisms, functions, and pathologies of cellular senescence. *Molecular Cell,* 36(1): 2-14.
66. Campisi J., & Robert L. (2014). Cell senescence: role in aging and age-related diseases. *Interdiscip Top Gerontol,* 39: 45-61.
67. Kaplon J., Zheng L., Meissl K., Chaneton B., Selivanov V.A., Mackay G., et al. (2013). A key role for mitochondrial gatekeeper pyruvate dehydrogenase in oncogene-induced senescence. *Nature,* 498(7452): 109-112.
68. Takebayashi S., Tanaka H., Hino S., Nakatsu Y., Igata T., Sakamoto A., et al. (2015). Retinoblastoma protein promotes oxidative phosphorylation through upregulation of glycolytic genes in oncogene-induced senescent cells. *Aging Cell,* 14(4): 689-697.
69. Passos J.F., Nelson G., Wang C., Richter T., Simillion C., Proctor C.J., et al. (2010). Feedback between p21 and reactive oxygen production is necessary for cell senescence. *Molecular Systems Biology,* 6: 347.
70. Wang W., Yang X., López de Silanes I., Carling D., & Gorospe M. (2003). Increased AMP:ATP ratio and AMP-activated protein kinase activity during cellular senescence linked to reduced HuR function. *Journal of Biological Chemistry,* 278(29): 27016-27023.

71. Young A.R., Narita M., & Narita M. (2013). Cell senescence as both a dynamic and a static phenotype. *Methods in Molecular Biology,* 965: 1-13.

72. Patschan S., Chen J., Polotskaia A., Mendelev N., Cheng J., Patschan D., et al. (2008). Lipid mediators of autophagy in stress-induced premature senescence of endothelial cells. *Am J Physiol Heart Circ Physiol,* 294(3): H1119-1129.

73. Herranz N., & Gil J. (2018). Mechanisms and functions of cellular senescence. *Journal of Clinical Investigation,* 128(4): 1238-1246.

74. Deschênes-Simard X., Gaumont-Leclerc M.F., Bourdeau V., Lessard F., Moiseeva O., Forest V., et al. (2013). Tumor suppressor activity of the ERK/MAPK pathway by promoting selective protein degradation. *Genes Dev,* 27(8): 900-915.

75. Ogrodnik M., Miwa S., Tchkonia T., Tiniakos D., Wilson C.L., Lahat A., et al. (2017). Cellular senescence drives age-dependent hepatic steatosis. *Nat Commun,* 8: 15691.

76. Ogrodnik M., Salmonowicz H., & Gladyshev V.N. (2019). Integrating cellular senescence with the concept of damage accumulation in aging: Relevance for clearance of senescent cells. *Aging Cell,* 18(1): e12841.

77. Seo Y.H., Jung H.J., Shin H.T., Kim Y.M., Yim H., Chung H.Y., et al. (2008). Enhanced glycogenesis is involved in cellular senescence via GSK3/GS modulation. *Aging Cell,* 7(6): 894-907.

78. Kwon S.M., Hong S.M., Lee Y.K., Min S., & Yoon G. (2019). Metabolic features and regulation in cell senescence. *BMB Rep,* 52(1): 5-12.

79. Lee H.W., Heo C.H., Sen D., Byun H.O., Kwak I.H., Yoon G., et al. (2014). Ratiometric two-photon fluorescent probe for quantitative detection of β-galactosidase activity in senescent cells. *Analytical Chemistry,* 86(20): 10001-10005.

80. Zhang J., Li C., Dutta C., Fang M., Zhang S., Tiwari A., et al. (2017). A novel near-infrared fluorescent probe for sensitive detection of β-galactosidase in living cells. *Analytica Chimica Acta,* 968: 97-104.

81. Lozano-Torres B., Galiana I., Rovira M., Garrido E., Chaib S., Bernardos A., et al. (2017). An OFF-ON Two-Photon Fluorescent Probe for Tracking Cell Senescence in Vivo. *Journal of the American Chemical Society,* 139(26): 8808-8811.

82. Wang Y., Liu J., Ma X., Cui C., Deenik P.R., Henderson P.K.P., et al. (2019). Real-time imaging of senescence in tumors with DNA damage. *Scientific Reports,* 9(1): 2102.

83. Agostini A., Mondragón L., Bernardos A., Martínez-Máñez R., Marcos M.D., Sancenón F., et al. (2012). Targeted cargo delivery in senescent cells using capped mesoporous silica nanoparticles. *Angew Chem Int Ed Engl,* 51(42): 10556-10560.

84. Muñoz-Espín D., Rovira M., Galiana I., Giménez C., Lozano-Torres B., Paez-Ribes M., et al. (2018). A versatile drug delivery system targeting senescent cells. *EMBO Molecular Medicine,* 10(9).

85. Thapa R.K., Nguyen H.T., Jeong J.H., Kim J.R., Choi H.G., Yong C.S., et al. (2017). Progressive slowdown/prevention of cellular senescence by CD9-targeted delivery of rapamycin using lactose-wrapped calcium carbonate nanoparticles. *Scientific Reports,* 7: 43299.

86. Chang J., Wang Y., Shao L., Laberge R.M., Demaria M., Campisi J., et al. (2016). Clearance of senescent cells by ABT263 rejuvenates aged hematopoietic stem cells in mice. *Nature Medicine,* 22(1): 78-83.

87. Wang Y., Chang J., Liu X., Zhang X., Zhang S., Zhang X., et al. (2016). Discovery of piperlongumine as a potential novel lead for the development of senolytic agents. *Aging,* 8(11): 2915-2926.

88. Jeon O.H., Kim C., Laberge R.M., Demaria M., Rathod S., Vasserot A.P., et al. (2017). Local clearance of senescent cells attenuates the development of post-traumatic osteoarthritis and creates a pro-regenerative environment. *Nature Medicine,* 23(6): 775-781.

89. Zhu Y., Tchkonia T., Pirtskhalava T., Gower A.C., Ding H., Giorgadze N., et al. (2015). The Achilles' heel of senescent cells: from transcriptome to senolytic drugs. *Aging Cell,* 14(4): 644-658.

90. Hickson L.J., Langhi Prata L.G.P., Bobart S.A., Evans T.K., Giorgadze N., Hashmi S.K., et al. (2019). Senolytics decrease senescent cells in humans: Preliminary report from a clinical trial of Dasatinib plus Quercetin in individuals with diabetic kidney disease. *EBioMedicine,* 47: 446-456.

91. Yousefzadeh M.J., Zhu Y., McGowan S.J., Angelini L., Fuhrmann-Stroissnigg H., Xu M., et al. (2018). Fisetin is a senotherapeutic that extends health and lifespan. *EBioMedicine,* 36: 18-28.

92. Fuhrmann-Stroissnigg H., Ling Y.Y., Zhao J., McGowan S.J., Zhu Y., Brooks R.W., et al. (2017). Identification of HSP90 inhibitors as a novel class of senolytics. *Nat Commun,* 8(1): 422.

93. Kang H.T., Park J.T., Choi K., Kim Y., Choi H.J.C., Jung C.W., et al. (2017). Chemical screening identifies ATM as a target for alleviating senescence. *Nature Chemical Biology,* 13(6): 616-623.

94. Krizhanovsky V., Yon M., Dickins R.A., Hearn S., Simon J., Miething C., et al. (2008). Senescence of activated stellate cells limits liver fibrosis. *Cell,* 134(4): 657-667.

95. Sagiv A., Burton D.G., Moshayev Z., Vadai E., Wensveen F., Ben-Dor S., et al. (2016). NKG2D ligands mediate immunosurveillance of senescent cells. *Aging,* 8(2): 328-344.

96. Kim K.M., Noh J.H., Bodogai M., Martindale J.L., Yang X., Indig F.E., et al. (2017). Identification of senescent cell surface targetable protein DPP4. *Genes Dev,* 31(15): 1529-1534.

97. Paez-Ribes M., González-Gualda E., Doherty G.J., & Muñoz-Espín D. (2019). Targeting senescent cells in translational medicine. *EMBO Molecular Medicine,* 11(12): e10234.

98. Sarkisian C.J., Keister B.A., Stairs D.B., Boxer R.B., Moody S.E., & Chodosh L.A. (2007). Dose-dependent oncogene-induced senescence in vivo and its evasion during mammary tumorigenesis. *Nature Cell Biology,* 9(5): 493-505.

99. Acosta J.C., & Gil J. (2012). Senescence: a new weapon for cancer therapy. *Trends in Cell Biology,* 22(4): 211-219.

100. Wang L., Leite de Oliveira R., Wang C., Fernandes Neto J.M., Mainardi S., Evers B., et al. (2017). High-Throughput Functional Genetic and Compound Screens Identify Targets for Senescence Induction in Cancer. *Cell Reports,* 21(3): 773-783.

101. Sieben C.J., Sturmlechner I., van de Sluis B., & van Deursen J.M. (2018). Two-Step Senescence-Focused Cancer Therapies. *Trends in Cell Biology,* 28(9): 723-737.

102. Liu S., Uppal H., Demaria M., Desprez P.Y., Campisi J., & Kapahi P. (2015). Simvastatin suppresses breast cancer cell proliferation induced by senescent cells. *Scientific Reports,* 5: 17895.

103. Alspach E., Fu Y., & Stewart S.A. (2013). Senescence and the pro-tumorigenic stroma. *Critical Reviews in Oncogenesis,* 18(6): 549-558.

104. Krtolica A., Parrinello S., Lockett S., Desprez P.Y., & Campisi J. (2001). Senescent fibroblasts promote epithelial cell growth and tumorigenesis: a link between cancer and aging. *Proceedings of the National Academy of Sciences of the United States of America,* 98(21): 12072-12077.

105. Lawrenson K., Grun B., Benjamin E., Jacobs I.J., Dafou D., & Gayther S.A. (2010). Senescent fibroblasts promote neoplastic transformation of partially transformed ovarian epithelial cells in a three-dimensional model of early stage ovarian cancer. *Neoplasia,* 12(4): 317-325.

106. Pazolli E., Luo X., Brehm S., Carbery K., Chung J.J., Prior J.L., et al. (2009). Senescent stromal-derived osteopontin promotes preneoplastic cell growth. *Cancer Research,* 69(3): 1230-1239.

107. Luo X., Ruhland M.K., Pazolli E., Lind A.C., & Stewart S.A. (2011). Osteopontin stimulates preneoplastic cellular proliferation through activation of the MAPK pathway. *Molecular Cancer Research,* 9(8): 1018-1029.

108. Guan X., LaPak K.M., Hennessey R.C., Yu C.Y., Shakya R., Zhang J., et al. (2017). Stromal Senescence By Prolonged CDK4/6 Inhibition Potentiates Tumor Growth. *Molecular Cancer Research,* 15(3): 237-249.

109. Liu D., & Hornsby P.J. (2007). Senescent human fibroblasts increase the early growth of xenograft tumors via matrix metalloproteinase secretion. *Cancer Research,* 67(7): 3117-3126.

110. Bavik C., Coleman I., Dean J.P., Knudsen B., Plymate S., & Nelson P.S. (2006). The gene expression program of prostate fibroblast senescence modulates neoplastic epithelial cell proliferation through paracrine mechanisms. *Cancer Research,* 66(2): 794-802.

111. Ohanna M., Cheli Y., Bonet C., Bonazzi V.F., Allegra M., Giuliano S., et al. (2013). Secretome from senescent melanoma engages the STAT3 pathway to favor reprogramming of naive melanoma towards a tumor-initiating cell phenotype. *Oncotarget,* 4(12): 2212-2224.

112. Canino C., Mori F., Cambria A., Diamantini A., Germoni S., Alessandrini G., et al. (2012). SASP mediates chemoresistance and tumor-initiating-activity of mesothelioma cells. *Oncogene,* 31(26): 3148-3163.

113. Ortiz-Montero P., Londoño-Vallejo A., & Vernot J.P. (2017). Senescence-associated IL-6 and IL-8 cytokines induce a self- and cross-reinforced senescence/inflammatory milieu strengthening tumorigenic capabilities in the MCF-7 breast cancer cell line. *Cell Commun Signal,* 15(1): 17.

114. Angelini P.D., Zacarias Fluck M.F., Pedersen K., Parra-Palau J.L., Guiu M., Bernadó Morales C., et al. (2013). Constitutive HER2 signaling promotes breast cancer metastasis through cellular senescence. *Cancer Research,* 73(1): 450-458.

115. Coppé J.P., Kauser K., Campisi J., & Beauséjour C.M. (2006). Secretion of vascular endothelial growth factor by primary human fibroblasts at senescence. *Journal of Biological Chemistry,* 281(40): 29568-29574.

116. Yang F., Tuxhorn J.A., Ressler S.J., McAlhany S.J., Dang T.D., & Rowley D.R. (2005). Stromal expression of connective tissue growth factor promotes angiogenesis and prostate cancer tumorigenesis. *Cancer Research,* 65(19): 8887-8895.

117. Demaria M., O'Leary M.N., Chang J., Shao L., Liu S., Alimirah F., et al. (2017). Cellular Senescence Promotes Adverse Effects of Chemotherapy and Cancer Relapse. *Cancer Discovery,* 7(2): 165-176.

118. Eggert T., Wolter K., Ji J., Ma C., Yevsa T., Klotz S., et al. (2016). Distinct Functions of Senescence-Associated Immune Responses in Liver Tumor Surveillance and Tumor Progression. *Cancer Cell,* 30(4): 533-547.

119. Iannello A., Thompson T.W., Ardolino M., Lowe S.W., & Raulet D.H. (2013). p53-dependent chemokine production by senescent tumor cells supports NKG2D-dependent tumor elimination by natural killer cells. *Journal of Experimental Medicine,* 210(10): 2057-2069.

120. Kang T.W., Yevsa T., Woller N., Hoenicke L., Wuestefeld T., Dauch D., et al. (2011). Senescence surveillance of pre-malignant hepatocytes limits liver cancer development. *Nature,* 479(7374): 547-551.

121. Zois C.E., Favaro E., & Harris A.L. (2014). Glycogen metabolism in cancer. *Biochemical Pharmacology,* 92(1): 3-11.

122. Adeva-Andany M.M., Gonzalez-Lucan M., Donapetry-Garcia C., Fernandez-Fernandez C., & Ameneiros-Rodriguez E. (2016). Glycogen metabolism in humans. *BBA Clin,* 5: 85-100.

123. Rybicka K.K. (1996). Glycosomes — the organelles of glycogen metabolism. *Tissue and Cell,* 28(3): 253-265.

124. Smythe C., & Cohen P. (1991). The discovery of glycogenin and the priming mechanism for glycogen biogenesis. *European Journal of Biochemistry,* 200(3): 625-631.

125. Minassian B.A., Lee J.R., Herbrick J.A., Huizenga J., Soder S., Mungall A.J., et al. (1998). Mutations in a gene encoding a novel protein tyrosine phosphatase cause progressive myoclonus epilepsy. *Nature Genetics,* 20(2): 171-174.

126. Ganesh S., Amano K., Delgado-Escueta A.V., & Yamakawa K. (1999). Isolation and characterization of mouse homologue for the human epilepsy gene, EPM2A. *Biochem Biophys Res Commun,* 257(1): 24-28.

127. Jiang S., Heller B., Tagliabracci V.S., Zhai L., Irimia J.M., DePaoli-Roach A.A., et al. (2010). Starch binding domain-containing protein 1/genethonin 1 is a novel participant in glycogen metabolism. *Journal of Biological Chemistry,* 285(45): 34960-34971.

128. Lomako J., Lomako W.M., & Whelan W.J. (1991). Proglycogen: a low-molecular-weight form of muscle glycogen. *FEBS Letters,* 279(2): 223-228.

129. Zois C.E., & Harris A.L. (2016). Glycogen metabolism has a key role in the cancer microenvironment and provides new targets for cancer therapy. *Journal of Molecular Medicine (Berlin, Germany),* 94(2): 137-154.

130. Nielsen J.N., & Richter E.A. (2003). Regulation of glycogen synthase in skeletal muscle during exercise. *Acta Physiologica Scandinavica,* 178(4): 309-319.

131. Hemmings B.A., Yellowlees D., Kernohan J.C., & Cohen P. (1981). Purification of glycogen synthase kinase 3 from rabbit skeletal muscle. Copurification with the activating factor (FA) of the (Mg-ATP) dependent protein phosphatase. *European Journal of Biochemistry,* 119(3): 443-451.

132. Baskaran S., Roach P.J., DePaoli-Roach A.A., & Hurley T.D. (2010). Structural basis for glucose-6-phosphate activation of glycogen synthase. *Proceedings of the National Academy of Sciences of the United States of America,* 107(41): 17563-17568.

133. Pederson B.A., Cheng C., Wilson W.A., & Roach P.J. (2000). Regulation of glycogen synthase. Identification of residues involved in regulation by the allosteric ligand glucose-6-P and by phosphorylation. *Journal of Biological Chemistry,* 275(36): 27753-27761.

134. Thorens B., & Mueckler M. (2010). Glucose transporters in the 21st Century. *American Journal of Physiology: Endocrinology and Metabolism,* 298(2): E141-145.

135. Baque S., Guinovart J.J., & Ferrer J.C. (1997). Glycogenin, the primer of glycogen synthesis, binds to actin. *FEBS Letters,* 417(3): 355-359.

136. Prats C., Cadefau J.A., Cusso R., Qvortrup K., Nielsen J.N., Wojtaszewski J.F., et al. (2005). Phosphorylation-dependent translocation of glycogen synthase to a novel structure during glycogen resynthesis. *Journal of Biological Chemistry,* 280(24): 23165-23172.

137. Prats C., Helge J.W., Nordby P., Qvortrup K., Ploug T., Dela F., et al. (2009). Dual regulation of muscle glycogen synthase during exercise by activation and compartmentalization. *Journal of Biological Chemistry,* 284(23): 15692-15700.

138. Prats C., Graham T.E., & Shearer J. (2018). The dynamic life of the glycogen granule. *Journal of Biological Chemistry,* 293(19): 7089-7098.

139. Gaboriaud-Kolar N., & Skaltsounis A.L. (2013). Glycogen phosphorylase inhibitors: a patent review (2008 - 2012). *Expert Opinion on Therapeutic Patents,* 23(8): 1017-1032.

140. Agius L. (2015). Role of glycogen phosphorylase in liver glycogen metabolism. *Molecular Aspects of Medicine,* 46: 34-45.

141. Kotoulas O.B., Kalamidas S.A., & Kondomerkos D.J. (2004). Glycogen autophagy. *Microsc Res Tech,* 64(1): 10-20.

142. Roach P.J., Depaoli-Roach A.A., Hurley T.D., & Tagliabracci V.S. (2012). Glycogen and its metabolism: some new developments and old themes. *Biochem J,* 441(3): 763-787.

143. McManus J.F.A. (1948). Histological and Histochemical Uses of Periodic Acid. *Stain Technology,* 23(3): 99-108.

144. Baba O. (1993). [Production of monoclonal antibody that recognizes glycogen and its application for immunohistochemistry]. *Kokubyo Gakkai Zasshi. The Journal of the Stomatological Society, Japan,* 60(2): 264-287.

145. Louzao M.C., Espiña B., Vieytes M.R., Vega F.V., Rubiolo J.A., Baba O., et al. (2008). "Fluorescent glycogen" formation with sensibility for in vivo and in vitro detection. *Glycoconjugate Journal,* 25(6): 503-510.

146. Witney T.H., Carroll L., Alam I.S., Chandrashekran A., Nguyen Q.D., Sala R., et al. (2014). A novel radiotracer to image glycogen metabolism in tumors by positron emission tomography. *Cancer Research,* 74(5): 1319-1328.

147. Ritterson Lew C., Guin S., & Theodorescu D. (2015). Targeting glycogen metabolism in bladder cancer. *Nat Rev Urol,* 12(7): 383-391.

148. Takahashi S., Satomi A., Yano K., Kawase H., Tanimizu T., Tuji Y., et al. (1999). Estimation of glycogen levels in human colorectal cancer tissue: relationship with cell cycle and tumor outgrowth. *Journal of Gastroenterology,* 34(4): 474-480.

149. Rousset M., Zweibaum A., & Fogh J. (1981). Presence of glycogen and growth-related variations in 58 cultured human tumor cell lines of various tissue origins. *Cancer Research,* 41(3): 1165-1170.

150. Favaro E., Bensaad K., Chong M.G., Tennant D.A., Ferguson D.J., Snell C., et al. (2012). Glucose utilization via glycogen phosphorylase sustains proliferation and prevents premature senescence in cancer cells. *Cell Metabolism,* 16(6): 751-764.

151. Cheng K.W., Agarwal R., Mitra S., Lee J.S., Carey M., Gray J.W., et al. (2012). Rab25 increases cellular ATP and glycogen stores protecting cancer cells from bioenergetic stress. *EMBO Molecular Medicine,* 4(2): 125-141.

152. Terashima M., Fujita Y., Togashi Y., Sakai K., De Velasco M.A., Tomida S., et al. (2014). KIAA1199 interacts with glycogen phosphorylase kinase beta-subunit (PHKB) to promote glycogen breakdown and cancer cell survival. *Oncotarget,* 5(16): 7040-7050.

153. Yang R., Zhang M., Gustafson A.R., Wang E., Cole M.P., Tooley C.E., et al. (2015). Loss of protein targeting to glycogen sensitizes human hepatocellular carcinoma cells towards glucose deprivation mediated oxidative stress and cell death. *Bioscience Reports,* 35(3).

154. Pescador N., Villar D., Cifuentes D., Garcia-Rocha M., Ortiz-Barahona A., Vazquez S., et al. (2010). Hypoxia promotes glycogen accumulation through hypoxia inducible factor (HIF)-mediated induction of glycogen synthase 1. *PloS One,* 5(3): e9644.

155. Shen G.M., Zhang F.L., Liu X.L., & Zhang J.W. (2010). Hypoxia-inducible factor 1-mediated regulation of PPP1R3C promotes glycogen accumulation in human MCF-7 cells under hypoxia. *FEBS Letters,* 584(20): 4366-4372.

156. Bhanot H., Reddy M.M., Nonami A., Weisberg E.L., Bonal D., Kirschmeier P.T., et al. (2015). Pathological glycogenesis through glycogen synthase 1 and suppression of excessive AMP kinase activity in myeloid leukemia cells. *Leukemia,* 29(7): 1555-1563.

157. Lee W.N., Guo P., Lim S., Bassilian S., Lee S.T., Boren J., et al. (2004). Metabolic sensitivity of pancreatic tumour cell apoptosis to glycogen phosphorylase inhibitor treatment. *British Journal of Cancer,* 91(12): 2094-2100.

158. Guin S., Ru Y., Agarwal N., Lew C.R., Owens C., Comi G.P., et al. (2016). Loss of Glycogen Debranching Enzyme AGL Drives Bladder Tumor Growth via Induction of Hyaluronic Acid Synthesis. *Clin Cancer Res,* 22(5): 1274-1283.

159. Guin S., Pollard C., Ru Y., Ritterson Lew C., Duex J.E., Dancik G., et al. (2014). Role in tumor growth of a glycogen debranching enzyme lost in glycogen storage disease. *Journal of the National Cancer Institute,* 106(5).

160. Curtis M., Kenny H.A., Ashcroft B., Mukherjee A., Johnson A., Zhang Y., et al. (2019). Fibroblasts Mobilize Tumor Cell Glycogen to Promote Proliferation and Metastasis. *Cell Metabolism,* 29(1): 141-155 e149.

161. Farwell M.D., Pryma D.A., & Mankoff D.A. (2014). PET/CT imaging in cancer: current applications and future directions. *Cancer,* 120(22): 3433-3445.

162. Kapoor V., McCook B.M., & Torok F.S. (2004). An introduction to PET-CT imaging. *Radiographics,* 24(2): 523-543.

163. Sai K.K.S., Zachar Z., Bingham P.M., & Mintz A. (2017). Metabolic PET Imaging in Oncology. *AJR: American Journal of Roentgenology,* 209(2): 270-276.

164. Mankoff D.A., & Katz S.I. (2018). PET imaging for assessing tumor response to therapy. *Journal of Surgical Oncology,* 118(2): 362-373.

165. Sharma R., & Aboagye E. (2011). Development of radiotracers for oncology--the interface with pharmacology. *Br J Pharmacol,* 163(8): 1565-1585.

166. Zhu A., & Shim H. (2011). Current molecular imaging positron emitting radiotracers in oncology. *Nucl Med Mol Imaging,* 45(1): 1-14.

167. Pauwels E.K., Ribeiro M.J., Stoot J.H., McCready V.R., Bourguignon M., & Maziere B. (1998). FDG accumulation and tumor biology. *Nuclear Medicine and Biology,* 25(4): 317-322.

168. Hara T., Kosaka N., Shinoura N., & Kondo T. (1997). PET imaging of brain tumor with [methyl-11C]choline. *Journal of Nuclear Medicine,* 38(6): 842-847.

169. Shoup T.M., Olson J., Hoffman J.M., Votaw J., Eshima D., Eshima L., et al. (1999). Synthesis and evaluation of [18F]1-amino-3-fluorocyclobutane-1-carboxylic acid to image brain tumors. *Journal of Nuclear Medicine,* 40(2): 331-338.

170. Witney T.H., Pisaneschi F., Alam I.S., Trousil S., Kaliszczak M., Twyman F., et al. (2014). Preclinical evaluation of 3-18F-fluoro-2,2-dimethylpropionic acid as an imaging agent for tumor detection. *Journal of Nuclear Medicine,* 55(9): 1506-1512.

171. Nguyen Q.D., & Aboagye E.O. (2010). Imaging the life and death of tumors in living subjects: Preclinical PET imaging of proliferation and apoptosis. *Integrative Biology: Quantitative Biosciences from Nano to Macro,* 2(10): 483-495.

172. Reshef A., Shirvan A., Akselrod-Ballin A., Wall A., & Ziv I. (2010). Small-molecule biomarkers for clinical PET imaging of apoptosis. *Journal of Nuclear Medicine,* 51(6): 837-840.

173. O'Dwyer P.J., King S.A., Hoth D.F., & Leyland-Jones B. (1987). Role of thymidine in biochemical modulation: a review. *Cancer Research,* 47(15): 3911-3919.

174. Shields A.F., Grierson J.R., Dohmen B.M., Machulla H.J., Stayanoff J.C., Lawhorn-Crews J.M., et al. (1998). Imaging proliferation in vivo with [F-18]FLT and positron emission tomography. *Nature Medicine,* 4(11): 1334-1336.

175. Schelhaas S., Heinzmann K., Honess D.J., Smith D.M., Keen H., Heskamp S., et al. (2018). 3'-Deoxy-3'-[(18)F]Fluorothymidine Uptake Is Related to Thymidine Phosphorylase Expression in Various Experimental Tumor Models. *Molecular Imaging and Biology,* 20(2): 194-199.

176. Schiepers C., Chen W., Dahlbom M., Cloughesy T., Hoh C.K., & Huang S.C. (2007). 18F-fluorothymidine kinetics of malignant brain tumors. *European Journal of Nuclear Medicine and Molecular Imaging,* 34(7): 1003-1011.

177. Heinzmann K., Nguyen Q.D., Honess D., Smith D.M., Stribbling S., Brickute D., et al. (2018). Depicting Changes in Tumor Biology in Response to Cetuximab Monotherapy or Combination Therapy by Apoptosis and Proliferation Imaging Using (18)F-ICMT-11 and (18)F-FLT PET. *Journal of Nuclear Medicine,* 59(10): 1558-1565.

178. Leyton J., Latigo J.R., Perumal M., Dhaliwal H., He Q., & Aboagye E.O. (2005). Early detection of tumor response to chemotherapy by 3'-deoxy-3'-[18F]fluorothymidine positron emission tomography: the effect of cisplatin on a fibrosarcoma tumor model in vivo. *Cancer Research,* 65(10): 4202-4210.

179. Leyton J., Alao J.P., Da Costa M., Stavropoulou A.V., Latigo J.R., Perumal M., et al. (2006). In vivo biological activity of the histone deacetylase inhibitor LAQ824 is detectable with

3'-deoxy-3'-[18F]fluorothymidine positron emission tomography. *Cancer Research,* 66(15): 7621-7629.

180. Rasey J.S., Grierson J.R., Wiens L.W., Kolb P.D., & Schwartz J.L. (2002). Validation of FLT uptake as a measure of thymidine kinase-1 activity in A549 carcinoma cells. *Journal of Nuclear Medicine,* 43(9): 1210-1217.

181. Schwartz J.L., Tamura Y., Jordan R., Grierson J.R., & Krohn K.A. (2003). Monitoring tumor cell proliferation by targeting DNA synthetic processes with thymidine and thymidine analogs. *Journal of Nuclear Medicine,* 44(12): 2027-2032.

182. Dittmann H., Dohmen B.M., Paulsen F., Eichhorn K., Eschmann S.M., Horger M., et al. (2003). [18F]FLT PET for diagnosis and staging of thoracic tumours. *European Journal of Nuclear Medicine and Molecular Imaging,* 30(10): 1407-1412.

183. Nishii R., Volgin A.Y., Mawlawi O., Mukhopadhyay U., Pal A., Bornmann W., et al. (2008). Evaluation of 2'-deoxy-2'-[18F]fluoro-5-methyl-1-beta-L: -arabinofuranosyluracil ([18F]-L: -FMAU) as a PET imaging agent for cellular proliferation: comparison with [18F]-D: -FMAU and [18F]FLT. *European Journal of Nuclear Medicine and Molecular Imaging,* 35(5): 990-998.

184. Sun H., Mangner T.J., Collins J.M., Muzik O., Douglas K., & Shields A.F. (2005). Imaging DNA synthesis in vivo with 18F-FMAU and PET. *Journal of Nuclear Medicine,* 46(2): 292-296.

185. Sun H., Sloan A., Mangner T.J., Vaishampayan U., Muzik O., Collins J.M., et al. (2005). Imaging DNA synthesis with [18F]FMAU and positron emission tomography in patients with cancer. *European Journal of Nuclear Medicine and Molecular Imaging,* 32(1): 15-22.

186. Buck A.K., Halter G., Schirrmeister H., Kotzerke J., Wurziger I., Glatting G., et al. (2003). Imaging proliferation in lung tumors with PET: 18F-FLT versus 18F-FDG. *Journal of Nuclear Medicine,* 44(9): 1426-1431.

187. Murayama C., Harada N., Kakiuchi T., Fukumoto D., Kamijo A., Kawaguchi A.T., et al. (2009). Evaluation of D-18F-FMT, 18F-FDG, L-11C-MET, and 18F-FLT for monitoring the response of tumors to radiotherapy in mice. *Journal of Nuclear Medicine,* 50(2): 290-295.

188. Abrantes A.M., Pires A.S., Monteiro L., Teixo R., Neves A.R., Tavares N.T., et al. (2020). Tumour functional imaging by PET. *Biochim Biophys Acta Mol Basis Dis,* 1866(6): 165717.

189. Wei W., Ni D., Ehlerding E.B., Luo Q.Y., & Cai W. (2018). PET Imaging of Receptor Tyrosine Kinases in Cancer. *Molecular Cancer Therapeutics,* 17(8): 1625-1636.

190. Yarden Y., & Sliwkowski M.X. (2001). Untangling the ErbB signalling network. *Nature Reviews: Molecular Cell Biology,* 2(2): 127-137.

191. Mishani E., Abourbeh G., Eiblmaier M., & Anderson C.J. (2008). Imaging of EGFR and EGFR tyrosine kinase overexpression in tumors by nuclear medicine modalities. *Current Pharmaceutical Design,* 14(28): 2983-2998.

192. Corcoran E.B., & Hanson R.N. (2014). Imaging EGFR and HER2 by PET and SPECT: a review. *Medicinal Research Reviews,* 34(3): 596-643.

193. Meng X., Loo B.W., Jr., Ma L., Murphy J.D., Sun X., & Yu J. (2011). Molecular imaging with 11C-PD153035 PET/CT predicts survival in non-small cell lung cancer treated with EGFR-TKI: a pilot study. *Journal of Nuclear Medicine,* 52(10): 1573-1579.

194. Alam I.S., Arshad M.A., Nguyen Q.D., & Aboagye E.O. (2015). Radiopharmaceuticals as probes to characterize tumour tissue. *European Journal of Nuclear Medicine and Molecular Imaging,* 42(4): 537-561.

195. Tsujikawa T., Yoshida Y., Kiyono Y., Kurokawa T., Kudo T., Fujibayashi Y., et al. (2011). Functional oestrogen receptor α imaging in endometrial carcinoma using 16α-[$^{18}$F]fluoro-17β-oestradiol PET. *European Journal of Nuclear Medicine and Molecular Imaging,* 38(1): 37-45.

196. Blankenberg F.G. (2008). In vivo detection of apoptosis. *Journal of Nuclear Medicine,* 49 Suppl 2: 81S-95S.

197. Zhou D., Chu W., Chen D.L., Wang Q., Reichert D.E., Rothfuss J., et al. (2009). [18F]- and [11C]-labeled N-benzyl-isatin sulfonamide analogues as PET tracers for apoptosis: synthesis, radiolabeling mechanism, and in vivo imaging study of apoptosis in Fas-treated mice using [11C]WC-98. *Organic & Biomolecular Chemistry,* 7(7): 1337-1348.

198. Podichetty A.K., Faust A., Kopka K., Wagner S., Schober O., Schäfers M., et al. (2009). Fluorinated isatin derivatives. Part 1: synthesis of new N-substituted (S)-5-[1-(2-methoxymethylpyrrolidinyl)sulfonyl]isatins as potent caspase-3 and -7 inhibitors. *Bioorg Med Chem,* 17(7): 2680-2688.

199. Nguyen Q.D., Smith G., Glaser M., Perumal M., Arstad E., & Aboagye E.O. (2009). Positron emission tomography imaging of drug-induced tumor apoptosis with a caspase-

3/7 specific [18F]-labeled isatin sulfonamide. *Proceedings of the National Academy of Sciences of the United States of America,* 106(38): 16375-16380.

200. Nguyen Q.D., Lavdas I., Gubbins J., Smith G., Fortt R., Carroll L.S., et al. (2013). Temporal and spatial evolution of therapy-induced tumor apoptosis detected by caspase-3-selective molecular imaging. *Clin Cancer Res,* 19(14): 3914-3924.

201. Nguyen Q.D., Challapalli A., Smith G., Fortt R., & Aboagye E.O. (2012). Imaging apoptosis with positron emission tomography: 'bench to bedside' development of the caspase-3/7 specific radiotracer [(18)F]ICMT-11. *European Journal of Cancer,* 48(4): 432-440.

202. Vassileva V., Stribbling S.M., Barnes C., Carroll L., Braga M., Abrahams J., et al. (2019). Evaluation of apoptosis imaging biomarkers in a genetic model of cell death. *EJNMMI Res,* 9(1): 18.

203. Challapalli A., Kenny L.M., Hallett W.A., Kozlowski K., Tomasi G., Gudi M., et al. (2013). 18F-ICMT-11, a caspase-3-specific PET tracer for apoptosis: biodistribution and radiation dosimetry. *Journal of Nuclear Medicine,* 54(9): 1551-1556.

204. Dubash S.R., Merchant S., Heinzmann K., Mauri F., Lavdas I., Inglese M., et al. (2018). Clinical translation of [(18)F]ICMT-11 for measuring chemotherapy-induced caspase 3/7 activation in breast and lung cancer. *European Journal of Nuclear Medicine and Molecular Imaging,* 45(13): 2285-2299.

205. Blankenberg F.G. (2008). In vivo imaging of apoptosis. *Cancer Biology & Therapy,* 7(10): 1525-1532.

206. Collingridge D.R., Glaser M., Osman S., Barthel H., Hutchinson O.C., Luthra S.K., et al. (2003). In vitro selectivity, in vivo biodistribution and tumour uptake of annexin V radiolabelled with a positron emitting radioisotope. *British Journal of Cancer,* 89(7): 1327-1333.

207. Wang F., Fang W., Zhang M.R., Zhao M., Liu B., Wang Z., et al. (2011). Evaluation of chemotherapy response in VX2 rabbit lung cancer with 18F-labeled C2A domain of synaptotagmin I. *Journal of Nuclear Medicine,* 52(4): 592-599.

208. Alam I.S., Neves A.A., Witney T.H., Boren J., & Brindle K.M. (2010). Comparison of the C2A domain of synaptotagmin-I and annexin-V as probes for detecting cell death. *Bioconjugate Chemistry,* 21(5): 884-891.

209. Cohen A., Shirvan A., Levin G., Grimberg H., Reshef A., & Ziv I. (2009). From the Gla domain to a novel small-molecule detector of apoptosis. *Cell Research,* 19(5): 625-637.

210. Reshef A., Shirvan A., Waterhouse R.N., Grimberg H., Levin G., Cohen A., et al. (2008). Molecular imaging of neurovascular cell death in experimental cerebral stroke by PET. *Journal of Nuclear Medicine,* 49(9): 1520-1528.

211. Sun L., Zhou K., Wang W., Zhang X., Ju Z., Qu B., et al. (2018). [18F]ML-10 Imaging for Assessment of Apoptosis Response of Intracranial Tumor Early after Radiosurgery by PET/CT. *Contrast Media & Molecular Imaging,* 2018: 9365174.

212. Allen A.M., Ben-Ami M., Reshef A., Steinmetz A., Kundel Y., Inbar E., et al. (2012). Assessment of response of brain metastases to radiotherapy by PET imaging of apoptosis with $^{18}$F-ML-10. *European Journal of Nuclear Medicine and Molecular Imaging,* 39(9): 1400-1408.

213. Conrad M., Angeli J.P., Vandenabeele P., & Stockwell B.R. (2016). Regulated necrosis: disease relevance and therapeutic opportunities. *Nature Reviews: Drug Discovery,* 15(5): 348-366.

214. Zhang D., Gao M., Jin Q., Ni Y., & Zhang J. (2019). Updated developments on molecular imaging and therapeutic strategies directed against necrosis. *Acta Pharm Sin B,* 9(3): 455-468.

215. Vakkila J., & Lotze M.T. (2004). Inflammation and necrosis promote tumour growth. *Nature Reviews: Immunology,* 4(8): 641-648.

216. Degenhardt K., Mathew R., Beaudoin B., Bray K., Anderson D., Chen G., et al. (2006). Autophagy promotes tumor cell survival and restricts necrosis, inflammation, and tumorigenesis. *Cancer Cell,* 10(1): 51-64.

217. Lotze M.T., & Tracey K.J. (2005). High-mobility group box 1 protein (HMGB1): nuclear weapon in the immune arsenal. *Nature Reviews: Immunology,* 5(4): 331-342.

218. Lee S.Y., Ju M.K., Jeon H.M., Jeong E.K., Lee Y.J., Kim C.H., et al. (2018). Regulation of Tumor Progression by Programmed Necrosis. *Oxidative Medicine and Cellular Longevity,* 2018: 3537471.

219. Chen S., Yu L., Jiang C., Zhao Y., Sun D., Li S., et al. (2005). Pivotal study of iodine-131-labeled chimeric tumor necrosis treatment radioimmunotherapy in patients with advanced lung cancer. *Journal of Clinical Oncology,* 23(7): 1538-1547.

220. Liang J., Sun Z., Zhang D., Jin Q., Cai L., Ma L., et al. (2018). First Evaluation of Radioiodinated Flavonoids as Necrosis-Avid Agents and Application in Early Assessment of Tumor Necrosis. *Molecular Pharmaceutics,* 15(1): 207-215.

221. Witney T.H., Kettunen M.I., Hu D.E., Gallagher F.A., Bohndiek S.E., Napolitano R., et al. (2010). Detecting treatment response in a model of human breast adenocarcinoma using hyperpolarised [1-13C]pyruvate and [1,4-13C2]fumarate. *British Journal of Cancer,* 103(9): 1400-1406.

222. Liu X., Feng Y., Jiang C., Lou B., Li Y., Liu W., et al. (2015). Radiopharmaceutical evaluation of (131)I-protohypericin as a necrosis avid compound. *Journal of Drug Targeting,* 23(5): 417-426.

223. Yun C.W., & Lee S.H. (2018). The Roles of Autophagy in Cancer. *International Journal of Molecular Sciences,* 19(11).

224. Trousil S., Kaliszczak M., Schug Z., Nguyen Q.D., Tomasi G., Favicchio R., et al. (2016). The novel choline kinase inhibitor ICL-CCIC-0019 reprograms cellular metabolism and inhibits cancer cell growth. *Oncotarget,* 7(24): 37103-37120.

225. Stetten M.R., Katzen H.M., & Stetten D., Jr. (1958). A comparison of the glycogens isolated by acid and alkaline procedures. *Journal of Biological Chemistry,* 232(1): 475-488.

226. Rasouli M., Shokri-Afra H., & Ostovar-Ravari A. (2015). A new protocol for separation of acid soluble and insoluble fractions from total glycogen and simultaneous measurements. *European Review for Medical and Pharmacological Sciences,* 19(10): 1785-1789.

227. Workman P., Aboagye E.O., Balkwill F., Balmain A., Bruder G., Chaplin D.J., et al. (2010). Guidelines for the welfare and use of animals in cancer research. *British Journal of Cancer,* 102(11): 1555-1577.

228. Warburg O. (1956). On the origin of cancer cells. *Science,* 123(3191): 309-314.

229. Rousset M., Paris H., Chevalier G., Terrain B., Murat J.C., & Zweibaum A. (1984). Growth-related enzymatic control of glycogen metabolism in cultured human tumor cells. *Cancer Research,* 44(1): 154-160.

230. Barot S., Abo-Ali E.M., Zhou D.L., Palaguachi C., & Dukhande V.V. (2019). Inhibition of glycogen catabolism induces intrinsic apoptosis and augments multikinase inhibitors in hepatocellular carcinoma cells. *Experimental Cell Research,* 381(2): 288-300.

231. Tate J.G., Bamford S., Jubb H.C., Sondka Z., Beare D.M., Bindal N., et al. (2019). COSMIC: the Catalogue Of Somatic Mutations In Cancer. *Nucleic Acids Research,* 47(D1): D941-D947.

232. Tsherniak A., Vazquez F., Montgomery P.G., Weir B.A., Kryukov G., Cowley G.S., et al. (2017). Defining a Cancer Dependency Map. *Cell,* 170(3): 564-576.e516.

233. Vasudevan K.M., Barbie D.A., Davies M.A., Rabinovsky R., McNear C.J., Kim J.J., et al. (2009). AKT-independent signaling downstream of oncogenic PIK3CA mutations in human cancer. *Cancer Cell,* 16(1): 21-32.

234. Zhang J.S., Koenig A., Harrison A., Ugolkov A.V., Fernandez-Zapico M.E., Couch F.J., et al. (2011). Mutant K-Ras increases GSK-3β gene expression via an ETS-p300 transcriptional complex in pancreatic cancer. *Oncogene,* 30(34): 3705-3715.

235. Pelletier J., Bellot G., Gounon P., Lacas-Gervais S., Pouysségur J., & Mazure N.M. (2012). Glycogen Synthesis is Induced in Hypoxia by the Hypoxia-Inducible Factor and Promotes Cancer Cell Survival. *Frontiers in Oncology,* 2: 18.

236. Keen H.G., Ricketts S.A., Maynard J., Logie A., Odedra R., Shannon A.M., et al. (2014). Examining changes in [18 F]FDG and [18 F]FLT uptake in U87-MG glioma xenografts as early response biomarkers to treatment with the dual mTOR1/2 inhibitor AZD8055. *Molecular Imaging and Biology,* 16(3): 421-430.

237. Fabian C., Koetz L., Favaro E., Indraccolo S., Mueller-Klieser W., & Sattler U.G. (2012). Protein profiles in human ovarian cancer cell lines correspond to their metabolic activity and to metabolic profiles of respective tumor xenografts. *FEBS Journal,* 279(5): 882-891.

238. Okubo M., Villar-Palasi C., Nagasaka Y., Larner J., Larner A.C., Bai G., et al. (1991). Long-term effects of insulin on the enzyme activity and messenger RNA of glycogen synthase in rat hepatoma H4 cells: an effect of insulin on glycogen synthase mRNA stability. *Arch Biochem Biophys,* 288(1): 126-130.

239. Muz B., de la Puente P., Azab F., & Azab A.K. (2015). The role of hypoxia in cancer progression, angiogenesis, metastasis, and resistance to therapy. *Hypoxia (Auckl),* 3: 83-92.

240. Kaelin W.G., Jr. (2008). The von Hippel-Lindau tumour suppressor protein: O2 sensing and cancer. *Nature Reviews: Cancer,* 8(11): 865-873.

241. Nagao A., Kobayashi M., Koyasu S., Chow C.C.T., & Harada H. (2019). HIF-1-Dependent Reprogramming of Glucose Metabolic Pathway of Cancer Cells and Its Therapeutic Significance. *International Journal of Molecular Sciences,* 20(2).

242. Wettersten H.I., Aboud O.A., Lara P.N., Jr., & Weiss R.H. (2017). Metabolic reprogramming in clear cell renal cell carcinoma. *Nat Rev Nephrol,* 13(7): 410-419.

243. Vengellur A., & LaPres J.J. (2004). The Role of Hypoxia Inducible Factor 1α in Cobalt Chloride Induced Cell Death in Mouse Embryonic Fibroblasts. *Toxicological Sciences,* 82(2): 638-646.

244. Du W., Zhang L., Brett-Morris A., Aguila B., Kerner J., Hoppel C.L., et al. (2017). HIF drives lipid deposition and cancer in ccRCC via repression of fatty acid metabolism. *Nat Commun,* 8(1): 1769.

245. Chen Z., Trotman L.C., Shaffer D., Lin H.K., Dotan Z.A., Niki M., et al. (2005). Crucial role of p53-dependent cellular senescence in suppression of Pten-deficient tumorigenesis. *Nature,* 436(7051): 725-730.

246. Nardella C., Clohessy J.G., Alimonti A., & Pandolfi P.P. (2011). Pro-senescence therapy for cancer treatment. *Nature Reviews: Cancer,* 11(7): 503-511.

247. Serra V., Markman B., Scaltriti M., Eichhorn P.J., Valero V., Guzman M., et al. (2008). NVP-BEZ235, a dual PI3K/mTOR inhibitor, prevents PI3K signaling and inhibits the growth of cancer cells with activating PI3K mutations. *Cancer Research,* 68(19): 8022-8030.

248. Fruman D.A., Chiu H., Hopkins B.D., Bagrodia S., Cantley L.C., & Abraham R.T. (2017). The PI3K Pathway in Human Disease. *Cell,* 170(4): 605-635.

249. Hemmings B.A., & Restuccia D.F. (2012). PI3K-PKB/Akt pathway. *Cold Spring Harbor Perspectives in Biology,* 4(9): a011189.

250. Chakravarti A., Zhai G., Suzuki Y., Sarkesh S., Black P.M., Muzikansky A., et al. (2004). The prognostic significance of phosphatidylinositol 3-kinase pathway activation in human gliomas. *Journal of Clinical Oncology,* 22(10): 1926-1933.

251. West K.A., Castillo S.S., & Dennis P.A. (2002). Activation of the PI3K/Akt pathway and chemotherapeutic resistance. *Drug Resist Updat,* 5(6): 234-248.

252. Garcia-Echeverria C., & Sellers W.R. (2008). Drug discovery approaches targeting the PI3K/Akt pathway in cancer. *Oncogene,* 27(41): 5511-5526.

253. Maira S.M., Stauffer F., Brueggen J., Furet P., Schnell C., Fritsch C., et al. (2008). Identification and characterization of NVP-BEZ235, a new orally available dual phosphatidylinositol 3-kinase/mammalian target of rapamycin inhibitor with potent in vivo antitumor activity. *Molecular Cancer Therapeutics,* 7(7): 1851-1863.

254. Azad A., Jackson S., Cullinane C., Natoli A., Neilsen P.M., Callen D.F., et al. (2011). Inhibition of DNA-dependent protein kinase induces accelerated senescence in irradiated human cancer cells. *Molecular Cancer Research,* 9(12): 1696-1707.

255. Francica P., Aebersold D.M., & Medová M. (2017). Senescence as biologic endpoint following pharmacological targeting of receptor tyrosine kinases in cancer. *Biochemical Pharmacology,* 126: 1-12.

256. Courtois-Cox S., Genther Williams S.M., Reczek E.E., Johnson B.W., McGillicuddy L.T., Johannessen C.M., et al. (2006). A negative feedback signaling network underlies oncogene-induced senescence. *Cancer Cell,* 10(6): 459-472.

257. Plas D.R., & Thompson C.B. (2005). Akt-dependent transformation: there is more to growth than just surviving. *Oncogene,* 24(50): 7435-7442.

258. Liu P., Cheng H., Roberts T.M., & Zhao J.J. (2009). Targeting the phosphoinositide 3-kinase pathway in cancer. *Nature Reviews: Drug Discovery,* 8(8): 627-644.

259. Phyu S.M., Tseng C.-C., Fleming I.N., & Smith T.A.D. (2016). Probing the PI3K/Akt/mTor pathway using 31P-NMR spectroscopy: routes to glycogen synthase kinase 3. *Scientific Reports,* 6(1): 36544.

260. Fang X., Yu S.X., Lu Y., Bast R.C., Woodgett J.R., & Mills G.B. (2000). Phosphorylation and inactivation of glycogen synthase kinase 3 by protein kinase A. *Proceedings of the National Academy of Sciences,* 97(22): 11960-11965.

261. Lheureux S., Lecerf C., Briand M., Louis M.H., Dutoit S., Jebahi A., et al. (2013). (18)F-FDG Is a Surrogate Marker of Therapy Response and Tumor Recovery after Drug Withdrawal during Treatment with a Dual PI3K/mTOR Inhibitor in a Preclinical Model of Cisplatin-Resistant Ovarian Cancer. *Translational Oncology,* 6(5): 586-595.

262. Makinoshima H., Takita M., Saruwatari K., Umemura S., Obata Y., Ishii G., et al. (2015). Signaling through the Phosphatidylinositol 3-Kinase (PI3K)/Mammalian Target of Rapamycin (mTOR) Axis Is Responsible for Aerobic Glycolysis mediated by Glucose

Transporter in Epidermal Growth Factor Receptor (EGFR)-mutated Lung Adenocarcinoma. *Journal of Biological Chemistry,* 290(28): 17495-17504.

263. Oishi T., Itamochi H., Kudoh A., Nonaka M., Kato M., Nishimura M., et al. (2014). The PI3K/mTOR dual inhibitor NVP-BEZ235 reduces the growth of ovarian clear cell carcinoma. *Oncology Reports,* 32(2): 553-558.
264. Potiron V.A., Abderrahmani R., Giang E., Chiavassa S., Di Tomaso E., Maira S.M., et al. (2013). Radiosensitization of prostate cancer cells by the dual PI3K/mTOR inhibitor BEZ235 under normoxic and hypoxic conditions. *Radiotherapy and Oncology,* 106(1): 138-146.
265. Mukherjee B., Tomimatsu N., Amancherla K., Camacho C.V., Pichamoorthy N., & Burma S. (2012). The dual PI3K/mTOR inhibitor NVP-BEZ235 is a potent inhibitor of ATM- and DNA-PKCs-mediated DNA damage responses. *Neoplasia,* 14(1): 34-43.
266. Imai T., Horiuchi A., Wang C., Oka K., Ohira S., Nikaido T., et al. (2003). Hypoxia attenuates the expression of E-cadherin via up-regulation of SNAIL in ovarian carcinoma cells. *American Journal of Pathology,* 163(4): 1437-1447.
267. Gomez-Roman N., Sahasrabudhe N.M., McGregor F., Chalmers A.J., Cassidy J., & Plumb J. (2016). Hypoxia-inducible factor 1 alpha is required for the tumourigenic and aggressive phenotype associated with Rab25 expression in ovarian cancer. *Oncotarget,* 7(16): 22650-22664.
268. Leiherer A., Geiger K., Muendlein A., & Drexel H. (2014). Hypoxia induces a HIF-1α dependent signaling cascade to make a complex metabolic switch in SGBS-adipocytes. *Mol Cell Endocrinol,* 383(1-2): 21-31.
269. Wang F., Li S.S., Segersvärd R., Strömmer L., Sundqvist K.G., Holgersson J., et al. (2007). Hypoxia inducible factor-1 mediates effects of insulin on pancreatic cancer cells and disturbs host energy homeostasis. *American Journal of Pathology,* 170(2): 469-477.
270. Zhang D., Cui L., Li S.S., & Wang F. (2015). Insulin and hypoxia-inducible factor-1 cooperate in pancreatic cancer cells to increase cell viability. *Oncology Letters,* 10(3): 1545-1550.
271. Liu G.M., & Zhang Y.M. (2018). Targeting FBPase is an emerging novel approach for cancer therapy. *Cancer Cell International,* 18: 36.
272. Leithner K. (2015). PEPCK in cancer cell starvation. *Oncoscience,* 2(10): 805.

273. Ning X.H., Li T., Gong Y.Q., He Q., Shen Q.I., Peng S.H., et al. (2016). Association between FBP1 and hypoxia-related gene expression in clear cell renal cell carcinoma. *Oncology Letters,* 11(6): 4095-4098.

274. Evans J.M., Donnelly L.A., Emslie-Smith A.M., Alessi D.R., & Morris A.D. (2005). Metformin and reduced risk of cancer in diabetic patients. *BMJ,* 330(7503): 1304-1305.

275. Dowling R.J., Lam S., Bassi C., Mouaaz S., Aman A., Kiyota T., et al. (2016). Metformin Pharmacokinetics in Mouse Tumors: Implications for Human Therapy. *Cell Metabolism,* 23(4): 567-568.

276. Andrzejewski S., Siegel P.M., & St-Pierre J. (2018). Metabolic Profiles Associated With Metformin Efficacy in Cancer. *Frontiers in Endocrinology,* 9: 372.

277. Zakikhani M., Dowling R., Fantus I.G., Sonenberg N., & Pollak M. (2006). Metformin is an AMP kinase-dependent growth inhibitor for breast cancer cells. *Cancer Research,* 66(21): 10269-10273.

278. Saini N., & Yang X. (2018). Metformin as an anti-cancer agent: actions and mechanisms targeting cancer stem cells. *Acta Biochim Biophys Sin (Shanghai),* 50(2): 133-143.

279. Rotondi M., Coperchini F., Pignatti P., Magri F., & Chiovato L. (2015). Metformin reverts the secretion of CXCL8 induced by TNF-α in primary cultures of human thyroid cells: an additional indirect anti-tumor effect of the drug. *J Clin Endocrinol Metab,* 100(3): E427-432.

280. Yi G., He Z., Zhou X., Xian L., Yuan T., Jia X., et al. (2013). Low concentration of metformin induces a p53-dependent senescence in hepatoma cells via activation of the AMPK pathway. *International Journal of Oncology,* 43(5): 1503-1510.

281. Moiseeva O., Deschênes-Simard X., St-Germain E., Igelmann S., Huot G., Cadar A.E., et al. (2013). Metformin inhibits the senescence-associated secretory phenotype by interfering with IKK/NF-κB activation. *Aging Cell,* 12(3): 489-498.

282. Chen D., Xia D., Pan Z., Xu D., Zhou Y., Wu Y., et al. (2016). Metformin protects against apoptosis and senescence in nucleus pulposus cells and ameliorates disc degeneration in vivo. *Cell Death & Disease,* 7.

283. Fang J., Yang J., Wu X., Zhang G., Li T., Wang X.e., et al. (2018). Metformin alleviates human cellular aging by upregulating the endoplasmic reticulum glutathione peroxidase 7. *Aging Cell,* 17(4): e12765.

284. Possik E., & Pause A. (2016). Glycogen: A must have storage to survive stressful emergencies. *Worm,* 5(2): e1156831.

285. Wojtaszewski J.F., Jørgensen S.B., Hellsten Y., Hardie D.G., & Richter E.A. (2002). Glycogen-dependent effects of 5-aminoimidazole-4-carboxamide (AICA)-riboside on AMP-activated protein kinase and glycogen synthase activities in rat skeletal muscle. *Diabetes,* 51(2): 284-292.

286. Hunter R.W., Treebak J.T., Wojtaszewski J.F., & Sakamoto K. (2011). Molecular mechanism by which AMP-activated protein kinase activation promotes glycogen accumulation in muscle. *Diabetes,* 60(3): 766-774.

287. Arad M., Benson D.W., Perez-Atayde A.R., McKenna W.J., Sparks E.A., Kanter R.J., et al. (2002). Constitutively active AMP kinase mutations cause glycogen storage disease mimicking hypertrophic cardiomyopathy. *Journal of Clinical Investigation,* 109(3): 357-362.

288. Roesch A., Vultur A., Bogeski I., Wang H., Zimmermann K.M., Speicher D., et al. (2013). Overcoming intrinsic multidrug resistance in melanoma by blocking the mitochondrial respiratory chain of slow-cycling JARID1B(high) cells. *Cancer Cell,* 23(6): 811-825.

289. Sun C., Wang L., Huang S., Heynen G.J., Prahallad A., Robert C., et al. (2014). Reversible and adaptive resistance to BRAF(V600E) inhibition in melanoma. *Nature,* 508(7494): 118-122.

290. Moore N., Houghton J., & Lyle S. (2012). Slow-cycling therapy-resistant cancer cells. *Stem Cells and Development,* 21(10): 1822-1830.

291. Ahn A., Chatterjee A., & Eccles M.R. (2017). The Slow Cycling Phenotype: A Growing Problem for Treatment Resistance in Melanoma. *Molecular Cancer Therapeutics,* 16(6): 1002-1009.

292. Wang Z., Kang F., Gao Y., Liu Y., Xu X., Ma X., et al. (2018). Metformin Promotes 2-Deoxy-2-[(18)F]Fluoro-D-Glucose Uptake in Hepatocellular Carcinoma Cells Through FoxO1-Mediated Downregulation of Glucose-6-Phosphatase. *Molecular Imaging and Biology,* 20(3): 388-397.

293. Mithieux G., Guignot L., Bordet J.C., & Wiernsperger N. (2002). Intrahepatic mechanisms underlying the effect of metformin in decreasing basal glucose production in rats fed a high-fat diet. *Diabetes,* 51(1): 139-143.

294. Bultot L., Guigas B., Von Wilamowitz-Moellendorff A., Maisin L., Vertommen D., Hussain N., et al. (2012). AMP-activated protein kinase phosphorylates and inactivates liver glycogen synthase. *Biochem J,* 443(1): 193-203.

295. Otto M., Breinholt J., & Westergaard N. (2003). Metformin inhibits glycogen synthesis and gluconeogenesis in cultured rat hepatocytes. *Diabetes, Obesity & Metabolism,* 5(3): 189-194.

296. Clark A.S., Karasic T.B., DeMichele A., Vaughn D.J., O'Hara M., Perini R., et al. (2016). Palbociclib (PD0332991)-a Selective and Potent Cyclin-Dependent Kinase Inhibitor: A Review of Pharmacodynamics and Clinical Development. *JAMA Oncol,* 2(2): 253-260.

297. Comstock C.E., Augello M.A., Goodwin J.F., de Leeuw R., Schiewer M.J., Ostrander W.F., Jr., et al. (2013). Targeting cell cycle and hormone receptor pathways in cancer. *Oncogene,* 32(48): 5481-5491.

298. Sobhani N., D'Angelo A., Pittacolo M., Roviello G., Miccoli A., Corona S.P., et al. (2019). Updates on the CDK4/6 Inhibitory Strategy and Combinations in Breast Cancer. *Cells,* 8(4).

299. Konecny G.E., Winterhoff B., Kolarova T., Qi J., Manivong K., Dering J., et al. (2011). Expression of p16 and retinoblastoma determines response to CDK4/6 inhibition in ovarian cancer. *Clin Cancer Res,* 17(6): 1591-1602.

300. Michaud K., Solomon D.A., Oermann E., Kim J.S., Zhong W.Z., Prados M.D., et al. (2010). Pharmacologic inhibition of cyclin-dependent kinases 4 and 6 arrests the growth of glioblastoma multiforme intracranial xenografts. *Cancer Research,* 70(8): 3228-3238.

301. Chou A., Froio D., Nagrial A.M., Parkin A., Murphy K.J., Chin V.T., et al. (2018). Tailored first-line and second-line CDK4-targeting treatment combinations in mouse models of pancreatic cancer. *Gut,* 67(12): 2142-2155.

302. Dean J.L., Thangavel C., McClendon A.K., Reed C.A., & Knudsen E.S. (2010). Therapeutic CDK4/6 inhibition in breast cancer: key mechanisms of response and failure. *Oncogene,* 29(28): 4018-4032.

303. Cristofanilli M., Turner N.C., Bondarenko I., Ro J., Im S.A., Masuda N., et al. (2016). Fulvestrant plus palbociclib versus fulvestrant plus placebo for treatment of hormone-receptor-positive, HER2-negative metastatic breast cancer that progressed on previous endocrine therapy (PALOMA-3): final analysis of the multicentre, double-blind, phase 3 randomised controlled trial. *Lancet Oncology,* 17(4): 425-439.

304. Flaherty K.T., Lorusso P.M., Demichele A., Abramson V.G., Courtney R., Randolph S.S., et al. (2012). Phase I, dose-escalation trial of the oral cyclin-dependent kinase 4/6 inhibitor PD 0332991, administered using a 21-day schedule in patients with advanced cancer. *Clin Cancer Res,* 18(2): 568-576.

305. Schwartz G.K., LoRusso P.M., Dickson M.A., Randolph S.S., Shaik M.N., Wilner K.D., et al. (2011). Phase I study of PD 0332991, a cyclin-dependent kinase inhibitor, administered in 3-week cycles (Schedule 2/1). *British Journal of Cancer,* 104(12): 1862-1868.

306. Finn R.S., Dering J., Conklin D., Kalous O., Cohen D.J., Desai A.J., et al. (2009). PD 0332991, a selective cyclin D kinase 4/6 inhibitor, preferentially inhibits proliferation of luminal estrogen receptor-positive human breast cancer cell lines in vitro. *Breast Cancer Research,* 11(5): R77.

307. Fry D.W., Harvey P.J., Keller P.R., Elliott W.L., Meade M., Trachet E., et al. (2004). Specific inhibition of cyclin-dependent kinase 4/6 by PD 0332991 and associated antitumor activity in human tumor xenografts. *Molecular Cancer Therapeutics,* 3(11): 1427-1438.

308. Bollard J., Miguela V., Ruiz de Galarreta M., Venkatesh A., Bian C.B., Roberto M.P., et al. (2017). Palbociclib (PD-0332991), a selective CDK4/6 inhibitor, restricts tumour growth in preclinical models of hepatocellular carcinoma. *Gut,* 66(7): 1286-1296.

309. Sumi N.J., Kuenzi B.M., Knezevic C.E., Remsing Rix L.L., & Rix U. (2015). Chemoproteomics Reveals Novel Protein and Lipid Kinase Targets of Clinical CDK4/6 Inhibitors in Lung Cancer. *ACS Chemical Biology,* 10(12): 2680-2686.

310. Vijayaraghavan S., Karakas C., Doostan I., Chen X., Bui T., Yi M., et al. (2017). CDK4/6 and autophagy inhibitors synergistically induce senescence in Rb positive cytoplasmic cyclin E negative cancers. *Nat Commun,* 8: 15916.

311. Kovatcheva M., Liu D.D., Dickson M.A., Klein M.E., O'Connor R., Wilder F.O., et al. (2015). MDM2 turnover and expression of ATRX determine the choice between quiescence and senescence in response to CDK4 inhibition. *Oncotarget,* 6(10): 8226-8243.

312. Alkhalaf M., El-Mowafy A.M., & Abou-Zeid L.A. (2005). Progesterone inhibition of MDM2 p90 protein in MCF-7 human breast cancer cell line is dependent on p53 levels. *Journal of Molecular and Genetic Medicine,* 1(1): 33-37.

313. Miettinen T.P., Peltier J., Hartlova A., Gierlinski M., Jansen V.M., Trost M., et al. (2018). Thermal proteome profiling of breast cancer cells reveals proteasomal activation by CDK4/6 inhibitor palbociclib. *EMBO Journal,* 37(10).

314. Leite de Oliveira R., & Bernards R. (2018). Anti-cancer therapy: senescence is the new black. *EMBO Journal,* 37(10).

315. Franco J., Balaji U., Freinkman E., Witkiewicz A.K., & Knudsen E.S. (2016). Metabolic Reprogramming of Pancreatic Cancer Mediated by CDK4/6 Inhibition Elicits Unique Vulnerabilities. *Cell Reports,* 14(5): 979-990.

316. Hsieh F.S., Chen Y.L., Hung M.H., Chu P.Y., Tsai M.H., Chen L.J., et al. (2017). Palbociclib induces activation of AMPK and inhibits hepatocellular carcinoma in a CDK4/6-independent manner. *Molecular Oncology,* 11(8): 1035-1049.

317. Rencuzogullari O., Yerlikaya P.O., Gurkan A.C., Arisan E.D., & Telci D. (2020). Palbociclib, a selective CDK4/6 inhibitor, restricts cell survival and epithelial-mesenchymal transition in Panc-1 and MiaPaCa-2 pancreatic cancer cells. *Journal of Cellular Biochemistry,* 121(1): 508-523.

318. Keen N., & Taylor S. (2004). Aurora-kinase inhibitors as anticancer agents. *Nature Reviews: Cancer,* 4(12): 927-936.

319. Manfredi M.G., Ecsedy J.A., Meetze K.A., Balani S.K., Burenkova O., Chen W., et al. (2007). Antitumor activity of MLN8054, an orally active small-molecule inhibitor of Aurora A kinase. *Proceedings of the National Academy of Sciences of the United States of America,* 104(10): 4106-4111.

320. Gire V., & Dulic V. (2015). Senescence from G2 arrest, revisited. *Cell Cycle,* 14(3): 297-304.

321. Hoar K., Chakravarty A., Rabino C., Wysong D., Bowman D., Roy N., et al. (2007). MLN8054, a small-molecule inhibitor of Aurora A, causes spindle pole and chromosome congression defects leading to aneuploidy. *Mol Cell Biol,* 27(12): 4513-4525.

322. Baus F., Gire V., Fisher D., Piette J., & Dulic V. (2003). Permanent cell cycle exit in G2 phase after DNA damage in normal human fibroblasts. *EMBO Journal,* 22(15): 3992-4002.

323. Charrier-Savournin F.B., Chateau M.T., Gire V., Sedivy J., Piette J., & Dulic V. (2004). p21-Mediated nuclear retention of cyclin B1-Cdk1 in response to genotoxic stress. *Molecular Biology of the Cell,* 15(9): 3965-3976.

324. Liu L.L., Long Z.J., Wang L.X., Zheng F.M., Fang Z.G., Yan M., et al. (2013). Inhibition of mTOR pathway sensitizes acute myeloid leukemia cells to aurora inhibitors by suppression of glycolytic metabolism. *Molecular Cancer Research,* 11(11): 1326-1336.

325. Xu L.Z., Long Z.J., Peng F., Liu Y., Xu J., Wang C., et al. (2014). Aurora kinase a suppresses metabolic stress-induced autophagic cell death by activating mTOR signaling in breast cancer cells. *Oncotarget,* 5(17): 7498-7511.

326. Gorgoulis V., Adams P.D., Alimonti A., Bennett D.C., Bischof O., Bishop C., et al. (2019). Cellular Senescence: Defining a Path Forward. *Cell,* 179(4): 813-827.

327. Carroll L., Witney T.H., & Aboagye E.O. (2013). Design and synthesis of novel 18F-radiolabelled glucosamine derivatives for cancer imaging. *MedChemComm,* 4(4): 653-656.

328. Yang Z., Xiong C., Zhang R., Zhu H., & Li C. (2012). Synthesis and evaluation of (68)Ga-labeled DOTA-2-deoxy-D-glucosamine as a potential radiotracer in μPET imaging. *American Journal of Nuclear Medicine and Molecular Imaging,* 2(4): 499-507.

329. Qi C.-M., He Y., Wang X., Feng M., Xu J.-L., Ding R., et al. (2011). Synthesis and evaluation of N-(2-[18F]fluoro-4-nitrobenzoyl)glucosamine: a preliminary report. *Journal of Radioanalytical and Nuclear Chemistry,* 287(3): 913-920.

330. Lee S.C., Kang N.Y., Park S.J., Yun S.W., Chandran Y., & Chang Y.T. (2012). Development of a fluorescent chalcone library and its application in the discovery of a mouse embryonic stem cell probe. *Chemical Communications (Cambridge, England),* 48(53): 6681-6683.

331. Aboagye E., Allott L., Brickute D., Chen C., Barnes C., & Wang N. Development of a fluorine-18 radiolabelled fluorescent chalcone: evaluated for detecting glycogen&quot. *EJNMMI Radiopharmacy and Chemistry*.

332. Xu Z.Y., & Li J.L. (2019). Comparative review of drug-drug interactions with epidermal growth factor receptor tyrosine kinase inhibitors for the treatment of non-small-cell lung cancer. *OncoTargets and Therapy,* 12: 5467-5484.

333. Flor A.C., & Kron S.J. (2016). Lipid-derived reactive aldehydes link oxidative stress to cell senescence. *Cell Death & Disease,* 7(9): e2366.

334. Dowson J.H., & Harris S.J. (1981). Quantitative studies of the autofluorescence derived from neuronal lipofuscin. *J Microsc,* 123(Pt 3): 249-258.

335. Evangelou K., & Gorgoulis V.G. (2017). Sudan Black B, The Specific Histochemical Stain for Lipofuscin: A Novel Method to Detect Senescent Cells. *Methods in Molecular Biology,* 1534: 111-119.

336. Salmonowicz H., & Passos J.F. (2017). Detecting senescence: a new method for an old pigment. *Aging Cell,* 16(3): 432-434.

337. Jung T., Höhn A., & Grune T. (2010). Lipofuscin: detection and quantification by microscopic techniques. *Methods in Molecular Biology,* 594: 173-193.

338. Innes A.J., & Gil J. (2019). IMR90 ER:RAS: A Cell Model of Oncogene-Induced Senescence. *Methods in Molecular Biology,* 1896: 83-92.

339. Krüger M., Cotton J., Zhou B., Wolter K., Schwenck J., Kuehn A., et al. (2019). Abstract 1146: [18F]FPyGal: A novel ß-galactosidase specific PET tracer forin vivoimaging of tumor senescence. *Cancer Research,* 79: 1146-1146.

340. Slade R.L., Pisaneschi F., Nguyen Q.D., Smith G., Carroll L., Beckley A., et al. (2016). Identification of ABC Transporter Interaction of a Novel Cyanoquinoline Radiotracer and Implications for Tumour Imaging by Positron Emission Tomography. *PloS One,* 11(8): e0161427.

341. Parrish K.E., Pokorny J., Mittapalli R.K., Bakken K., Sarkaria J.N., & Elmquist W.F. (2015). Efflux transporters at the blood-brain barrier limit delivery and efficacy of cyclin-dependent kinase 4/6 inhibitor palbociclib (PD-0332991) in an orthotopic brain tumor model. *J Pharmacol Exp Ther,* 355(2): 264-271.

342. Li Y.J., Lei Y.H., Yao N., Wang C.R., Hu N., Ye W.C., et al. (2017). Autophagy and multidrug resistance in cancer. *Chinese Journal of Cancer,* 36(1): 52.

343. Shuhua W., Chenbo S., Yangyang L., Xiangqian G., Shuang H., Tangyue L., et al. (2015). Autophagy-related genes Raptor, Rictor, and Beclin1 expression and relationship with multidrug resistance in colorectal carcinoma. *Human Pathology,* 46(11): 1752-1759.

344. James E.L., Michalek R.D., Pitiyage G.N., de Castro A.M., Vignola K.S., Jones J., et al. (2015). Senescent human fibroblasts show increased glycolysis and redox homeostasis with extracellular metabolomes that overlap with those of irreparable DNA damage, aging, and disease. *Journal of Proteome Research,* 14(4): 1854-1871.

345. Dörr J.R., Yu Y., Milanovic M., Beuster G., Zasada C., Däbritz J.H., et al. (2013). Synthetic lethal metabolic targeting of cellular senescence in cancer therapy. *Nature,* 501(7467): 421-425.

346. van Deursen J.M. (2014). The role of senescent cells in ageing. *Nature,* 509(7501): 439-446.

347. Bouskila M., Hunter R.W., Ibrahim A.F., Delattre L., Peggie M., van Diepen J.A., et al. (2010). Allosteric regulation of glycogen synthase controls glycogen synthesis in muscle. *Cell Metabolism,* 12(5): 456-466.

348. von Wilamowitz-Moellendorff A., Hunter R.W., Garcia-Rocha M., Kang L., Lopez-Soldado I., Lantier L., et al. (2013). Glucose-6-phosphate-mediated activation of liver glycogen synthase plays a key role in hepatic glycogen synthesis. *Diabetes,* 62(12): 4070-4082.

349. Villar-Palasi C., & Guinovart J.J. (1997). The role of glucose 6-phosphate in the control of glycogen synthase. *FASEB Journal,* 11(7): 544-558.

350. Meijer L., Flajolet M., & Greengard P. (2004). Pharmacological inhibitors of glycogen synthase kinase 3. *Trends in Pharmacological Sciences,* 25(9): 471-480.

351. Halse R., Fryer L.G., McCormack J.G., Carling D., & Yeaman S.J. (2003). Regulation of glycogen synthase by glucose and glycogen: a possible role for AMP-activated protein kinase. *Diabetes,* 52(1): 9-15.

352. Casella G., Munk R., Kim K.M., Piao Y., De S., Abdelmohsen K., et al. (2019). Transcriptome signature of cellular senescence. *Nucleic Acids Research,* 47(21): 11476.

353. Hernandez-Segura A., de Jong T.V., Melov S., Guryev V., Campisi J., & Demaria M. (2017). Unmasking Transcriptional Heterogeneity in Senescent Cells. *Current Biology,* 27(17): 2652-2660 e2654.

Permissions Table

| Page No. | Type of work: | Name of work | Source of work | Copyright holder and contact | permission requested on | I have permission yes /no |
|---|---|---|---|---|---|---|
| 54 | Figure | **Figure 1.11** Examples of [$^{18}$F]FLT-PET to assess anticancer treatment response in preclinical mice models. **(B)** Examples of [$^{18}$F]FLT-PET images of RIF-1 tumour-bearing mice after cisplatin treatment. | Early Detection of Tumor Response to Chemotherapy by 3'-Deoxy-3'-[$^{18}$F]Fluorothymidine Positron Emission Tomography: The Effect of Cisplatin on a Fibrosarcoma Tumor Model *In vivo* | ©2005 American Association for Cancer Research | 21.09.20 | Yes |
| 54 | Figure | **Figure 1.11** Examples of [$^{18}$F]FLT-PET to assess anticancer treatment response in preclinical mice models. **(C)** Examples of [$^{18}$F]FLT-PET images of HCT116 tumour-bearing mice after LAQ824 treatment. | *In vivo* Biological Activity of the Histone Deacetylase Inhibitor LAQ824 Is detectable with 3'-Deoxy-3'-[$^{18}$F]Fluorothymidine Positron Emission Tomography | ©2006 American Association for Cancer Research | 21.09.20 | Yes |